DISORDERED QUANTUM WELL WAVEGUIDE FABRICATION AND ULTRAFAST OPTICAL CHARACTERIZATION

by

Kristin Kay Anderson

B.S.E.E., University of Minnesota
(1984)

S.M., Massachusetts Institute of Technology
(1986)

Submitted in partial fulfillment of the
requirements for the degree of

DOCTOR OF PHILOSOPHY

at the

MASSACHUSETTS INSTITUTE OF TECHNOLOGY

October, 1989

Signature of
Author____
Department of Electrical Engineering and Computer Science
October 15, 1989

Certified
by____
Professor Hermann A. Haus
Thesis Supervisor

Accepted
by____
Professor Arthur C. Smith
Chairman, Departmental Committee on Graduate Students

DISORDERED QUANTUM WELL WAVEGUIDE FABRICATION AND ULTRAFAST OPTICAL CHARACTERIZATION

by

KRISTIN KAY ANDERSON

Submitted to the Department of Electrical Engineering
and Computer Science on October 15, 1989 in partial fulfillment
of the requirements for the degree of Doctor of Philosophy
in Electrical Engineering and Computer Science

ABSTRACT

A new method has been developed for compositional mixing of heterostructures using elevated-temperature ion bombardment (ETBD). Complete mixing of a 1-μm-thick GaAs/AlGaAs 40-period multiple quantum well layer was achieved by bombardment with 380 keV Ne^+ ions. The resulting alloy has an aluminum mole fraction that is the average of the original quantum well layer. Intermixing using lighter N^+ and heavier Ar^+ for bombardment was also demonstrated, though He^+ and H^+ bombardment did not cause mixing. Unlike other mixing techniques, ETBD is a collisional process and does not require dopants that can increase absorption in the layer. In addition, the elevated target temperature reduces residual damage caused by bombardment. From a first order model of ETBD, it was predicted, and subsequently demonstrated, that intermixing can be achieved for a target temperature as low as 400°C, the lowest temperature reported for achieving mixing by any technique. Also, intermixing was achieved for a bombardment time as short as 5 minutes. Successful patterning of ETBD was developed using both epitaxially grown AlGaAs and thick SiO_2 layers as masks. Post-ETBD annealing was shown to reduce residual damage. Elevated temperature bombardment disordering was used to fabricate index-guided multiple quantum well waveguides. Waveguide far field measurements verify the index-guided mode profile. Waveguide losses were 3-7 cm^{-1}, significantly less than the lowest reported loss at comparable wavelengths for waveguides fabricated by impurity-induced disordering.

The second part of the thesis concerns ultrafast all-optical switching properties of semiconductor waveguides. The measurements utilize a new technique based on a single-arm interferometer. Precise measurements of the nonlinear index of refraction, n_2, are obtained in the absence of thermal and acoustic parasitics. The first femtosecond measurement of n_2 as a function of wavelength below the band gap in AlGaAs was performed. The measured n_2 represents the largest reported nonresonant value in any semiconductor. Measurements indicate that two-photon absorption, which generates free carriers and causes additional insertion loss, provides a limit to the usefulness of the nonlinearity. Additionally, self-phase modulation coupled with group velocity dispersion causes limitations for all-optical switching due to pulse broadening. By optimizing the wavelength and pulse intensity, the largest phase shift that can be obtained for 500 fs pulse durations is $\approx\pi$. Preliminary optical characterization of multiple quantum well waveguides fabricated with ETBD indicates this material behaves similarly to bulk AlGaAs.

Thesis supervisor:	Professor Hermann A. Haus
Title:	Institute Professor of Electrical Engineering

ACKNOWLEDGEMENTS

For his guidance, encouragement, enthusiasm and wisdom, I am grateful to Prof. Hermann A. Haus. He is truly an inspiration. Dr. Joe Donnelly, who conceived ETBD, was a constant source of helpful ideas and support. His help on the manuscript is also appreciated. Prof. James Fujimoto's encouragement and insight were very helpful. I appreciate Prof. Cliff Fonstad's guidance and support throughout the project, and thank Prof. Leslie Kolodzeijski for serving on my committee with short notice. Dr. Christine Wang supplied high quality material for the majority of the thesis work. Her enthusiasm and hard work are appreciated. Dr. Robert Rediker has been a constant source of advice and support throughout graduate school. His efforts are sincerely appreciated.

I enjoyed collaboration with Dr. Michael LaGasse. His expertise coupled with his sense of humor made a long and tiring project more bearable. I am also grateful to Richard Singer for providing material and other technical help as well as friendly discussions.

Many individuals at Lincoln Laboratory helped to make my experience there very rewarding. Dr. Dick Williamson and Dr. Dave Spears provided not only the resources of the group, but helpful advice as well. John Woodhouse was a source of ideas, support and friendship. Mark McAleese's many hours on the ion implanter and efforts to keep me laughing are appreciated. Paul Nitishin provided SEM and TEM expertise as well as many hours of friendly and helpful discussions. I am grateful to Mary Finn for providing Auger electron spectroscopy, and Dr. George Turner for photoluminescence. Dr. Bill Goodhue's help with TEM and Jerry Johnson's aid in sample preparation is appreciated. I am grateful to Joe Ferrante for teaching me about processing and for always being cheerful, helpful and supportive. Leon Belanger's friendly assistance with the spectrophotometer is appreciated.

The friendship, technical assistance and helpful ideas of many other people at Lincoln Laboratory are appreciated: Dr. Brian Aull, Dr. Charlie Cox, Dr. Vicky Diadiuk, Dr. Zong-Long Liau, Lynn Ericksen, Glenn Brigham, Ben DiGiorgio, Dan Calawa, Tom Lind, Skip Hoyt, Steve Conner, Dan Mull, Bob Bailey, Katie Coble and Steve Rabe. Nancy Blue's helpful assistance is also appreciated.

On campus, whether she likes it or not, Cindy Kopf was very helpful and has a great sense of humor. Also, I thank Wei-Ping Huang for sharing his waveguide expertise. The freindship, technical work and discussions with Don Bossi have been invaluable. I have also enjoyed the friendship of and technical discussions with my fellow graduate students, Janice Huxley, Mary Phillips, Steve Hannon, Dr. Dan Yap, Dr. Lynne Orre, Stuart Brorson, Chris Corcoran and Susanne Lau.

Special thanks to my father, Dr. Bruce D. Anderson, my mother, Nancy Anderson, and my sister, Kari Anderson, for their constant support and love. My new husband, Dr. Kurt Rauschenbach, has been an inspiration for me. He has helped in all aspects of my work. The understanding and love of my family made everything easier and more meaningful.

I appreciate the resources made available to me at Lincoln Laboratory. Finally, I would like to thank the Fannie and John Hertz Foundation for their generous support over the years.

TABLE OF CONTENTS

LIST OF TABLES

Table Page

LIST OF FIGURES

Figure Page

Chapter 1

INTRODUCTION

Section 1.1 Motivation

Integrated optics is an active subject of research because of its potential uses in optical communications and signal processing. To utilize the large bandwidths achievable in optical systems, very high-speed modulation is required. To achieve this, all-optical configurations are necessary. The first picosecond all-optical switch in a $LiNbO_3$ waveguide was demonstrated in 1983 (Lattes et al.). III-V semiconductor materials have the advantage that lasers and electronic devices can be integrated with the all-optical switch. In addition the fabrication technologies for III-V materials are well established. The work presented in this thesis involves both the development of a compositional intermixing technique that allows fabrication of a variety of semiconductor integrated optical devices, and experimental characterization of optical switching in semiconductor waveguides.

The progress of integrated all-optical switching using semiconductors has been limited because the optical nonlinearities examined to date are largest close to the band edge where linear absorption is high. Residual carriers generated by absorption must recombine, which slows down the response times and leads to temperature increases that can degrade device performance. While large optical nonlinearities may occur in new materials such as doped glasses or organic polymers (Friberg and Smith; and Chang, T.Y.), the impetus for semiconductor-based devices remains strong. Recent investigations of the optical Stark effect show promise for ultrafast switching in multiple quantum well devices. Semiconductor optical properties are inherently linked to the band-structure, and this can be manipulated by precisely controlled material growth. Therefore, the possibility of new optical phenomena in these semiconductor structures is strong. In particular, resonantly enhanced transport through quantum-well barriers could lead to faster carrier-based optical devices. Optical processes between energy levels that result from quantum confinement effects (Yuen), including phonon assisted transitions, may be utilized. Strained layer materials can be used to create large electric dipoles which enhance nonlinear optical properties. Development of mode-locked semiconductor laser diodes with short output pulses makes the study and development all-optical integrated switching devices even more essential.

For realizing the potential applications of semiconductor materials to all-optical switching devices, the waveguide geometry is beneficial for several reasons. First, it is easily integrated with other optical devices on one chip. Second, it provides a long length of interaction with a tightly confined light beam so smaller nonlinear optical coefficients may be used. The mode size determines the overlap of the control and signal beams in a device configuration. Additionally, birefringence of the two orthogonal modes may be beneficial in some device configurations.

In this thesis a novel technique to compositionally disorder, or intermix, semiconductor heterojunctions that can be used for fabrication of nonlinear optical waveguide devices is described. Intermixing heterojunctions provides control of the refractive index and absorption laterally across a wafer. As is discussed in Section {7.2}, intermixing causes changes in the optical properties by changing the material composition. The current methods reported to achieve intermixing utilize incorporation of dopants into a layer and using a high-temperature annealing process. The drawbacks of the current methods include the use of dopants, which can increase absorption, and the long high-temperature annealing. The new intermixing technique described here utilizes elevated temperature ion bombardment, and can successfully intermix thick multiple quantum well layers and so that a uniform alloy with an aluminum concentration which is the average of the original multiple quantum well layer is formed (Anderson et al., 1988). This elevated temperature bombardment disordering, or ETBD, is based on collisions so that electrically inactive ion species may be used and dopants are not required. The technique is general, and may be used with a variety of semiconductor materials for many optical device applications. By means of this technique, thicker quantum well layers may be disordered at lower temperatures than the annealing temperatures employed after implantation or bombardment at room temperature.

The changes in the optical properties due to intermixing have been used to fabricate lasers and passive waveguide devices (Holonyak et al.; Gavrilovic et al., b.; Deppe et al., 1986; Thornton et al., 1986; Deppe et al., 1987; Guido et al, b.; Epler et al, 1988, b.; and Julien et al.). Another application for disordered materials is for nonabsorbing mirrors for quantum well lasers. Facet damage due to heating can limit the total output power from semiconductor lasers. If a small section of nonabsorbing material adjacent to the active region provides the cleaved facet for laser feedback, the peak output power in diode lasers can be increased. In addition disordering of multiple quantum wells has application to all-optical switching devices. As mentioned earlier, the large linear absorption which accompanies large optical nonlinearities resonant with the material band edge can significantly increase insertion loss. A number of μm-thick nonlinear Fabry-Perot switching devices that operate with the light incident perpendicular to the layer plane have been demonstrated. However, for many applications, such as integrating lasers and modulators, and for optical interconnection, waveguide geometries are necessary. Compositional disordering allows the fabrication of small areas of multiple quantum wells that are designed to be resonant with the incoming light source and surrounded by the nonresonant, low loss, compositionally intermixed alloy. Waveguides could be formed in the low loss alloy regions, with the nonlinear interaction occur in the multiple quantum well regions.

This thesis emphasizes the application of the new intermixing technique to fabricating semiconductor multiple quantum well waveguides. The new technique has the potential for making impurity-free buried symmetric waveguide structures. Except for etch and regrowth, intermixing is currently the only fabrication method that allows this. The new intermixing technique produces lower losses than the previously demonstrated compositionally disordered waveguides using impurities. A compositionally disordered waveguide fabricated by a Si-impurity-disordered process was reported with 9 cm^{-1} of linear loss (Werner et al.). The waveguides tested in this thesis show 3-7 cm^{-1} of loss, which is encouraging for a preliminary demonstration. Lower losses should be achieved with more development. In addition to eliminating excess impurities, the ion bombardment process provides more control over lateral mixing than is possible with a diffusion process. This produces a well-defined waveguide edge.

In the second part of this thesis, experiments that demonstrate the optical switching properties of AlGaAs are presented. Preliminary optical characterization of multiple quantum wells is also included. The work provides the first investigation of the switching phenomena on a sub-picosecond time scale. This allows ultrafast switching properties to be distinguished from slower processes. The measurements are performed with a new measurement technique, time-division interferometery (Lagasse et al., 1989), that allows the nonlinear index of refraction to be measured while minimizing thermal contributions. The nonlinear properties are studied as a function of wavelength near the band edge to determine the resonant behavior. These wavelengths are also important because they are the optical frequencies characteristic of an optical laser device on the same wafer as the waveguide. The nonlinear index of refraction for femtosecond switching is measured as a function of detuning from the band edge. The magnitude of the nonlinearity is comparable to the largest measured nonlinear index of refraction in semiconductor materials. Nonlinear absorption, specifically two-photon absorption, is also characterized. The results indicate that the carrier generation and induced absorption due to the two-photon absorption process limits the usefulness of the large refractive index nonlinearity for switching applications. These results are important for future optical switching devices from semiconductor materials.

Section 1.2 Previous Work

The research presented in this thesis can be divided into two parts: the first being compositional disordering or layer intermixing in semiconductor heterostructures, and the second being optical switching properties of AlGaAs/GaAs materials. The previous work in these areas is reviewed in this section.

1.2.a Layer Intermixing

Compositional intermixing relies on the fact that atomic diffusion is enhanced in the presence of defects, namely vacancies and interstitials. In fact, radiation-enhanced diffusion in metals due to the creation of defects was predicted as much as thirty years ago (Dienes and Damask). Also, the enhancement of Zn diffusion in GaAs due to high concentrations of zinc was found experimentally in 1962 (Longini). In the early 1970's, enhanced diffusion of impurities in semiconductors during elevated temperature ion implantation was reported by several groups (Tsuchimoto and Tokuyama; Namba et al.; and Guseva and Mansurova).

Impurity-induced Disordering

Although enhancing diffusion constants in solids has been in existence for some time, it was not until the demonstration of compositional disordering of semiconductor multiple quantum wells and abrupt heterojunctions by Laidig et al. in 1981 that the potential for fabricating optical devices was made apparent. Laidig's work utilized 650°C, 20 minute Zn diffusion to intermix a multiple quantum well 1 μm thick. Fukuzawa used the technique to fabricate laser devices three years later (Fukuzawa et al.). These first results spawned a great deal of interest in compositional disordering of semiconductor heterojunctions. Most of the work reported to date has been centered on developing and understanding the various methods to achieve intermixing. A few optical devices, lasers and waveguides, have been fabricated with disordering techniques. In what follows, some of the important results to date are given. Previous work that is directly applicable to the thesis work is described in more detail.

In addition to zinc, compositional disordering of GaAs-AlGaAs superlattices has also been achieved using other dopant species. Silicon induced intermixing has been demonstrated with significantly less efficiency than the zinc. Diffusion times of up to 10 hrs. at 850°C are required with the silicon (Meehan et al.). Even so, laser devices (Deppe et al., 1987) and even a monolithic laser and waveguide modulator (Thornton et al.) were fabricated by the Si diffusion technique. Other dopants, Sn (Rao et al., 1987), Ge (Kaliski et al., 1985), Se (Kaliski et al., 1987), Be (Kamata et al.), and Mg (Kaliski et al., 1987) have also been used. Dopants are introduced into the layer during growth as well as through diffusion. The other dopants typically require annealing times of several hours and temperatures ranging from 750°C to 950°C.

Impurities used for disordering are also incorporated into the layer with ion implantation. Most of the work has focused on Si^+ ion implantation. Post-implantation annealing temperature and times are typically 850°C for 1-3 hrs (Venkatesan et al.; Ishda et al.; and Schwarz et al.). The results indicate intermixing of <0.5-μm-thick regions. In contrast, rapid thermal annealing at 1050°C for 10 s of Si^+ implanted layers causes disordering of ≈0.2-μm-thick regions of a GaAs/AlGaAs superlattice material (Tong-Lee et al.). Si-implantation and post-implant annealing were used to fabricate stripe-geometery lasers (Gavrilovic et al., b.). Ion implantation of other species, Be^+, Mg^+, and Se^+, has also been attempted (Ralston et al., 1986). After implantation and post-implantation annealing, the layers all show significant damage in the form of dislocation loops that are evident in TEM cross-sections. Laser-incorporated silicon and subsequent 4 hr. 850°C annealing result in intermixing thicknesses of 1 μm (Epler et al., 1988, a.). In fact, laser induced melting and subsequent recrystallization have also been shown to produce mixing (Epler et al., 1986). This technique has been used to fabricate a laser device (Epler et al, 1988, b.). These methods described above utilize impurities. A review of impurity-induced layer disordering has recently been published that provides a more complete summary of the results reported to date (Deppe et al., 1988).

Impurity-free methods

Particularly for optical devices, impurity band-tail and free carrier absorption and refractive index changes are undesirable. In fact, complete quenching of the photoluminescence was reported due to high dopant concentrations in layers disordered with Si diffusion (Meehan et al.). Impurity-free methods have been developed to circumvent the problem. In particular, and closely related to the thesis work, vacancies created by ion implantation of elements that are not dopants in GaAs have been shown to induce intermixing of multiple quantum wells during post-implantation annealing procedures. Thus far, ions of the constituent elements Al^+, Ga^+, and As^+, as well as the ion of the inert element Kr have been used with limited success (Gavrilovic et al., a.; Hirayama et al.; Cibert et al.; and Mei et al.). The best results are summarized in Table {1.1} below.

ION	ENERGY keV	TARGET TEMP. °C	ANNEAL TEMP./ TIME	THICKNESS MIXED µm	REFERENCE
Ga^+	100	25°	750°C/1hr	0.055	Hirayama et al.
Al^+	390	25°	850°/8.3hr	0.76	Gavrilovic et al., a.
Kr^+	390	25°	850°/8.3hr	0.80	Gavrilovic et al., a.

These results indicate that very long post-implantation annealing is required to achieve mixing of thicknesses close to a micron.

Defects in ion-implanted layers for both impurity and impurity-free processes have proven to be a significant drawback of the implantation and post-annealing disordering techniques. To reduce damage, one attempt was made using Si^+, and S^+ implantation with various target temperatures from 77°K to 210°C (Dobisz et al.). The prediction was that lower temperatures would freeze in more vacancies and produce more mixing, but that higher target temperatures, while reducing the effectiveness of the intermixing, should decrease the residual damage. The results did indicate the most effective disordering occurs for implants performed at 77 K, but the layer shows significant damage. Reduced damage, and enhanced mixing occurred in the samples implanted at 210°C compared to room temperature. Though the result was not explained, it is likely related to mixing during implantation, the effect reported in this thesis. The 210°C target temperature investigated is significantly lower than the temperatures used for the work presented here. This is evidenced by the fact that the thicknesses that were intermixed were less than 2000Å and had significant damage clearly defined in TEM cross-sections.

In addition to ion implantation of neutral and isoelectronic elements and post-process annealing, one other method of impurity-free intermixing has been reported. The technique utilizes the creation of vacancies through out-diffusion of Ga into a SiO_2 encapsulant. Selectivity is possible because Ga diffusion will not occur into Si_3N_4 (Guido et al., a.). Through this method, 0.9-µm-thick quantum well layers are typically completely disordered after 10 and 25 hr annealing at temperatures of 875°C and 825°C respectively. Lasers, with a fairly high threshold, 45 mA, have been demonstrated with the technique (Deppe et al., 1986). The lasers were 11 µm and 15 µm wide. Rapid thermal annealing to produce partial disordering under SiO_2 has been used to shift the band edge of quantum well ridge waveguides (Ralston et al., 1989). The waveguide ridges were 26 µm wide. This method was tried in this thesis, as described in Chapter 2. It was discovered that strain affects the diffusion constant. The significant strain produced in underlying GaAs by the Si_3N_4 and SiO_2 encapsulants cause nonuniform intermixing patterns. The exact patterns are not repeatable because they are highly dependent on the encapsulant growth process as well as thickness of the dielectric layers. Because of the stress problems, though encapsulant dependent disordering is nominally free of impurities, it is not useful for reliably delineating narrow regions of disordered materials.

Intermixing Other Materials

Disordering in III-V compound other than GaAs based systems has also been demonstrated. The compounds include GaInP layers (Dabkowski et al.) and InGaAs-InP multiple quantum wells (Pape et al.; and Sumida et al.) InGaAs/GaAs strained-layer superlattices have also been intermixed by ion implantation and annealing (Myers et al, 1986). In an attempt to reduce damage in ion implanted strained-layer materials, target temperatures up to 400°C during implantation of Ar^+ was used by one group (Myers et al., 1987). They also reported limited compositional modulation over very thin regions, accompanied by a large extended defect density in the strained-layer quantum wells. The intent of these researchers was to investigate damage production, and their indication of intermixing was not clearly evident in their report. However, the effect they report is similar to the results of the elevated temperature ion bombardment procedure that was developed in this thesis for the GaAs/AlGaAs material system.

Theories

Although the experimental demonstrations of compositional disordering are very prevalent, a well developed theory has not yet emerged. A theory of radiation enhanced diffusion was put forth 30 years ago by Dienes and Damask. The model assumes the diffusion constant is directly proportional to the number of vacancies created. A model was applied to diffusion of impurities in silicon in the presence of vacancies in 1970 by Tsuchimoto and Tokuyama. They expanded the earlier work by including spatial diffusion of the vacancies in their model. In the area of Zn impurity induced intermixing, Laidig provided the first explanation. He claimed that single vacancies interacting with zinc interstitials enhance diffusion (Laidig et al.). Van Vechten, on the other hand, claims enhanced diffusion in the presence of Zn is due to the presence of divacancies, not single point defects, interacting with the charge zinc interstitials. Another model, which is not specific to Zn, but rather any impurity, has recently been put forth (Tan and Gosele). In this model, the enhanced diffusion is assumed to be due to a Fermi-level effect. Thus the theory of the enhanced diffusion must be further developed. In fact the nature of the mechanism for impurity-induced disordering is still unclear. Very recently, Kahen et.al. reported a model and a Monte Carlo simulation to explain the interdiffusion of AlGaAs-GaAs interfaces during post-Si^+ implantation rapid thermal annealing. Because rapid thermal annealing does not allow enough time for the implanted dopant to migrate, they claim only the vacancies from the implantation cause mixing. Therefore, these results are of interest for the technique described in this thesis. They assume the aluminum diffusion constant is proportional to the ratio of the number of vacancies in excess of the equilibrium to the equilibrium number of vacancies. This is similar to the approach used in this thesis to model the elevated temperature ion bombardment mixing process.

Section 1.2.b Optical Switching

Nonlinearities in semiconductors

Recent interest in all-optical switching has led to investigation of nonlinear optical properties in semiconductor optical waveguides (Jin et al.; Stegeman et al.; Kam Wa and Robson; and Cotter et al.). The switching properties of the semiconductor materials are intrinsically related to the fundamental optical properties of the materials. Near the band edge of GaAs materials bound electrons, coherent virtual electron-hole pairs, free-carriers and thermal effects all contribute to the optical properties. The effects all occur on different time scales, which is important for the applicability of any process to optical switching.

The ultrafast nonlinearities are due to bound electron and coherent virtual electron-hole pairs. The theory of the bound electron contribution to the nonlinearity was given in early work by Jha and Bloembergen. They theoretically estimate $\chi^{(3)}$ to be $\approx 10^{-11}$ esu, or $n_2 \approx 10^{-14}$ cm^2/W, at 10.6 μm, and they predict some enhancement close to the band edge. No measurement of this bound electron contribution to $\chi^{(3)}$ on ultrafast time scales has been reported. In 1986, an ultrafast blue shift of the exciton peak in a multiple quantum well due to strong optical excitation (10^6-10^9 W/cm^2) below the band edge was demonstrated by Mysyrowicz et al. and Von Lehmen et al. The blue shift was explained in a theory based on the excitation of virtual electron-hole pairs known as the optical Stark effect (Schmitt-Rink et al.). The theory is detailed in a paper by Schmitt-Rink and Chemla. It was recently applied to other material systems including organic materials (Schmitt-Rink). The first application of the effect in a switching configuration, a nonlinear Fabry-Perot interferometer, was shown by Hulin et al. in 1986. Though the modulation of the device was only 2:1 at T=150K for an excitation energy of 1 GW/cm^2, the time response of less than 1 ps is the first ultrafast switching response achieved. To achieve those very high peak intensities, high power pulsed lasers are needed.

In contrast to the ultrafast processes which are very small in magnitude, resonant effects where free-carriers are created, while typically slower, are orders of magnitude larger. Band-gap-resonant excitation of multiple quantum well materials were shown experimentally to produce very large nonlinear absorption and refractive index by Miller et al. in 1982. They measured a saturation intensity of I_s=580W/cm^2 for the absorption saturation of the exciton peak at room temperature, and predicted a corresponding $n_2 \approx 2\mathrm{X}10^{-5}$ cm^2/W very close to resonance. This was followed by a theory of the saturation mechanism based on screening effects, and further experiments with picosecond and femtosecond time resolution which are presented in a paper by Chemla and Miller. A comprehensive review of the work is found in the paper by Chemla, Miller and Smith. Chemla and Miller found that the excitons are more effective at saturating the absorption than free electron-hole pairs. Because of this they were able to interpret absorption saturation dynamics data of Knox (1985) and determine the exciton lifetime is ≈300 fs from the decay of the absorption saturation. The mechanism for the enhancement of the excitonic saturation was due to more effective bandfilling and exchange phenomena for excitons compared with free-electron-hole-pairs (Shcmitt-Rink et al.). The enhancement is only about a factor of 1.5, and depends on the excitation frequency.

It is still unclear in which cases quantum well materials are needed to produce the large nonlinear optical effects. This issue was addressed in a 1985 paper by Ovadia. They found that the room-temperature bistability achieved with samples made of multiple quantum wells and those made of bulk material operated similarly on resonance. Their measurement was made with 0.5 μs pulses. In addition to measurements on resonance, refractive index changes below the band edge due to excitation with optical frequencies above the band gap have been measured. In bulk GaAs (Lee et al., b.), measurements were performed using nonlinear Fabry-Perot fringe shifts. In GaAs multiple quantum wells (Park et al.) measurements were performed using a two-arm interferometer. In both instances, the wavelength dependence of the refractive index change due to a steady state carrier population is measured. The refractive index changes they measured are successfully predicted from a Kramers-Kronig transformation of the change in absorption lineshape due to absorption saturation from the carrier population. The results indicate that nonlinear phase changes due to resonant excitation are nearly identical in the two systems. This is because excitons are present in both systems, and so saturation mechanisms due to band filling effects occur in both systems. One of the interesting aspects of the work presented in this thesis is that the nonresonant dynamics of the nonlinear phase shift in the two systems can be examined for the first time. This provides an additional comparison between quantum wells and bulk materials.

Switching Devices

In addition to predicting and measuring the nonlinearities in semiconductors, work has also been carried out on all-optical switching devices based on intensity dependent effects. A review of the progress in the field over the last 15 years was published in 1988 by Stegeman et al. The optical switching elements that have been demonstrated include bistable devices, couplers, and Mach-Zender interferometers.

Optical bistable devices have been attempted in semiconductor materials for over 10 years. A tutorial review of developments in bistable devices with an emphasis on the use of semiconductor materials is given by Peyghambarian and Gibbs, and more recently by Koch et. al. Thin films of GaAs materials are often used as bistable elements. They have turn-on times of less than 1 ps, but turn-off is limited by the carrier recombination and was as long as several nanoseconds in the early devices (Peyghambarian and Gibbs). However, they require only about 1 pJ of switching energy operated on resonance with the band edge, and may be switched using cw diode lasers. The report in 1985 of reducing the carrier lifetime in quantum wells to 150 ps without significantly reducing the integrity of the band edge, and as such maintaining large optical nonlinearities, provided hope for improving the recovery of the devices (Silberberg et al.). Recovery times of less than 150 ps resulted in degradation of the nonlinear optical effects. Even without using proton bombardment, recoveries of 200 ps were achieved simply by reducing the size of the etalon to decrease the diffusion time away from the active area (Lee et al., a.). Bistability has also been demonstrated in waveguides, both in bulk GaAs waveguides (Aitchison et al.) and multiple quantum well waveguides (Warren et al.; and Kam Wa and Robson). The bulk waveguides showed low power (10 mW) switching with a response time of microseconds due to thermal index changes. The multiple quantum well samples showed electronic bistability for pulse durations <100 ns, and thermal contributions for longer pulses. The switching powers were between 10 and 60 mW, and response times were ≈20 ns for the electronic bistability, commensurate with carrier recombination times.

Nonlinear couplers, while not bistable, are also important switching elements (Jensen, S.M.). The first semiconductor waveguide all-optical coupler was demonstrated by Cada et al. in 1988 using stacked multiple quantum well waveguides. The device required 25 μW of cw power to go from a cross-state with roughly equal intensity in both guides to a straight-through condition with a contrast of 2:1. The first side-by-side waveguide couplers in GaAs semiconductors were demonstrated in 1988 by Jin et al. They had slightly better results than Cada et al., showing cross-states with 1:3 ratios and through-states with 3:1 ratios. The switching energy was 400 pJ, the turn-on was <10 ps and turn-off was 4 ns.

An all-optical nonlinear Mach-Zender interferometer was demonstrated in 1983 in $LiNbO_3$ (Lattes et al.). However, to date, though electro-optic Mach-Zender interferometers and couplers have been demonstrated (Donnelly et al.), no all-optical Mach-Zenders have been shown in GaAs materials.

Thermal Effects

Thermal effects can be significant in semiconductor optical devices. This is particularly true when large carrier populations are created. As indicated by Gabriel et al., thermal index changes can overwhelm the nonlinear response, particularly for cw excitation. One other important conclusion of that work was that the carrier populations that cause heating may be created by below band gap excitation via two-photon absorption mechanisms. Two-photon absorption was found in this thesis to be significant at the intensities necessary for optical switching even very close to the band edge. Therefore, thermal effects due to two-photon induced carriers should be considered in the design and characterization of optical devices.

Two-photon absorption

In fact, the importance of two-photon processes found in the thesis work warrants some discussion of the previous work in the area of two-photon absorption in GaAs and related semiconductor materials. Very early measurements of the two-photon absorption coefficient, β, in GaAs materials produced wide ranging values. In 1976, Bechtel and Smith, using picosecond pulses at 1.06 μm measured $\beta = 0.023 \pm 0.007$ cm/MW with a high degree of accuracy. The wavelength dependence of β was predicted by Pidgeon et al. using a nonparabolic, three-band model in 1979 and found to gradually increase as the frequency approaches the band edge. This theory was expanded to include exciton effects by Weiler, which resulted in a more constant wavelength dependence near the band edge than in Pidgeon et al.'s theory. More recent measurements on optical limiting in GaAs claim the value of β at 1.06 μm is 26 ± 8 cm/GW (Boggess et al.). These workers include the very significant effect of self-defocusing due to free-carrier generation on the measurement. The effects described above are discussed in a review paper by Van Stryland et al. More recently, two-photon absorption has been shown to play a role in photorefractive effects (Smirl et al.) in GaAs by creating electron-hole pairs. Two-photon absorption also produces undesirable side effects in measurements of the nonlinear optical Stark effect (Knox, 1989).

The study of the optical switching properties of semiconductor waveguides presented in this thesis provides the first measurement of the nonlinear refractive index dynamics with minimal thermal side effects. From the large body of previous work in the area of optical switching, only a small fraction of which can be included here, the work provides important insight into the contributions to the nonlinearities from various effects. In this way, the potential for ultrafast switching can be better assessed.

Section 1.3 Thesis Outline

The topics in this thesis and how they are organized in the chapters is outlined here. The first seven chapters concern compositional disordering. In Chapter 2, preliminary experiments using the established SiO_2/Si_3N_4 encapsulation technique are presented. The third chapter describes the work on development of the new technique, ETBD, for achieving impurity-free disordering with lower temperatures and process times than other intermixing methods. To better understand the process and determine the limitations of the technique, experiments, presented in Chapter 4, that determine the effects of ion mass, target temperature, and bombardment time on the mixing were performed. Also in Chapter 4, a model is presented that provides a guideline for determining the various parameters in ETBD. From this model, the possibility of mixing with lower temperatures and shorter high temperature process times than any currently established mixing method was predicted. The experimental verification is presented in Chapter 4.

For delineating devices patterning is of key importance. In Chapter 5, two masking techniques are described, and the experimental demonstration of their feasibility is presented. For ETBD to be useful in fabricating waveguide devices, there should be minimal residual damage in the disordered layer. This topic is covered in Chapter 6 where post-ETBD annealing is used to improve the quality of the intermixed layers.

The work on ETBD culminates in the design, fabrication, and characterization of intermixed quantum well waveguides, the topic of Chapter 7. Waveguide output far field patterns are measured and compared with those expected from index guided structures. Waveguide loss measurements are also shown and compared to the losses in waveguides fabricated with other intermixing techniques. With the successful demonstration of waveguide devices, work began on characterizing the optical switching properties of waveguides. This work is contained in Chapters 8 and 9.

The optical characterization concerned the intensity dependent optical phase and amplitude changes near the band gap of semiconductor material. These properties are of key importance to determine the all-optical switching potential of these materials. What sets this work apart from previous measurements of the optical nonlinearities is both the time resolution of less than 500 fs, and the use of a new interferometer technique that minimizes thermal effects. While one goal of the experiments was to characterize the switching properties of the quantum well waveguides fabricated with ETBD, most of the experiments centered on bulk AlGaAs waveguides. The studies of the bulk AlGaAs were undertaken because the system is fairly well understood, and it does not have the peculiarities associated with the quantum well system such as anisotropy. Because of this, the switching properties could be easily quantified. We were able to detect, for the first time, a nonlinear index change in this material that turns on and off within 500 fs. The properties that were quantified include group velocity dispersion and pulse broadening, linear and nonlinear (two-photon) absorption, as well as the nonlinear refractive index that leads to the ultrafast index change. All of the measurements were performed as a function of wavelength detuning from the band edge. The results are detailed in Chapter 8. Finally, measurements aimed at comparing the optical response of the multiple quantum well material to the bulk system are discussed in Chapter 9. These experiments were carried out on waveguides that were fabricated with ETBD. Conclusions are found in Chapter 10, and future work is contained in Chapter 11.

Chapter 2
SILICON DIOXIDE ENCAPSULATION TECHNIQUE

Section 2.1 Introduction

Early thesis research focused on an established disordering technique with the hope that it could be readily applied to making nonlinear devices with small active areas. The technique is based on vacancy enhanced disordering by SiO_2 dielectric capping that was first demonstrated by Holonyak et al. The process was examined in a preliminary way. The results indicate that the technique would not prove useful for fabricating nonlinear switching devices primarily because it is difficult to control and to pattern the disordered region. After some background, the experimental results and discussion about the SiO_2 technique are presented.

Compositional disordering using dielectric encapsulation (Guido et al., a.), relies on creating vacancies by out-diffusion of Ga into a SiO_2 encapsulant. The Ga out-diffusion is retarded under an Si_3N_4 encapsulant, so the process is selective. Through this method, 0.9-μm-thick quantum well layers are typically completely disordered after 10 and 25 hr annealing at temperatures of 875°C and 825°C, respectively. The major drawback of this method is that strain affects the diffusion constant, and Si_3N_4 and SiO_2 encapsulants produce significant strain in underlying AlGaAs or GaAs material. In addition, the exact patterns are not repeatable because they are highly dependent on encapsulant growth process, the thickness of the dielectric layers and the width of the SiO_2 and Si_3N_4 stripes.

The experiments on dielectric encapsulation were designed to determine several properties of the process. The most important issues are the quality of the disordered material, the quality of the multiple quantum wells which were not disordered, and the integrity of the masked edge. Also, surface degradation during processing must be negligible. One final question was whether disordering via this method could be achieved through a thick epitaxial layer above the multiple quantum wells. In this section, the experimental results of the encapsulation-based disordering process are presented. First, details of the material and the processing are given, and then the characterization of the materials is presented.

Section 2.2 Material Processing

These investigations were carried out with the help of Richard Singer, who grew the multiple quantum well layer by molecular beam epitaxy (MBE) and assisted with the annealing procedures. The layer structure is shown in Figure {2.1}. First there is an n-type 0.8-µm-thick $Al_{0.5}Ga_{0.5}As$ layer grown on the GaAs substrate. This is followed by 40 periods of 100-Å-thick GaAs and 100-Å-thick $Al_{0.3}Ga_{0.7}As$ that form the multiple quantum well layer. This layer is nominally undoped. A 0.8-µm-thick $Al_{0.5}Ga_{0.5}As$ p-type layer, and a 200-Å-thick GaAs p^+-type were then grown. Thus the layers form a p-i-n diode that is designed to be an optical waveguide with the optical mode confined within the intrinsic multiple quantum well layer.

For patterning, a 1500Å Si_3N_4 dielectric layer was deposited by low temperature plasma deposition (250°C) on both the bottom and top of the sample. This layer is densified by 750°C annealing in a N_2 atmosphere for 4 minutes. The Si_3N_4 on the back of the sample prevents degradation of the GaAs substrate during annealing. Photoresist is applied to the top of the sample and exposed through a mask with 2-µm- to 10-µm-wide stripes. In these stripes, the Si_3N_4 is removed using buffered hydrofluoric acid. Finally, a 1000Å SiO_2 layer is deposited over the entire sample by chemical vapor deposition. This results in 2-µm- to 10-µm-wide SiO_2 stripes across the sample bounded by areas of Si_3N_4. For some samples, the Si_3N_4 was completely removed from half the sample before the SiO_2 was deposited. The samples were placed in evacuated quartz ampoules with a small piece of As to provide an As overpressure. The tubes were placed in large diffusion furnaces at 825°C and 875°C for 5, 10, and 20 hours. After annealing, the samples were removed from the quartz tubes for analysis.

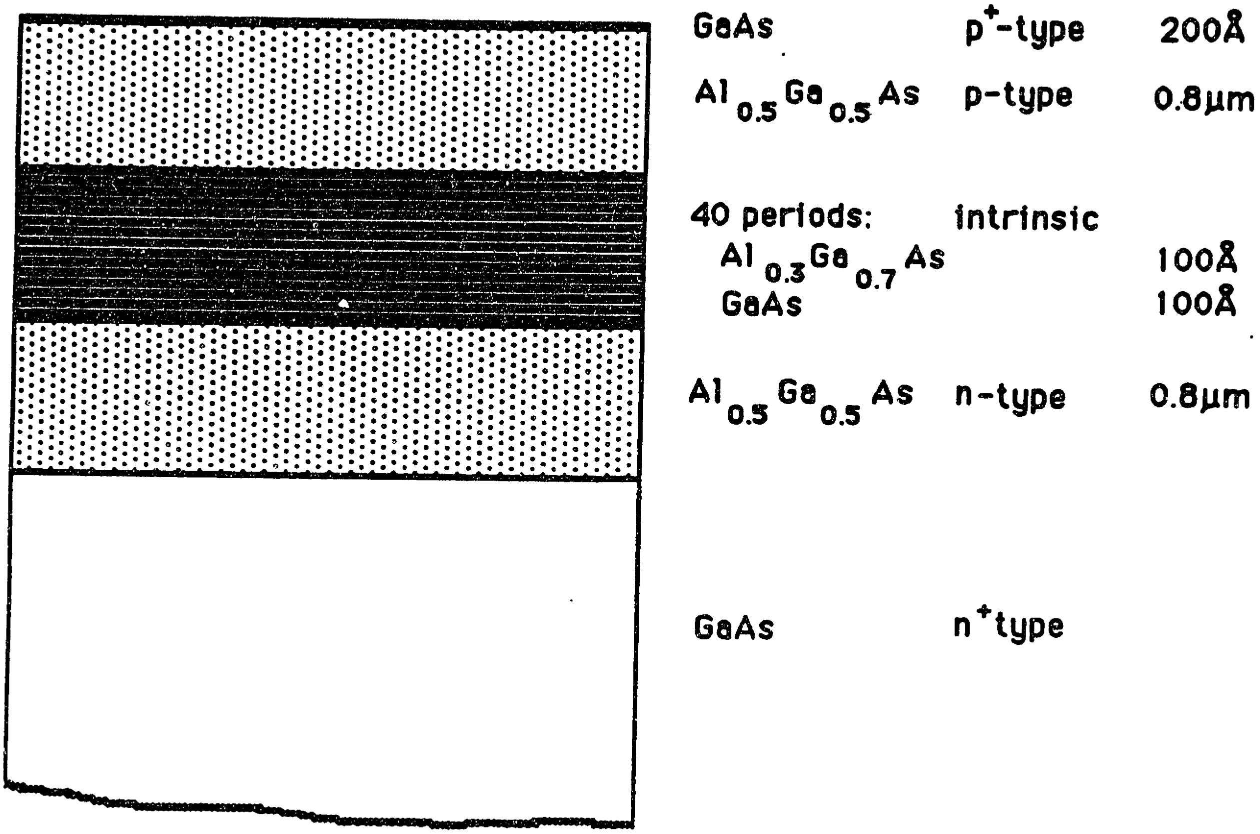

Figure 2.1. Layer structure used for dielectric encapsulation disordering experiments.

In the first set of samples, the quality of the surface was very poor. Holes developed in the dielectric layers, and As was lost from the sample. To improve the annealing process, a diffusion furnace with two controlled heating areas, which allows the As overpressure to be adjusted, was used. This process was developed by Dr. Matsayoshi Matsui. Using this furnace, 875°C annealing for ten hours produced only minor deterioration of the dielectric, and no apparent damage to the GaAs surface. Two anneals were performed in this way. One lasted 10 hours at 875°C, and the second lasted 5 hours at 875°C.

Section 2.3 Characterization

Optical transmission measurements were used to characterize the layers. For these measurements it is necessary to remove the substrate from the sample, leaving just the thin (≈2 μm) epitaxially grown layers. This is done by first mounting the sample, using crystal bond wax, epitaxial layer down, to a sapphire substrate. Both the wax and the substrate are transparent in the infrared, although the sapphire is birefringent. The GaAs substrate is lapped and chemically polished to a thickness of ~25 μm. Sodium hypochlorite 5% is sprayed to remove the remaining GaAs, and stop at the AlGaAs buffer layer. This etches GaAs 200 times faster than AlGaAs. The resulting layer is supported by the sapphire.

The integrity of the mask edge was determined by using an infrared transmission microscope. The substrate was removed, and infrared transmission through the samples was viewed on a video screen. A difference in transmission between intermixed regions and multiple quantum wells is expected because the band edge of the two materials in the infrared is different. In particular, the disordered region will pass more infrared radiation because the band edge is at a higher energy than the multiple quantum well. To enhance contrast, an infrared pass-band filter, centered on 800 nm wavelength, was used after the broadband infrared source.

A photograph of the video image of the transmission from a sample that was annealed for 10 hours at 850°C is shown in Figure{2.2}. The central stripe in the photograph is transmission through a disordered stripe that was defined by a 10-μm-wide mask. The most important feature in this photograph is the significant lateral diffusion from the mask edge. The disordered areas, appearing as lighter colored areas on the photograph, are up to 30 μm wider than the original SiO_2 mask. Uneven transmission through the layer is the result of the poor surface quality of this particular sample. This sample was annealed in the single chamber annealing furnace. Other sets of samples, in which the encapsulants were deposited at a different time showed various amounts of the lateral diffusion, though all samples showed at least 5 to 10 μm of lateral diffusion.

More detailed understanding of the material is obtained by examining the normal incidence transmission spectra. A normal-incidence transmission spectrum from the original multiple quantum well layer is shown in Figure {2.3}. It shows well defined excitonic resonances at the two-dimensional density of states energy levels, and has a band edge at a wavelength of ≈865 nm. Typical perpendicular incidence transmission spectra from the areas of the sample covered with the SiO_2 and the Si_3N_4 are shown in Figure {2.4}. The spectrum from the SiO_2 encapsulated intermixed region exhibits a well defined bulk alloy band edge which corresponds to an average aluminum concentration of the original quantum-well material. The Si_3N_4 encapsulated areas, which should be unmixed, show evidence of some mixing because the exciton line is shifted to shorter wavelengths and the resonance is somewhat broader than that of the original material.

Section 2.4 Conclusions

These results indicated that the original hope to realize well defined, small areas, < 5 μm, of high quality multiple-quantum-well material would not be readily achieved by this technique. We unsuccessfully attempted to fabricate waveguides using this technique. Stress effects did not allow enough control to make feasible device delineation. Also, the

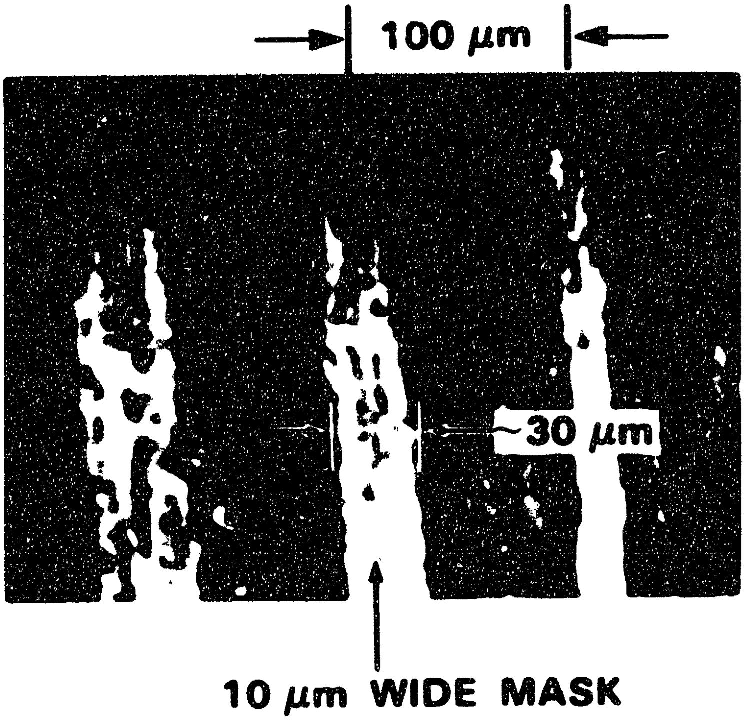

Figure 2.2. Video image of back-illuminated infrared microscope image of intermixed sample. Mask width for central stripe: 10 μm.

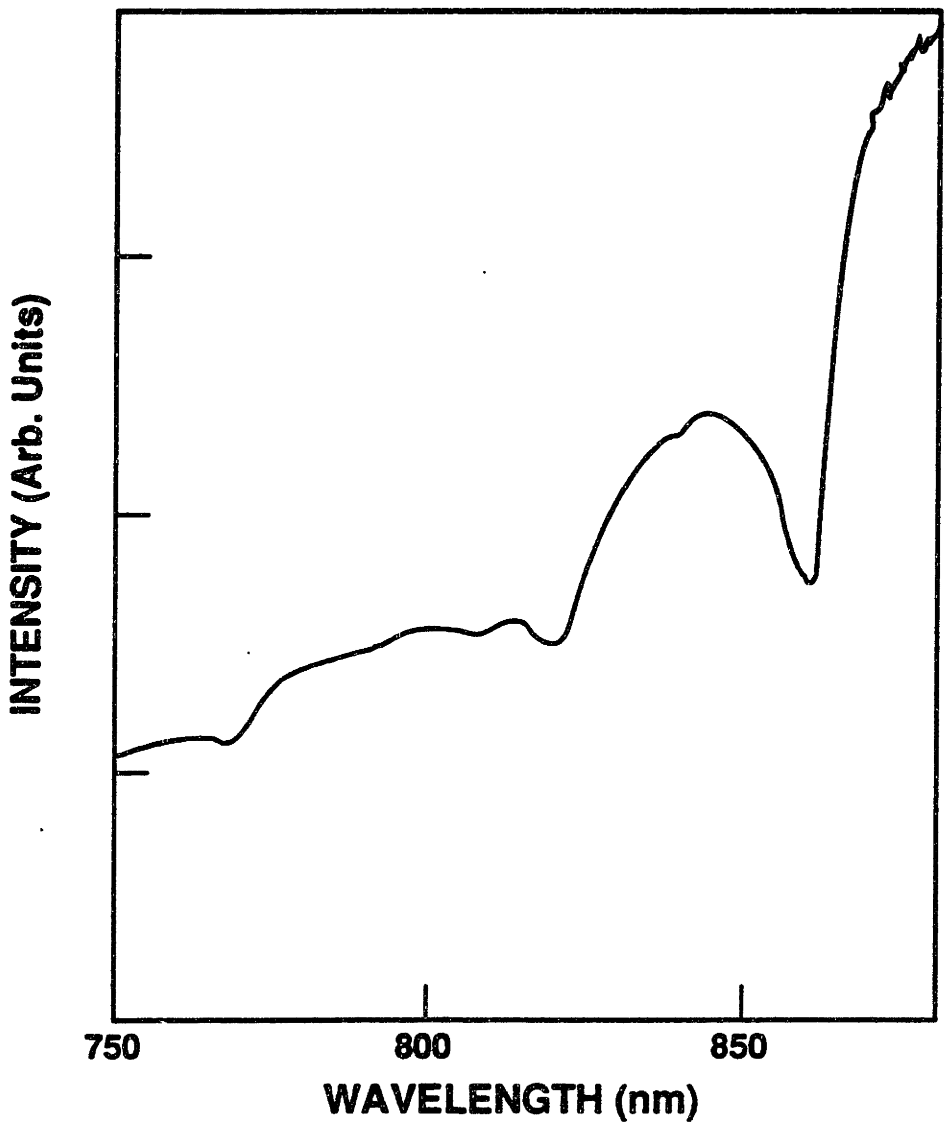

Figure 2.3. Normal-incidence transmission spectrum for 40-period multiple quantum well sample.

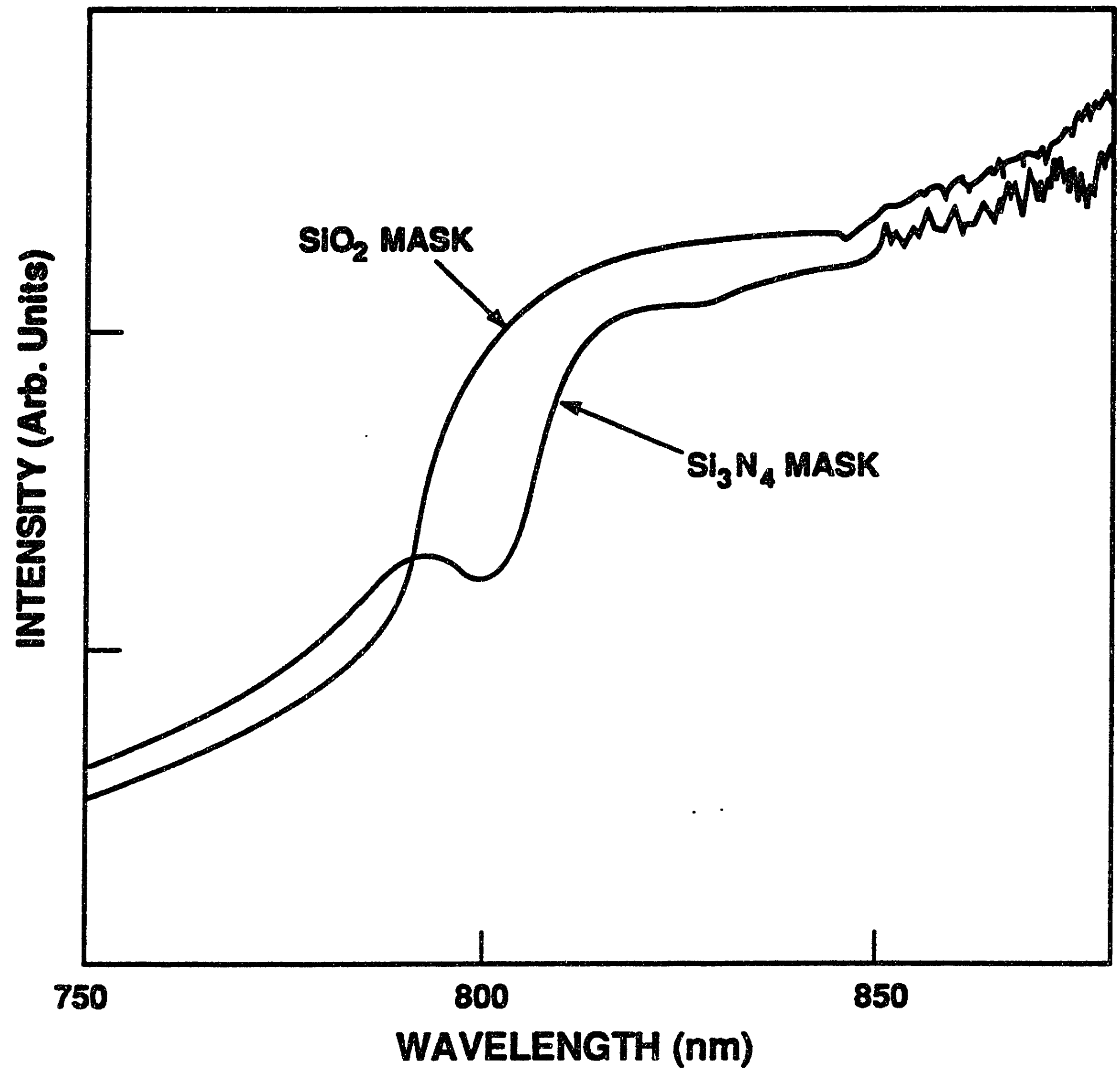

Figure 2.4. Normal incidence transmission spectra for multiple quantum well sample after annealing at 875°C for 10 hrs: spectra from a sample region encapsulated with SiO_2 and a region encapsulated with Si_3N_4.

partially mixed region did not produce enough of an index difference with the alloy to make a waveguide. Because of these issues, further attempts at SiO_2 induced mixing were curtailed, and attention was focussed on the new mixing technique. The conclusion of this portion of the work is that although encapsulant dependent disordering is nominally free of impurities, it is not useful for reliably delineating devices.

Chapter 3

ELEVATED TEMPERATURE BOMBARDMENT DISORDERING -- (ETBD)

Section 3.1 Description

Elevated temperature bombardment disordering (ETBD) is a technique to selectively cause enhanced diffusion of the atomic species in the GaAs semiconductor system. This will cause degradation of the heterojunctions by migration of the constituent elements across the heterojunction boundaries. Eventually, complete intermixing of the junction will produce a material with a uniform composition. In the specific case of a multiple quantum well layer, complete intermixing results in a uniform alloy that has an aluminum mole fraction that is the average of the original quantum well and barrier layers.

Ion bombardment at elevated temperatures--temperatures of between 400°C and 700°C, much higher than those used to reduce defect populations--allows the interstitials and vacancies created by bombardment to diffuse as well as recombine. Also, the steady state interstitial-vacancy population created by the bombardment enhances the mixing of the quantum-well layer. A schematic of the atoms in the crystal at an AlAs-GaAs interface during ion bombardment is shown in Figure {3.1}. Arsenic is left off the figure for simplicity. This figure illustrates the ion-atom collisions that create interstitials and vacancies. Vacancies will result if energy greater than the displacement energy of the atom in its lattice position is imparted to the atom. As is shown in the figure, an interstitial Ga atom may diffuse and recombine in an Al vacancy. Alternatively, Al interstitials may migrate and recombine in Ga vacancies. In addition, the bombardment creates a steady-state population of vacancies that is dependent on the generation and recombination rates of the vacancies. Vacancies enhance atomic migration in the lattice by allowing atom hopping to an adjacent lattice site without having to go through exchange or ring mechanisms

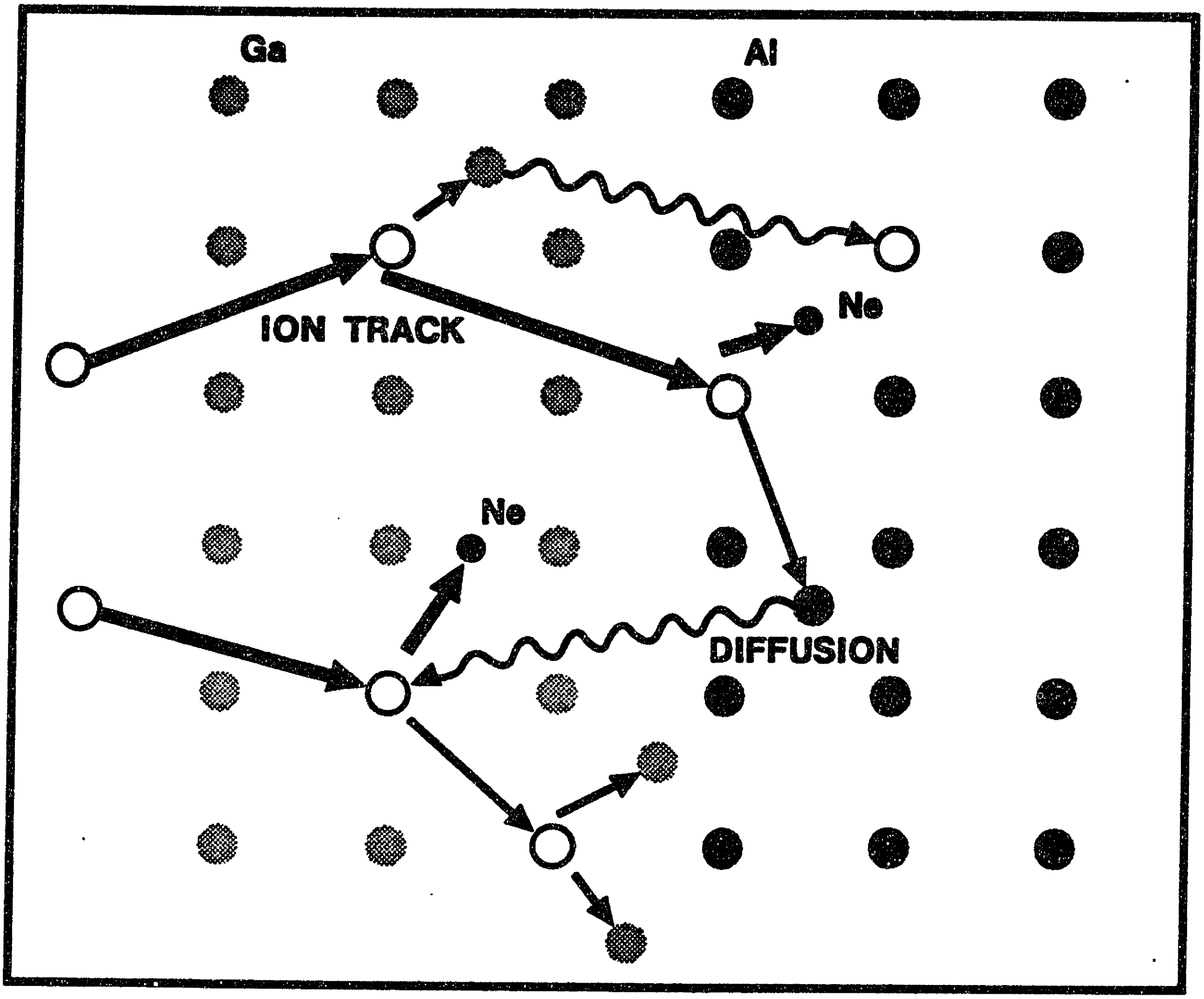

Figure 3.1. Schematic diagram of atoms at an interface between GaAs and AlAs in a crystal. ◍ -- Ga atoms, ● -- Al atoms, O --vacancies, • -- Ne$^+$.

(Manning). Both effects induce intermixing during the high temperature bombardment in the regions where the ions penetrate the layer.

Section 3.2 Experimental Demonstration

In this section the initial experimental results that demonstrate the ETBD technique are described. The goal of the experiments was to determine whether ion bombardment at elevated temperatures is a viable alternative method to achieve layer intermixing. For the initial results, the highest reasonable ion flux was used. The target temperature and bombardment duration were chosen to be high enough to produce positive results, but within the range of or less than those required in most of the other disordering techniques. Experiments aimed at reducing the bombardment parameters are described in Chapter 4.

For these studies, multiple quantum well structures were grown by low pressure organometallic vapor-phase epitaxy (OMVPE). The structure is illustrated schematically in Figure {3.2}. The layers, grown on undoped, semi-insulating GaAs substrates tilted 2° off the (100) towards the (110), consisted of a 1-μm-thick $Al_{0.5}Ga_{0.5}As$ buffer layer, followed by 40 alternating 120Å thick GaAs and $Al_xGa_{1-x}As$ layers and then a 200Å GaAs cap layer. All the layers were nominally undoped. The Al mole fractions for the $Al_xGa_{1-x}As$ barrier layers in the two samples studied are $x=0.5$ and $x=0.3$, respectively. The samples were encapsulated with 750Å of pyrolitic silicon nitride to prevent surface degradation during the high-temperature ion-bombardment process.

For ion bombardment, each sample was mounted on a graphite heater strip misoriented by 7° to the ion beam to minimize channeling. Half the sample was masked with a graphite stencil mask to provide an unbombarded control region. The samples were heated to 700°C and bombarded with 380-keV Ne^+ ions at a current density of 10 $\mu A/cm^2$. Neon was selected as the implant species because it is an inert ion with a mass close to Al, and with available implantation energies, has a mean range of penetration into the multiple quantum well layer of ≈ 0.5 μm. Bombardment was 1 hour and 2 hours for the sample

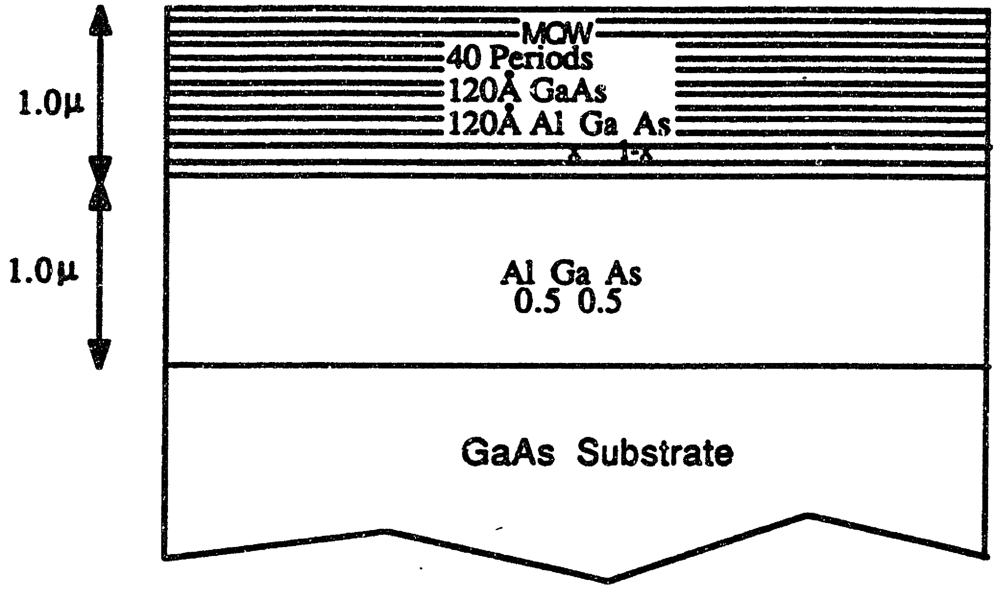

Figure 3.2. Schematic diagram of multiple quantum well layer structure used for ETBD demonstration.

with x=0.3 and x=0.5 in the layers, respectively. This difference in the bombardment times is not important for the results presented in this section.

Sputter-profile Auger electron spectroscopy, cross-sectional transmission electron microscopy, and perpendicular incidence optical transmission measurements were used to evaluate the disordering of the quantum wells. In Figure {3.3}, the atomic concentrations of As, Ga, and Al are plotted as a function of depth for a sample with x=0.5 in the barriers. Figure {3.3a} shows the atomic concentrations from the masked portion of the sample. Although the depth resolution of the analysis decreases with increasing depth because of the surface roughening, each of the 40 GaAs quantum wells is resolved. In contrast, Figure {3.3b} shows that complete mixing of the 1-µm quantum well layer took place within the bombarded region of the sample. In this bombarded disordered region, there is a uniform Al concentration corresponding to x≈0.25, one-half the value for the as-grown barrier layers. The buffer layer, which has x=0.5, is evident in both figures. It should be noted that although bombardment of large mass ions through some encapsulents will cause encorporation of the elements of the encapsulent to be introduced into the layer, Auger indicated no significant amounts of Si in the layer.

Cross-sectional transmission electron micrographs of the bombarded and masked regions of the same sample are shown in Figure {3.4}. Complete mixing of the 1-µm-thick quantum well layer is indicated, while the quantum wells are still defined in the masked region. The $Al_{0.5}Ga_{0.5}As$ buffer layer is distinguishable at the lower part of each micrograph. The electron diffraction pattern from the disordered region, shown in the inset to Figure {3.4}, indicates that this region remains crystalline. The dark areas within the disordered region, which are not found in the buffer layer beyond the ion range, are indicative of residual damage.

Optical transmission measurements were made to determine the changes in spectrum that occurred due to disordering. The samples were prepared as described in Section 2.3. Figure {3.5a} shows the transmission spectra from the masked and

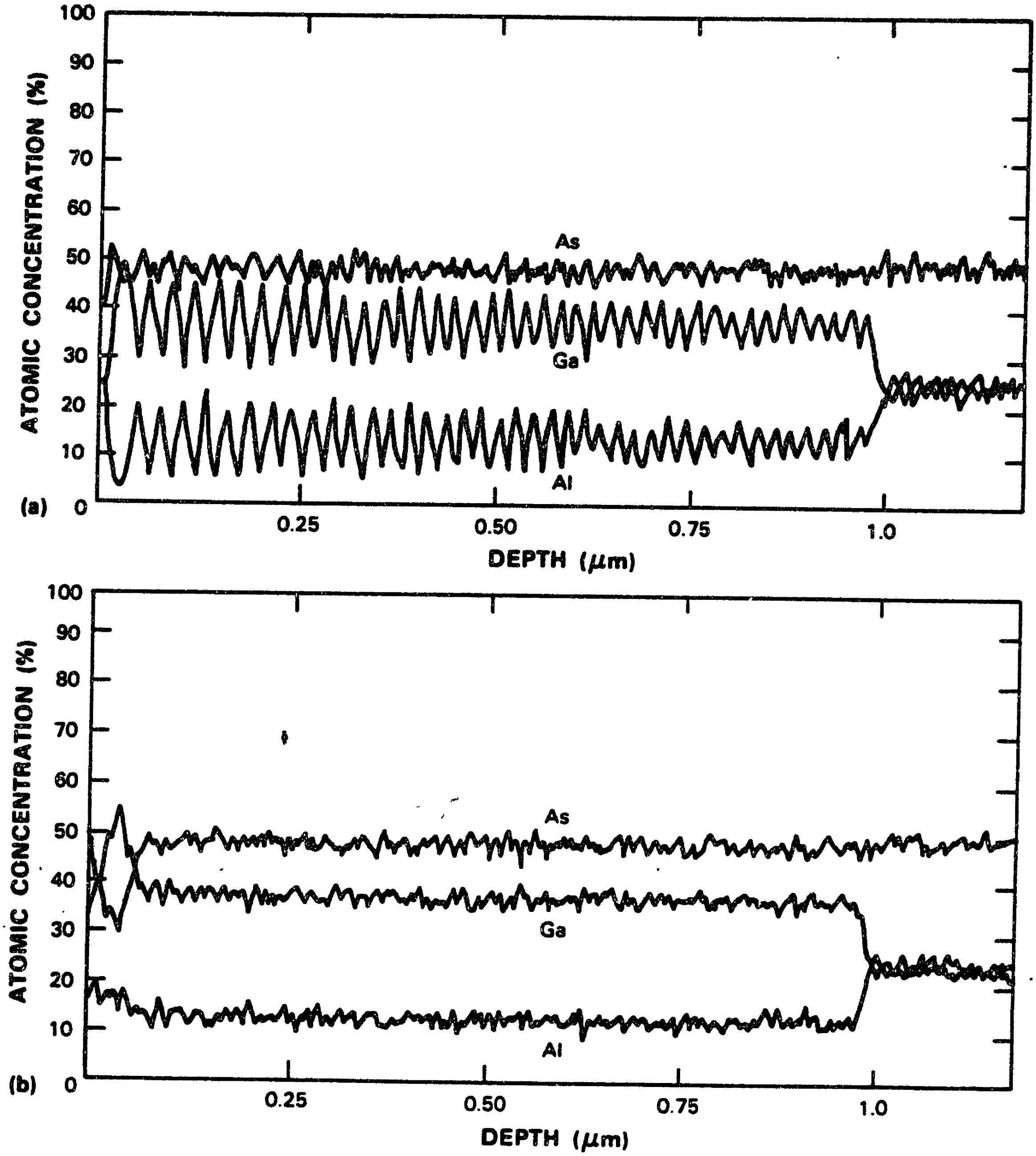

101681-2

Figure 3.3. Sputter-profile Auger electron spectroscopy trace showing atomic concentration of As, Ga, and Al as a function of depth in the multiple quantum well sample. (a) From the masked portion of the sample; (b) from the unmasked, bombarded region of the sample.

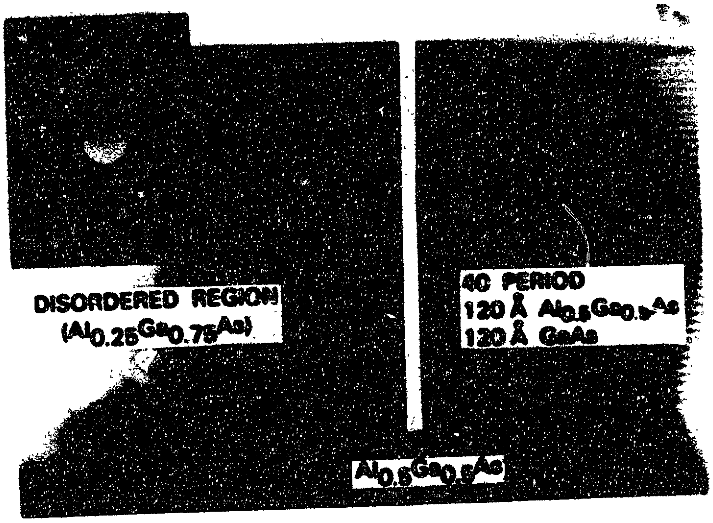

Figure 3.4. Cross-sectional transmission electron micrographs. Left micrograph: from the masked region of the sample; Right micrograph: masked region of the sample. The inset shows the selected-area crystalline diffraction pattern from the bombarded, intermixed region of the sample.

bombarded regions of the same sample. The spectrum from the masked area is indistinguishable from a spectrum of the sample with no processing. In the bombarded region, the three-dimensional band edge expected from a disordered material is apparent. Figure {3.5b} compares transmission spectra from the disordered regions of two samples, one with $x=0.5$ and the other with $x=0.3$ in the barrier layers of the original quantum wells. The two samples exhibit different band edges because the resulting alloys have different Al concentrations. In each case, the band edge is the same as that of an alloy with an Al concentration equal to the average for the original multiple-quantum-well layer.

The extent of lateral diffusion under the masked edge was examined in a very preliminary way by looking at an angle-lapped cross section of the end face of the sample at the point where the graphite strip mask began. Angle lapping with a degree α produces a magnification of the features on the facet by a factor of $1/\sin(\alpha)$. For 0.5° this is a factor of 115. Therefore, 100Å quantum wells are visible with around 1 μm resolution available on a good optical microscope. The angle lapping procedure was carefully developed to obtain a good quality surface. Several different combinations of polishing agents and grit sizes were tried. Also various polishing flats were used, some with cloth pads, others without. The best combination proved to be 0.6 μm alumina grit with a polished glass lapping flat. This provides a flat surface, and produces minimum damage on the lapped surface. Sodium hypochlorite 5% (Clorox) is used to stain the sample. It provides a coloration as well as relief because it oxidizes the areas where aluminum is present.

An optical micrograph of the angle-lapped cross section is shown in Figure {3.6}. Because this measurement was not anticipated, the mask was at an angle to the cleaved edge. Therefore, the intermixed region appears angled through the layer. In fact, this is due to the orientation of the mask. The actual intermixed edge follows the line of the graphite mask. This positive result led to further studies of masking that are described in Chapter 5.

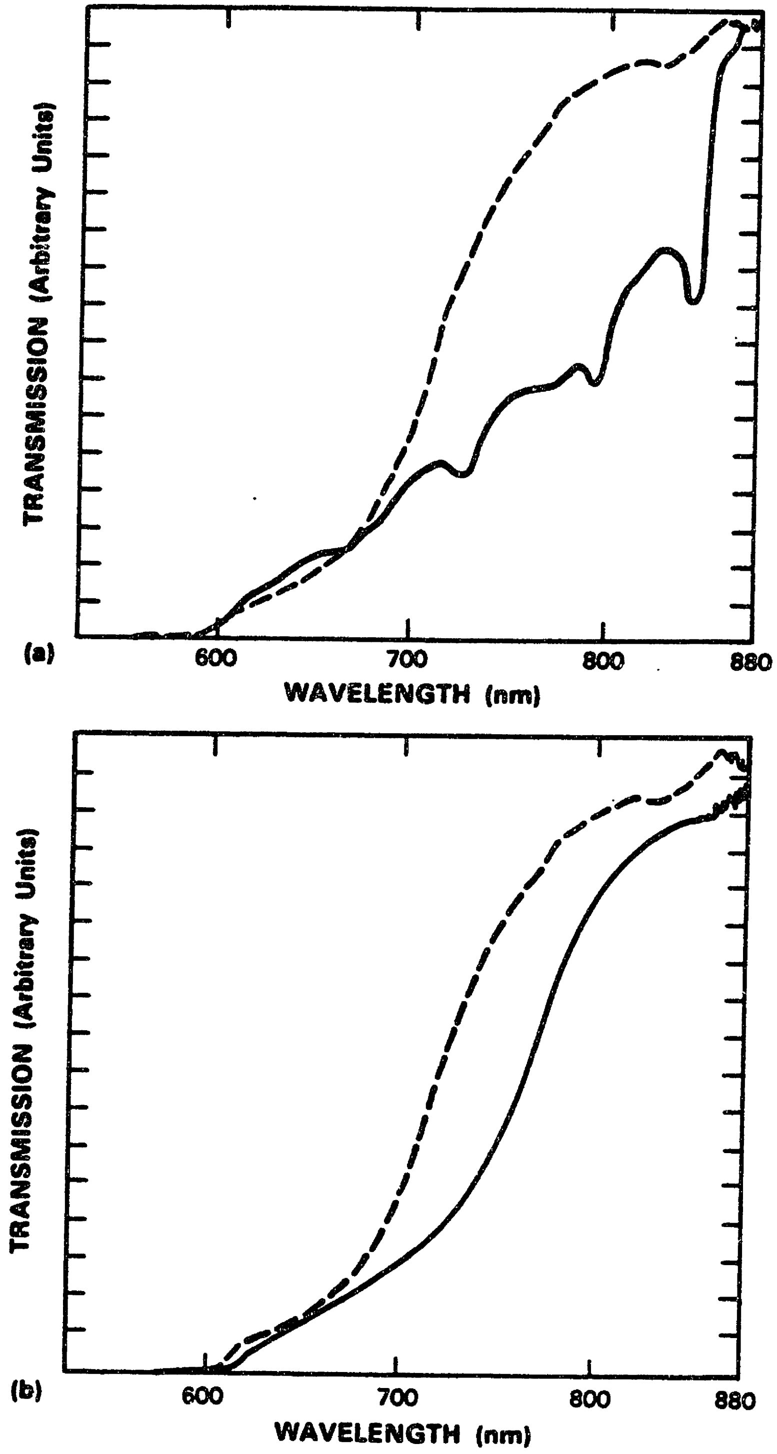

Figure 3.5. Normal-incidence transmission (linear scale) vs wavelength for the multiple quantum well samples after ETBD. (a) Solid line, masked region; dashed, bombarded region of the sample with x=0.5 in the barrier layers; (b) transmission of the bombarded regions: solid line sample with x=0.3 in the barrier layers; dashed, sample with x=0.5 in the barrier layers.

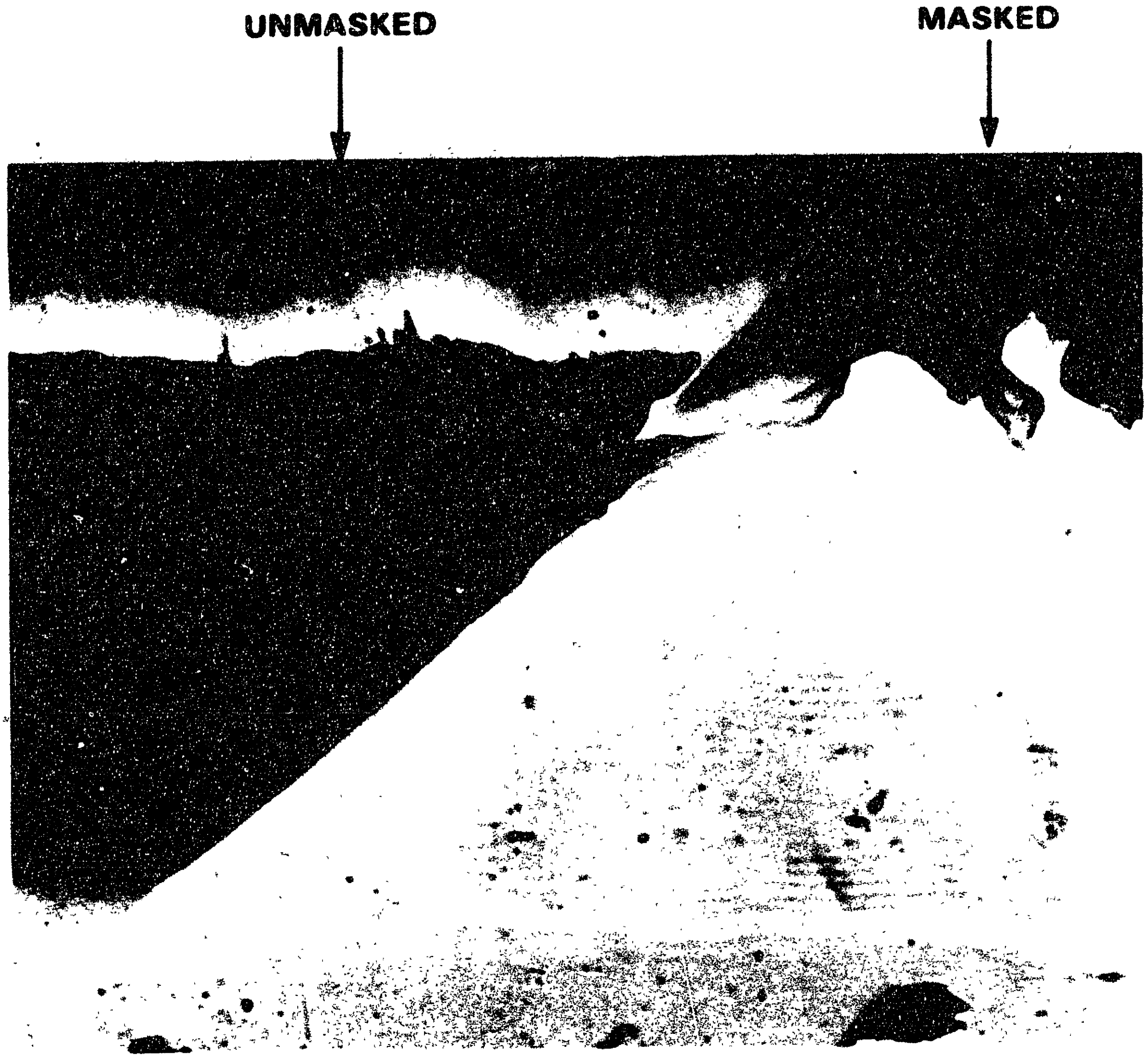

Figure 3.6. Optical micrograph of a 0.5°-angle-lapped end face of the multiple quantum well sample after ETBD showing the delineation between the masked and the unmasked regions. Mask was at an angle to the end face.

Section 3.3 Conclusions

The preliminary results indicate the potential of the new disordering technique. The temperature of 700°C is lower than all other disordering techniques except the Zn diffusion. These positive results led to further study aimed at determining the limits of the technique. For this study to be more effective, a model of the ETBD process was developed. The model, in conjunction with systematic experiments designed to reduce the ion bombardment time, temperature and flux, provide more insight into the technique and its potential for creating compositional intermixed materials. This study is detailed in the following chapter.

Chapter 4

ETBD PARAMETER DEPENDENCE: EXPERIMENT AND THEORY

Section 4.1 Introduction

With the ETBD technique, there is flexibility in the ion bombardment parameters that achieve mixing. The ion mass, energy, and flux determine the generation of vacancies and the depth over which they are created. In general, for the same energy, smaller mass ions will penetrate further into the layer, but create fewer vacancies than the heavier ions. Ion flux will determine the generation rate of vacancies, although there is a practical limit to the available flux. Increased temperatures provide for more atomic migration, but also enhance vacancy recombination. Longer bombardment times allow more diffusion to occur, but increase the dose of bombarding species and may increase residual damage. With these issues in mind, studies of intermixing with lighter and heavier ions, lower target temperatures, shorter bombardment times, and lower ion flux than the initial demonstration described in the previous chapter were undertaken.

Section 4.2 Ion Mass

4.2.a Introduction

To determine the effect of ion mass on the disordering process, four ion species other than neon, in particular hydrogen, helium, nitrogen and argon, were investigated. The projected range and standard deviation of the implant distribution for the energies used in the studies are listed in Table {4.1} (Gibbons et al.). Also included on the table are the projected ranges for the ions with the acceleration energies that could be achieved with an MeV ion implanter. Although MeV bombardment was not studied in this thesis, these numbers indicate the potential depths where efficient mixing might be achieved using the high energy implanters. The applicability of ETBD to higher energy implantation would require experimental study.

ION	ENERGY (keV)	PROJECTED RANGE (μm)	PROJECTED STANDARD DEVIATION (μm)	ENERGY (keV)	PROJECTED RANGE (μm)
H^+	380	3.16	0.29	1000	12.2
H_2^+	400	1.61	0.23	1000	4.43
He^+	380	1.37	0.21	1000	2.86
N^+	380	0.56	0.08	1000	1.20
Ne^+	380	0.47	0.15	1000	1.11
Ar^+	380	0.26	0.10	1000	0.40

Table 4.1

4.2.b Experiments

Hydrogen is very desirable to use because of the large projected range, over 3 μm at 380 keV, into GaAs. Thus, with hydrogen, true buried structures could be realized with the existing implanter. For the experiments with hydrogen ions, the sample had the same geometry of the structure described in Section {3.2}, but a 1-μm-thick $Al_{0.5}Ga_{0.5}As$ layer was included on top of the 40 period multiple quantum wells. The sample was prepared by the procedure described in Section {3.2}. Ion bombardment with 400 keV H_2^+ was performed with the target at 700°C. The 400 keV H_2^+ have a projected range of 1.6 μm. The process times were 4, 2, and 1 hour.

Normal incidence transmission and angle-lapped cross sections were used to determine the extent of the disordering. A transmission spectrum from the sample that underwent the 4 hr bombardment is shown in Figure {4.1}. The featureless spectrum indicates damage that extinguishes the excitonic resonances, but little shifting of the band edge. This spectrum is typical of the samples that were subjected to the 1 hr and 2 hr bombardment times. Inspection of the angle-lapped cross sections also confirmed no apparent mixing. Therefore, although the large penetration depth of hydrogen would prove beneficial, with the ion bombardment parameters that are achievable on the available equipment, hydrogen is not able to produce intermixed layers.

Ion bombardment with helium produced similar results to the hydrogen. The tests on helium were made with the same samples as in the hydrogen case. The projected range of helium with an acceleration energy of 380 keV is $\approx$1.4 μm, similar to the 200 keV hydrogen. Both the transmission spectrum of the bombarded regions and the angle-lapped cross-sections indicate the helium ion does not induce significant mixing.

Nitrogen has an atomic mass almost four times larger than helium. Consequently, the projected range of 380 keV nitrogen is R_p=0.49 μm, less than half that of helium. As a result, the experiments with nitrogen ions required using a layer structure that did not have a thick $Al_{0.5}Ga_{0.5}As$ layer over the quantum wells. The layer structures used for these experiments is the same as those described in Section {3.2}. The first attempt at intermixing the multiple quantum well layer with nitrogen utilized bombardment with 380 keV N^+ ions with an ion current density of 10 μA/cm^2 for 60 minutes with the target at 700°C. Although the spectrum of the nitrogen sample showed a less well define band edge than the neon bombarded samples, the angle-lapped cross section did indicate mixing. On this sample, Auger electron spectroscopy also indicated mixing. Nitrogen is the lightest ion that was tested that produced compositional mixing.

The results with neon ions were described in detail in Chapter 3. In addition to neon, the heavier column VIII element argon was tested. Complete intermixing was

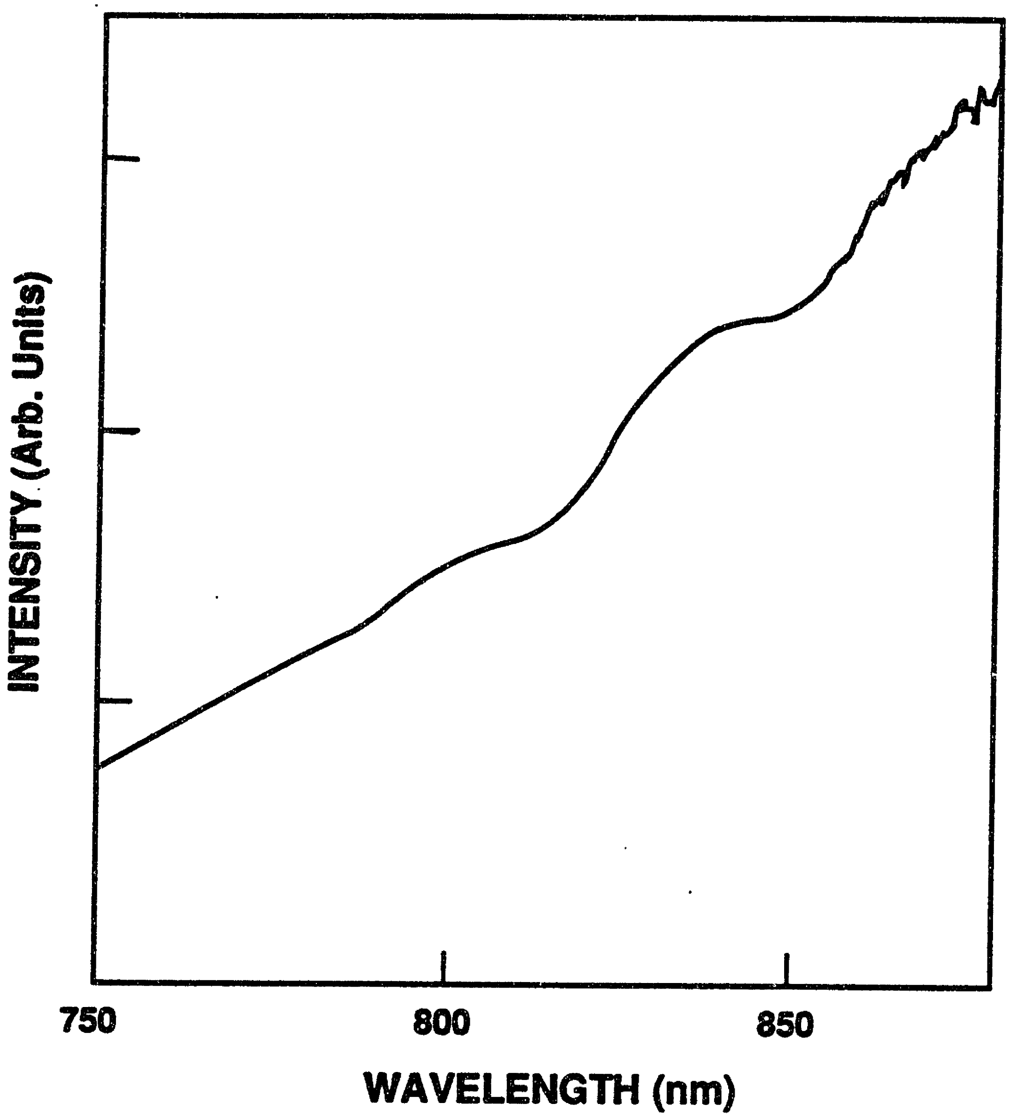

Figure 4.1. Normal-incidence transmission spectrum (linear scale) from multiple quantum well sample after ETBD with 400 keV H_2^+, with an ion flux of 10 μA/cm^2, for 4 hr at 700°C.

achieved with 380 keV Ar^+ ion bombardment for 60 minutes with the target at 700°C. The ion current density was 10 $\mu A/cm^2$. Because the projected range of argon is less than 0.3 μm, and 1 MeV acceleration energies will increase that to only 0.6 μm, the potential for argon at forming buried waveguide structures is limited. Therefore, argon was not studied extensively after the initial demonstration of successful mixing.

4.2.c Discussion

There are several reasons why the heavier mass ions are better at inducing intermixing. Intermixing relies on the creation of vacancies, which occur only when the atomic collisions transfer enough energy to the atom in the lattice to overcome the displacement energy barrier. This energy, though difficult to know exactly, has been estimated to be between 10 and 30 eV (Appleton). In a simple "billiard ball" description of the atoms, the energy transferred to a lattice ion of mass m_l, E_{trans}, in a head on collision from an incident ion with energy E_i and a mass m_i is given by the expression:

$$E_{trans} = \frac{4 m_i m_l}{(m_i + m_l)^2} E_i \tag{4.1}$$

This picture ignores the energy transfer dependence on the atomic potential and scattering cross section, but it still provides insight into the mass dependence of the vacancy production. The energy transfer is maximized when the atomic mass of the incident ions equals that of the atom in the lattice.

Not all energy lost by the ion as it penetrates into the layer is lost in collisions with the lattice ions. Some energy is lost from electronic collisions. The relative amount of nuclear, or lattice ion, energy loss versus electronic energy loss for the ion is contained in the nuclear and electronic stopping powers that are derived in a theory developed by Lindhard, Scharff and Schiott (see also: Rief). This theory is often used to determine projected range and standard deviation information for ion implantation.

In LSS theory, the electronic stopping dominates for lighter ions, at higher energies, and does not significantly change the path of the incident ion. Nuclear stopping results from collision with the target nuclei. It is more important with heavier ions, generally occurs at the end of the ion range where the energy and velocity are lower, and does alter the incident ion path. The energy loss of the impinging ions depends on an ion stopping power, which is assumed to have independent contributions from electronic and nuclear effects:

$$\frac{dE}{dx} = - N\,(S_n(E) + S_e(E)) \qquad (4.2)$$

where E is the energy of the ion at a point x along the path, S_n is the nuclear stopping power, S_e is the electronic stopping power and N is the number of target atoms per unit volume. Approximate expressions for S_n and S_e in GaAs are given by (Rief; and Carter and Grant):

$$S_n = 2.8X10^{-15} \bullet \frac{Z_1Z_2}{\left(Z_1{}^{2/3} + Z_2{}^{2/3}\right)^{1/2}} \bullet \frac{M_1}{M_1 + M_2} \qquad (4.3)$$

and:

$$S_e = k\,E^{1/2} \qquad (4.4)$$

The $E^{1/2}$ dependence in electronic stopping arises because S_e is proportional to velocity. In these equations, Z_a refers to the atomic number and M_a is the mass, where a=1 is the ion and a=2 is the target, and k is a constant which is a function of the ion and target material. From these approximate expressions S_n is a constant, while S_e is an increasing function of energy. This leads to a critical value E_c below which nuclear stopping power dominates, and above which electronic dominates. For GaAs:

$$\sqrt{E_c} \propto \frac{32Z_1}{\left(32^{2/3} + Z_1{}^{2/3}\right)^{1/2}} \bullet \frac{M_1}{(M_1 + 71)} \sqrt{eV} \qquad (4.5)$$

This equation indicates why nuclear stopping is more important for larger mass ions since E_c is higher. The ratio of E_c for Ne^+ to E_c for He^+ is ≈ 40. Therefore, nuclear processes dominate over more of the ion path for Ne^+ than for He^+, where electronic stopping is more significant. As such, Ne^+ is expected to be more efficient at generating the lattice ion vacancies than the lighter He^+ ions.

The calculations and experiments presented above provide some insight into the effect that ion mass has on inducing intermixing. While the intermixing process is considerably more complex than the theory allows, with atom-atom collisions and collision cascades occurring, the need for higher ion masses is indicated. This was also verified experimentally. The results of experiments indicate that very light ions, such as hydrogen and helium, will not intermix the quantum wells as efficiently as larger mass ions: neon, nitrogen and argon.

Section 4.3 Ion Flux, Bombardment Time, and Target Temperature

In addition to ion mass, the ion flux, target temperature and bombardment time also affect the intermixing. In this section the implications of reducing these parameters on the intermixing process are discussed, and the experimental results are given. The results are used in Section {4.3} where a first-order model that accounts for the observations, and provides a guideline for determining the process parameters necessary to achieve complete mixing in a thick multiple quantum well layer, is presented.

All the experiments designed to explore the effects of these parameters were carried out with neon ions for consistency. The samples for these experiments are describe in Section {3.2}. The heater strip temperature in the target chamber of the implanter is controlled to ± 3°C and monitored with a thermocouple attached to the strip. Monitoring the surface of the sample with pyrometer established that the surface temperatures exceed the heater strip temperature by <25°C. This temperature increase is due to heat generated by the incident ion flux. As in the other experiments, half of the sample is masked from the ion flux by a piece of graphite to provide a control region for comparing bombarded and unbombarded regions of the sample. Complete intermixing is distinguished from incomplete mixing by examining 0.5°-angle-lapped optical micrographs of the cleave end face of the sample in both the masked and unmasked regions. Normal-incidence optical transmission measurements are also used. Transmission spectra give an indication of the degree of mixing as well as the material quality.

In the first set of measurements, the target temperature was held constant at 700°C, and the ion flux and bombardment time were reduced from the 10 $\mu A/cm^2$ flux and 1 hr time of the initial demonstration of mixing. The results of these experiments are summarized in table {4.2}. On the table, a yes indicates complete mixing, and no indicates incomplete mixing. Complete mixing is considered to occur when over 90% of the layer is completely intermixed on the angle-lapped cross sections, and the transmission shows a shifted band edge and does not have excitonic features characteristic of the two-dimensional system. This is contrasted to incomplete mixing where the quantum wells are still apparent on the angle-lapped cross section, and the transmission spectrum does not show a shifted band edge.

Intermixing of the layer occurred with an ion current density as low as 1 $\mu A/cm^2$ when the bombardment time was 30 minutes but not for a shorter bombardment time of 15 minutes. For 10 $\mu A/cm^2$ ion flux, it is possible to reduce the bombardment time down to 5 minutes for the 700° C target temperature and still achieve nearly complete mixing. The transmission spectrum for this sample is shown in Figure {4.2}. A well defined band edge is apparent that occurs at a wavelength characteristic of an alloy with and aluminum mole fraction of $x=0.25$, which is the compositional average of the original quantum well layer. The oscillations at the longer wavelengths are due to Fabry-Perot resonances. This is verified by taking several spectra at different points in the sample that have slightly different thicknesses. The fringes shift in wavelength as expected. An optical micrograph of the angle-lapped cross-section is shown in Figure {4.3}. The photograph shows both the region that was masked for the bombardment, where the quantum wells are intact, and the bombarded region where mixing occurred. Some of the quantum wells at the bottom of the

CONSTANT TARGET TEMPERATURE
T = 700°C

PROCESS TIME	ION FLUX ($\mu A/cm^2$)		
	1	3	10
60 min	YES	YES	YES
30 min	YES	YES	YES
15 min	NO	YES	YES
5 min	—	—	YES

Table 4.2. Summary of the intermixing results for a constant target temperature of 700°C. YES indicated complete mixing and NO indicates incomplete mixing.

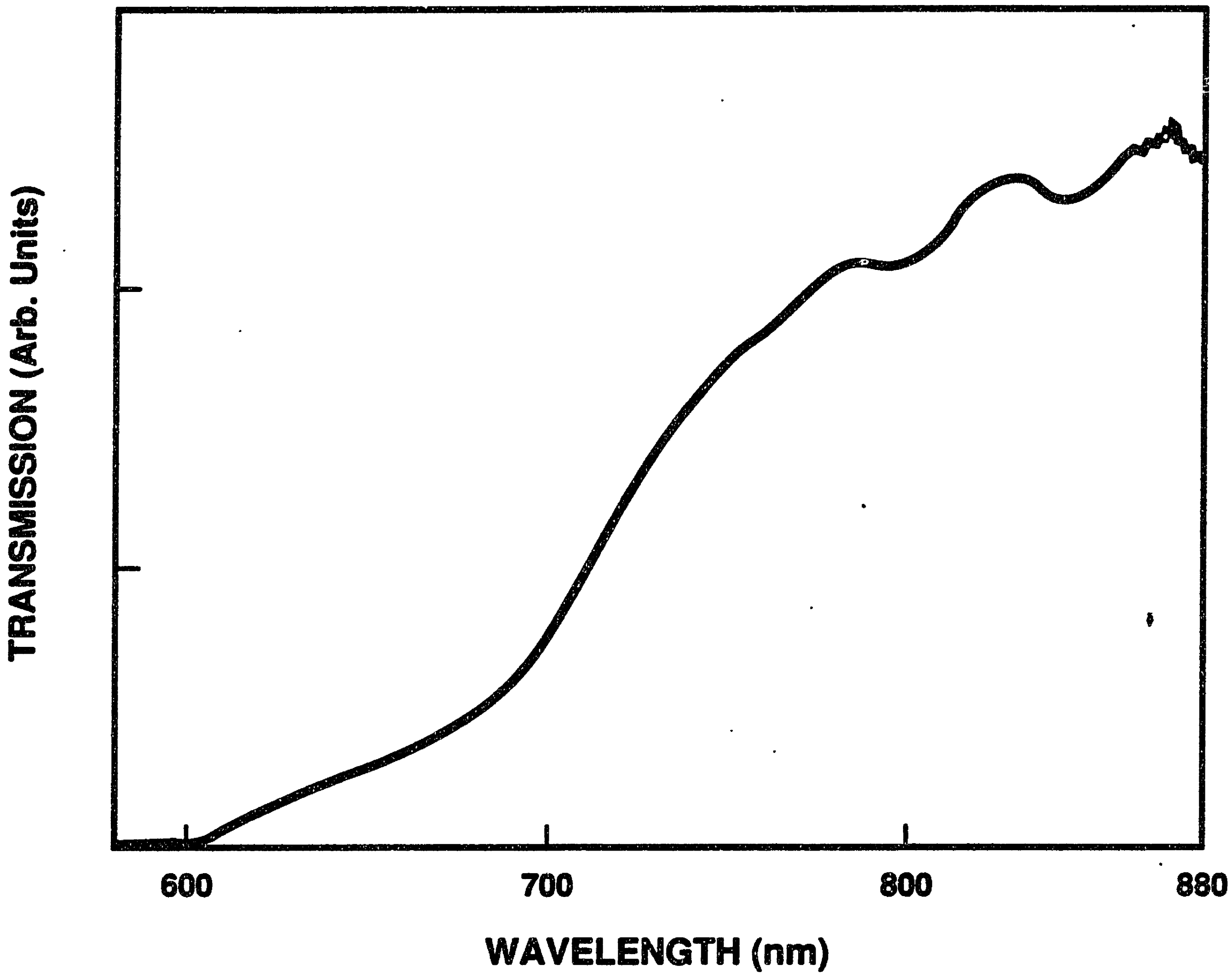

Figure 4.2. Normal-incidence transmission spectrum (linear scale) from multiple quantum well sample after ETBD with 380 keV Ne$^+$, with an ion flux of 10 μA/cm^2, for 5 min at 700°C.

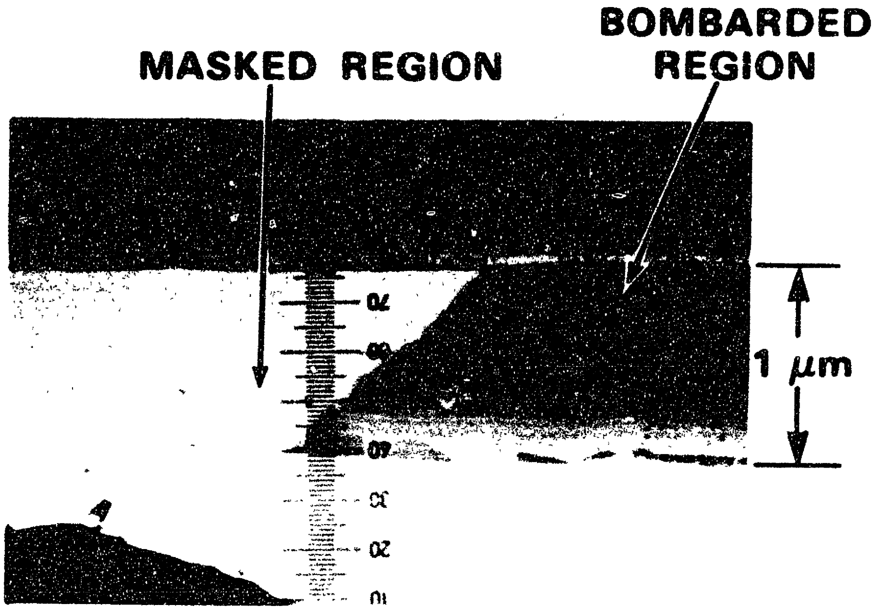

Figure 4.3. Optical micrograph of a 0.5°-angle-lapped end face from a multiple quantum well sample after ETBD with 380 keV Ne$^+$, with an ion flux of 10 μA/cm^2, for 5 min at 700°C.

bombarded region were only partially mixed, but they are much broader than the quantum wells in the masked region. The five minute bombardment time is the shortest reported to date for any of the intermixing processes mixing a 1-μm-thick region. Five minutes was the shortest time attempted.

For the next set of experiments, the bombardment time was held constant at 15 minutes and the target temperature was reduced in 100° C increments. Ion flux was kept at 10 $\mu A/cm^2$. The results are summarized in Table {4.3}. Complete mixing was evident for target temperatures of 500° C but not 400° C with a 15 minute bombardment time. Further studies were carried out with the 15 minute bombardment time and 500°C target temperature. The ion current density was reduced to 4 $\mu A/ cm^2$. The transmission spectrum from this sample is shown in Figure {4.4}. The spectrum is broad and featureless, and does not indicate a band edge. Further evidence of no mixing is provided in Figure {4.5} which show the angle-lapped cross section of the sample. Quantum wells are evident through the sample. The experimental results of this section led to the development of a model to help explain the parameter effects on the intermixing process. This model is presented in the following section.

Section 4.4 Intermixing Model

This first order model is based on an effective diffusion coefficient, D, that is used in the diffusion equation. The value of D is obtained by fitting the theory to the experimentally determined target temperature, ion flux and bombardment times used to achieve complete mixing. The number for the diffusion coefficient that is obtained is not a precise determination of the atomic diffusion constant under the influence of the ions, because there is not accurate numerical information about the degradation of the heterojunctions. Rather the theory is aimed at providing a useful tool for predicting the flux, time and temperature trade offs in the intermixing process.

CONSTANT PROCESS TIME
PROCESS TIME: 15 min

TEMPERATURE	ION FLUX ($\mu A/cm^2$)	
	3	10
700°C	YES	YES
600°C	YES	YES
500°C	—	YES
400°C	—	NO

Table 4.3. Summary of the intermixing results for a constant process time of 15 minutes. YES indicated complete mixing and NO indicates incomplete mixing.

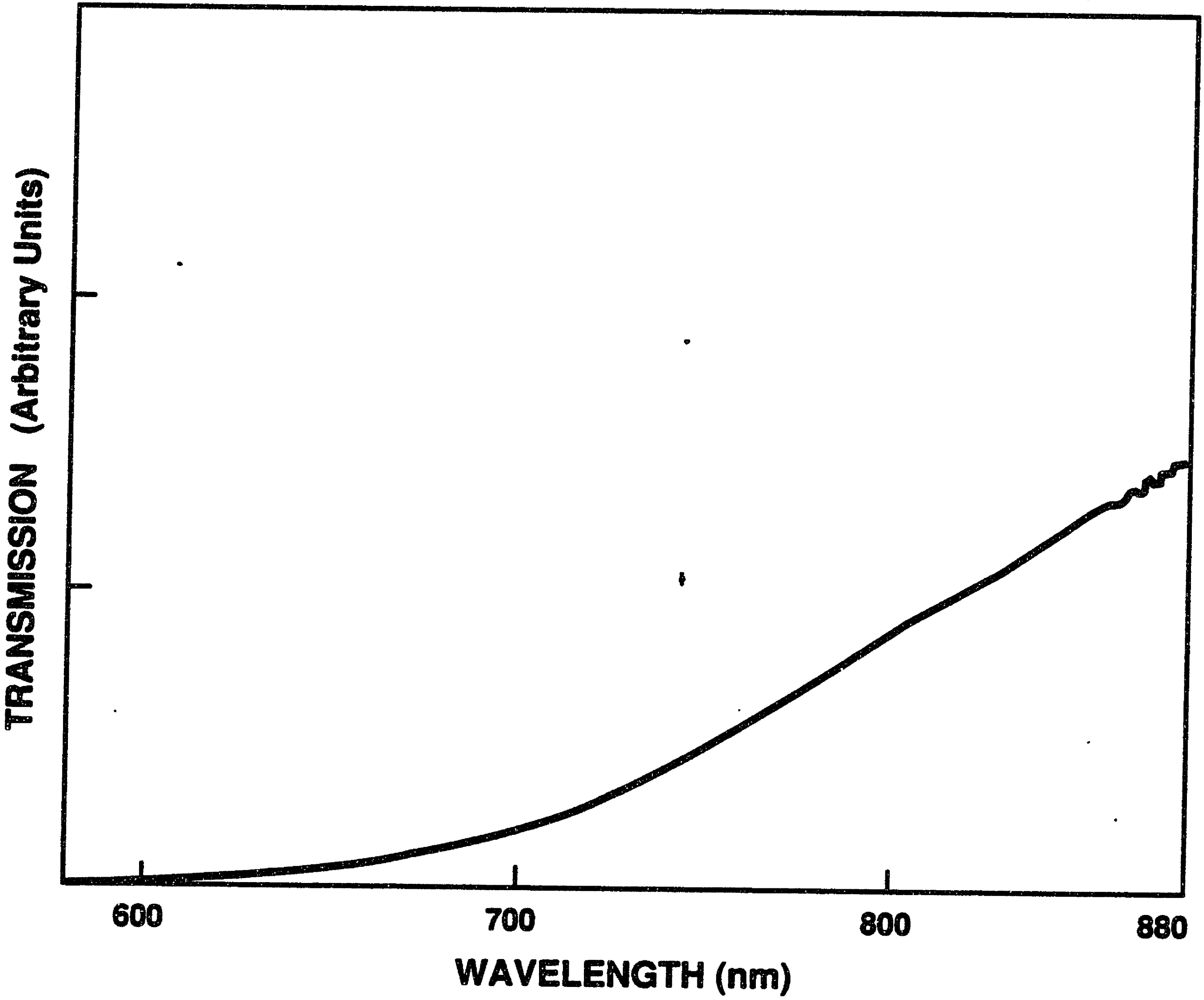

Figure 4.4. Normal-incidence transmission spectrum (linear scale) from multiple quantum well sample after ETBD with 380 keV Ne^+, with an ion flux of 4 μA/cm^2, for 15 min at 500°C.

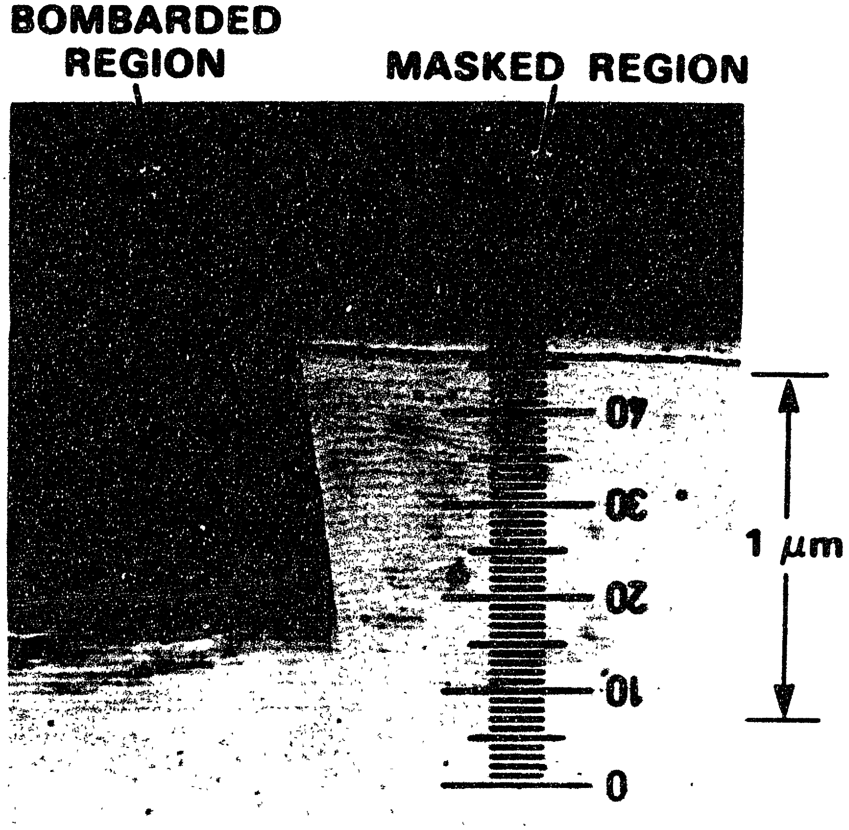

Figure 4.5. Optical micrograph of a 0.5°-angle-lapped end face from a multiple quantum well sample after ETBD with 380 keV Ne^+, with an ion flux of 4 $\mu A/cm^2$, for 15 min at 500°C.

For this calculation, the quantum-well layer is modelled as a square-wave concentration profile, assumed infinite in extent. The ion mass is not considered in the calculation. Therefore, the model is specific to bombardment with Ne^+ though an analogous procedure could be used to determine the parameter dependence of mixing with other ions. This model assumes the mixing is dominated by enhanced diffusion due to the steady-state vacancy population created by the ions. It ignores mixing due to interstitial migration and recombination, though this also occurs in the layer.

Following the models proposed in early work on radiation enhanced diffusion (Dienes and Damask), the diffusion constant is assumed proportional to the concentration of defects, specifically vacancies and interstitials, that lead to an enhanced atomic migration. This approach is also similar to a recent study of intermixing in AlGaAs/GaAs systems (Kahen et al.). Ion flux is assumed proportional to the steady-state background population of vacancies, and so is directly proportional to the magnitude of the diffusion constant. This assumption implies that the vacancies in the lattice result solely from primary ion-atom collisions. In fact, the detailed relationship is complicated. The ions make several collisions as they lose energy, and the number of collisions is dependent on the energy. Also, there are secondary atom-atom collisions that create additional vacancies. These effects rapidly make the problem intractable, and they are not included in this model.

The functional dependence of the vacancy population on flux also depends on the mechanism by which the vacancies recombine (Dienes and Damask). In particular, if the vacancies and interstitials recombine at fixed sinks, the linear assumption is good, however, if the recombination is due to direct interstitial-vacancy recombination the steady state vacancy population is proportional to the square root of the flux. This is found by rate equation analysis. Therefore, the model used for this analysis assumes that the recombination of the vacancies are due to recombination at fixed sinks.

The theory additionally assumes that the vacancies created by the bombardment are uniformly distributed through the layer. This assumption will yield a low estimate on the required flux because the ions end up in a Gaussian distribution within the layer. Recent Monte Carlo calculations (Kahen et al.) indicate that the density of vacancies created during bombardment of Si^+ into AlGaAs/GaAs multiple quantum wells is small at the surface, peaks close to the projected range, and falls off after the projected range. The implant depth in GaAs is ≈0.5μm for Ne^+ in GaAs, and the standard deviation is ≈0.3μm. So while a uniform distribution is not a bad approximation for the accuracy demanded of this calculation, it should be accounted for in a more accurate model. With these assumptions, the calculation proceeds as detailed below.

The one-dimensional diffusion equation in the absence of recombination phenomena with a constant diffusion constant, D(f,T) (cm^2/s), where T is temperature and f is ion flux, is:

$$D(f,T)\,\frac{\partial^2 A}{\partial x^2} = \frac{\partial A}{\partial t} \qquad (4.6)$$

A is the relative aluminum concentration that makes up the concentration profile. The profile is shown in Figure {4.6}. According to the model:

$$D(f,T) = D_0\, f \exp\left[-\frac{E_0}{kT}\right] \qquad (4.7)$$

where k is Boltzmann's constant, f is the flux, and E_0 and D_0 are parameters determined by a fit to experimental data. Diffusion equation solutions are sinusoidal in the x-variable, and exponential with time. The boundary condition on the time is that A=A(x) at t=0 and A=0 at t=∞. So the solution for the time variable has an exponential dependence as follows:

$$A(t)=A(x)\exp\left[-\frac{t}{\tau_n}\right] \qquad (4.8)$$

A Fourier transform facilitates the solution of the x-variable. The Fourier transform of the square wave initial condition for the concentration profile is expressed, including the time dependence, as:

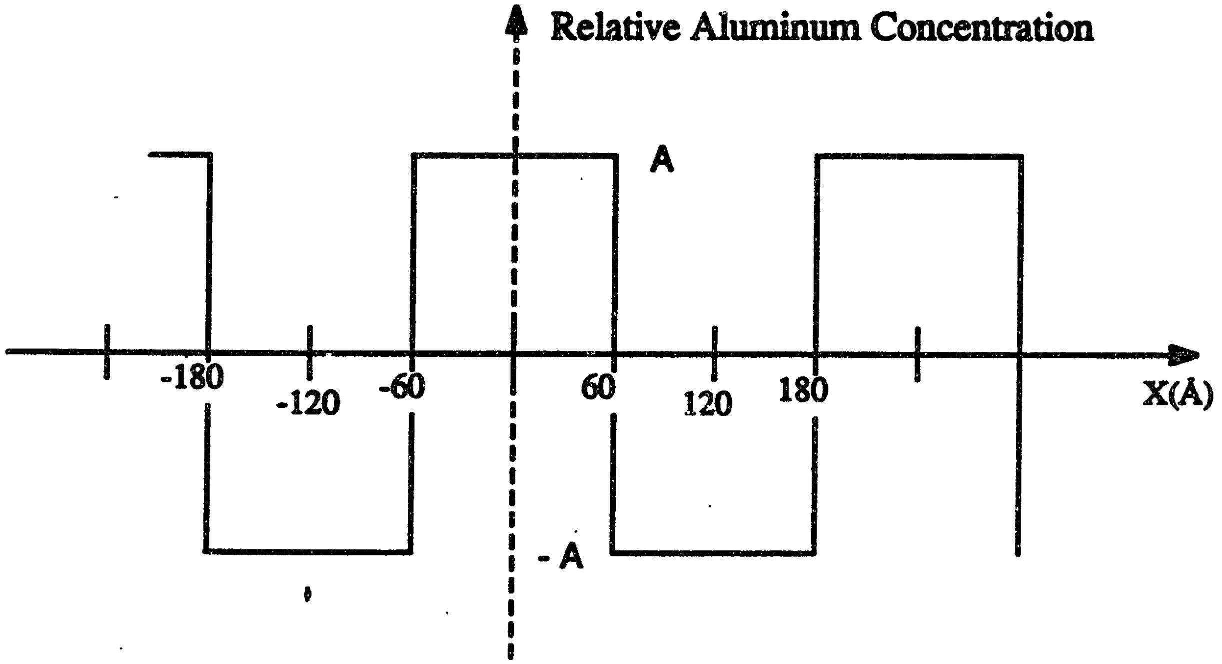

Figure 4.6. Aluminum concentration profile used in the diffusion calculation.

$$A(x,t) = \frac{4A}{\pi}\sum_{n=1}^{\infty}\frac{(-1)^{n+1}}{2n-1}\cos\left(\frac{\pi(2n-1)x}{d}\right)\exp\left[-\frac{t}{\tau_n}\right] \qquad (4.9)$$

where the width of the multiple quantum well barriers, L_b, and wells, L_w, are $L_b = L_w = d = 120Å$. Defining $k_n = \frac{\pi(2n-1)}{d}$, the n^{th} term in the expansion, plugged into the diffusion equation, {4.6}, yields:

$$-k_n^2 D(f,T)\,A = -\frac{1}{\tau_n}A \qquad (4.10)$$

so that:

$$\tau_n = \frac{1}{k_n^2 D} \qquad (4.11)$$

We consider $t = \tau_n$, where the concentration difference is down by 1/e, to be the time required for approximately complete mixing. Only the n=1 solution is considered since higher order terms decay faster. From Equations {4.7} and {4.11}, an expression for f(T) that indicates the flux required, for a given temperature, to produce complete mixing in a bombardment time, t_o, is given by:

$$f(T) > \left[\frac{d}{\pi}\right]^2 \frac{1}{D_o t_o}\exp\left[\frac{E_o}{kT}\right] \qquad (4.12)$$

For a t_o = 15 min bombardment time, there are two experimentally obtained sets of flux and temperature at which mixing does not appear to be complete. D_o and E_o are determined by using these experimentally determined temperatures, in the condition of Equation {4.12}. This produces a fit that yields D_o= 1.7 X 10^{-12} (cm^4/µA-min), and E_o= 0.433 eV.

It is interesting to compare the diffusion constant at a flux of 10 µA/cm^2 at 700°C calculated from the model to the diffusion constant of Al in as-grown heterojunctions. For $Al_{0.3}Ga_{0.7}As$/GaAs. the activation energy for diffusion is 6 eV (Chang and Koma; and Schlesinger et al.). Using the theory and experiment of Schlesinger, the diffusion constant at 700°C is about 10^{-23} cm^2/s. Under the influence of the ions the diffusion constant calculated by the model is about 10^{-16} cm^2/s. Thus the ion bombardment at a temperature of 700°C is equivalent to annealing an unbombarded sample at a temperature of 975°C using Schlesinger's diffusion constant.

Using the values of D_0 and E_0, a universal curve that shows the flux-time product as a function of sample temperature required for complete mixing of the multiple quantum well layer is found. The curve is shown in Figure {4.7}. Also shown on this graph are the experimental points for complete and incomplete mixing. The graph shows that lower ion flux requires higher target temperatures and higher flux requires lower temperatures to achieve mixing as expected.

From this graph it is apparent that complete mixing at a temperature of 400° C is possible with ion flux of 8 $\mu A/cm^2$ for 30 minutes. This was subsequently demonstrated. The 0.5°-angle-lapped optical micrograph of the bombarded region the sample after bombardment with these parameters are shown in Figure {4.8}. The transmission spectrum is shown in Figure {4.9}. The band edge is characteristic of an alloy with the average aluminum mole fraction of the original quantum well layer. Although it is possible that the residual damage is higher in the low temperature annealing procedure, these effects were not explored. The normal-incidence transmission spectra signal from this sample was not significantly different than the other samples.

Section 4.5 Conclusions

This chapter has reported experiments and a model aimed at determining the parameter dependence of the intermixing process. Experiments with different ion masses indicate that mixing occurs for ion masses equal to nitrogen and larger. In particular, hydrogen and helium were not able to produce mixing. The model predicts the expected result that lower incident ion flux requires higher target temperatures and/or longer process times to achieve the same degree of mixing. Experiments have shown it is possible to intermix 1-μm-thick layers with an ion flux of only 1 $\mu A/cm^2$ for a thirty minute bombardment time, and 700°C target temperature. Also, intermixing in less than 5 minutes

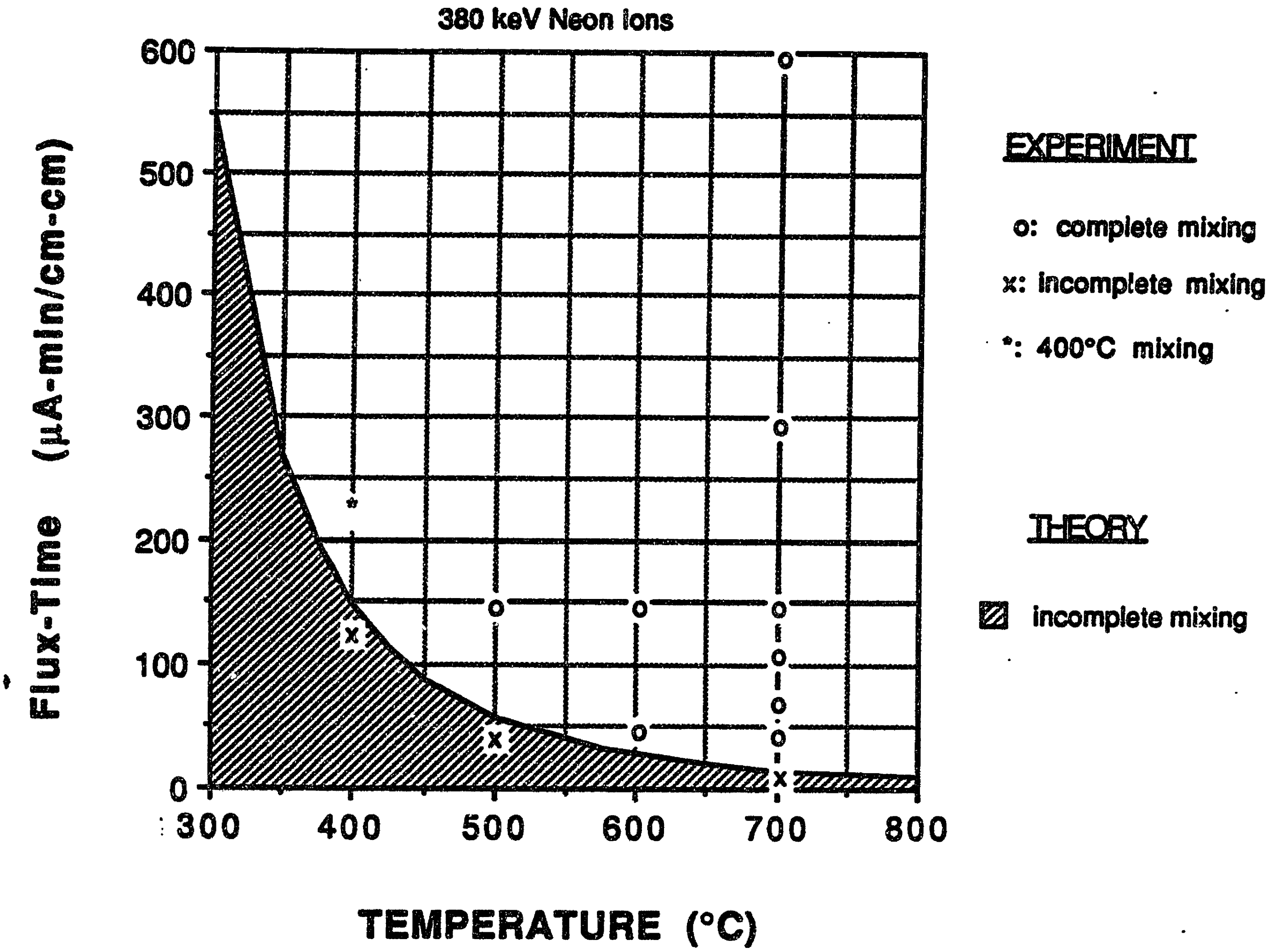

Figure 4.7. Flux-time product vs temperature for complete mixing using Ne+ ions. Also shown are the experimental points that demonstrate complete (O) and incomplete (x) mixing.

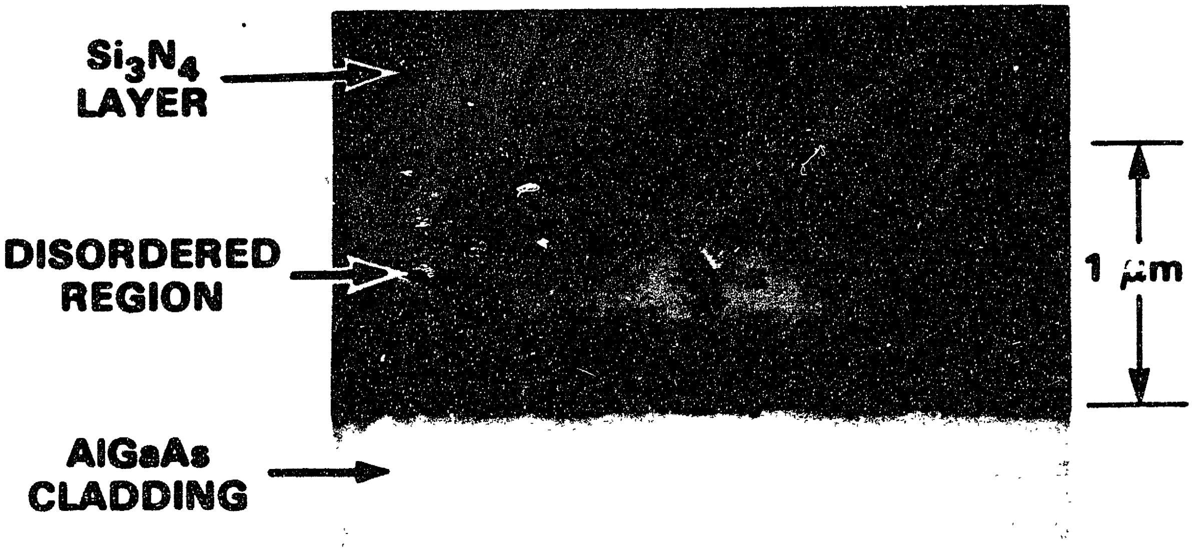

Figure 4.8. Optical micrograph of a 0.5°-angle-lapped end face from a multiple quantum well sample after ETBD with 380 keV Ne^+, with an ion flux of 8 $\mu A/cm^2$, for 30 min at 400°C.

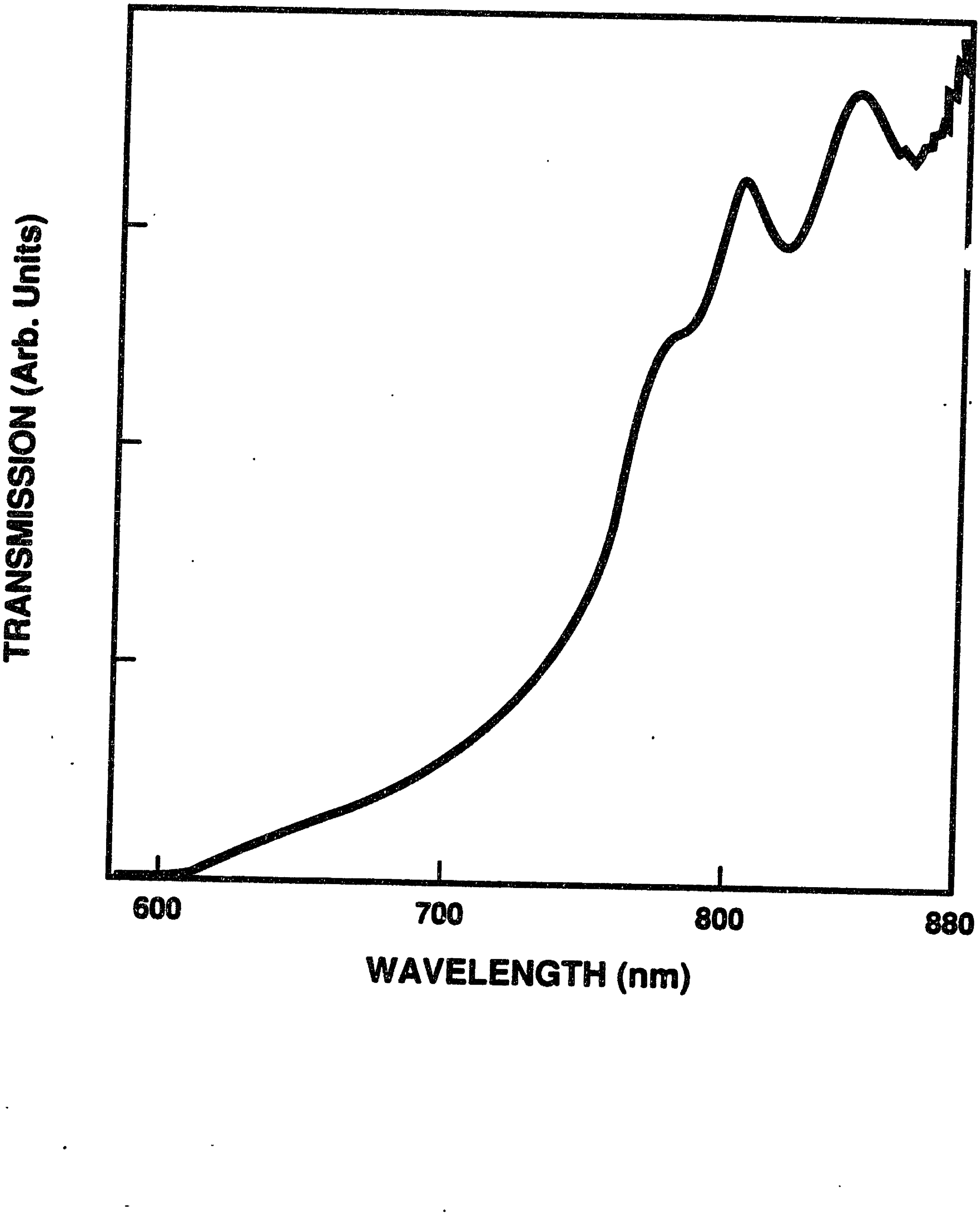

Figure 4.9. Normal-incidence transmission spectrum (linear scale) from multiple quantum well sample after ETBD with 380 keV Ne+, with an ion flux of 8 μA/cm^2, for 30 min at 400°C.

was accomplished. This is as short as the shortest mixing times in the Zn diffusion process. Intermixing at 400°C has also been demonstrated, and this is the lowest temperature reported for any mixing process. However, the relative material quality between this and the higher temperature mixing materials is not fully known.

The elevated temperature bombardment disordering technique should prove to be a viable alternative to impurity induced disordering in applications where dopants are undesirable, and also to minimize the high temperature processing required for impurity based methods. In addition, the TEM micrographs of Chapter 3 indicate the residual damage in the ETBD samples are significantly improved over ion bombardment at room temperature and then subsequent annealing procedures. Further experiments were performed that were aimed at reducing the residual damage in the materials, and also to investigate the masking possibilities. These are outlined in the following chapters.

Chapter 5
PATTERNING TECHNIQUES

Section 5.1 Introduction

For ETBD to be useful, the process must be capable of being patterned onto a epitaxially grown wafer. In the ETBD process, because the temperatures and bombardment times are short, no intermixing will occur in the absence of ion bombardment. This will be true even if there are dopants such as Si Se, Be or B, in the layer given the reports in the literature as to the efficiency of intermixing with these materials (Ralston et al., 1986). However, it will not be true of Zn, because Zn induced disordering is very efficient (Laidig et al.). Therefore, for masking to be effective in ETBD, there must not Zn near the heterostructure to be intermixed. In general, any mask which prevents the ions from penetrating the region of the heterostructure will successfully prevent intermixing.

Several characteristics of the masking process are important. First, the mask must be able to withstand high temperatures. This eliminates the possibility of thick photoresist. As was made clear in the results of experiments described in Chapter 2, strain affects the diffusion process. Strain effects should be less in the ETBD process than in the dielectric-encapsulation disordering because the elevated temperature duration is about thirty times shorter, and the temperatures are lower. Probably the most stringent requirement on the mask is the ability to stop the high energy ions. Therefore, thick mask layers are required.

The lateral diffusion under the mask in the absence of strain effects can be approximated theoretically. The expression for the ion distribution under a long mask with a sharp edge of width 2a is a complimentary error function (Pikar):

$$n(x) \propto \frac{1}{\sqrt{\pi}} \operatorname{erfc}\left(\frac{x-a}{\sqrt{2}\Delta R_T}\right) \qquad (5.1)$$

where x is along the plane of the layer. The parameter ΔR_T is the lateral standard deviation that is dependent on the ion, the target material, and the ion acceleration energy and may be found in table of the Projected Range Standards for Ion Implantation (Gibbons et al.). For 380 keV N^+ implanted through a 2-µm-wide mask in GaAs, the resulting ion distribution at a set depth is shown in Figure {5.1}. The plot for Ne^+ ions is very similar. The plot indicates that the lateral straggle is small for these ions. The ion distribution is down to one-tenth that in the center of the mask only 0.25 µm away from the masked edge. It is likely that the vacancy production, and therefore also the enhanced diffusion, would roughly follow the ion distribution, but a more detailed analysis would be required to determine the exact relationship.

In the work reported here, two masking techniques were investigated. The first used thick AlGaAs epitaxially grown over the quantum wells. The AlGaAs may be patterned with standard photolithographic techniques, and removed where the ions are to penetrate the quantum well layer. The thick AlGaAs will stop the ions where intermixing is not desired. This layer is removed by selective etching. The second technique uses a thick silicon dioxide layer as a mask. This is a more general and easier technique. It also can be considered a demonstration of the feasibility of using other dielectrics such as PSG or Si_3N_4. Both deposition and removal of the silicon dioxide is less complicated than AlGaAs. The demonstration of these two methods is describe below. Good masking results were obtained using both techniques. The crucial issue was whether stress between silicon dioxide and GaAs would result in poor quality mask edges. This was not a problem, and therefore, this dielectric masking method should prove viable for delineating devices. Both techniques have been used to fabricate waveguides as described in Chapter 7.

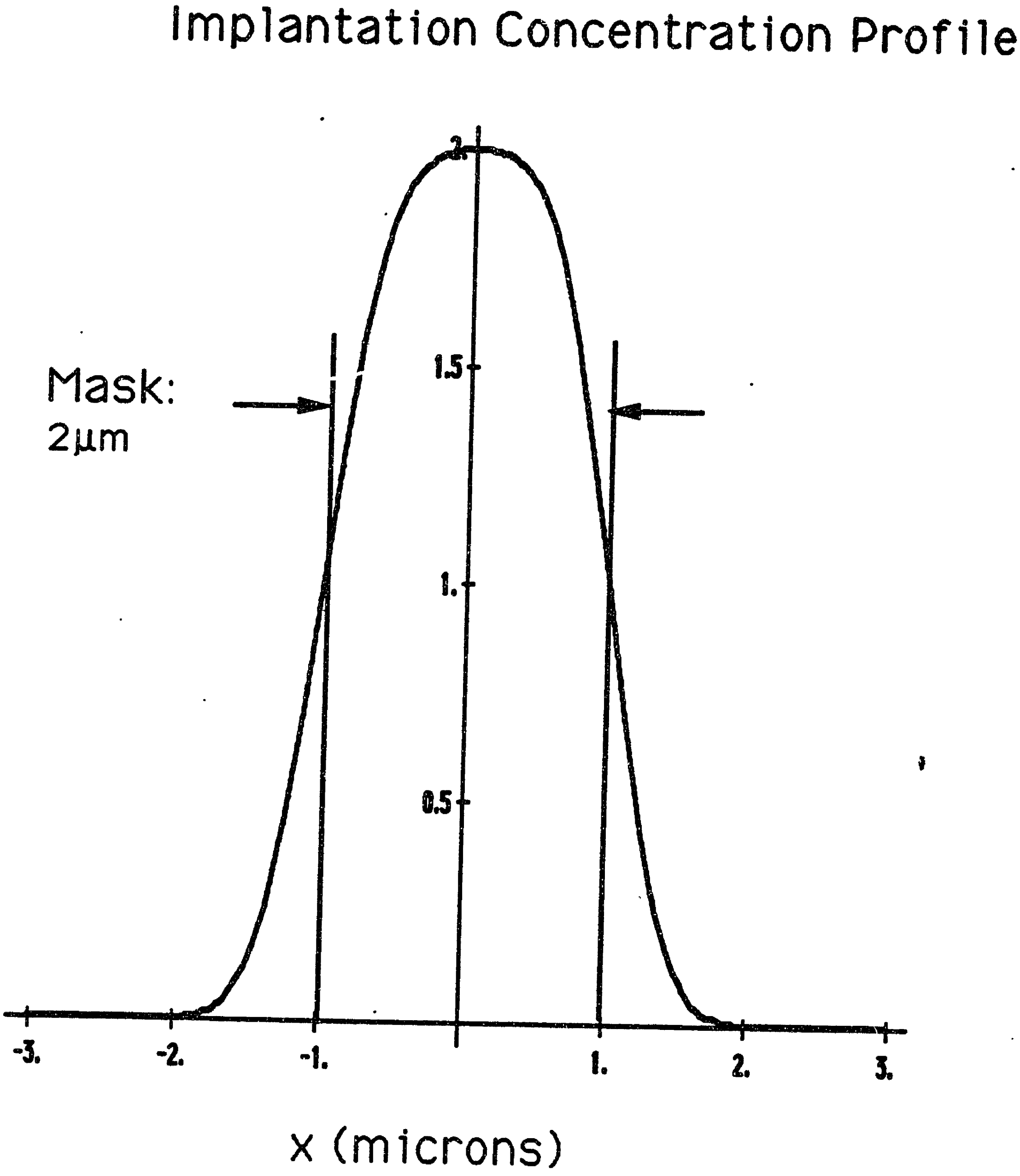

Figure 5.1. Implant concentration profile using a 2-μm-wide mask. Calculation for 380 keV N^+ ions.

Section 5.2 Epigrown AlGaAs Technique

The epitaxially grown AlGaAs technique was undertaken as the first attempt to pattern devices with the ETBD technique. Two issues, the layer thickness and the Al mole fraction, x, in the $Al_xGa_{1-x}As$ layer, had to be determined. The layer must be thick enough to absorb all the incident ions, but not so thick as to shadow the unmasked regions, not pattern appropriately, or be difficult to remove. The stopping distance or projected range of 380 keV nitrogen ions in GaAs is R_p=0.65 μm with 0.19 μm standard deviation (Gibbons et al.). Therefore, assuming that the stropping distance is comparable in AlGaAs, a 1.5 μm thick AlGaAs layer was used. Also, this layer must be removed by a selective etch. The etch will be more selective for larger differences in the Al concentration in the two layers. However, as the Al mole fraction increases the material oxidizes more readily and the number of background impurities in the layer increases. An Al mole fraction of x=0.5 was chosen as a good compromise.

Two layers were grown to test the process. The lower cladding of the layer structure, grown on GaAs, consists of a 3-μm-thick $Al_{0.5}Ga_{0.5}As$ layer. This is followed by 40 alternating 120-Å-thick GaAs and $Al_{0.3}Ga_{0.7}As$ layers that form the waveguide core region. A 1.5-μm-thick $Al_{0.5}Ga_{0.5}As$ layer and a 25Å GaAs cap layer were then grown. All layers were nominally undoped. The second structure was grown with the same specifications as the first, but an 0.8-μm-thick $Al_{0.15}Ga_{0.85}As$ layer was grown in place of the multiple quantum well layer. Thus this sample should be similar to the multiple quantum well layer after intermixing.

Preliminary experiments were performed to test the usefulness of this masking technique. The ability of the 1.5-μm-thick layer to stop the ions and prevent the multiple quantum wells from being intermixed was tested by bombarding the layer with 380 keV Ne^+ ions at an ion current density of 10 $\mu A/cm^2$ for 15 minutes with the target at 700°C. Half the sample was masked from bombardment. Normal incidence transmission spectra from the two layers were compared, and no difference between the two layers was evident.

The second important issue was removal of the $Al_{0.5}Ga_{0.5}As$. Only two etchants were found that etch materials with higher mole fractions of Al significantly faster than lower concentrations. These were HCl at 80°C (Vossen and Kern), and HF at 80°C (Wu et al.). These two etches were tested on the sample with $Al_{0.15}Ga_{0.85}As$ in place of the quantum wells. While the HCl etch did stop effectively at the $Al_{0.15}Ga_{0.85}As$ surface, the surface quality was very poor. Etch pits formed on the surface. The HF etch, on the other hand, worked very well, removing the $Al_{0.5}Ga_{0.5}As$ and stopping at the $Al_{0.15}Ga_{0.85}As$ with a smooth surface.

The promising initial results led to further testing. The technique was applied to fabricating stripes. For this, the $Al_{0.5}Ga_{0.5}As$ was covered with photoresist and exposed through a mask with stripes ranging from 2 µm to 10 µm thick. The photoresist was removed from the sample everywhere except the stripes. The sample was then etched with a sulfuric acid etchant: H_2SO_4:H_2O_2:H_2O in ratios of 1:1:8. The room temperature etch rate of this etch is about 3µm per minute. 1.4 µm of the $Al_{0.5}Ga_{0.5}As$ was etched away. Care was taken that the sample was oriented so that the anisotropic etch produced sidewalls that sloped away from the sides of the mask. The photoresist was then removed. A 1000Å thick Si_3N_4 layer was deposited by pyrolytic deposition. This layer was used to minimize surface degradation. The nitride was inspected under a microscope to assure that complete coverage of the AlGaAs surface had occurred. After standard ion bombardment procedures with 380 keV neon ions for 15 minutes with 10 $\mu A/cm^2$ of ion flux, and the target at 700°C, the nitride was removed with room temperature HF. Then the 80°C HF etchant was used to remove the $Al_{0.5}Ga_{0.5}As$ ridges.

A scanning electron micrograph of a stained end face of the layers just before removal of the $Al_{0.5}Ga_{0.5}As$ layers is shown in Figure {5.2}. The stain is a slightly selective $K_3Fe(CN_4)$-KOH solution. It etches both AlGaAs and GaAs slightly, and rounds the edges as is apparent in the micrograph. The delineation of the multiple quantum wells with respect to the intermixed AlGaAs material is indicated. The slant to the pattern is a

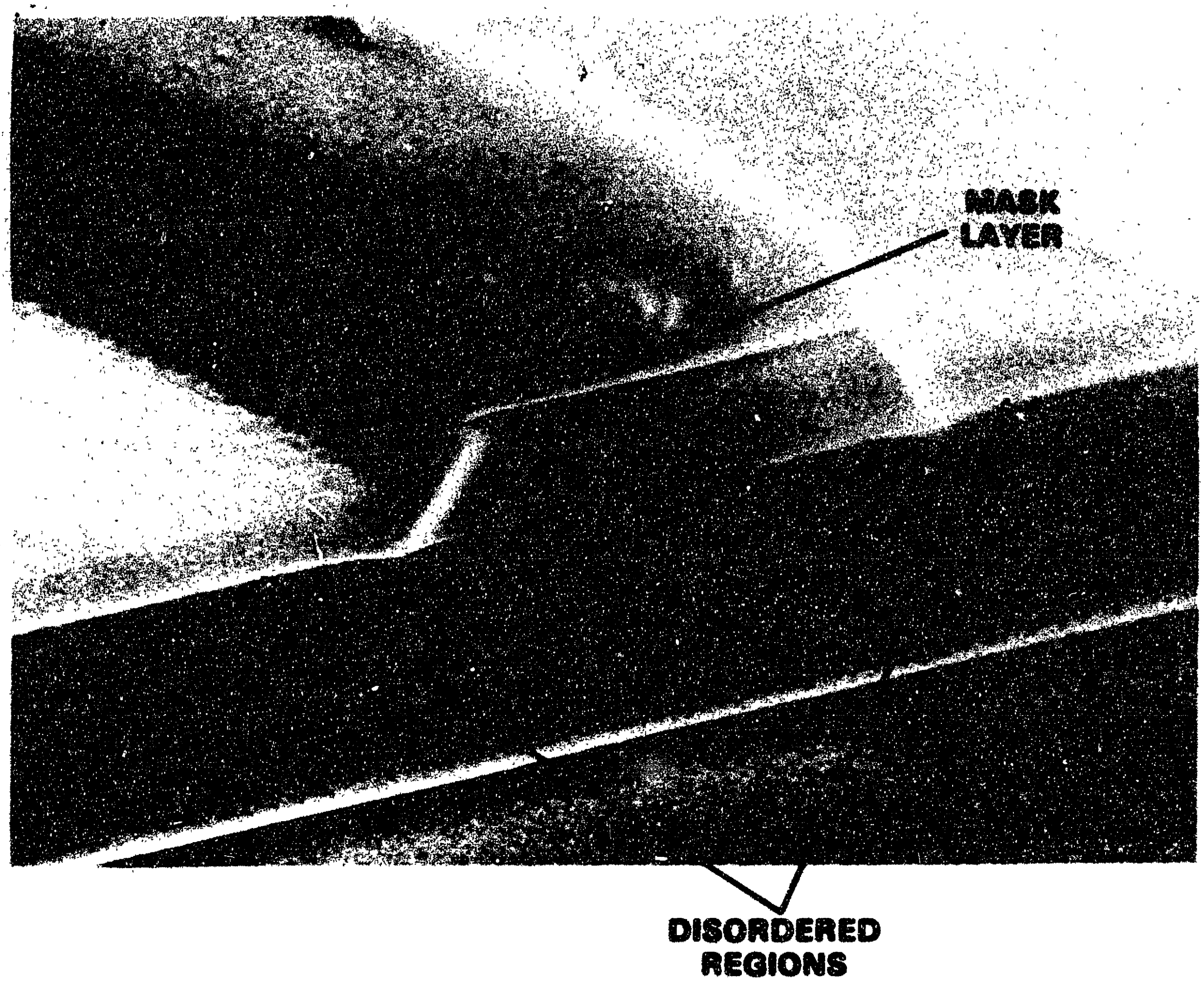

Figure 5.2. Scanning electron micrograph of stained end face of the multiple quantum well sample with $Al_{0.5}Ga_{0.5}As$ masking layer.

result of the slanting sidewalls of the AlGaAs mask. There is no significant lateral diffusion using ETBD with this mask.

While these results indicate strong potential for the masking technique, one drawback was discovered in the removal of the $Al_{0.5}Ga_{0.5}As$ layer. A small ridge is formed on the part of sample that covers the quantum wells. The ridge can be seen in a SEM micrograph of a stained sample after removal of the AlGaAs ridge shown in Figure {5.3}. This ridge was approximately 200Å to 300Å, and occurred consistently each time the process was used. It arises due to a combination of residual $Al_{0.5}Ga_{0.5}As$ and slight etching into the $Al_{0.15}Ga_{0.85}As$ layer. The small ridge is undesirable for waveguide fabrication because the ridge will provide waveguiding in the underlying multiple quantum well layer without any index guiding due to the compositional changes introduced by the intermixing process. Thus, another masking technique was examined that used a thick layer of SiO_2 to stop the incident ions and keep them from penetrating the multiple quantum well layer.

Section 5.3 Silicon Dioxide Mask

Masking for ion bombardment using silicon dioxide is well known (Pikar). The ions do create damage in the SiO_2 layer that increases the etch rate of the SiO_2, and makes removal more difficult, but it was determined that this is only a minor inconvenience, and the SiO_2 can be removed completely with chemical etchants. The main issue to be determined in these experiments was the integrity of the masked edge, and whether stress would cause lateral diffusion. The results indicate that the technique works very well. The mask edge is very good, and we have demonstrated masking narrow stripes, <2 µm wide, of intermixed layers surrounded by quantum wells and similarly narrow regions of quantum wells surrounded by intermixed material. These results are detailed below.

For SiO_2 to be an effective mask for 380keV ions with masses of neon and nitrogen, the SiO_2 must be over 1.5µm thick. This thickness results in a masking

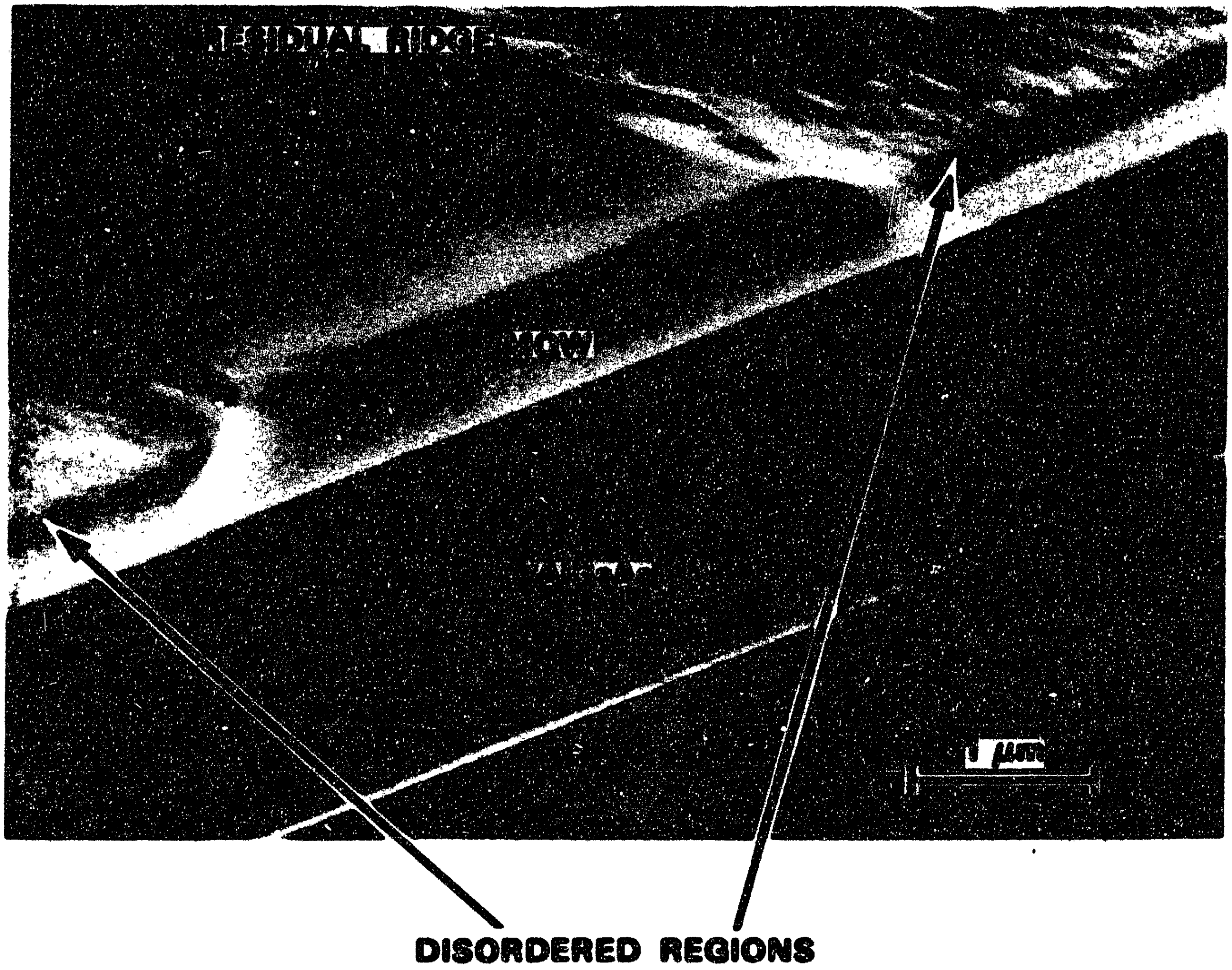

Figure 5.3. Scanning electron micrograph of stained end face of the multiple quantum well sample after removal of the $Al_{0.5}Ga_{0.5}As$ masking layer.

effectiveness of 99.99% (Ghandi, p.350). The requirements on the mask for the ETBD technique are less stringent than for doping, because the intermixing requires a large steady-state number of ion collisions with atoms. Therefore, the intermixing process is less efficient in the tails of the ion distribution. A silicon dioxide layer of 1.5 μm thick was used for the experiment. To prevent undercutting, and provide well controlled etch depth, reactive ion etching was used to form the stripes in the SiO_2.

For these experiments the layer structure used consisted of a 3-μm-thick $Al_{0.5}Ga_{0.5}As$ layer grown on the GaAs substrate, followed by 40 alternating 120-Å-thick GaAs and $Al_{0.3}Ga_{0.7}As$ layers and a 25Å GaAs cap layer. All layers were nominally undoped. 1.5 μm of SiO_2 was deposited in a pyrolytic deposition system. Photoresist was applied to the sample and it was exposed through a mask. Two masks were used. One consisted of 1.5-μm transparent stripes, and the other had opaque stripes, between 2 and 10 μm thick. In this way, small regions of disordered material surrounded by quantum wells, and thin regions of quantum wells surrounded by intermixed material could be studied. The photoresist was patterned, and the SiO_2 layer was etched to a thickness of 700 Å. The 700-Å layer covering the areas around the 1.5-μm-thick masked areas minimizes surface degradation of the GaAs cap layer. The residual photoresist is removed with acetone.

For ion bombardment, each sample was mounted on a graphite heater strip misoriented to the ion beam 7° to minimize channeling. The sample was heated to 700° C and bombarded with 380 keV N^+ ions. The ion current density was 10 $\mu A/cm^2$ and the bombardment time was 15 minutes. The SiO_2 was partially removed from the sample using reactive ion etching, and the remainder was removed with Buffered HF.

Optical micrographs of the angle-lapped end face of the sample with 1.5 μm stripes etched away in the SiO_2 mask are shown in Figures {5.4} and {5.5}. The figures indicate the layer intermixing extends completely through the 1 μm thick multiple quantum well layer. There is no apparent lateral diffusion under the mask. The expanded view in Figure

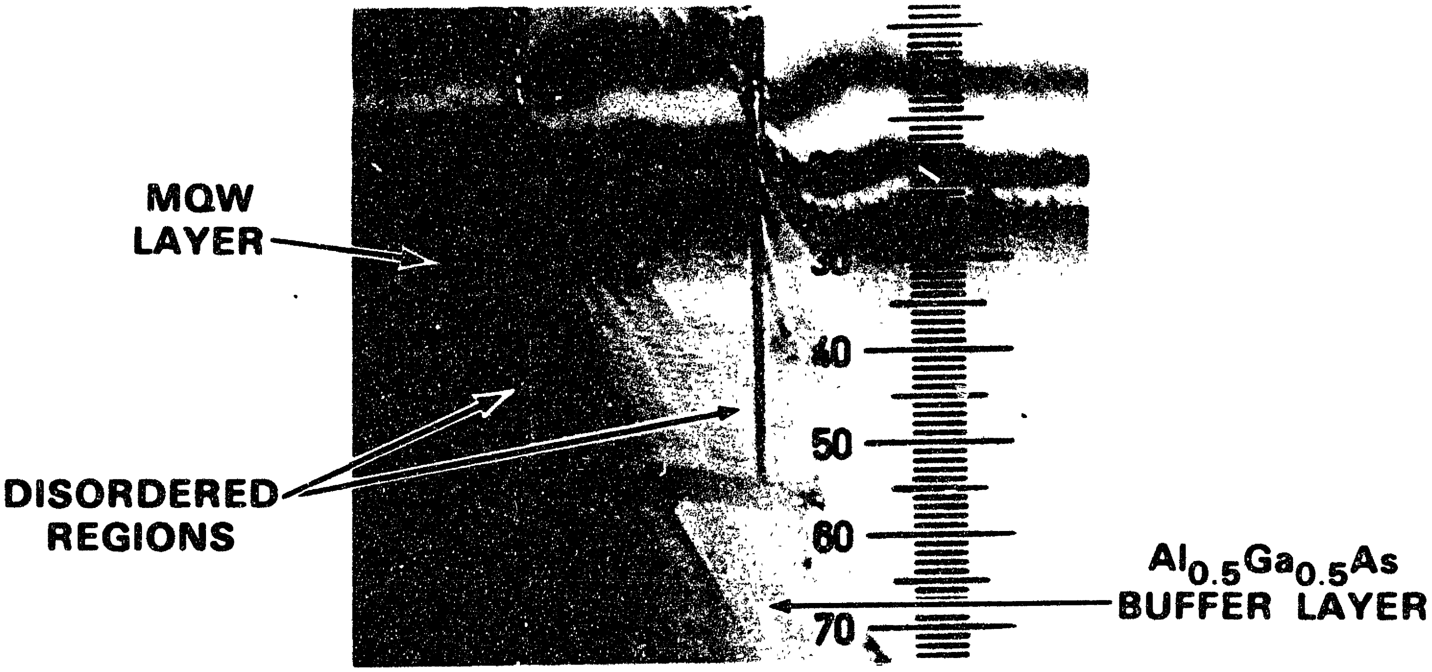

Figure 5.4. Optical micrograph of 0.5°-angle-lapped end face of sample masked with 1.5-µm-thick SiO_2. The two mask openings were 4.0 µm wide.

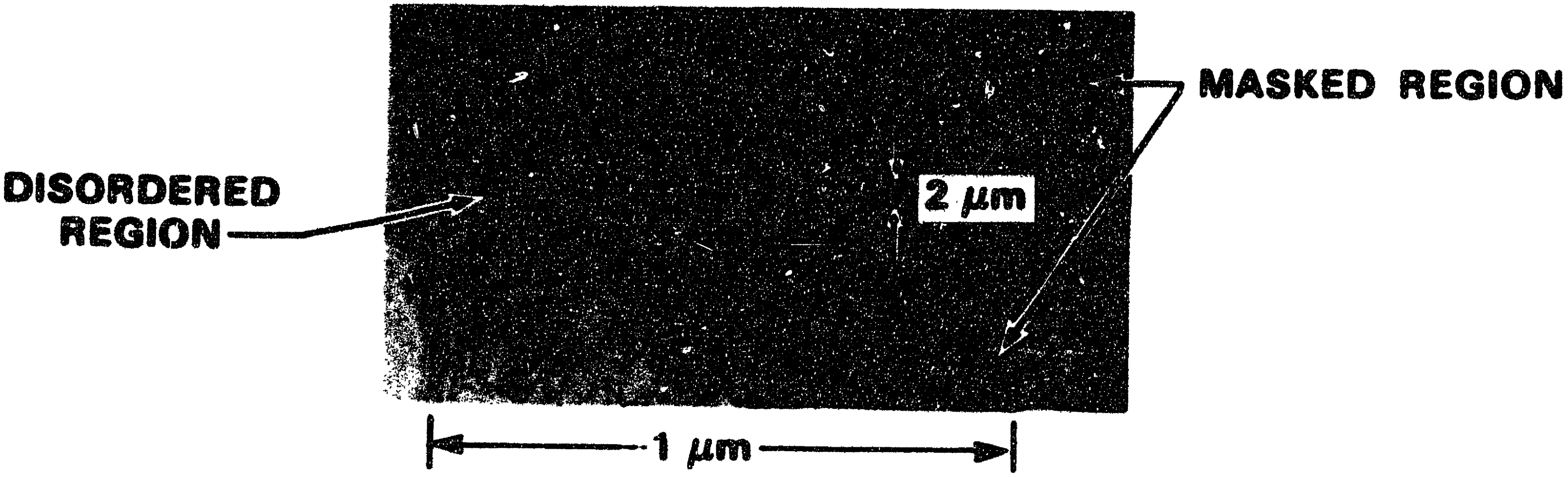

Figure 5.5. Optical micrograph of 0.5°-angle-lapped end face of sample masked with 1.5-μm-thick SiO_2. The mask opening was ≈2.0 μm wide.

{5.5} shows the intermixed region is less than 2 µm thick. This thickness is equivalent to the thickness of the SiO_2 layer measured just after the reactive ion etching. There is some lateral etching with reactive ion etching, but not with the disordering process.

The same characterization was performed on the samples that were patterned with the second mask. An optical micrograph of the angle-lapped end face of this sample is shown in Figure {5.6}. In this photograph, the two 10-µm stripes have multiple quantum wells that are still intact. Unfortunately, the quality of the photograph is poor. However, the well defined edges where the intermixed regions meet the multiple quantum wells are apparent because the multiple quantum well layer is not etched by the Clorox. This picture also shows that the region in between the two stripes, which is less than 4 µm thick, was intermixed.

Section 5.4 Conclusions

Two different masking techniques have been used to pattern ETBD across a wafer. The first of these used epitaxially grown AlGaAs to stop the incident ions. The AlGaAs layer was removed by selective etching. The integrity of the multiple quantum well layer was well maintained and there was no significant lateral diffusion under the mask with this technique. The drawback was that the selective etch removal step left a small residual ridge on the surface. This is undesirable for many applications.

The second technique studied used thick SiO_2 to stop ion penetration into the quantum wells to prohibit mixing. The results indicate the potential of dielectric capping in patterning ETBD. Both thin regions of quantum well and thin regions of disordered material were successfully formed. The thickness of the layer disordered was 1 µm, and the mask widths were less than 2 µm. In this work, silicon dioxide was investigated because the reactive ion etching system was prepared to etch that material. Silicon nitride or PSG would also be a good mask materials for several reasons. Silicon nitride is better at preventing surface degradation than SiO_2, and there is a higher potential for the multiple

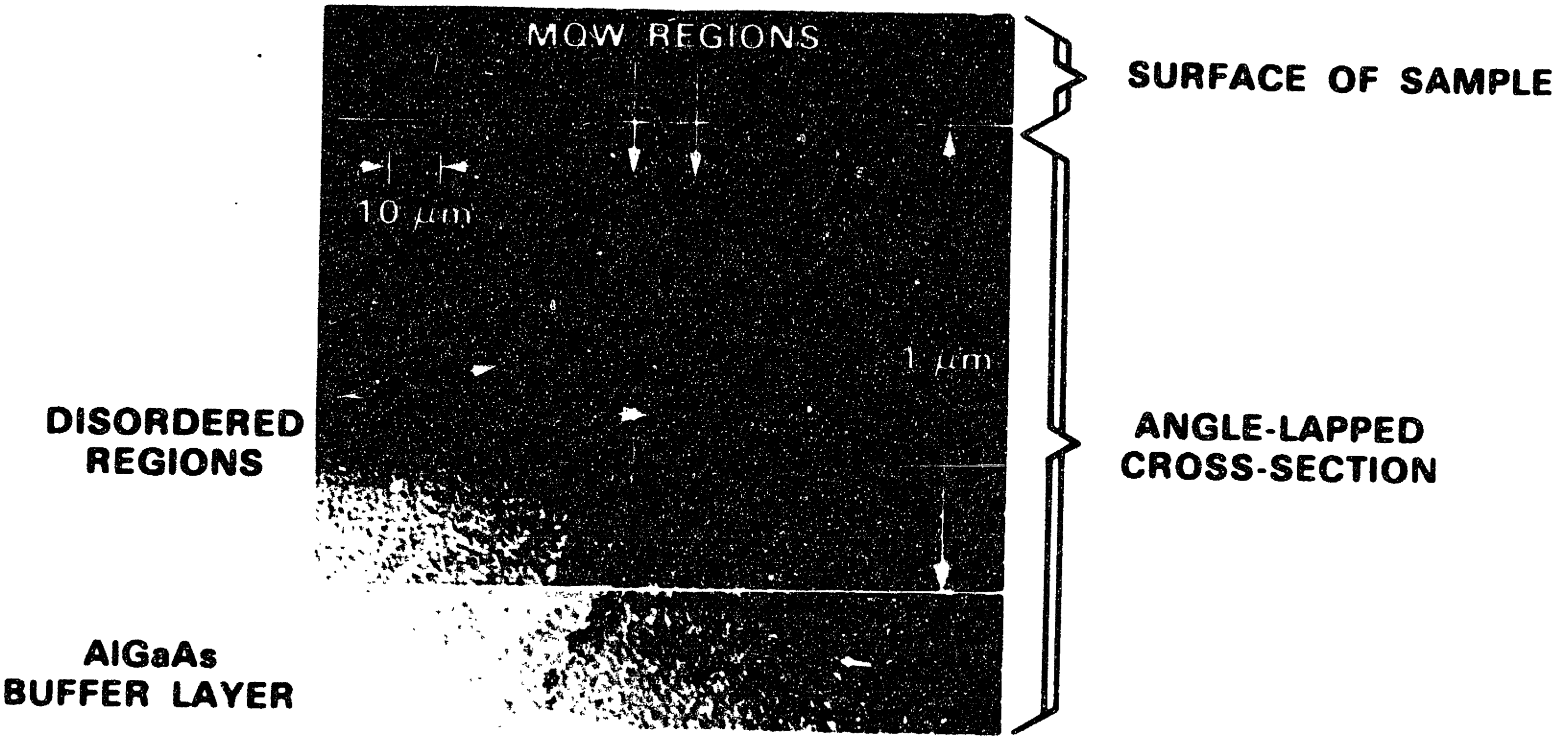

Figure 5.6. Optical micrograph of 0.5°-angle-lapped end face of sample masked with 1.5-μm-thick SiO_2. The masked regions are 10 μm wide, separated on 14-μm centers. The dark regions on the photograph are intermixed, mixing did not extend the full 1.0-μm-thick multiple quantum well layer.

quantum wells to be partially intermixed under the SiO_2 via the disordering process described in Chapter 2. While this would not be a factor in the low temperatures and short process times of ETBD, it would be a factor if post-bombardment annealing was used with higher temperatures over 900°C (Ralston et al., 1989). In addition, silicon nitride is slightly more effective at stopping the high energy ions than silicon dioxide. The benefit of PSG is that the thermal expansion coefficient is similar to GaAs. The transfer to these materials should be straightforward.

Chapter 6

REDUCING RESIDUAL DAMAGE

Section 6.1 Introduction

The evidence of residual damage in the disordered regions shown in the TEM cross section of Figure {4.3} led to concern about the optical quality of the material. As is discussed below, the damage results in increased loss near the band edge of the quantum well material. This is undesirable for the applications of near resonant optical device fabrication. Thus, post-process annealing was studied to try to reduce the residual material damage. Two annealing procedures were investigated. The first involved furnace annealing at 600-850°C for 10-30 minutes, and the second involve rapid thermal annealing at 950°C for times of less than one minute. The results indicate that post-process annealing will reduce damage, however, to maintain integrity of the multiple quantum wells, low temperatures and shorter annealing times are required. After a brief background on radiation damage and damage annealing, experimental results on the intermixed quantum well samples are presented.

Section 6.2 Background

It is well known that post-implantation annealing will reduce radiation damage. Annealing is often used to regain electrical properties of mobility, carrier lifetime, and electrical activation energy in GaAs materials. In this work, the goal is to reduce the optical loss. Below band gap, absorption is affected by increased recombination velocity that acts to broaden the band edge. An enhancement of the recombination velocity is often caused by defect states in the band gap. Also, optically active defect states within the band will increase absorption. In addition to post implantation annealing, elevated target temperatures during implantation also are known to reduce damage. Because ETBD utilizes elevated temperature targets, the residual damage is less than with room temperature bombardment procedures.

Radiation induced damage is related to the dose of the implant, the ion mass and acceleration energy. Damage typically begins as creation of isolated vacancies and interstitials. The defects migrate in the sample, and also recombine. The details of the migration and recombination are dependent on the target temperature. As the density of these defects increase, they begin to agglomerate and form large clusters that eventually form dislocation loops. As the density is increased, the formation of amorphous zones also occurs. The formation of amorphous zones is strongly dependent on target temperature, and is most probable at low target temperatures such as 77°K. From the TEM cross sections obtained for the bombarded layers at 700°C for 1 hour shown in Figure {4.3}, there is no evidence of either dislocation loops, or amorphization. However, the dark regions in the bombarded, intermixed region do indicate residual damage.

Recently, furnace annealing at 800°C for 15 minutes was used to reduce the damage in GaAs superlattices after implantation of 40 keV and 120 keV Si^+ ions (Matsui et al). The results indicates nearly complete recrystallization of the amorphized regions as measured by Rutherford backscattering. Photoluminescence (PL) yield, which provides information about the optical properties of the materials, was measured in superlattices implanted with a 10^{15} cm^{-2} of 80 keV Si^+ (Kobayashi et al.). The ratio of the PL peak near the band edge of the superlattice from a sample after implantation to that from a sample with no implantation was 10^{-3}. With rapid thermal annealing at 770°C for 5 s, 860°C for 5 s, and 900°C for 2 s, the ratio was improved to ≈0.3. Furnace annealing at 850°C for 30 min. showed a ratio of 0.5, although part of the lost yield was due to some partial intermixing that shifted the band edge. The best improvement was found with 970°C for 10 s, with a 0.8 ratio. These workers used capless annealing and found no intermixing at the 970°C temperature. This is in contrast to Kahen et al. who did find superlattice intermixing during post-Si^+-implantation rapid thermal annealing at 950°C for 10 s (Kahen et al.).

For the work presented in this thesis, the aim was to reduce the damage, and not to affect the integrity of the quantum well layers. Furnace annealing was used to determine the effects of long annealing times. Also, rapid thermal annealing was investigated.

Section 6.3 Experiment

6.3.a Measurement Techniques

To determine material quality, normal-incidence transmission and transmission through a slab waveguide were investigated. Normal-incidence transmission provides an indication of the material quality through the relative broadening of the absorption edge. Damage can lead to enhanced nonradiative recombination that reduces carrier lifetime and broadens the band edge. In normal-incidence transmission the light passes through thin (<3 μm thick) epitaxially grown layers. Therefore the loss is small even if the loss per unit length is large. In addition, Fabry-Perot resonances are evident because the front and back faces of the sample provide a resonant cavity for the incident light. To some degree, the modulation depth of these resonances is an indication of the loss in the material, because the Q of the cavity is related to loss. However, the cavity Q is also dependent on the reflectivities of the front and back facet which are sensitive to the processing of the sample. So although the Fabry-Perot fringes are used to provide and indication of loss, this comparison is only good when the samples were processed together.

A final measure of loss is obtained by looking at the transmission through a slab waveguide. For this measurement, one half of the waveguide consists of a bombarded, intermixed, region and the other half is masked from the ion bombardment. The slab measurement quantifies the loss in the disordered layer relative to the loss through the multiple quantum well layer that is masked from the ion bombardment. It is difficult to obtain precise quantitative transmission measurements of a slab waveguide. To get around this problem, the relative loss is estimated by looking at the image of the near field pattern on a CCD camera. Neutral density filters are placed in the laser beam until the transmission through the slab that is not ion bombarded is equal to that through the disordered regions with no filters. Since the two regions tested are adjacent to each other, discrepancies in the input coupling are minimized. Although this provides only a rough estimate of the loss, it is more quantitative than the perpendicular incidence measurements. The experimental results for post-bombardment annealing that use these transmission measurement techniques are presented below.

6.3.b Furnace Annealing Experiments

The annealing experiments were carried out on compositionally disordered samples that were prepared as described in Chapter 3. For the low temperature annealing experiments the samples were all intermixed using neon ion bombardment. The ion current density was 10 $\mu A/cm^2$, the target temperature was 700°C, and the bombardment time was 15 minutes. Note that intermixing has been achieved in one-third of this bombardment time, and with ion current densities of one-third of this density. It is possible that damage would be less with these lower doses. Half of the samples were masked from bombardment to provide a control region that is not intermixed. The samples all had ≈750Å of pyrolytic Si_3N_4 to prevent surface degradation. Annealing was performed as follows: 650°C for 30 minutes, 750°C for 20 minutes and 10 minutes, and 800°C for 10 minutes. All of the annealing was performed in an annealing stage that maintained a constant nitrogen atmosphere.

After annealing, the samples were prepared as described in Section {2.3}, and the normal incidence transmission spectrum was obtained. A check of the normal incidence transmission from the masked portion of the material indicated that annealing did not degrade the quantum wells. All the annealing times and temperatures yielded a sharper band edge in the mixed material, and there was no perceptible difference between any of the times an temperatures. As an example, the normal-incidence transmission spectrum from the sample annealed at 650 °C for 30 minutes is compared to the spectrum from the sample before annealing in Figure {6.1}. The band edge is significantly sharper, and the transmission at the longer wavelengths is higher for the annealed material. It is not possible to quantify the improvement however, with the thin samples. For more quantitative results, the slab waveguide measurement is used.

For this measurement, two laser frequencies were used: one at 1.3 μm and one at 0.87 μm. The first sample tested had no post annealing processing. At 1.3 μm the loss through the disordered region is approximately 3 dB/cm more than that through the masked portion. At 0.87 μm however, the loss in the disordered region is 100 dB/cm more than the masked region. With post-bombardment annealing, the transmission at 1.3 μm through the disordered region can not be distinguished from the transmission through the masked portion of the sample. At 0.87 μm, the loss in the disordered region is about 40 dB/cm higher than the nondisordered sample.

6.3.c Nitrogen Bombardment and Rapid Thermal Annealing Experiments

One other possible way to reduce loss is to reduce the ion mass. The lighter mass should result in fewer vacancies per collision, and thus less agglomeration of the vacancies into defects. Experimentation with other ion masses was discussed in Section {4.1}. The lightest ion tested that causes mixing is nitrogen. On these nitrogen bombarded samples, rapid thermal annealing was also investigated to see the effect on residual damage.

Rapid thermal annealing has certain advantages over furnace annealing for certain applications. Rapid thermal annealing uses banks of halogen lamps to rapidly heat the sample up to 950 °C for well controlled short time periods such as 10-30 seconds. The cooling period shorter than conventional annealing furnaces because the rapid thermal annealing system uses high pressure water cooling. Rapid thermal annealing is typically

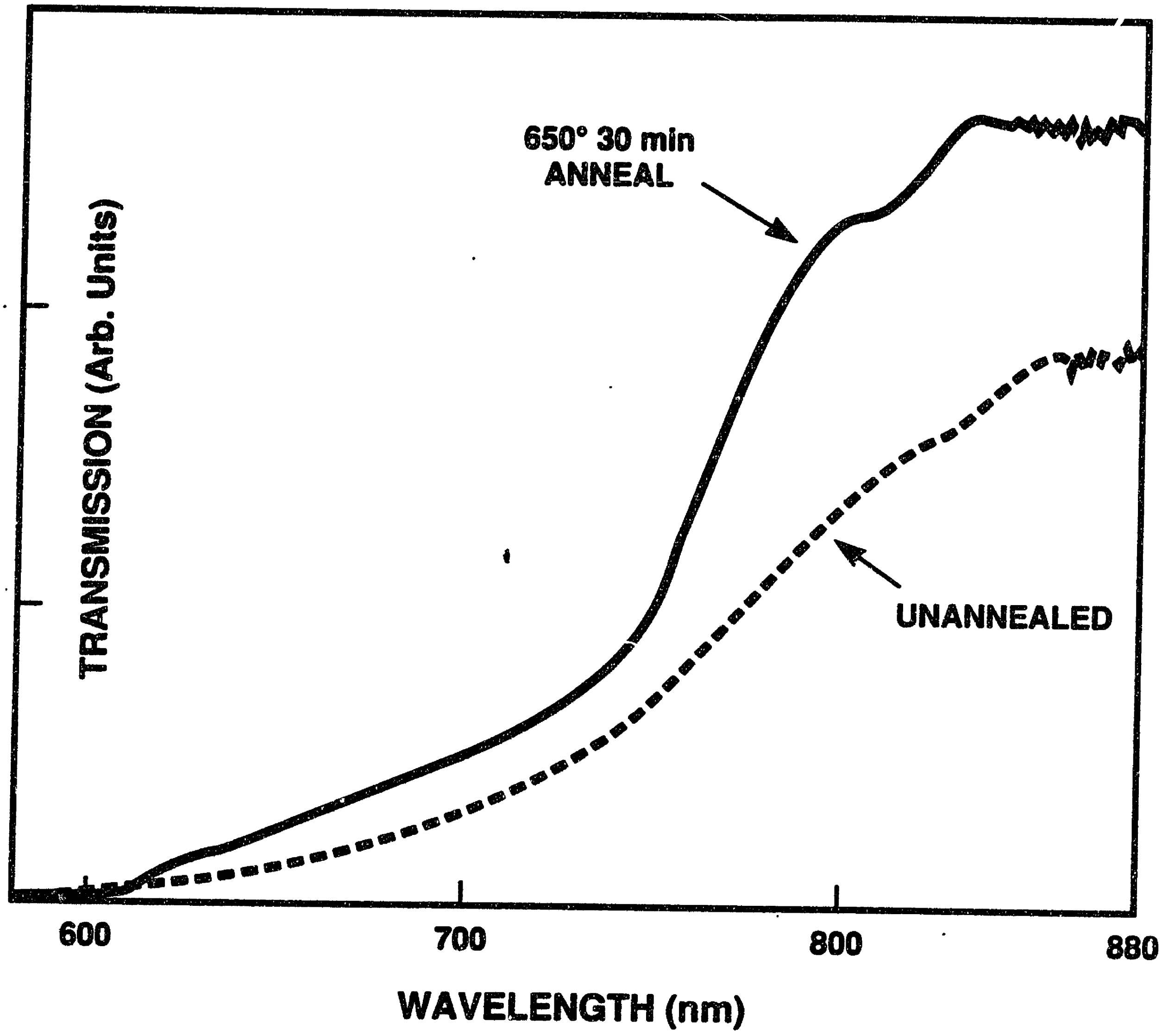

Figure 6.1. Normal-incidence transmission from bombarded, intermixed, region of an ETBD sample. Solid line -- region of sample that underwent post-ETBD annealing at 650°C for 30 min. Dashed line -- region of sample with no post-ETBD annealing.

used for activation of implanted dopants or alloying elements such as Au-Ge. The primary advantage of rapid thermal annealing is that the short periods of time do not allow elements, i.e. dopants, to diffuse away from their initial distribution in the sample. This is clearly advantageous in device fabrication.

For these experiments the ion bombardment was performed with 380 keV N^+ at an ion current density of 10 $\mu A/cm^2$ at 700°C for 15 minutes. Half of each sample was masked from the bombardment with a piece of graphite. The samples had 750Å of pyrolytic Si_3N_4 as an encapsulant. Some samples were subject to rapid thermal annealing at 950 °C for 30 seconds. The annealing is performed in a nitrogen atmosphere.

A transmission spectrum from two ion bombarded, intermixed regions is shown in Figure {6.2}. One sample was subjected to post-process rapid thermal annealing, and the other was not. What is evident from these spectra is that the material quality of the nitrogen bombarded samples is high, and in fact Fabry-Perot resonances can be seen at shorter wavelengths than in spectra from neon bombarded samples. Also apparent for the data is that the rapid thermal annealing process did not produce significant improvement in the integrity of the band edge. Normal-incidence transmission from the masked portion of the sample with and without rapid thermal annealing is shown in Figure {6.3}. The rapid thermal annealing has shifted and broadened the first excitonic peak in the transmission spectrum. This occurs because the quantum wells have been partially intermixed by the rapid thermal annealing process. As the Al from the AlGaAs quantum well barrier migrates into the GaAs well region, the band edge shifts to a higher energy. As the sharpness of the quantum well and barrier is degraded nonuniformly through the layer, the spectra will broaden. The shift and the broadening are not as significant as that which occurs during the long 10 hr furnace annealing that was described in Chapter 2, however.

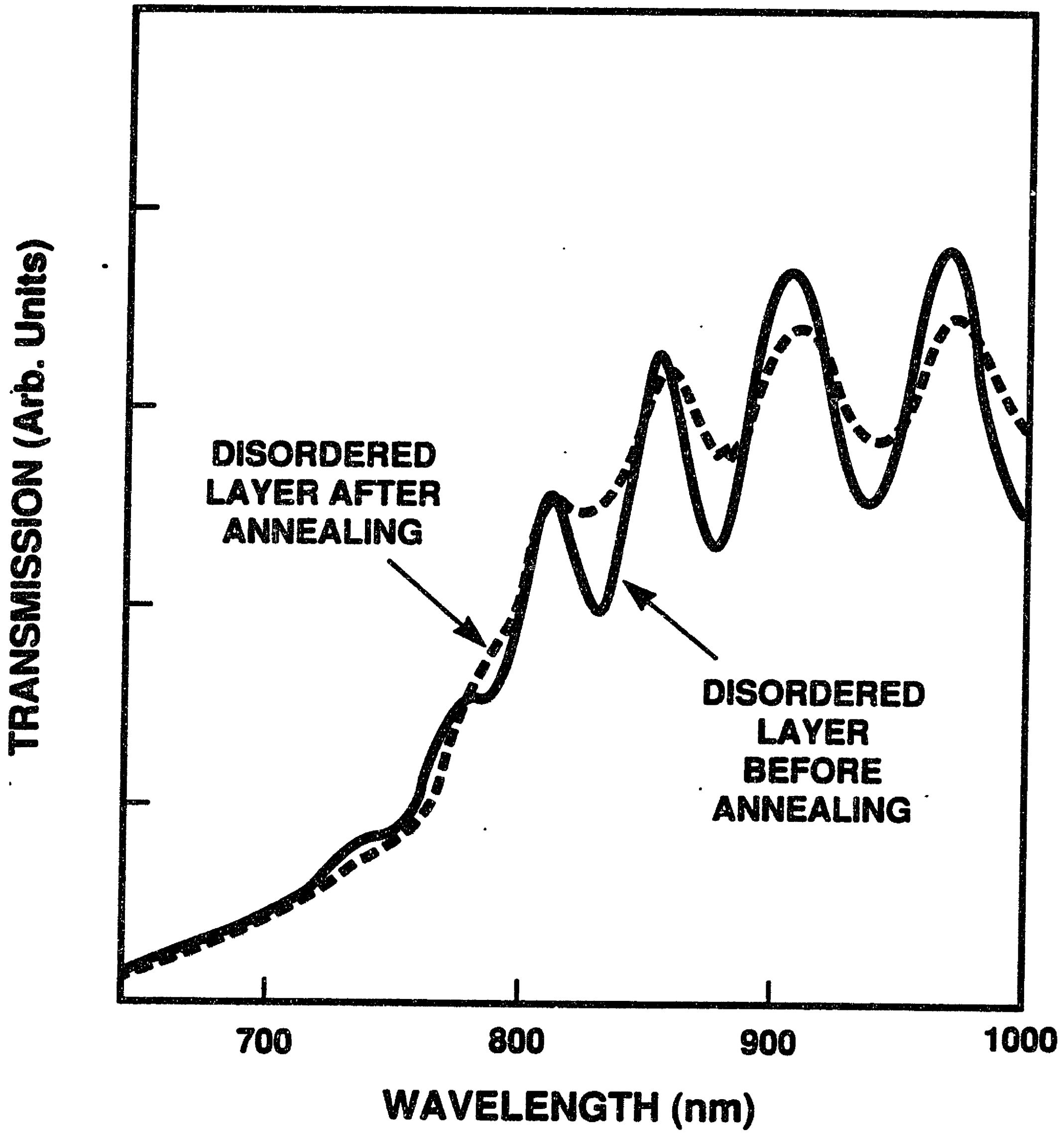

Figure 6.2. Normal-incidence transmission from bombarded, intermixed, region of an ETBD sample. Dashed line -- region of sample that underwent post-ETBD annealing at 950°C for 30 s. Solid line -- region of sample with no post-ETBD annealing.

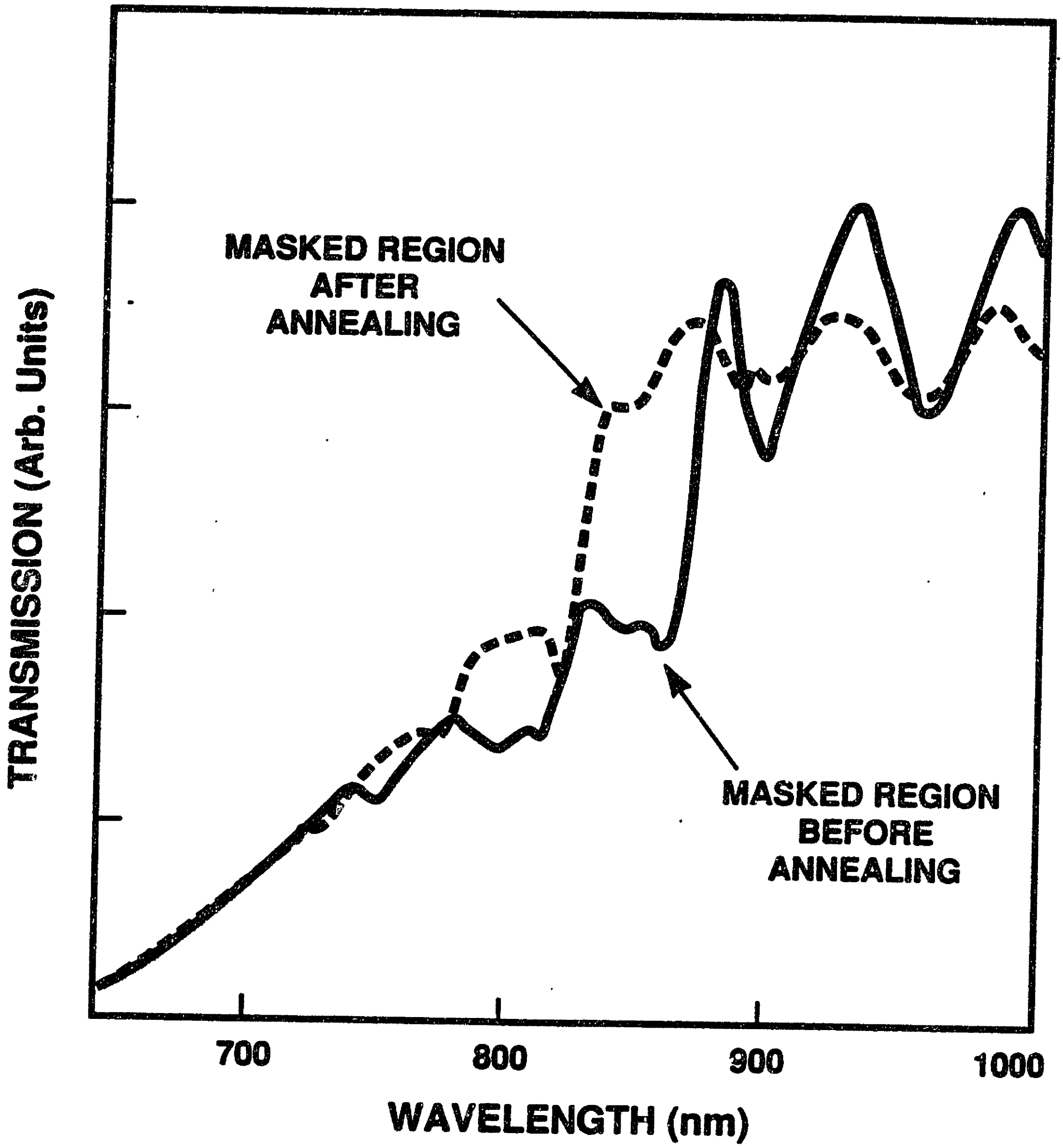

Figure 6.3. Normal incidence transmission from the masked portion of an ETBD sample. Dashed line -- region of sample that underwent post-ETBD annealing at 950°C for 30 s. Solid line -- region of sample with no post-ETBD annealing.

Section 6.4 Conclusions

Several conclusions can be drawn from the work presented in this chapter. The intermixed material after ion bombardment has residual damage that severely reduces the transmission at wavelengths near the band edge. The transmission is not as bad at longer wavelengths such as 1.3 µm. Annealing will improve the transmission, however, annealing at temperatures over about 900°C may cause intermixing of the multiple quantum wells. Lower temperature annealing processes do not have this effect, and possibly rapid thermal annealing times shorter than 30 s would reduce the partial mixing. The amount of intermixing will also likely be dependent on the encapsulant. To avoid the problem however, lower temperatures and times should be used.

The lighter nitrogen ion apparently leaves less residual damage than neon. Post process annealing did not cause significant changes in the spectrum of the N^+ bombarded samples. However, slab waveguides near resonance do show there is loss in the disordered regions compared to the quantum wells. Although the slab waveguide tests indicate higher loss in the intermixed regions than in the quantum wells near resonance, the intermixed regions have less loss than the quantum wells on resonance as a result of the shifted band edge. Though this is not an issue for the intentions of this thesis where near resonance operation is important, it is very significant for the application to integrated waveguide modulators for lasers where resonant operation is used. This work indicates the importance of post-bombardment annealing to improve material quality. It also shows the potential for improvement in material quality by reducing ion mass. It is also possible that better material quality will result from lower ion doses.

Chapter 7
ETBD WAVEGUIDES

Section 7.1 Introduction

Integrated optical device fabrication requires control of the refractive index and absorption laterally across a wafer. Particularly for wavelengths near the band edge, the absorption edge and refractive index of the multiple quantum well is different from that of the intermixed alloy. The selectivity of the intermixing process allows fabrication of waveguides for both active and passive devices (Laidig et al., Holonyak et al., Julien et al.). Elevated temperature bombardment disordering may potentially be used to fabricate buried structures, and the absorption changes afforded by the mixing process are useful for integrated lasers and waveguide modulators. Thus, the motivation for developing ETBD waveguide fabrication techniques is strong. In this chapter the characteristics of passive optical waveguides in AlGaAs/GaAs multiple quantum well material fabricated by ETBD are described. The results indicate that ETBD provides an alternative to current waveguide fabrication techniques. While more improvement in the material quality of the disordered layer is needed before the waveguide loss approaches that of high quality ridge waveguides, the quality of these guides is as good or better than waveguides fabricated by the other intermixing techniques (Werner et al.).

The chapter is organized as follows. After some background on disorder-defined waveguides, the details of the ETBD fabrication process are given. Theoretical calculations of the waveguide loss and optical mode structure are presented. These are compared with experimentally determined loss and far fields of several disordered waveguides. The comparison allows interpretation of the strengths and weaknesses of the ETBD technique, and also gives information on the refractive index difference between the disordered material and the multiple quantum well material.

Section 7.2 Background

The lateral patterning of refractive index due to intermixing is achieved by changing the material composition. In the $Al_xGa_{1-x}As$ material system, the energy band gap increases with increasing aluminum mole fraction, x. Along with the increase in the band edge energy, through Kramers-Kronig relations, increasing x causes a decrease in the refractive index below the band edge. For the multiple quantum well system, the absorption spectrum near the band edge has well resolved exciton peaks at two-dimensional density of states energy levels. The band edge of the multiple quantum well is primarily determined by the width of the quantum well, and to a lesser extent by the amount of aluminum in the barrier, although this does depend specifically on the geometry and composition. In contrast, the alloy material has a smooth band edge characteristic of the three-dimensional system. The alloy layer that results from the compositional intermixing has a band edge that is strongly influenced by the aluminum content in the barrier because of the compositional averaging. Therefore, with the intermixing process, a wide variety of refractive index and absorption profiles may be achieved.

Ridge structures, metal and dielectric strip-loading, strain, and impurities can all be used to form waveguides. Ridge waveguides use the semiconductor-air surface as one boundary for transverse waveguiding. This leads to an asymmetric mode pattern which may be unsuitable for some applications. Also, the scattering losses from the ridge can be significant and are highly dependent on processing procedures as well as surface contaminants such as dust or moisture. Strip-loaded waveguides, which rely on the deposition of a metal or dielectric on top of an epitaxially grown material to achieve waveguiding, suffer less from the scattering losses, because it is usually the cladding layer which has the etched, exposed surface. However, again the mode patterns are asymmetric, and often the strips have significant material loss. Buried structures are free from surface problems. To achieve buried structures, dopants are used to decrease the index of refraction via the incorporation of free-carriers. Dopants may be either diffused into the materials at high temperature or ion implanted.

Compositional disordering is another method by which buried waveguides may be achieved. Several of the impurity-based disordering methods have been used in waveguide fabrication (Julien et al.). The drawback of these techniques is that the free carriers cause loss due to free-carrier absorption at long wavelengths, and impurity-band-tail absorption at shorter wavelengths close to the band edge. The impurity-free dielectric encapsulation method described in Chapter 2 has been utilized to fabricate waveguides for diode lasers (Holonyak et al.). However, as indicated in Chapter 2, the encapsulation method is difficult to use because of poor mask edge integrity. Elevated temperature bombardment disordering would allow impurity-free waveguide fabrication with an excellent patterning capability.

With these benefits in mind, the fabrication of optical waveguides using ETBD was undertaken. Because the energy of the implanter available for this work limited the projected range of the neon and nitrogen ions used for the process to 0.5 μm, buried structures could not be attempted. However, the results presented here demonstrate the feasibility of ETBD fabricated waveguides.

Section 7.3 Waveguide Fabrication

For waveguide fabrication, compositional disordering is used to create regions of low index of refraction around regions of higher index of refraction. For the waveguides reported here, the multiple quantum well region forms the high refractive index waveguide core, and the intermixed alloy forms the lower index lateral waveguide cladding. A schematic of the waveguide is shown in Figure {7.1}.

The samples for the waveguides were grown by OMVPE. The layers were grown on undoped semi-insulating GaAs substrates tilted 2° off the (100) towards the (110). The lower cladding of the waveguide layer structure consists of a 3-μm-thick $Al_{0.5}Ga_{0.5}As$

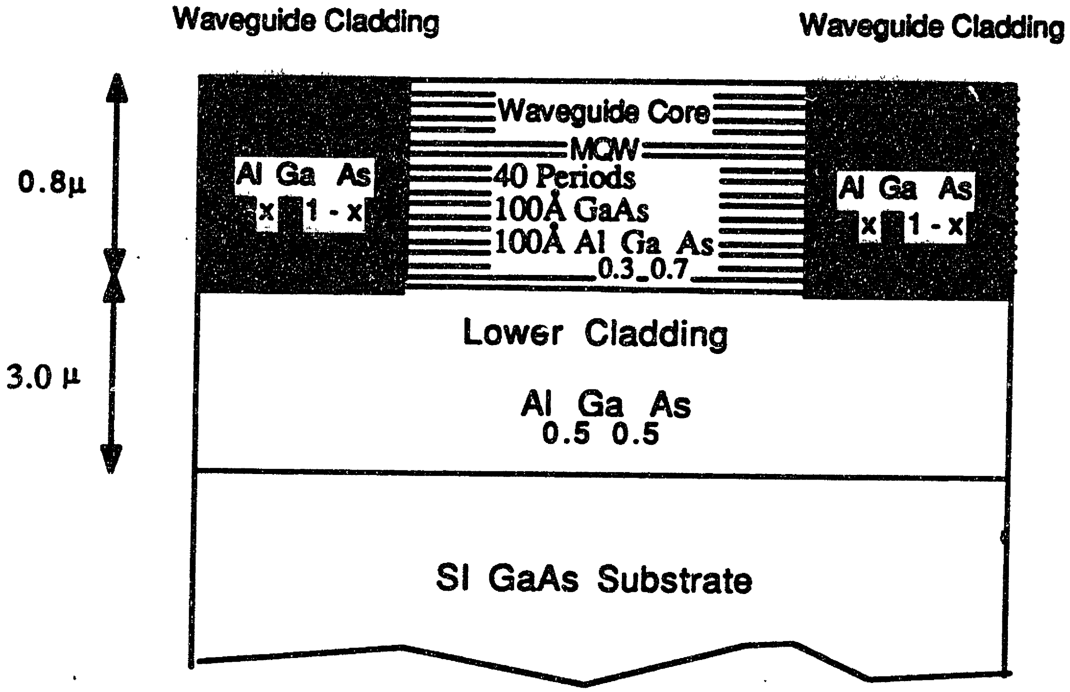

Figure 7.1. Schematic diagram of an ETBD fabricated waveguide.

layer. This is followed by 40 alternating 100-Å-thick GaAs and 100-Å-thick $Al_{0.3}Ga_{0.7}As$ layers that form the waveguide core region. A 1.5-μm-thick $Al_{0.5}Ga_{0.5}As$ layer and a 25-Å GaAs cap layer were then grown. All layers were nominally undoped.

The samples were patterned by etching the top 1.5-μm-thick AlGaAs layer to a depth of 1.4 μm in stripes across the wafer leaving 2- to 10-μm-wide stripes of AlGaAs. The masking procedure is discussed in more detail in Section {5.2}. The thick AlGaAs prevents the incident ions form penetrating the multiple quantum well so these regions are not intermixed. These multiple quantum well regions form the waveguide cores. After bombardment, the thick AlGaAs strip is remove using a selective etch. A residual ridge, measured to be 300 Å, remains over the waveguide core region. For this layer structure, a 300-Å ridge acts as a waveguide, and these effects must be considered to properly assess the index guiding due to the intermixing process. In Section {7.6}, preliminary results on waveguides that were fabricated with the SiO_2 masking technique described in Section {5.3} are presented. These guides do not have the small ridge, though they were not as extensively studied as the waveguides reported in this section. All waveguide samples were covered with 1000 Å of silicon nitride deposited in a pyrolytic deposition system to prevent surface degradation.

For ion bombardment, each sample was mounted on a graphite heater strip misoriented to the ion beam 7° to minimize channeling. The samples were heated to 700° C and bombarded with 380 keV Ne^+ ions. The ion current density was 10 $\mu A/cm^2$ and the bombardment time was 15 minutes. A small section of the sample was masked from the incident ions with a piece of graphite. This provides a region of the sample that is not intermixed for comparison. For the two samples bombarded with neon ions, one sample was subject to rapid thermal annealing at 950°C for 30 seconds, and the other sample was tested without annealing. Waveguides 1 mm, 2 mm, and 3 mm in length were cleaved from the two samples. The waveguides were tested for loss and far field intensity profiles. The results are compared with theoretical calculations of the waveguide characteristics, given below.

Section 7.4 Waveguide Loss

7.4.a Calculation

The waveguide mode structure, and near-field and far-field intensity profiles are estimated theoretically by using the effective index method (Haus, Chapter 6). This analysis provides a means to calculate the loss expected for the waveguides, and allows the refractive index difference between the waveguide core and the cladding regions to be estimated. It is important to point out the validity of the effective index approximation for this application. The effective index method is a way to approximate the lateral mode profile of a two-dimensional waveguide. The transverse modes for the region that forms the lateral waveguide core and the region that forms the lateral waveguide cladding are calculated using the exact solutions to the paraxial wave equation for a slab waveguide. Then an effective index in each region is calculated from the propagation constants in each region. The lateral dimension is calculated using the two effective indexes and the width of the core. This calculation for the lateral direction also assumes an infinite slab. The effective index calculation results in two propagation constants, one for each direction. The exact solution has only one propagation constant that results from accounting for the boundary conditions at all four sides of the guide simultaneously. However, the calculated propagation constants for each dimension differ by less than 0.007%, in the calculations here, so the difference is small. Error is also present in the mode pattern, particularly at the corners of the waveguide. The approximation is not as bad in the center regions of the waveguide. As a result, all far field measurements are made at the peak of the intensity profile for the perpendicularly directed mode.

In this calculation, the transverse mode profiles in the waveguide core region, and in the region adjacent to the core are calculated to obtain the z-directed propagation constants, β_1 for the core and β_2 for the adjacent region. Figure {7.2} indicates the geometry. The calculation is performed using an iterative technique to solve the determinantal equation that determines the β_i, i=1,2, from the known refractive indexes and layer thicknesses. This expression is obtained by solving the paraxial wave equation. The solution is obtained for the lowest order TE mode, because that is the polarization used in the experiment. First, solutions for the mode profile in the waveguide core, region I, are assumed to be given by:

$$\begin{aligned} E_y &= A \cos (k_{x1} x - \phi) \exp(-j\beta_1 z), & |x| < \frac{h}{2} \\ E_y &= B_1 \exp(-j\beta_1 z) \exp(-\alpha_{11} x), & x > \frac{h}{2} \\ &= B_2 \exp(-j\beta_1 z) \exp(\alpha_{12} x), & x < -\frac{h}{2} \end{aligned} \tag{7.1}$$

where α_{11} is the decay into the air α_{12} is the decay into the lower cladding. A, B_1 and B_2 and ϕ are constants. The boundary conditions provide a determinantal expression for the decay constants, and k_{x1}:

$$\tan (k_{x1} h/2) = \frac{(\alpha_{12}/k_{x1}) + (\alpha_{11}/k_{x1})}{1 - (\alpha_{11}\alpha_{12}/k_{x1}^2)} \quad . \tag{7.2}$$

The expression for ϕ is:

$$\tan (2\phi) = \frac{(\alpha_{12} - \alpha_{11})\, k_{x1}}{\alpha_{11}\alpha_{12} + k_{x1}^2} \quad . \tag{7.3}$$

Also from the wave equation:

$$\beta_1^2 + k_{x1}^2 = k^2 n^2 \tag{7.4}$$

$$\beta_1^2 - \alpha_{11}^2 = k^2 n_1^2 \tag{7.5}$$

$$\beta_1^2 - \alpha_{12}^2 = k^2 n_2^2 \tag{7.6}$$

where n, n_1, and n_2 are the refractive index of the waveguide core, air, and lower cladding respectively, k is the wave vector of the field. The boundary conditions also impose the condition that:

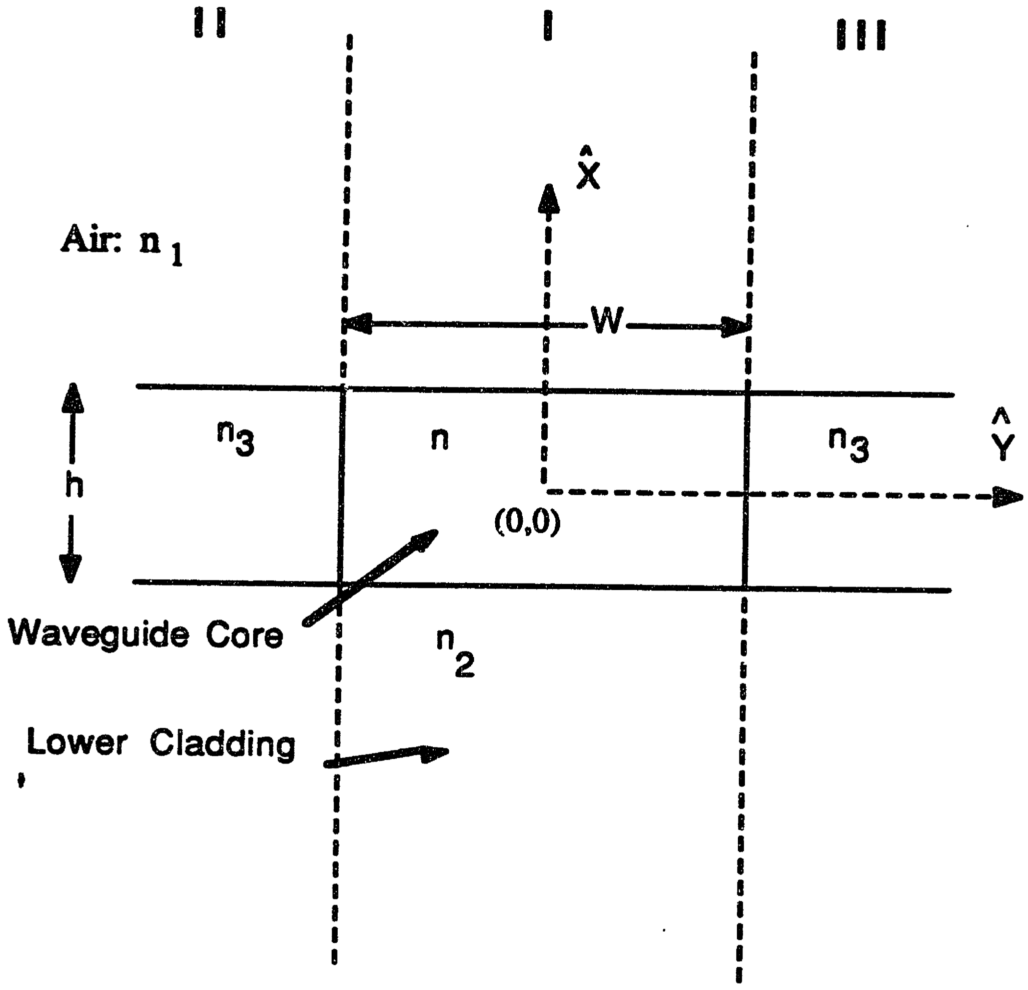

Figure 7.2. Waveguide geometry used in the calculation of the waveguide optical mode profiles.

$$B_1 = A\frac{\cos\left(\frac{k_x h}{2} - \phi\right)}{\exp\left(-\frac{\alpha_{11} h}{2}\right)}; \tag{7.7}$$

$$B_2 = A\frac{\cos\left(-\frac{k_x h}{2} - \phi\right)}{\exp\left(-\frac{\alpha_{12} h}{2}\right)}. \tag{7.8}$$

An effective index is assigned to this layer, given by the expression:

$$N_{eff1} = \frac{\beta_1}{k}. \tag{7.9}$$

A similar calculation is performed for the regions adjacent to the waveguide core, regions II & III in Figure {7.2}, using the refractive indexes and thicknesses of the layers in that region. Because of symmetry, only one region must be calculated. The calculation yields a value for the effective index in this region:

$$N_{eff2} = \frac{\beta_2}{k}. \tag{7.10}$$

The β_2 is analogous to β_1 in the waveguide core.

The lateral field profile is calculated by a similar procedure using the two effective indexes and the known guide width, W. In the lateral direction, the waveguide is operating approximately in a TM configuration. The tangential H-field is expressed:

$$\begin{aligned} H_x &= A' \cos(k_{y1}\, y) \exp(-j\beta_{eff}\, z), && |y| < \frac{W}{2} \\ H_x &= B' \exp(-j\beta_{eff}\, z) \exp(-\alpha\, y), && y > \frac{W}{2} \\ &= B' \exp(-j\beta_{eff}\, z) \exp(\alpha\, y), && y < -\frac{W}{2} \end{aligned} \tag{7.11}$$

For the lateral waveguide, the field pattern is symmetric. The boundary conditions yield the determinantal equation:

$$\tan\left(k_y \frac{W}{2}\right) = \frac{N_{eff1}^2}{N_{eff2}^2} \frac{\alpha}{k_y} \tag{7.12}$$

also:

$$\beta_{eff}^2 + k_y^2 = k^2 N_{eff1}^2 \tag{7.13}$$

$$\beta_{eff}^2 - \alpha^2 = k^2 N_{eff2}^2 \tag{7.14}$$

The field patterns are calculated for a wavelength of 0.87μm. As is discussed in the next section, the index of refraction of the multiple quantum well core region is taken to be ≈3.53 , the disordered region, ≈3.49, and the lower cladding, ≈3.291 at a wavelength of 0.87μm. The measured thickness of the quantum well layer is 0.83 μm. The small residual ridge over the multiple quantum well region is 300Å thick,which was included in the calculation by using the disordered region thickness of 0.8 μm.

The calculation indicates the waveguides should be double mode in the transverse direction, and also multimode in the lateral direction, with the number of modes dependent on the width. Experimentally these higher order modes are not visible at the output. This may be partly due to the fact that the effective index method overestimates the value of the index in the core. It is also an indication that higher loss due to intermixing discriminates against the higher order modes. In the transverse direction, discrimination also seems to occur. This loss is possibly due to surface and interface scattering.

The near field intensity pattern in both the transverse and the lateral directions are calculated by the relation:

$$I \propto |E \times H^*| \tag{7.15}$$

The normalized results are plotted in Figure {7.3}.

The above information may be used to calculate the excess loss in the waveguides due to disordering. This loss is dependent on the amount of the field that penetrates into the disordered material, so only the lateral direction at x=0 is considered. Using the near field pattern calculated above, the relative amount of light in the cladding region is found. Only the y > 0 region is considered by symmetry. The ratio of the integrated intensity in

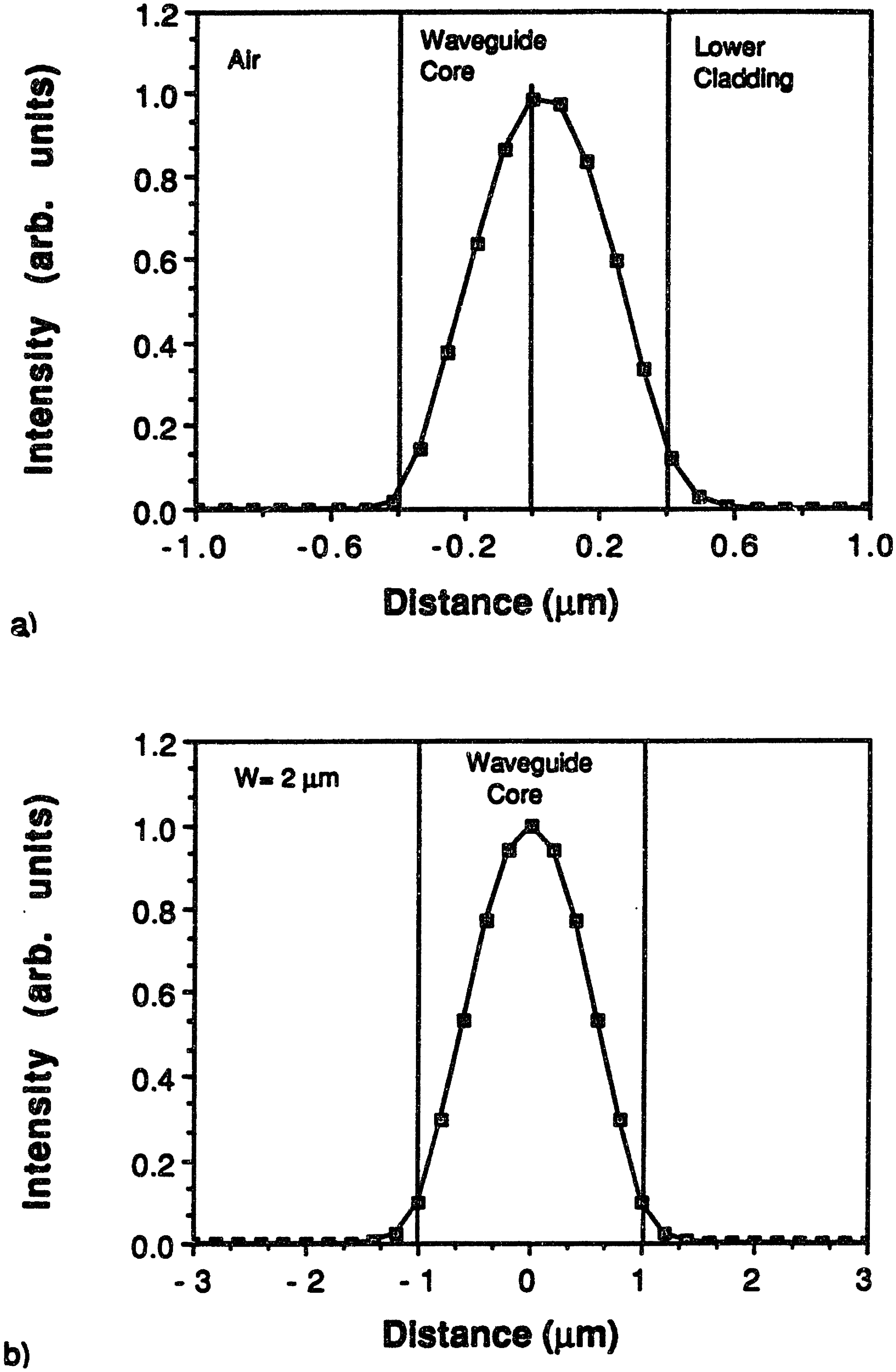

Figure 7.3. Near-field optical intensity mode profiles for a) the transverse, and b) the lateral direction.

the cladding P_{cl}, to the total integrated intensity, P_t is $\Gamma_{cl} = \frac{P_{cl}}{P_t}$. In the core: $\Gamma_{co} = \frac{P_{co}}{P_t}$. Expressions for P_t, P_{co}, and P_{cl} are:

$$P_t \propto A'^2 \int_0^{\frac{h}{2}} \cos^2 (k_y\, y)\, dy + (B' \frac{N_{eff2}}{N_{eff1}})^2 \int_{\frac{h}{2}}^{\infty} \exp(-2\alpha\, y)\, dy, \tag{7.16}$$

$$P_{cl} \propto (B' \frac{N_{eff2}}{N_{eff1}})^2 \int_{\frac{h}{2}}^{\infty} \exp(-2\alpha\, y)\, dy, \tag{7.17}$$

$$P_{co} \propto A'^2 \int_0^{\frac{h}{2}} \cos^2 (k_y\, y)\, dy. \tag{7.18}$$

The small factor $\frac{N_{eff2}}{N_{eff1}}$ is due to the discontinuity in the normal E-field across the boundary. Performing the integration with the calculated values of k_y and α results in, $\Gamma_{cl} = 0.012$, and $\Gamma_{co} = 0.988$. Thus even if the light in the cladding is completely absorbed, the loss coefficient only increases by 0.1 cm^{-1}.

7.4.b. Loss Measurements

Waveguide loss is measured by looking at the power transmitted through the waveguide for several waveguide lengths. Multiple lengths eliminates the need to know the input coupling, although differences in coupling for the two measurements limits the accuracy of the technique to approximately 1 cm^{-1}, as determined by the measurements. Loss measurements were performed on two different sets of guides. The first were waveguides fabricated with neon ion bombardment, and utilized no post process annealing. The waveguide loss at a wavelength of 0.87 μm was 13 cm^{-1}, or 56 dB/cm. The second waveguide sample was annealed by rapid thermal annealing for 30 seconds at 950°C. These waveguides exhibited 3.5 cm^{-1} of loss, or 15 dB/cm. However, the partial disordering of the multiple quantum well material means the measurement wavelength is further from the band edge than in the previous waveguides, which accounts for some loss reduction. This encouraging low loss measurement led to further study of the waveguides and the ion bombardment procedure as detailed in Section {7.6}. Loss measurements are discussed further in that section. In addition to loss, the waveguide calculation provides information on the far field pattern of the waveguides. Far fields are calculated and compared to theory in the next section.

Section 7.5 Waveguide Far Field Patterns

7.5.a Calculation

In this study of waveguide far field patterns, the field is measured in the Fraunhofer diffraction limit (Haus, Chapter 4). In this limit, the far field amplitude distribution of the electromagnetic field pattern is given by the Fourier transform of the near field. The Fraunhofer limit occurs when the distance from the output end face of the waveguide to the measuring detector, z, is related to the waveguide size, d, and the wavelength of radiation, λ, as follows:

$$z \gg \frac{2\pi d^2}{\lambda}. \qquad (7.19)$$

For the waveguide geometry and wavelength we require $z \gg 0.1$ mm. Far fields are measured by scanning a detector in a plane at a set distance from the guide. Any practical scan position, z, that can be achieved is well within the Fraunhofer condition. Under these conditions, the field measured at the detector, $u_d(x,y,z{=}D)$, is expressed in terms of the field at the output face of the waveguide, $u_{wg}(x',y',z{=}0)$, as:

$$u_d = \frac{j}{\lambda z} e^{-j[k(x^2 + y^2)/2z]} \int_{-\infty}^{\infty} dx' \int_{-\infty}^{\infty} u_{wg}(x',y') \exp\left[\frac{jk}{z}(xx' + yy')\right] dy' \qquad (7.20)$$

where $k = 2\pi/\lambda$. This expression is used to calculate the far field at a position $z=D$, for the amplitude distribution at the waveguide output facet that was derived in Equation {7.11}. The lateral field at $x=0$ is calculated. A variable $K = \frac{k}{z} y$, the conjugate variable to y' in a Fourier transform relation, is used. The expression which results in the lateral direction is:

$$u_d = \underline{A} \left\{ \frac{2 c_1 e^{-(\alpha W/2)}}{\alpha^2 + K^2} \left(\alpha \cos (KW/2) - K \sin(Kh/2) \right) \right. \\ \left. + \frac{1}{k_y{}^2 - K^2} \left[(k_y - K) \sin(K + k_y) + (k_y + K) \sin (k_y - K) \right] \right\}. \qquad (7.21)$$

In this expression, the complex constant $\underline{A}$ is given by:

$$\underline{A} = C \frac{j}{\lambda z} e^{-j[ky^2/2z]} \qquad (7.22)$$

where C is the arbitrary amplitude of the electric field.

A Fortran computer code is used to calculate the theoretical pattern. The detector measures intensity, so the magnitude-squared of u_d is calculated. The program is sufficiently general that it can calculate the far field of any waveguide where the refractive index profile and two-dimensional geometry is given. The far field can be calculated at any distance. Comparing the full width at half maximum of the far fields calculated with the program to the divergence expected from diffraction by a slit of similar dimension to the waveguide provides evidence that the program is operating correctly.

7.5.b Measurement

Far field patterns are obtained by scanning a detector with a small aperture across a plane at a fixed distance from the waveguide. Care is taken to assure that the plane is perpendicular to the line between the waveguide and the detector at $x' = y' = 0$. In this case, the calculated far fields should correctly describe the intensity pattern that is measured. Light from a $\lambda = 0.86$ μm diode laser is coupled into the waveguide using a 10X microscope objective. The laser is polarized to excite the TE mode of the transverse guide. Far fields were obtained for the waveguide sample that did not have a post process annealing step. This assured that the waveguide core had good quality multiple quantum wells. Far fields were taken on guides with three different widths: 2 µm, 3 µm, and 4 µm.

The theoretical curves were calculated using values for bulk refractive index and multiple quantum well refractive index from the literature. Although data on the bulk refractive index can be found, the quantum well refractive index is less well tabulated. This is partly due to the fact that the quantum well refractive index is dependent on the exact well thicknesses and compositions used. The multiple quantum well refractive index is guessed at based on the values in the literature (Sonek et al.), and then changed to fit the waveguide far field profiles. The bulk refractive index values are n=3.291 for $Al_{0.5}Ga_{0.5}As$, and n=3.490 for $Al_{0.15}Ga_{0.85}As$ at a wavelength of 0.87 µm (Adachi). The thicknesses were determined by inspecting the samples under an optical microscope and are well known.

The lateral far field patterns are shown in Figures {7.4}, {7.5}, and {7.6} for waveguide widths of 2.0 µm, 3.0 µm, and 4.0 µm respectively. As the waveguide size is increased the full width at half maximum of the far field pattern decreases as expected. A good fit was obtained for each width when the refractive index difference between the intermixed $Al_{0.15}Ga_{0.85}As$ and the multiple quantum well was Δn=0.04. The sensitivity of the far field to the value of refractive index is demonstrated in Figure {7.7} which shows comparison of theoretical far fields for Δn= 0.015, 0.04, and 0.06. The best fit is obtained with Δn=0.04, and this is also the fit which works best for all three widths. This indicates a refractive index for TE polarization in the multiple quantum well at λ=0.87 µm of n= 3.53. This is consistent with the values obtained by Kahen and Leburton (1986 a). The field in the lateral dimension is sensitive to the refractive index in the multiple quantum well layer only to the second decimal place.

As mentioned earlier, the waveguides that were tested had a small ridge on the surface. To ascertain how much waveguiding occurs due to the ridge alone, a theoretical

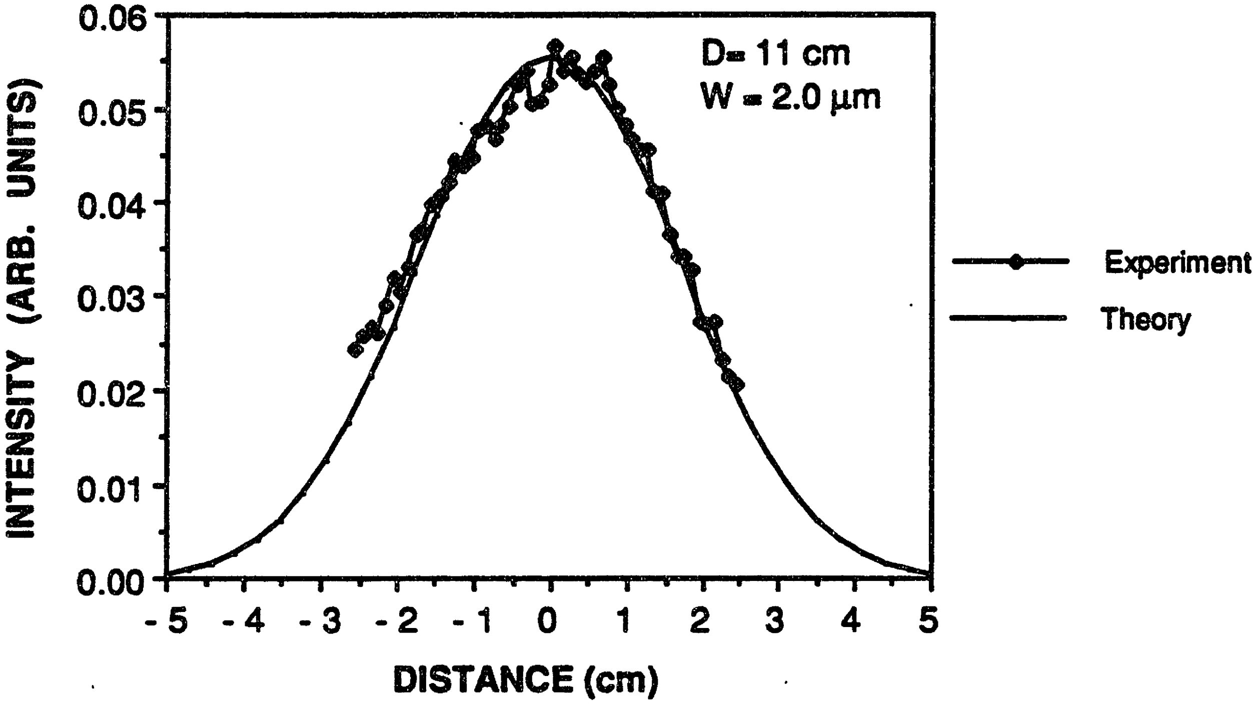

Figure 7.4. Lateral far-field intensity patterns comparing experiment to theory for a 2-μm-wide intermixed waveguide with a 300 Å ridge using Δn=0.04.

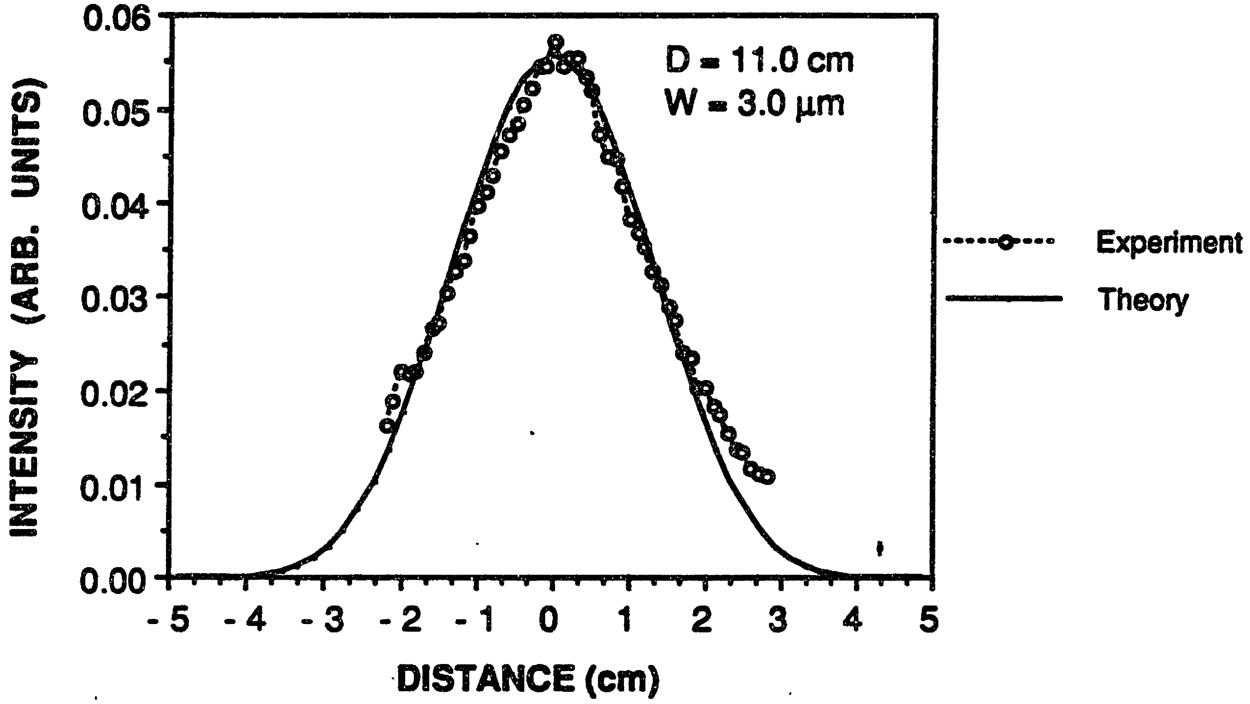

Figure 7.5. Lateral far-field intensity patterns comparing experiment to theory for a 3-μm-wide intermixed waveguide with a 300 Å ridge using Δn=0.04.

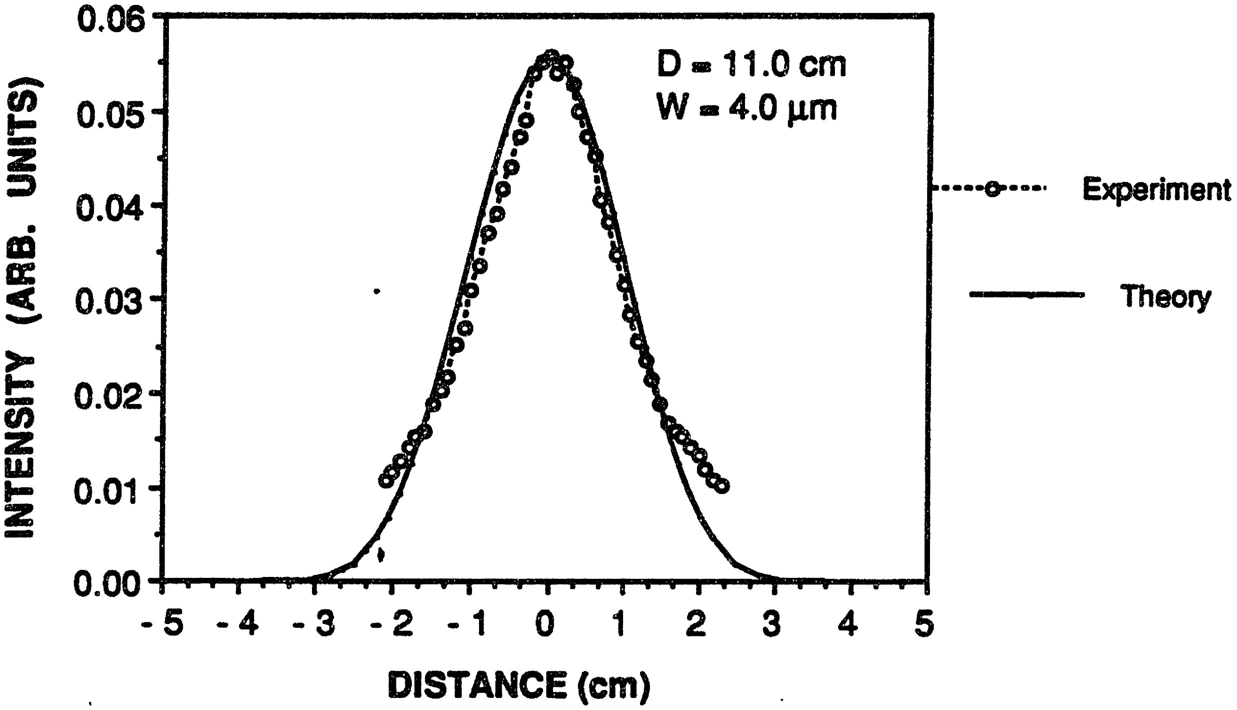

Figure 7.6. Lateral far-field intensity patterns comparing experiment to theory for a 4-μm-wide intermixed waveguide with a 300 Å ridge using Δn=0.04.

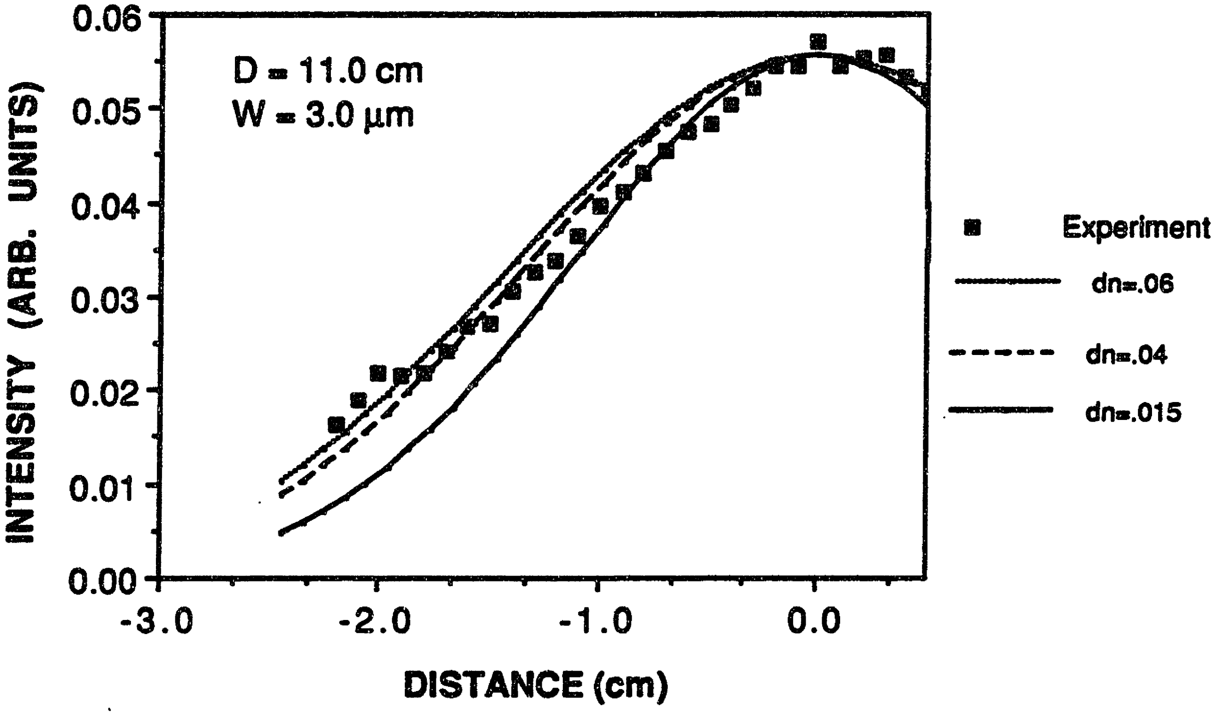

Figure 7.7. Lateral far-field intensity patterns comparing experiment to theory using three different Δn, the refractive index difference between the multiple quantum well and the intermixed alloy, indicated on the figure.

calculation of a waveguide with no layer intermixing, and so no refractive index difference in the lateral direction, was made. The calculated far field for this case is superimposed on the graph of the far field for a ridge of width W=3 μm in Figure {7.8}. The far field is significantly narrower which is a result of the fact that the guided mode is less tightly confined in the absence of the index guiding. This is clear evidence that there is significant index guiding due to the intermixing process. For comparison, far fields were taken from waveguides on the part of the sample that was masked from the ion bombardment, and so had no intermixing and hence no index guiding. The transverse far fields from these waveguides were identical to the transverse far fields from the waveguides that had intermixed claddings. A lateral far field pattern from a 3-μm-wide unmixed waveguide is shown in comparison to theory in Figure {7.9}. The fit is very good. The oscillations in the wings of the far field pattern are due to light that passes through the cladding adjacent to the waveguide. This light is not apparent in the intermixed waveguides because the cladding has higher loss, and light does not propagate through it.

Section 7.6 Waveguides Patterned with SiO_2

7.6.a Introduction

In addition to the waveguides discussed in the previous section, a set of waveguides were fabricated using the SiO_2 masking technique (Section {5.3}). Therefore, these waveguides do not have a small ridge on the surface. For these final samples, nitrogen ions were used for the bombardment, because of potentially lower loss (see Section {6.4}). No post bombardment annealing was performed to avoid having the multiple quantum wells intermixed. These waveguides were intended to be used to investigate optical switching properties, and so the integrity of the quantum wells was important. The fabrication, and characterization of these waveguides is described below.

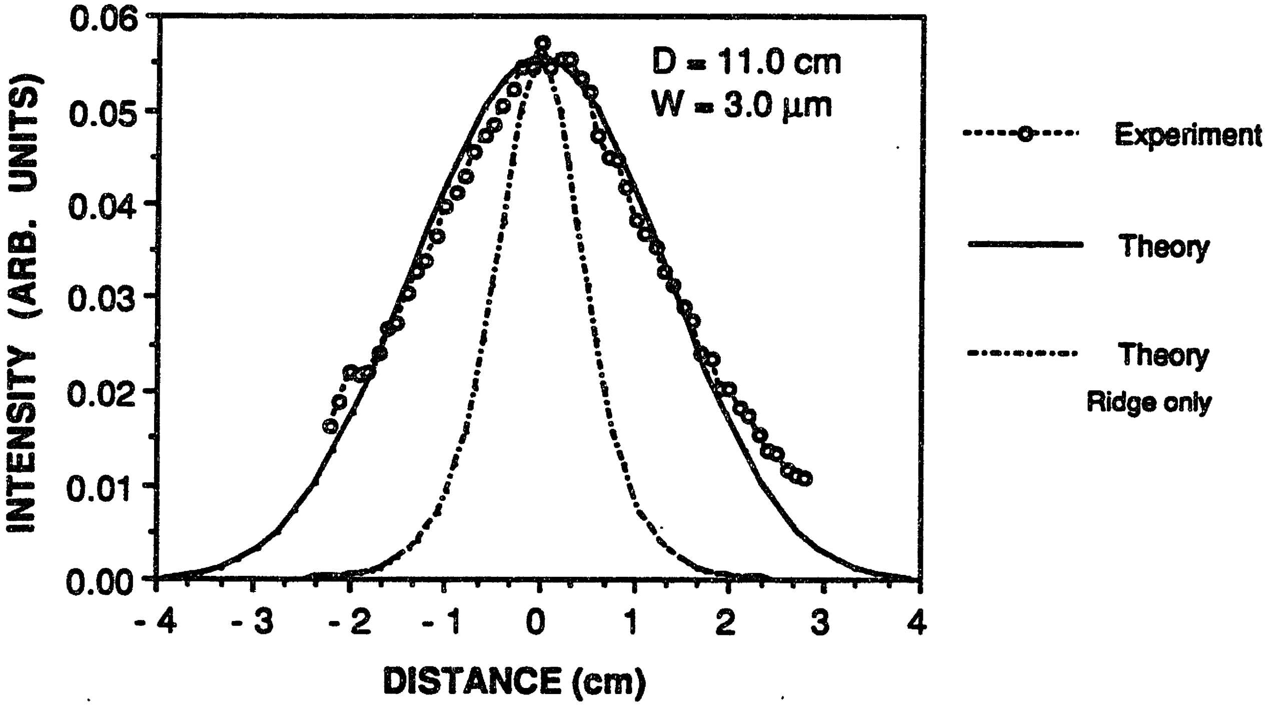

Figure 7.8. Lateral far-field intensity patterns comparing experiment and theory for a 3-μm-wide intermixed waveguide with a 300 Å ridge to a 3-μm-wide, 300 Å ridge waveguide.

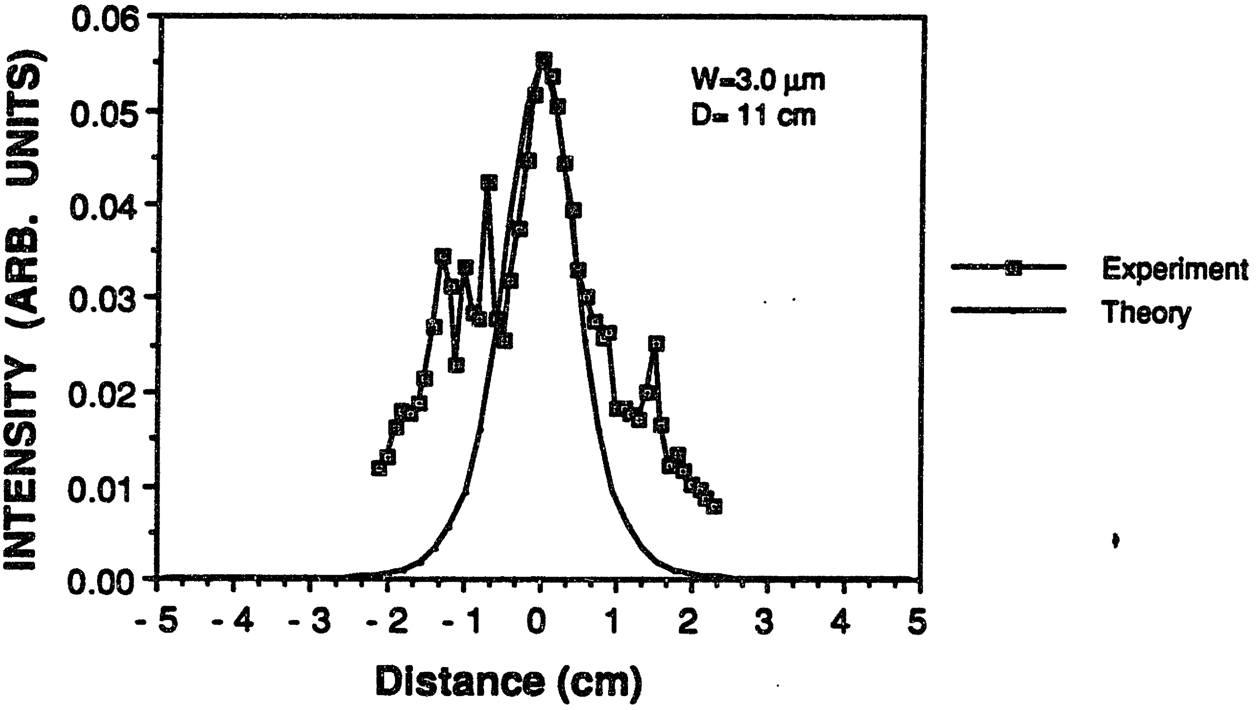

Figure 7.9. Lateral far-field intensity patterns comparing experiment to theory for a 3-μm-wide, 300 Å ridge waveguide.

7.6.b Fabrication

The samples for these waveguides were grown by OMVPE. The layers were grown on undoped semi-insulating GaAs substrates. The lower cladding of the waveguide layer structure is a 3-μm-thick $Al_{0.5}Ga_{0.5}As$ layer. Forty alternating 120-Å-thick GaAs and $Al_{0.3}Ga_{0.7}As$ layers and a 25-Å GaAs cap layer form the waveguide core region. All layers were nominally undoped. 1.3 μm of SiO_2 was deposited in a pyrolytic deposition system to provide a mask for the ion bombardment. Using standard photolithographic processing techniques, stripes of silicon oxide ranging from 2 μm to 8 μm wide were patterned on the sample. A thin layer (<1000 Å) of SiO_2 was left covering the area between the stripes to minimize surface degradation of the GaAs cap layer.

The sample was heated to 700° C and bombarded with 380 keV N^+ ions. The ion current density was 10 $\mu A/cm^2$ and the bombardment time was 15 minutes. The SiO_2 was removed from the sample using reactive ion etching. Waveguides 1 mm, 2 mm and 3 mm in length were cleaved from the sample.

7.6.c Characterization

An optical micrograph of a 0.5°-angle-lapped sample is shown in Figure {7.10}. The SiO_2 mask provides a well defined intermixed region with no significant lateral diffusion underneath the mask. The multiple quantum well region indicated in the figure forms the waveguide core. The $Al_{0.5}Ga_{0.5}As$ layer forms the lower cladding, and air forms the upper cladding for guiding in the transverse direction, and the two disordered $Al_{0.15}Ga_{0.85}As$ intermixed alloys form the cladding for waveguiding in the lateral direction. There is a small region ≈0.1 μm thick at the bottom of the multiple quantum well layer that does not get completely intermixed in the 15 minute process time. The degree of mixing is influenced by the thickness of the SiO_2 that is left on the regions that are to be disordered. Although measurements of the thickness of the oxide indicate this thickness should be about 1000 Å, it could be somewhat thicker, reducing the penetration depth of

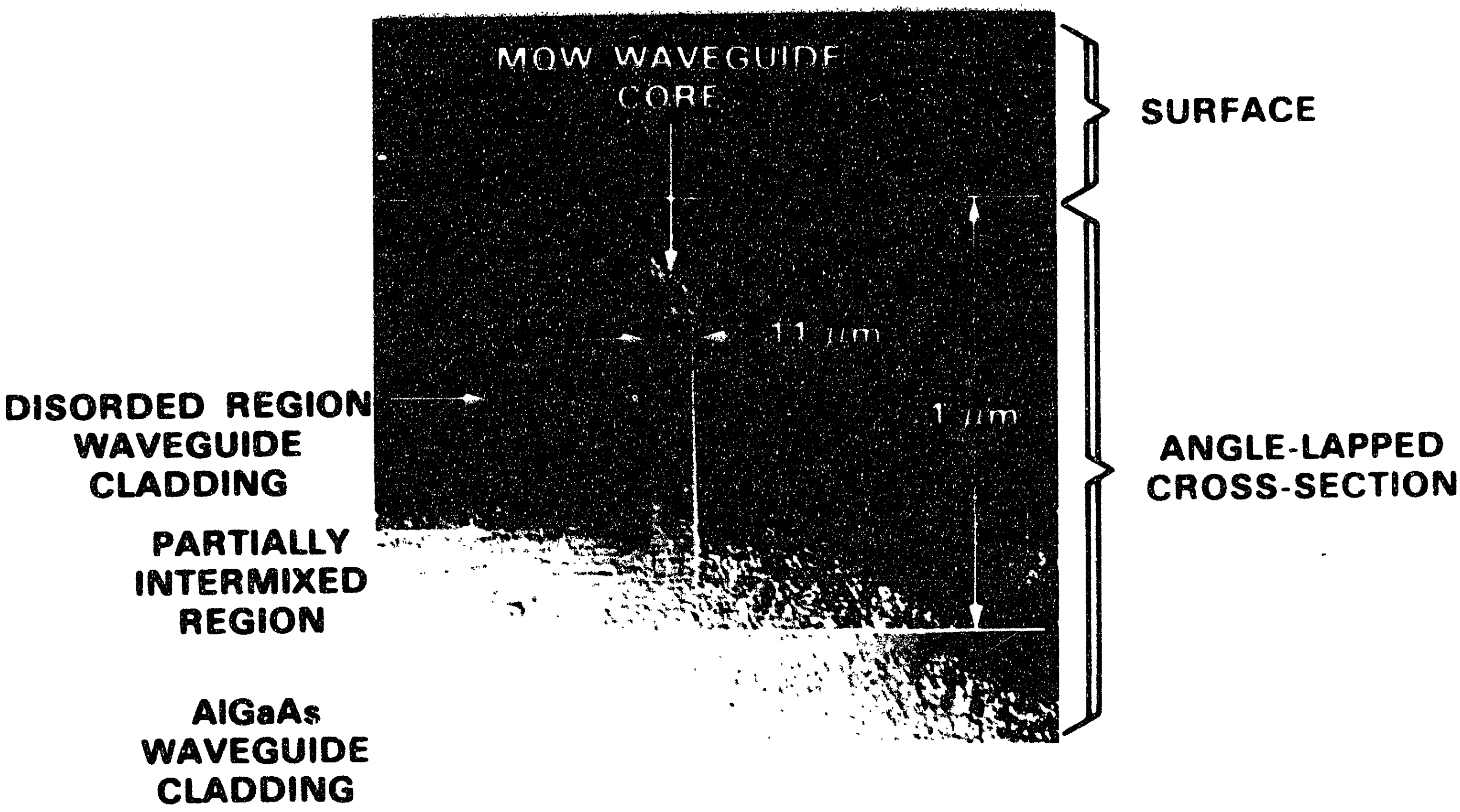

Figure 7.10. Optical micrograph of a 0.5°-angle-lapped end face of an intermixed waveguide sample.

the incident ions. These additional quantum wells do not reduce the effectiveness of the waveguide. However, they would tend to slightly distort the optical mode pattern. The expectation is that the mode would peak slightly more toward the lower cladding in the presence of the quantum wells. If this occurred, it was not dramatic enough to be seen in the near field image of the mode.

Waveguide loss at a wavelength of 0.87 µm, ≈20 nm below the band edge of the multiple quantum well, was determined by measuring the power at the output of the waveguides for three lengths, 1 mm, 2 mm and 3 mm. The loss in the waveguides is 7 cm^{-1} or 30 dB/cm. Although direct comparison is difficult because of the sensitivity of the loss coefficient to wavelength near the band edge, the loss number measured for these ETBD waveguides is lower than the 35 dB/cm and 100 dB/cm soon to be reported by Yang et. al. (to be published) using the ETBD technique on the InGaAs strained layer superlattice materials. Also, the numbers are lower than reports of 9 cm^{-1} near resonance using Si^+ ion implantation and subsequent annealing (Werner).

In addition to loss in the disordered region that forms the waveguide cladding, the measured loss could be caused by surface degradation during the processing. The fact that the surface is causing residual loss is evident by the fact that although the layer should support multiple waveguide modes in the transverse direction, none are apparent in these guides. Further experimentation with different types of masking and processing would likely lead to improvement of the loss. To reduce losses even further, reduction in the bombardment times and flux as well as some post bombardment annealing would be required.

Section 7.7 Conclusions

In conclusion, we have demonstrated fabrication of integrated optical waveguides with ETBD. The waveguides have a linear losses ranging from ≈ 3 cm^{-1} to 7 cm^{-1} at a wavelength 20 nm from the band edge of the multiple quantum well. This is compared to other waveguides fabricated by other disordering techniques that have losses around 9 cm^{-1}. The far field patterns indicate the refractive index difference is $\delta n=0.04$, indicating complete intermixing in the AlGaAs regions that form the waveguide cladding.

One benefit of ETBD for waveguide fabrication is that the higher loss, bombarded region is in the cladding where the tails of the optical mode pattern are. This means that higher order modes, which have more energy in the tails, see higher loss. In this way, the higher order modes are discriminated against compared to the lowest order mode, which means larger waveguide areas can be fabricated, and single mode waveguide outputs would result. This is particularly important for optical signal processing where single mode propagation is needed to avoid interference at the output, but large mode areas provide for better coupling.

The ETBD technique is useful because of the potential for buried waveguide structures without the need to etch and regrow. The results presented here indicate that low loss waveguides may be achievable with this technique, but that further work optimizing some type of post process annealing and further optimization of the ETBD parameters must be done.

Chapter 8
OPTICAL SWITCHING PROPERTIES OF AlGaAs WAVEGUIDES

Section 8.1 Introduction

The intention of the work presented in the next two chapters is to determine the optical switching properties of semiconductor waveguides near the band edge. Waveguides fabricated from bulk AlGaAs materials are examined in detail. Also, preliminary measurements on multiple quantum well waveguides fabricated with the ETBD technique are presented. Recently several workers have investigated nonlinear optical properties in semiconductor optical waveguides, including multiple quantum wells, optical fibers and semiconductor doped glasses (Park et al., Lee et al., Cotter et al., Banyai et al., 1989). The waveguide geometry has the advantage of providing a long length of interaction between a control beam and a signal beam that enables weaker optical nonlinearities to be used for switching. The largest optical nonlinearities measured in semiconductors occur at wavelengths resonant with the absorption peak (Miller et al., 1981, Miller et al., 1982, Chemla and Miller) . However, at these wavelengths, the linear loss, $>1000\ \mathrm{cm}^{-1}$, is prohibitively high, and propagation through a waveguide is not possible. Even off resonance, nonlinearities are enhanced near the band edge, and therefore are accompanied by increased linear loss. The increased linear loss reduces the effective length of interaction between the control beam and the signal beam, and reduces the switching effectiveness. The measurements presented here provide the first quantitative study of the optical nonlinearities and the linear loss as a function of the wavelength detuning from the band edge so that the trade-offs between loss and enhanced nonlinearities may be assessed.

In III-V semiconductor systems, several processes contribute to the optical nonlinearities at optical frequencies near the band edge (Haug and Schmitt-Rink). These processes include bound electron effects, free electron effects, and heating (Gabriel et al.). The various effects operate on different time scales. Bound electron effects occur on very fast time scales. Free electron effects turn off slowly --dominated by either carrier recombination or diffusion. Free carriers are generated through both linear absorption and two-photon nonlinear absorption processes, and the turn-on time of phase changes induced by free carriers is different for the two carrier generation mechanisms. Temperature effects typically occur on microsecond time scales. In the measurements presented here, the use of a femtosecond laser system allows the dynamic response to be measured with a 500 fs time resolution, so the various effects may be separated out.

Measurements of the optical nonlinearities in semiconductors have proven difficult. This is because the magnitude of the nonlinear coefficients are small, and most common interferometer techniques used to measure refractive index nonlinearities are plagued by thermal and acoustic imbalances. Part of what sets the work in this thesis apart from other work is the use of the time-division interferometer measurement technique (LaGasse et al. 1989 b.). The technique is based on a single-arm interferometer, proposed by Shirasaki et. al. (1987) that reduces the thermal and acoustic imbalances

The measurements have produced several important and interesting conclusions. First, measurements of the wavelength dependence of the nonlinear refractive index, n_2, in AlGaAs show a dramatic increase as the absorption edge of the semiconductor is approached. This is accompanied by an increase in linear absorption. Two-photon absorption processes figure significantly in the optical response of the waveguides. The two-photon absorption is found to be constant for the wavelengths investigated here. This information, along with n_2 and the linear loss leads to conclusions as to the wavelength dependence of the optical switching properties. Another aspect of ultra-fast optical switching in semiconductors is the dispersion in the waveguide that leads to pulse broadening that reduces the peak power and limits the distance over which a pulse train of a given repetition rate can travel without pulse overlap. In these measurements the pulses propagate in orthogonal polarizations, so the walk-off due to group velocity mismatch for the two modes is a consideration. The effects of dispersion and group velocity are quantified. These experiments are described in detail below. They were carried out in collaboration with Mike LaGasse.

This chapter is outlined as follows. First the background for the nonlinear processes near the band edge of AlGaAs is presented in Section {8.2}. The details of the experiments are given and the interferometer operation is described in Section {8.3}. Then the preliminary measurements on AlGaAs waveguides are presented. These measurements provided direction for more detailed measurements on another AlGaAs waveguide, better suited for the desired experiments, and these measurements are presented in Section {8.5}. Measurements of linear loss, two-photon absorption, and n_2 are given. The dynamics of the nonlinear absorption and nonlinear index of refraction as a function of wavelength are shown, followed by a detailed analysis of the results in section {8.7} and conclusions.

Section 8.2 Band Edge Nonlinear Processes in AlGaAs

As mentioned in the introduction to this chapter, several optical nonlinear processes in III-V semiconductors contribute to the optical response near the band edge. A schematic of the conduction band and valence band of AlGaAs that illustrates the optical processes that influence these measurements is shown in Figure {8.1}. In these experiments we pump and probe with an optical frequency that is close to the band gap of the AlGaAs, and look for an intensity dependent phase change. This is a $\chi^{(3)}$ process that leads to an intensity dependent index of refraction given by the expression:

$$n = n_0 + n_2 I \qquad (8.1)$$

where n_0 is the linear index, n_2 is the intensity dependent refractive index coefficient, and I is the light intensity. Also, at the intensities necessary for optical switching, two-photon absorption is present. Two-photon absorption leads to an intensity dependent loss expressed as:

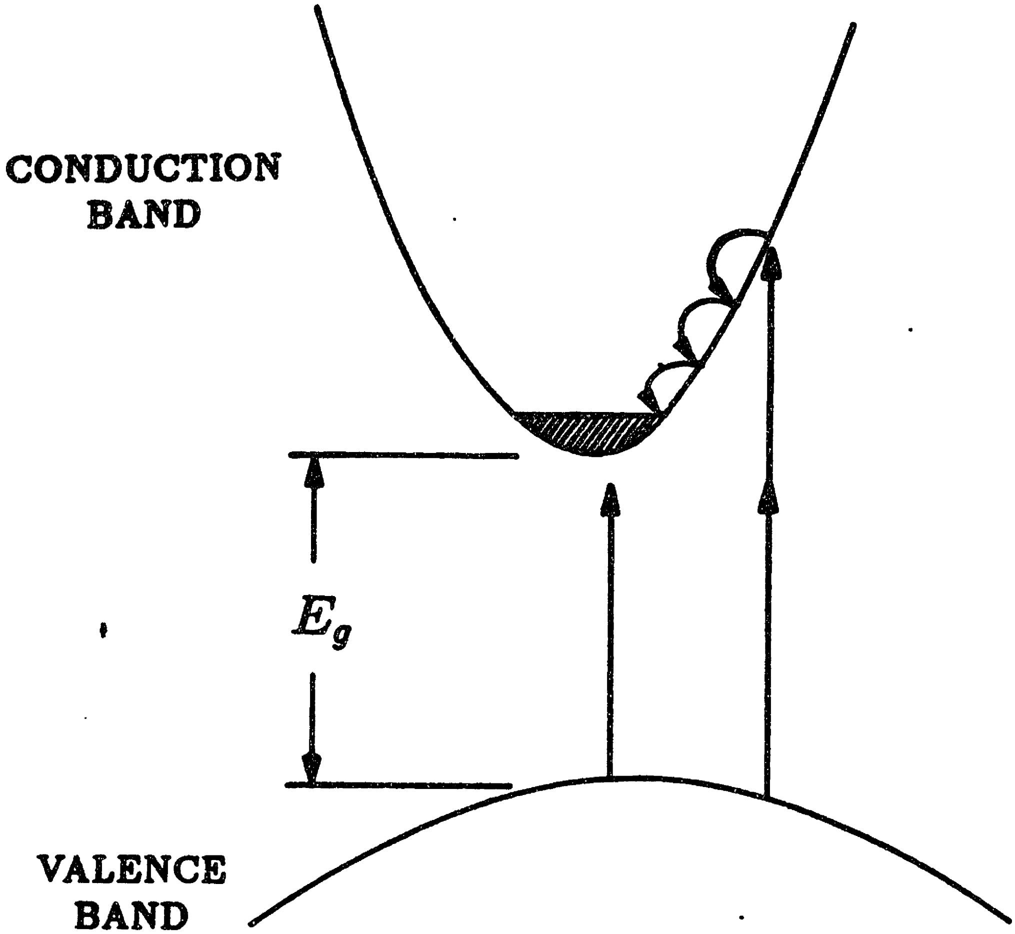

Figure 8.1. Schematic diagram of the AlGaAs conduction band and valence band. The optical excitation is represented by arrows which show one- and two-photon processes.

$$\alpha = \alpha_0 + \beta I \qquad (8.2)$$

where α_0 is the linear absorption coefficient, β is the two-photon absorption coefficient and I is the light intensity. Two-photon absorption causes carriers to be lifted from the valence band into the conduction band with a large amount of excess energy. As these carriers cool to the lattice temperature, they occupy states at the bottom of the bands. This causes further phase and amplitude changes due to band filling and state filling mechanisms. The relative magnitude of these processes is dependent on the frequency of the incident radiation. One intention of the work presented here is to ascertain the relative magnitudes of the processes, so that the nonlinear optical properties of the materials will be better characterized. The experimental techniques used are described in the next section.

Section 8.3 Measurement Techniques

In this section the experimental details of the measurements are presented. The laser system is described, followed by a description of the single-arm interferometer that indicates the strengths of this new measurement scheme. The experimental configuration for the pump-probe measurements that give information about nonlinear amplitude changes is also described. Finally, the cross-correlation measurement used to measure the group velocity and dispersion is explained.

8.3.a Laser

The laser system used for this work is a synchronously-pumped dye laser like that developed by Kafka and Baer. Laser pulses 90 ps in duration from the output of a mode-locked dye laser are compressed by a fiber-grating compression technique down to 6 ps. These pulses are frequency doubled to 532 nm. A dye laser operating with Styrl 9 dye is synchronously pumped with the green pulses. The dye laser, with a birefringent filter to control the wavelength, produces ≈500 fs pulses in the near infrared: 780-900 nm.

8.3.b Single-Arm Interferometer Technique

Background

The single-arm interferometer technique used to measure n_2 has certain advantages over other measurement techniques. These strengths are best appreciated by comparison to these other methods. One method to determine nonlinear refractive indices is by degenerate-four-wave-mixing experiments. This technique provides information only on the magnitude of n_2, not the sign. It has been used to measure n_2 in many materials, including recent measurements in nonlinear glasses (Friberg and Smith). Interferometry has also been used (Olbright and Peyghambarian, Park et al., Banyai et al., 1989, Cotter et al.). While interferometry provides information directly on the magnitude and sign of the phase changes, standard two-arm interferometers are subject to thermal and acoustic imbalances that often require complicated stabilization schemes (Cotter), though it appears that modified Twyman-Green two-arm interferometers are more stable (Olbright). Integrated optical Mach-Zender interferometers are less sensitive to changes in the physical path length, however, the effective path length changes due to thermal effects. Many times these thermal effects are created by the optical signals themselves. Fabry-Perot interferometers have significantly reduced imbalance problems, but they are limited in use because the multiple passes make determination of time constants more complicated, and they are limited to fairly thin samples.

The new nonlinear refractive index measurement technique uses a single-arm interferometer arrangement shown schematically in comparison to a two-arm Mach-Zender interferometer in Figure {8.2}. In this technique, the reference pulse is polarized along the same direction as the pump pulse and orthogonal to the probe pulse direction. Instead of being diverted into a separate arm as in the two-arm interferometers, the reference is put into a separate time slot. Specifically, the probe is delayed from the reference, and the

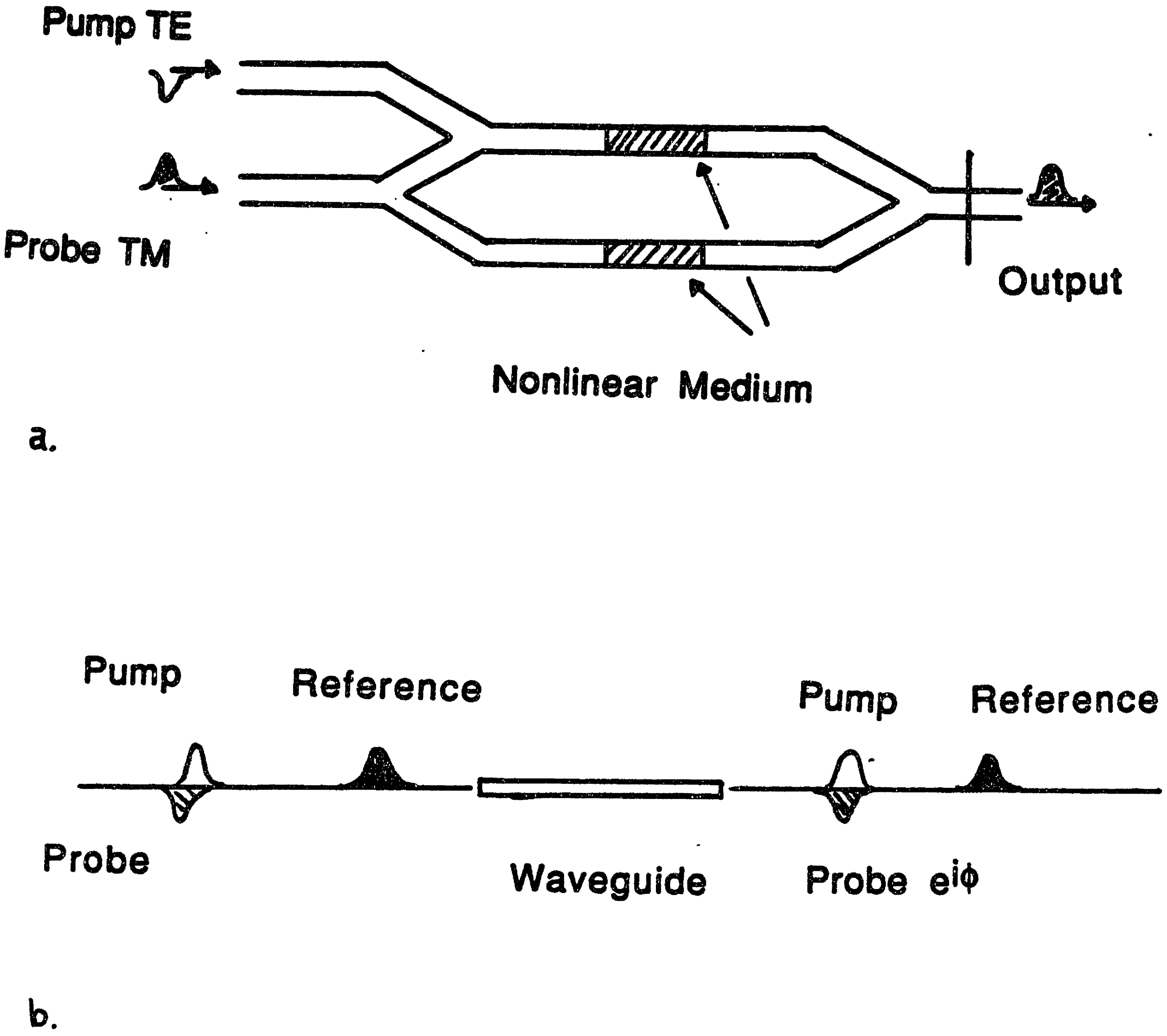

Figure 8.2. Schematic diagram of two interferometers: a) conventional Mach-Zender interferometer, and b) new single-arm interferometer.

pump pulse is variably delayed with respect to the probe before all three pulses are coupled into the waveguide. Because both the probe and reference beams travel through the same arm of the interferometer, changes in ambient conditions that occur on time scales slower than the delay between the signal and reference do not imbalance the interferometer. As such, temperature and other long-lived phase changes only affect the output based on reductions in the nonlinear coefficients, and not due to the changes in the linear coefficients. For example, if a long-lived free-carrier population is created due to two-photon absorption, the index of refraction will correspondingly decrease. For a two-arm interferometer, this would cause a change in the bias point of the interferometer for subsequent pulses, since the path length in one arm is changed. In the single-arm interferometer, though the path length is different than before the population was created, it is the same for both the signal and the reference, so the bias point is unchanged. These free carriers could, however, affect the magnitude of the nonlinearity through screening, or other carrier related effects, and these effects would be evident at the output of the interferometer.

Description

A schematic of the interferometer measurement set-up is shown in Figure {8.3}. Pulses from the laser are split into two beams. One beam, the pump beam, is sent into a variable delay stage. The other beam is rotated with a waveplate and the two orthogonal projections of this light are split with a polarizing beam splitter. A ≈200 ps time delay is put between the pulses in the two polarizations, the probe and reference pulses. When the pulses are recombined at the second beam splitter, a reference pulse precedes both the pump and probe by 200 ps. The reference is polarized along the same direction as the pump. The time delay of the pump is delayed with respect to the orthogonally polarized probe beam by the variable delay stage. All three collinearly travelling pulses are coupled into the waveguide with a microscope objective. At the output of the waveguide, the

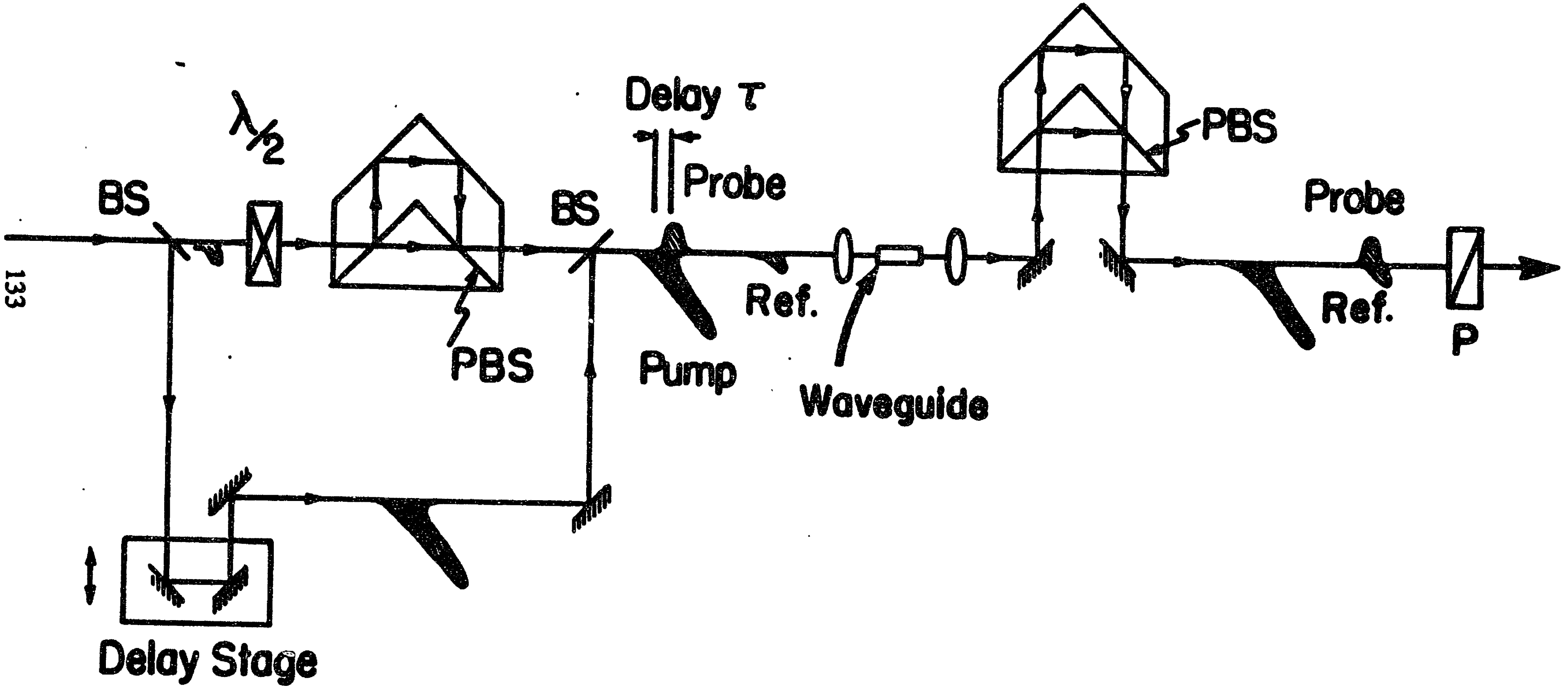

Figure 8.3. Schematic of the single-arm interferometer measurement set-up.

reference and probe are recombined in time using a polarization sensitive delay, similar to that at the input. In general, there is a phase shift induced on the probe due to the presence of the pump. There are also pump induced amplitude changes on the probe. These changes are dependent on the pump intensity as well as the time delay of the pump with respect to the probe.

At the interferometer output the electric fields of the probe and reference pulses are polarized as indicated in Figure {8.4}. The expression for the electric field at the output of the guide, $\underline{E}$, is given by:

$$\underline{E} = \hat{i}\,\underline{E}_{ref} + \hat{j}\,\underline{E}_{probe}\,e^{i\phi(I_{pump},\tau)} \qquad (8.3)$$

In this expression, $\underline{E}_{ref}$ is the reference pulse electric field, $\underline{E}_{probe}$ is the probe electric field, and $\phi(I_{pump},\tau)$ is the phase difference between the pump and reference pulse.

This field is split into the two projections of the polarizing beam splitter cube, $\hat{i}'$ and $\hat{j}'$. The projection of the E-field on these coordinates is written:

$$\underline{E} = \hat{i}'\left\{\frac{\underline{E}_{ref} + \underline{E}_{probe}\,e^{i\phi(I_{pump},\tau)}}{\sqrt{2}}\right\} + \hat{j}'\left\{\frac{\underline{E}_{ref} - \underline{E}_{probe}\,e^{i\phi(I_{pump},\tau)}}{\sqrt{2}}\right\} \qquad (8.4)$$

so that the intensity out of each port is expressed:

$$I_{i'} = |E_{ref}|^2 + |E_{probe}|^2 + 2\,E_{probe}\,E_{ref}\cos(\phi(I_{pump},\tau)) \qquad (8.5)$$

and

$$I_{j'} = |E_{ref}|^2 + |E_{probe}|^2 - 2\,E_{probe}\,E_{ref}\cos(\phi(I_{pump},\tau)). \qquad (8.6)$$

For most of the measurements, the difference between the signals from the two ports is used to eliminate fluctuations due to intensity changes in the two pulses. The signal output, S, is then:

$$S \propto E_{probe}\,E_{ref}\cos(\phi(I_{pump},\tau)). \qquad (8.7)$$

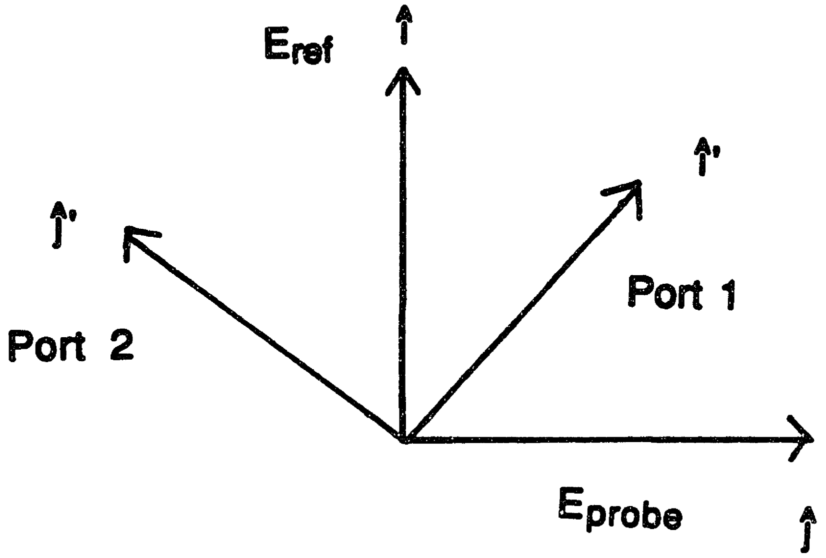

Figure 8.4 Output pulse configuration for the single-arm interferometer. The reference pulse is polarized along $\hat{\jmath}$. The probe is polarized along $\hat{\imath}$. The signal is taken from the two ports of the beam splitter cube: $\hat{\imath}'$ $\hat{\jmath}'$.

In general, $\phi(I_{pump}, \tau) = \phi_{nl}(I_{pump}, \tau) + \phi_b$, where ϕ_{nl} is due to nonlinear interactions and ϕ_b is a bias phase. Note that E_{probe} is a function of pump intensity and pump delay because of nonlinear amplitude changes. The interferometer may be biased to any point within the cosine period. The phase is adjusted by a micrometer and PZT adjustment of the recombination of the probe and reference. Amplitude changes affect the signal at all bias points. If the interferometer is biased at $\phi_b = 0$, the interferometer is more sensitive to amplitude changes than phase changes, though both contribute to the measured signal. At $\phi_b = \pi/2$, amplitude changes alone can not produce a signal, however, once a phase signal is measured, amplitude changes affect the measured signal. If measurements are performed with two independent bias points, both the amplitude changes and the phase changes may be determined.

A typical interferometer signal for a pump intensity of $\approx$150 MW/cm^2 at a wavelength detuning 20 nm from the band edge of the waveguide is shown in Figure {8.5}. This figure demonstrates the operation of the interferometer with four different interferometer bias points indicated on the figure. The pump, probe and reference have the same intensity for all four traces. The output of the interferometer is shown as a function of time delay of the pump with respect to the probe. Negative delays indicate the pump is behind the probe. There is a phase change that occurs at the zero delay when the pump and probe are overlapped. In one trace the interferometer is biased at the maximum of the cosine, or $\phi_b = 0$. With this bias, amplitude changes alone could produce a signal similar to the one indicated, however pump-probe measurements indicate pump-induced amplitude changes on the probe are small at these intensities. In addition, in another trace the interferometer is biased so a negative phase change gives a positive signal, or $\phi_b = \pi/2$. For this bias, there must be a phase change to cause a signal, though amplitude changes will tend to reduce the peak value of the signal. The other traces represent biases of $\phi_b = 3\pi/2$ and $\phi_b = \pi$. The details of the signal are described in Section {8.6}. For all of the phase measurements, the ON level represents the output of the interferometer when the

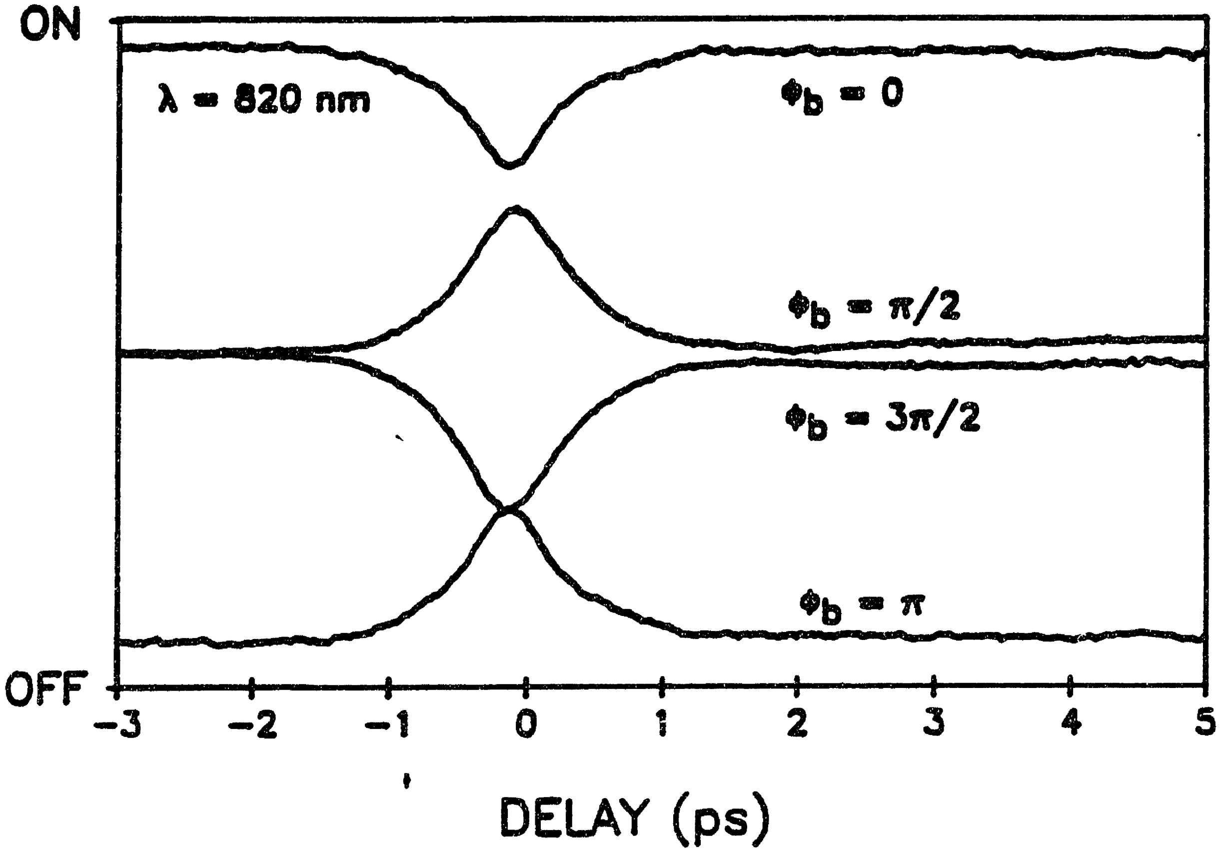

Figure 8.5. Interferometer output vs. time delay at λ=820 nm. Pump intensity is ≈100 MW/cm^2. Pump, probe, and reference intensities are the same for all four traces, which show operation for the four different bias points indicated on the figure.

pump is blocked and the bias phase is set to 0. OFF represents the output of the interferometer when the pump is blocked and the bias phase is set to π.

In the single-arm interferometer, only the polarization sensitive delay at the input and the output require interferometer accuracy. The components in these parts of the set up are compact, and there is only limited mechanical motion. Thus, the interferometer is inherently very stable. In fact, we are able to detect phase changes of less than π/500 with no active stabilization of the interferometer. A measurement of a phase shift of π/50 that indicates the sensitivity is shown in Figure {8.6}. Significant signal averaging (500 samples) is needed to obtain this sensitivity. This can be compared to the modified Twyman-Green interferometer that obtains sensitivity of π/100 over 1000 samples (Olbright).

8.3.c Pump-Probe Measurement Technique

To measure the dynamics of nonlinear amplitude changes, a pump-probe measurement geometry shown in Figure {8.7} is used. The pump and probe are in orthogonal polarizations, and the time delay between the pump and probe is varied by a delay stage. At the output, the pump beam is discriminated by a polarizer that passes only the probe polarization. The discrimination is better than 200 to 1. The transmission changes are quantified by first determining the magnitude of the probe transmission by chopping the probe with a mechanical chopper and measuring the full transmission signal on the lock-in. Then the pump is chopped, and pump-induced transmission changes on the probe are found by monitoring the output after the polarizer at the chopper frequency on a lock-in amplifier. This measured signal is divided by the full probe transmission, to show percent changes.

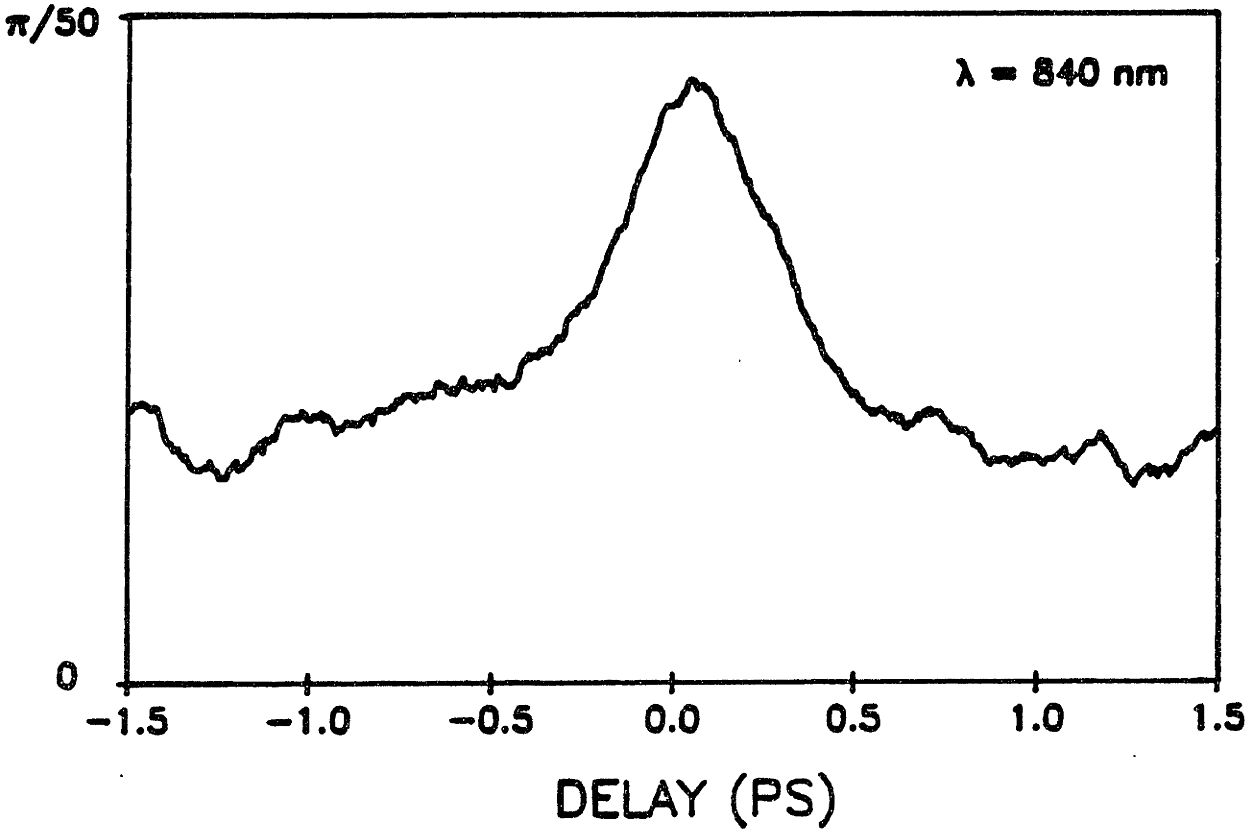

Figure 8.6. Interferometer output at λ=840 nm showing measurement sensitivity. Pump intensity is ≈ 1MW/cm^2.

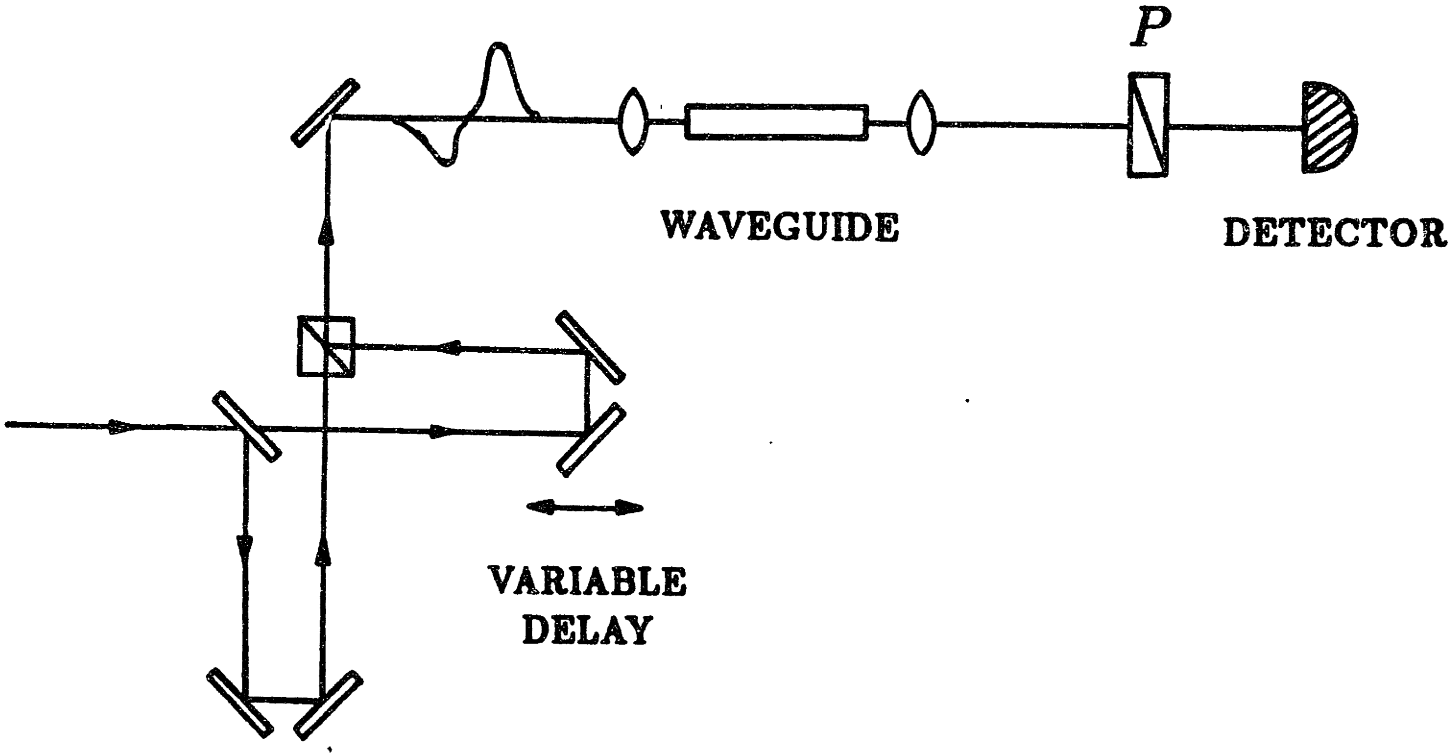

Figure 8.7. Pump/probe measurement set-up.

8.3.d Cross-Correlation Measurement Technique

Cross-correlation of the waveguide output is used to determine pulse spreading through the waveguide. It also can be used to measure the group velocity of the waveguide modes by looking at echo pulses from reflections at the waveguide facets. The cross-correlation set-up is shown in Figure {8.8}. The pulses from the laser are split by a beamsplitter and part of the light from the laser is coupled into the waveguides while part of the light is diverted around the waveguide into a second path. The output from the waveguide is mixed with pulses in the second path in a frequency doubling crystal. The intensity of the frequency doubled light is monitored as the time delay between the pulses in the two paths is varied via the delay stage. This produces a convolution of the pulse at the output of the guide with a pulse of constant known duration, so the output pulse duration may be determined by assuming a pulse shape. In addition to pulse width, group velocity in the waveguide may be found. This is because the light reflected back at the end facet of the waveguide (≈30%) makes another round trip through the guide and then is transmitted. The intensity of this second "echo" pulse is significantly lower than the primary pulse due to two 30% reflections, one 70% transmission and two additional trips through the loss of the guide. The time delay between the primary and "echo" pulses is a measure of the group velocity.

Section 8.4 Preliminary Measurements

8.4.a Introduction

Initial measurements were undertaken to determine the feasibility of using the new single-arm interferometer technique on semiconductor waveguides. The technique had been used previously to measure the switching properties of an optical fiber (LaGasse, 1989 c.). Interferometer measurements with this time resolution had not been performed

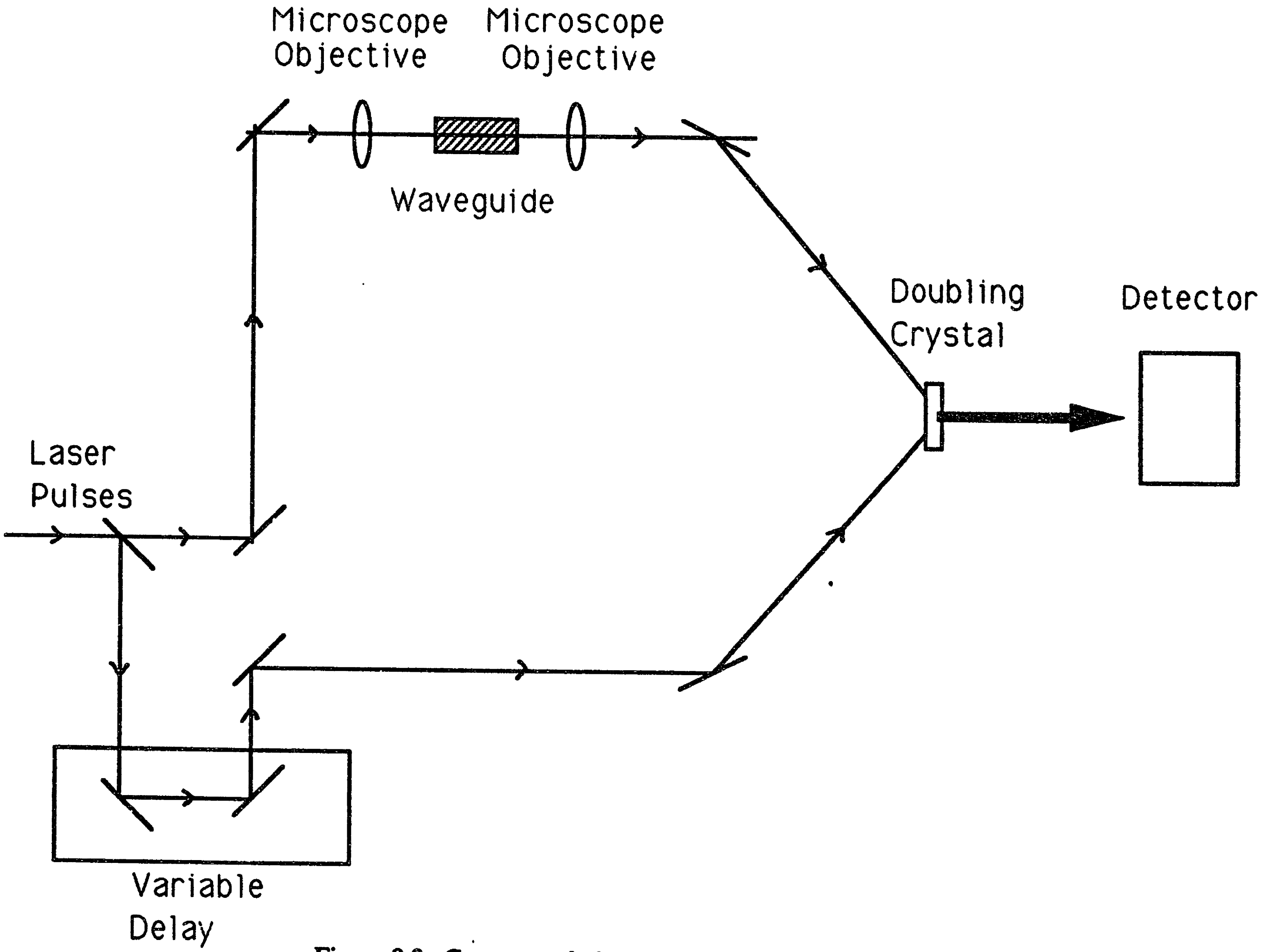

Figure 8.8. Cross-correlation measurement set-up.

on semiconductor materials, so there was a question whether the nonlinearities could be resolved by the measurement technique. In addition, it was unclear whether dispersion would prevent the measurement. The experiments described below provided the first information about the ultrafast optical switching properties in AlGaAs. However, they raised many questions as well, and prompted the further experimentation that is described in Section {8.5}.

8.4.b Experiments

A schematic of the waveguide structure used in the first measurements is shown in Figure {8.9}. The ridge waveguide is fabricated by wet chemical etching techniques. The layer structure is grown by OMVPE on semi-insulating GaAs substrate. The lower cladding layer of the waveguide consists of a 2-μm-thick $Al_{0.5}Ga_{0.5}$ layer. The waveguide core is 0.45-μm-thick $Al_{0.15}Ga_{0.85}As$ with a band edge of 760 nm. The ridges are 500 Å high and 3 μm wide. The index difference between the waveguide core and the lower cladding is very high. This leads to a tightly confined waveguide mode. The large index difference makes the waveguide intensity mode patterns less sensitive to detuning from the band edge. However, it also necessitates the very thin waveguide core and shallow ridge to assure single mode operation. The waveguide was 1 mm long.

These initial measurements were performed with the laser operating at 785 nm. The pulse duration was 400 fs. The linear absorption coefficient for the waveguide at this wavelength, determined by monitoring output power of the guide for two guide lengths, was ≈ 3.5 cm^{-1}. The interferometer output vs. time delay between the pump and probe is shown in Figure {8.10} for three different pump intensities. The peak pump intensity is approximately 1 GW/cm^2. All measurements were taken with the interferometer biased at $\phi_b=\pi/2$. For this measurement the output was the signal from one port of the beamsplitter cube. Therefore, the $\phi_b=\pi/2$ is not half-way between ON and OFF because E_{ref} does not

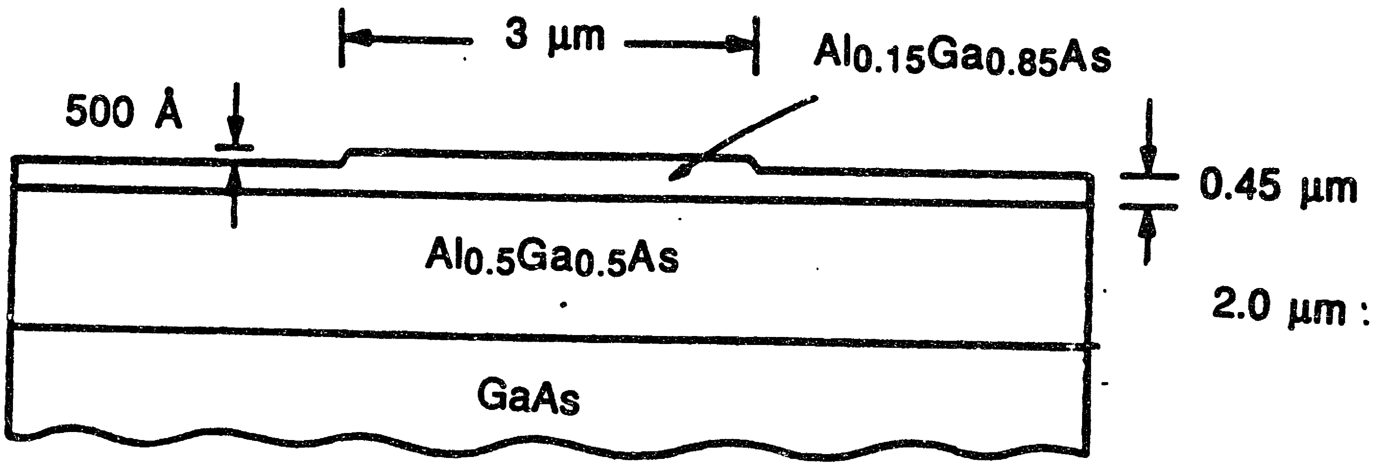

Figure 8.9. AlGaAs ridge waveguide structure.

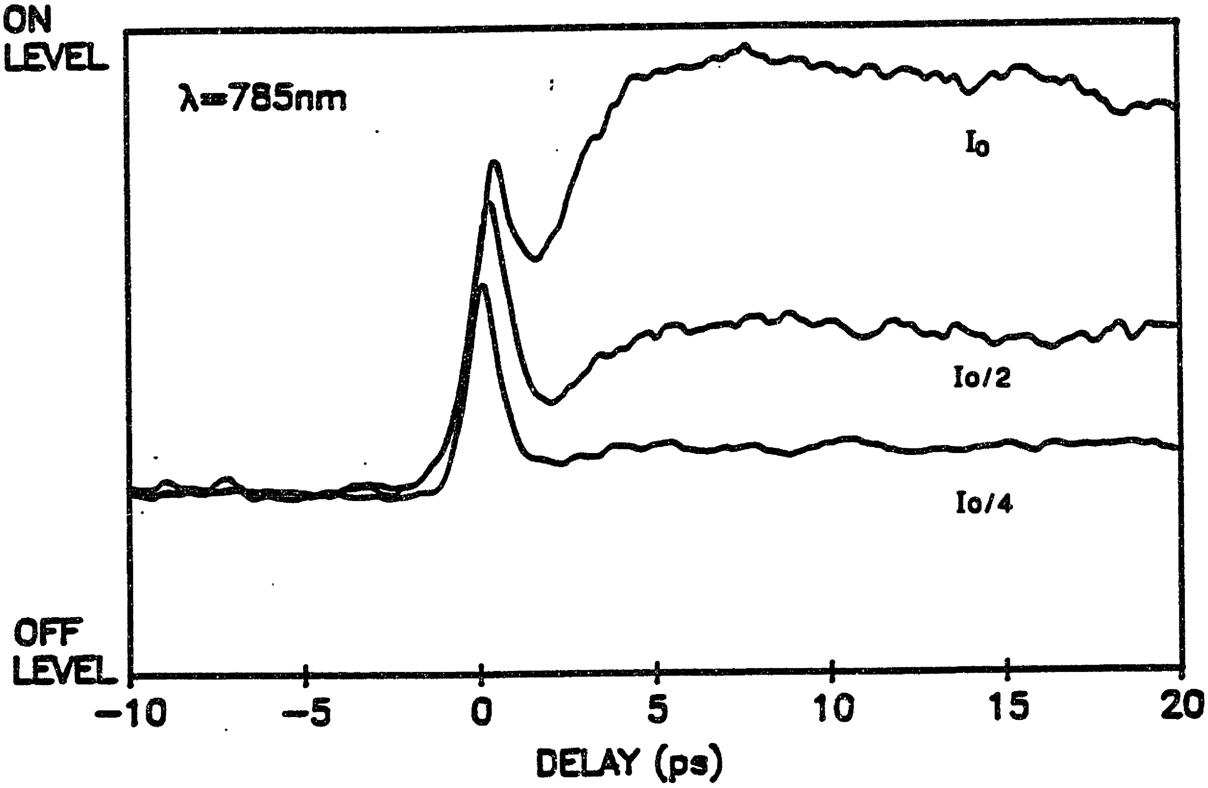

Figure 8.10. Interferometer output at λ=785 nm. I_0=1 GW/cm^2.

exactly equal E_{probe}. This does not affect the measurement signal significantly for these measurements.

The measured signals indicate an ultra-fast (< 500 fs) phase change at the zero-delay where the pump and probe are overlapped. The signal is also affected by amplitude changes, though to a lesser degree. The amplitude changes are discussed in the following paragraph. The presence of a phase change was verified by examining various bias points. The sign of the phase shift is negative indicating a decrease in the refractive index. The time response of this phase shift is within the pump pulse duration. This is followed by a long lived signal that rises on a 3 ps time scale and decays over 200 ps. The magnitude of the fast portion of the signal increases with increasing pump power, but the slower component shows a more dramatic increase. Three picoseconds is consistent with the time scales for hot carrier populations to cool to the lattice temperature, and the 200 ps decay is consistent with a carrier diffusion time out of the waveguide core. Therefore, one explanation for the results is that hot electrons are created by two-photon absorption processes. As these carriers cool to the lattice temperature they occupy the states at the bottom of the band and cause band filling phase changes. The sign of the phase change is consistent with this explanation.

To test the validity of this explanation, pump-probe measurements were performed to determine the nonlinear amplitude changes that were occurring. The pump-probe trace for the full intensity case, 1 GW/cm^2, is shown in Figure {8.11}. There is a 50% decrease in probe transmission at the zero delay that occurs on the time scale of the pulse duration. This is followed by complete recovery of the probe transmission. Two-photon absorption processes would yield this type of signal. The two-photon process will only occur when the pump and probe are present together. Since the probe frequency is below the band gap of the AlGaAs, there are no real states for direct transitions. Therefore, the two-photon generated carriers do not have an effect on the transmission at the positive time delays. It is possible to use the information on the decrease in amplitude in the probe beam to ascertain

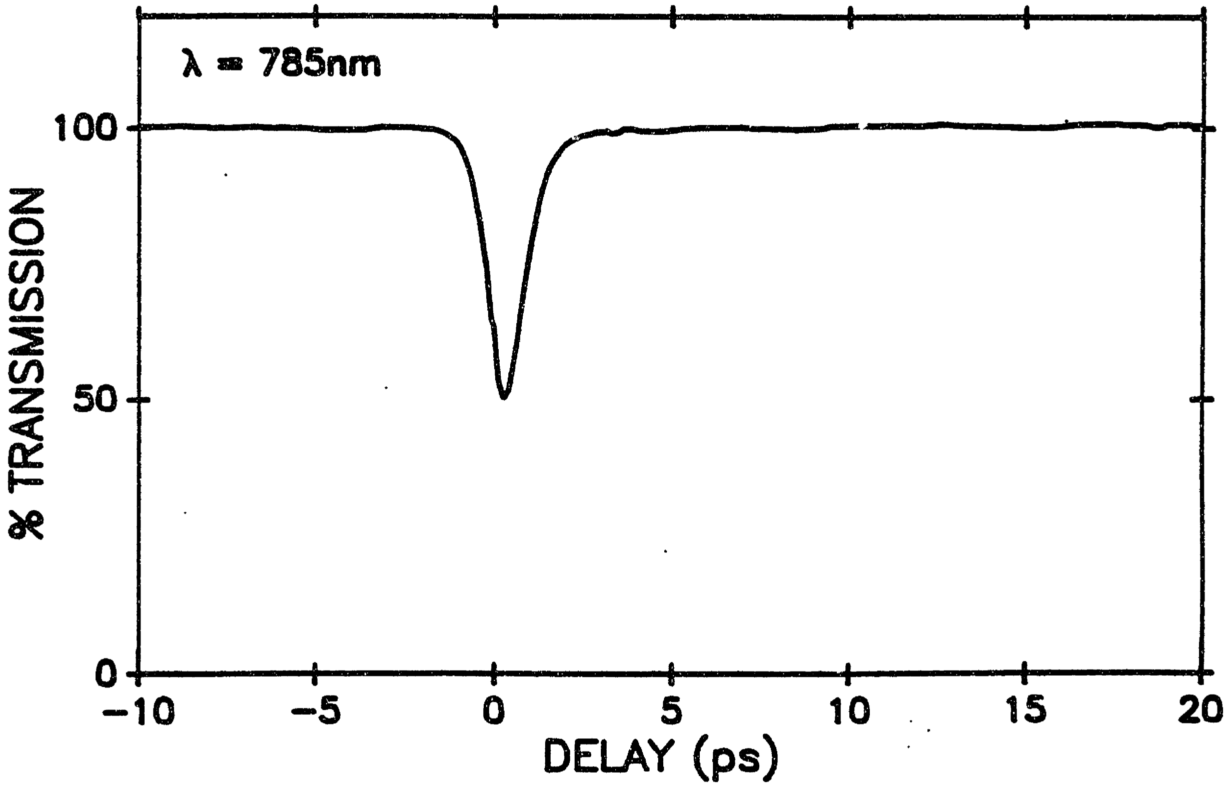

Figure 8.11. Probe transmission vs. pump delay for I≈1GW/cm^2 at λ=785 nm.

that the phase change measured at the zero delay is not due to amplitude changes alone. In fact, at zero delay, induced absorption reduce the signal toward the origin by reducing the probe intensity.

8.4.c Discussion

These experiments led to several interesting conclusions that helped to determine further avenues of investigation. It was apparent from the measurements that there is a measurable signal. Dispersion and walk-off, while likely affecting the measured signal, are not prohibitive. Two-photon absorption was shown to have a significant effect on the measured signal. For further investigation, the magnitude of the n_2 that produces the phase shift at the zero-delay and the wavelength dependence of the process is of interest, as is the relative magnitude of the ultrafast and long-lived phase change. Also, effects of linear absorption near the band edge must be considered. Because the tuning range of the laser prohibited further measurements on this waveguide, a second structure was fabricated and detailed measurements of n_2, α, and β as well as pulse broadening and walk-off were performed. These are described in the following section

Section 8.5 Optical Switching Properties of AlGaAs Waveguides

8.5.a Waveguide Description

The second set of measurements was much more detailed than the first. One requirement was to have a high quality waveguide structure. A schematic of the waveguide structure used for the second set of measurements is shown in Figure {8.12}. The ridge waveguide structure is fabricated by wet chemical etching techniques. The layer structure is grown by OMVPE on a semi-insulating GaAs substrate. The lower cladding layer of the waveguide consists of a 3-µm-thick $Al_{0.5}Ga_{0.5}$ layer. This is thicker than the previous guide to reduce reflections off the GaAs substrate and to reduce propagation of defects

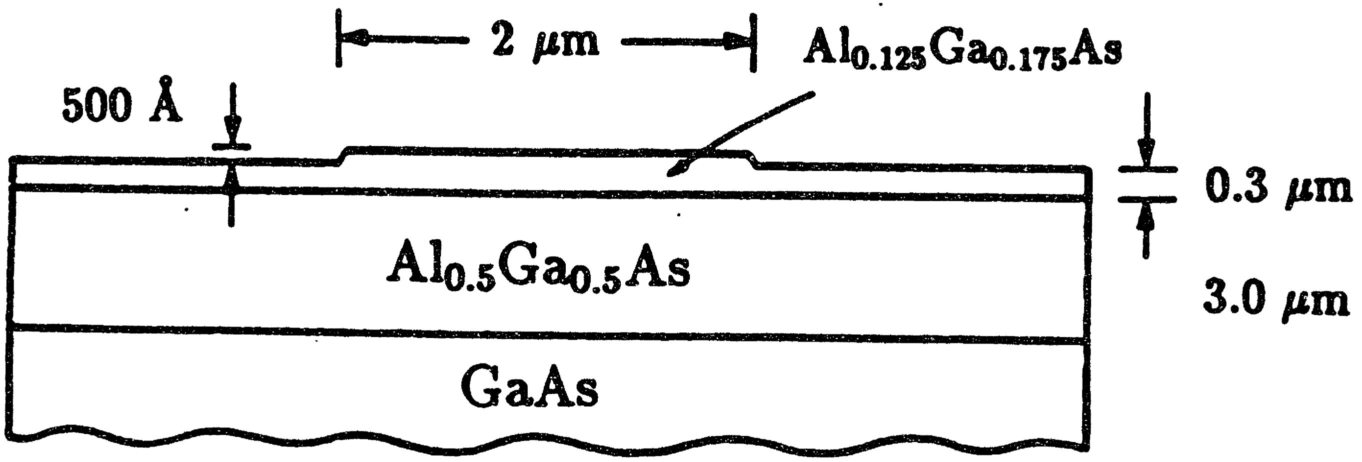

Figure 8.12. AlGaAs ridge waveguide structure.

from the substrate during growth. The waveguide core is 0.3-μm-thick $Al_{0.15}Ga_{0.85}As$ with a band edge of 790 nm. The ridges are 500Å high and 2 μm wide. The index difference between the waveguide core and the lower cladding is very high leading to a tightly confined waveguide mode. The theoretical near field profiles of the guide as calculated by the effective index method, described in Section {7.3}, are shown in Figure {8.13}. As in the first waveguide structure, the large index difference makes the waveguide intensity mode patterns less sensitive to detuning from the band edge. Although this facilitates the measurements, it also necessitates the very thin waveguide core and shallow ridge to assure single mode operation. Waveguides were cleaved to 1 mm, 2 mm, and 3 mm lengths.

8.5.b Experiments

Dispersion and Walk-off

In this section the results of measurements of group velocity and pulse broadening are presented. Cross-correlation measurements were performed on 1-mm-long waveguides. A typical cross-correlation trace at a wavelength of 820 nm is shown in Figure {8.14}. The small signal at 20 ps is an artifact of the measurement apparatus as is verified by removing the waveguide and retaking the cross-correlation. The signal at 20 ps is present even in the absence of the guide. The "echo" pulse at 32 ps is seen more clearly on the 50X scale. The time delay measured off the cross-correlation traces is shown for the wavelengths of interest in Figure {8.15}. Also plotted on the graph is the theoretical group velocity at each wavelength which is calculated from a theory of the refractive index that was published by Jensen and Torabi. The refractive index was derived as a function of the Al mole fraction in the material for different wavelengths near the band edge. The theoretical group velocity is related to the first derivative of the refractive index. The close agreement between theory and experiment is expected because the waveguide mode is

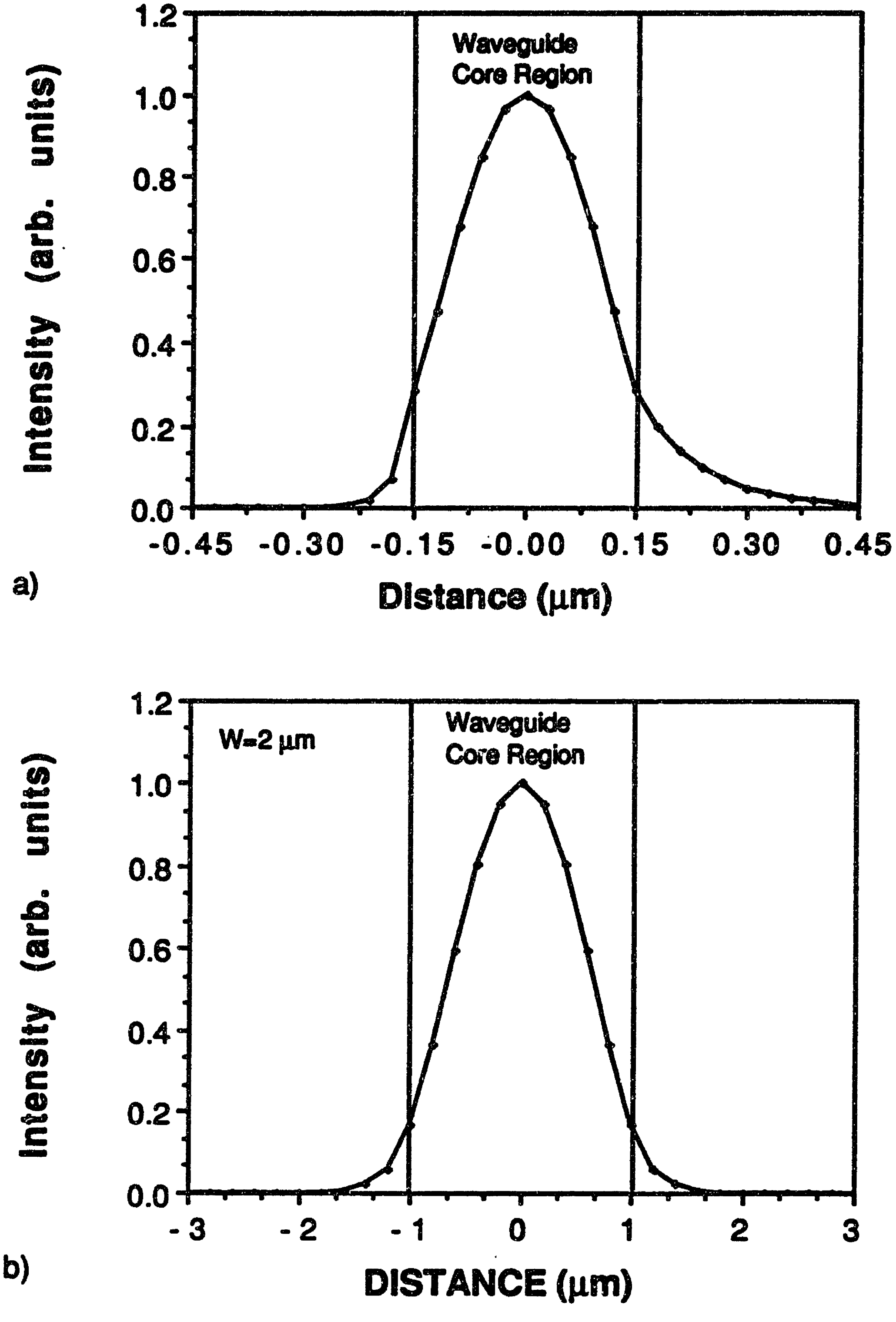

Figure 8.13. Near field optical intensity mode profile for a) the transverse, and b) the lateral direction.

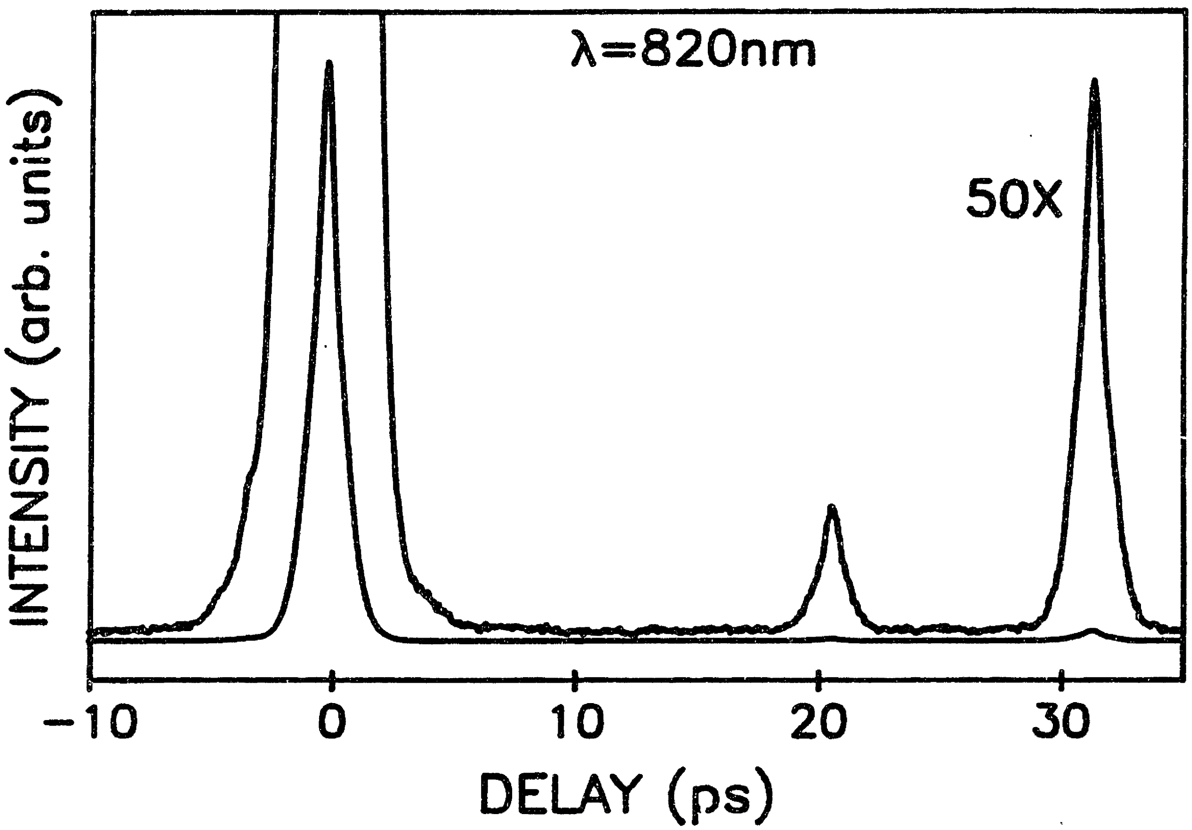

Figure 8.14. Waveguide output cross-correlation trace including a 50X expansion. The small signal at 20 ps is a measurement artifact.

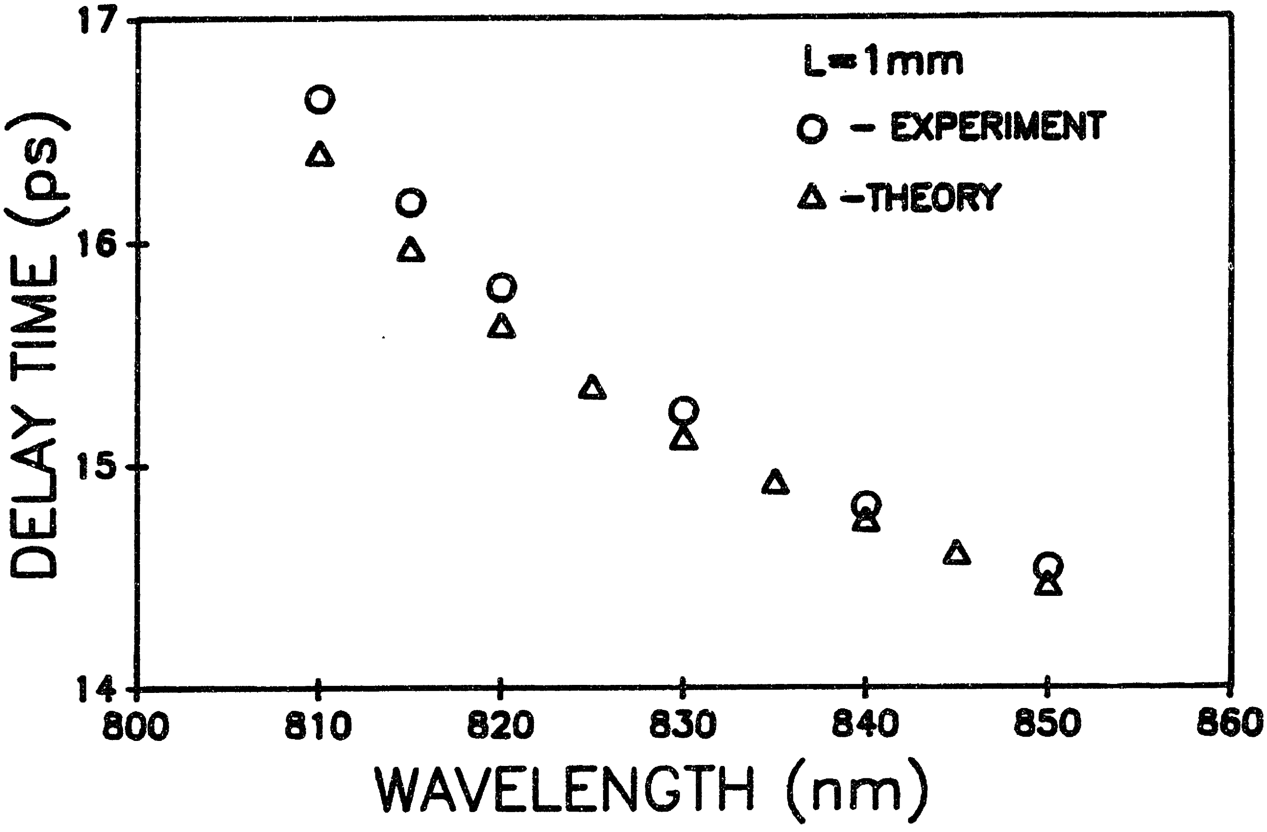

Figure 8.15. Group velocity vs wavelength for the AlGaAs waveguide: O-Experiment, and Δ-Theory.

tightly confined to the waveguide core region. The contribution from the waveguide is apparently small. Comparing the time delay between the primary and "echo" pulses for two orthogonal polarizations indicates the group velocity mismatch between the two modes is less than 260 fs over 1 mm at 810 nm where the mismatch would be most severe.

Pulse broadening is another important consideration. Pulse broadening is most severe near the band edge where dispersion is the highest. At a wavelength of 815 nm, near the band edge, the pulse broadening is indicated in Figure {8.16}. In this figure, trace (a) shows the input pulse auto correlation. Deconvolution of the trace yields a pulse width of 430 fs. Cross-correlation of the waveguide output for input intensities of 40 MW/cm^2 and 4 GW/cm^2 are shown in traces (b) and (c) respectively. Large pulse broadening at high powers is not unexpected because the increased spectral bandwidth brought on by self-phase modulation causes more dispersion of the pulse. The quality of the pulse is also poor. This is due to two-photon absorption causing pulse distortion. The deconvolved pulse widths are determined to be 650 fs and 1500 fs for the low and high intensities, although the deconvolution of distorted pulse shapes is not necessarily accurate. The results indicate that quantitative measurements with the high intensities must be approached with caution because of changes in the pulse shape through the waveguide. At the lower intensities the effect is not as dramatic. Additional measurements, performed before the cross-correlation, using autocorrelation of the waveguide output indicate pulse broadening of less than 10 % at very low intensities, ≈5 MW/cm^2. Cross-correlation measurements at these very low intensities are not available.

The measurements indicate that the walk-off in the waveguide is small for the 1-mm length used in the experiments. However, the walk-off measured in these particular guides would limit the interaction length for 1 ps pulses to less than 5 mm. This is important information in determining the potential for optical switching if propagation in two orthogonal modes is required. The dispersion measurements indicate that the pulses are broadened slightly at low intensities due to dispersion, but that broadening becomes

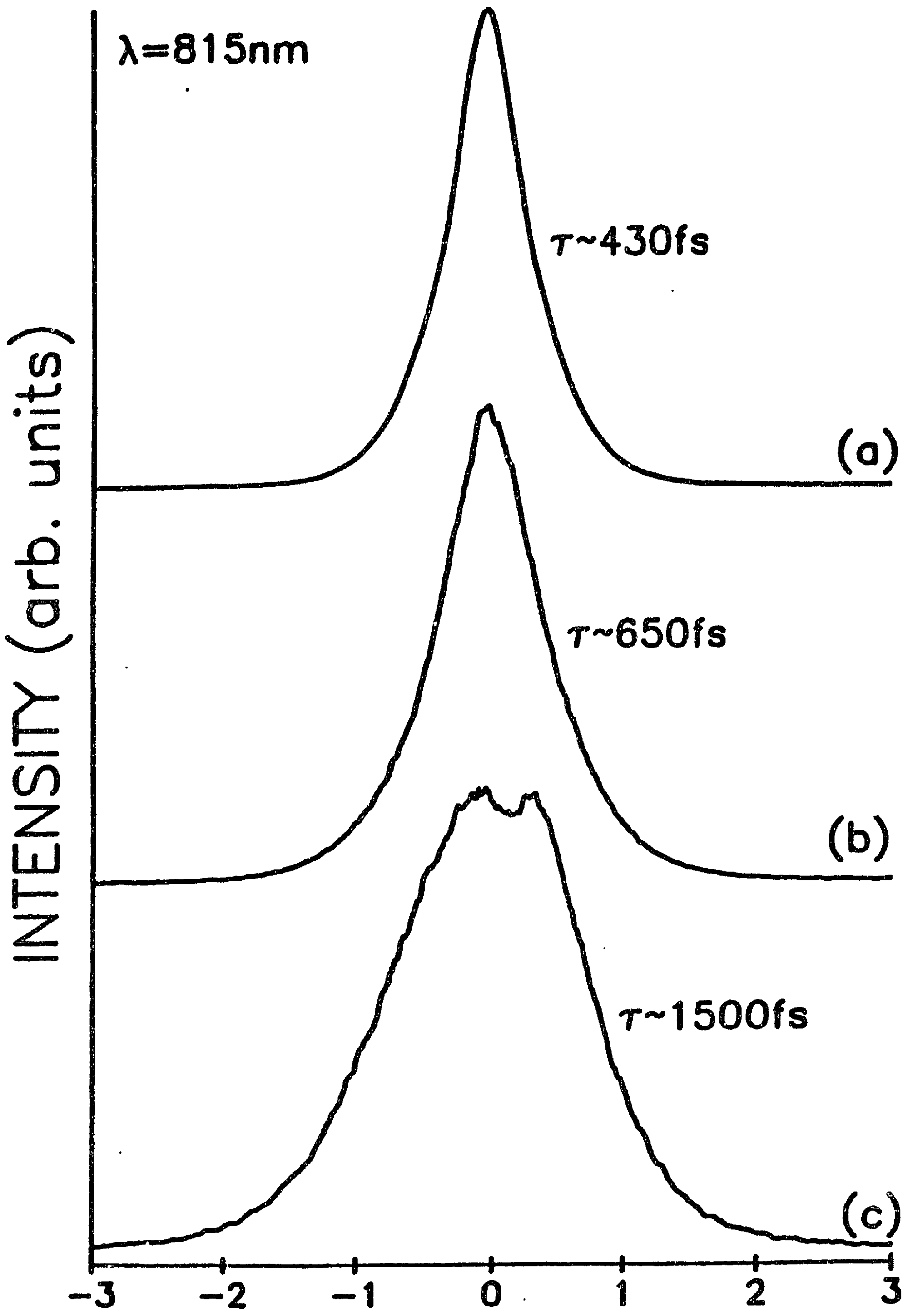

Figure 8.16. a) Input pulse auto-correlation. b) Waveguide output pulse cross-correlation for ≈ 40 MW/cm^2 at the waveguide input, and c) waveguide output cross-correlation for ≈ 4 GW/cm^2 at the waveguide input. The wavelength is 815 nm for all three traces.

significant (over a factor of 3) at the high intensities. This is a consequence of the fact that self-phase modulation broadens the frequency spectrum of the pulse, and so dispersion becomes more severe.

Linear Loss and Beta Measurement

In this section the measurements of the wavelength dependence of α and β are described. The two quantities are determined from experimental measurements of power at the output of the waveguide as a function of increasing input power. The measurements are fitted to a theoretical curve that includes both linear and two-photon absorption processes. The output intensity from the waveguide under the influence of two-photon absorption is obtained by integrating the expression for the intensity along the z-directed length of the waveguide:

$$dI/dz = - \alpha I, \tag{8.8}$$

where

$$\alpha = \alpha_0 + \beta I \ . \tag{8.9}$$

In this expression, α is the total loss coefficient of the material, α_0 is the linear loss, and I is the intensity of the light in the waveguide. Integrating these equations yields the following expression for output power, I_o, as a function of input power, I_i, for the waveguide:

$$I_o = C_0 \frac{C_i I_i \exp(-\alpha_0 l)}{1 + \frac{\beta}{\alpha} C_i I_i \left[1 - \exp(-\alpha_0 l)\right]} \tag{8.10}$$

where C_0, and C_i are the output and input coupling constants, and l is the waveguide length.

The measured values of I_o vs. I_i for two different waveguide lengths, 1 mm and 3 mm, are fitted to determine α and β. This eliminates the need to know C_i. The output coupling is known to within 5%, and the power measurement is accurate to within 10%. An example of the measurement at a wavelength of 810 nm is shown in Figure {8.17}. The plot is on a LOG-LOG scale. The I_o vs. I_i are characterized by a linear regime at low input intensities, and a saturation of the signal at larger intensities (see Equation {8.10}). At very high intensities, the pulse begins to broaden, and reduces the peak intensity so the signal appears to increase again. This points toward the drawback of using a pulsed laser system to measure these effects accurately. However, the measurements are accurate enough to determine optical switching properties, and the dye laser allows the wavelength dependence to be measured. To minimize discrepancies, the fit was obtained only up to peak powers of 500 MW/ cm^2. The fit of β is accurate to about ± .01 cm/MW. The fit of α is accurate to approximately 0.8 cm^{-1}.

The measured wavelength dependence of α is shown in Figure {8.18}. It indicates the increase in linear loss as the wavelengths approach the absorption edge of the material. The loss at the long wavelength of 850 nm is less than the 0.8 cm^{-1} measurement accuracy. This is a very low loss, although greater measurement accuracy is required to compare the loss to the lowest reported loss measurements in ridge waveguides of 0.3 cm^{-1} at 1.52 μm by Deri et al. (1987). However, that measurement was significantly further from the band edge. The measured value of β as a function of wavelength is shown in Figure {8.19}; β is constant, independent of wavelength, as expected for this wavelength range. The value of β, 0.02 cm/MW, is consistent with recent measurements in bulk GaAs at 1.06 μm wavelength by Boggess et al.

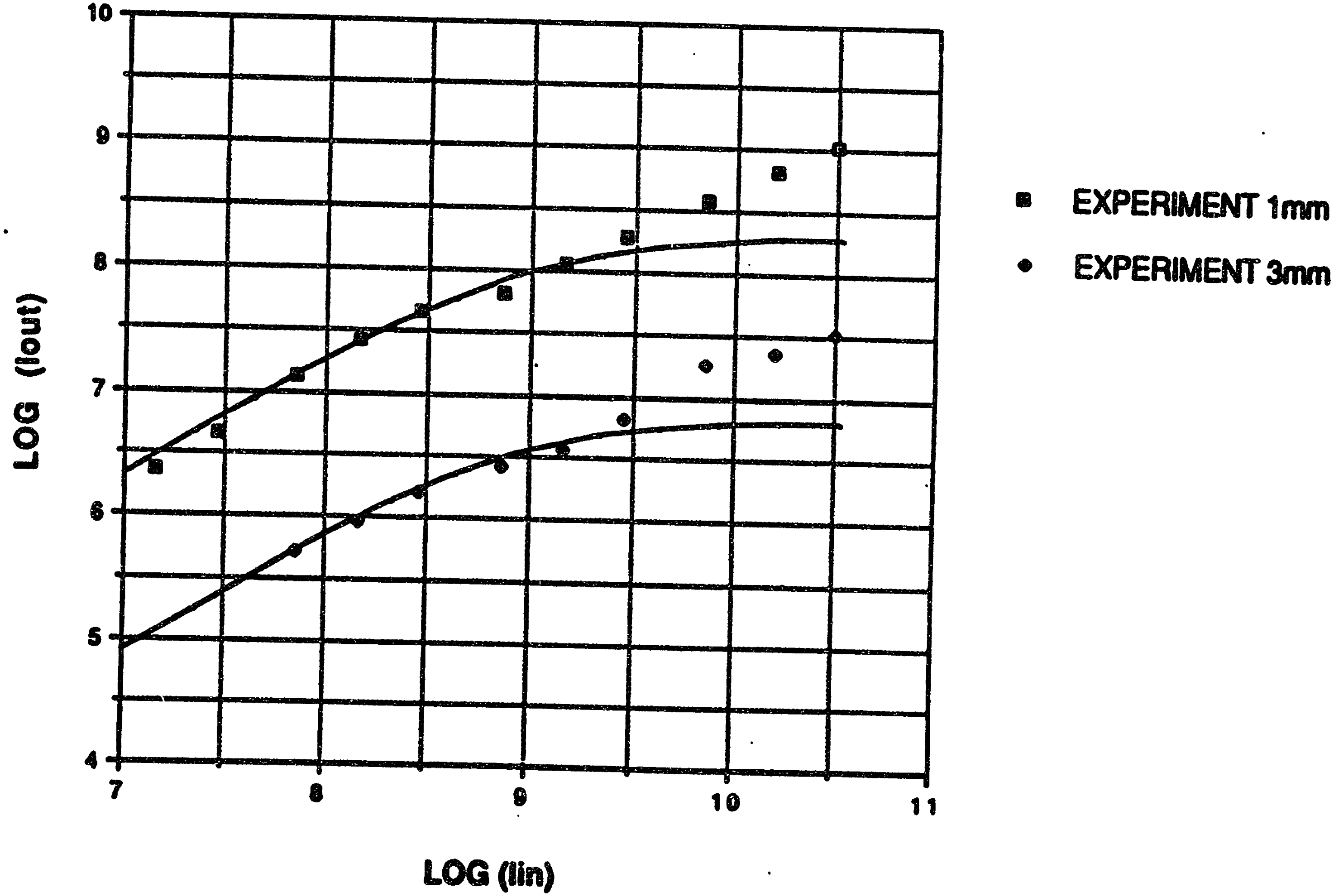

Figure 8.17. Waveguide output intensity vs input intensity on Log-Log scale for $\lambda = 810$ nm. Experimental (characters) and theoretical (solid lines) curves for two waveguide lengths, 1 mm and 3 mm, are shown.

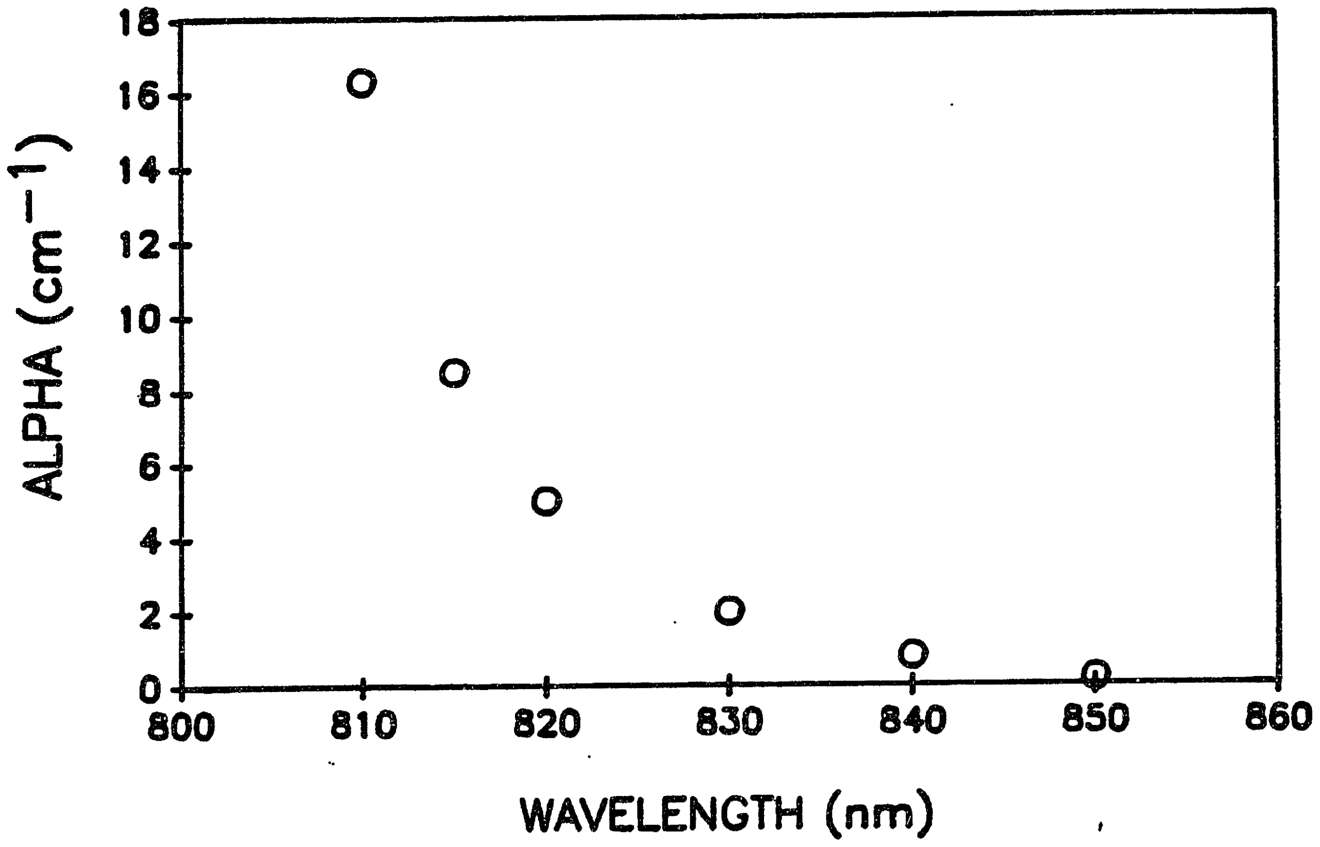

Figure 8.18. Waveguide linear loss vs wavelength.

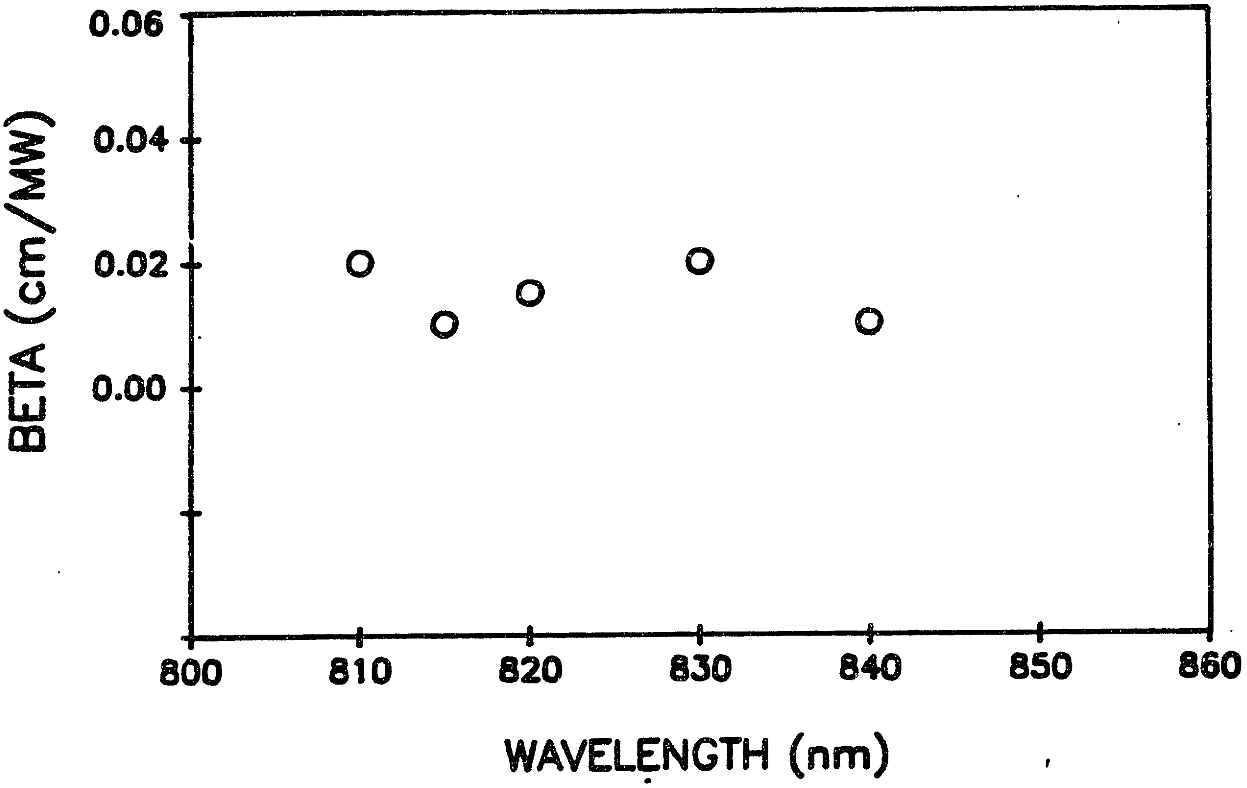

Figure 8.19. Two-photon absorption coefficient, β, vs wavelength.

n_2 Measurement

In this section the measurements of the magnitude and sign of the nonlinear coefficient, n_2, that produces the ultrafast part of the intensity dependent nonlinear phase change are presented. The measured values of n_2 are $-3X10^{-13}$ cm^2/W at long wavelengths with a resonant enhancement of a factor of 10 for shorter wavelengths near the band edge. At the long wavelengths, the values of n_2 are consistent with measurements in bulk GaAs a 1.06 μm by Burns and Bloembergen. However their measurements were not performed with time resolution, and more recent information indicates that thermal effects may have been present in the measurement (Gabriel). These numbers are the largest known nonresonant values of n_2 (see Chang, 1981). The measurement of n_2 is discussed below.

Several factors contribute to the measurement of n_2. The input pulse width was kept constant for all the wavelengths at ≈500 fs. It was essential that the pulse intensities be kept very low to keep two-photon absorption induced amplitude changes, and two-photon generated carriers negligible. These effects are discussed more completely below.

The ultrafast phase shift in a wavelength of length l, $\phi_{nl}(I_{pump}, t)$, due to the pump in the absence of nonlinear absorption is expressed:

$$\phi_{nl}(I_{pump}, t) = \frac{2\pi}{\lambda} n_2 \; I_{pump}(t) \left(\frac{1-e^{-\alpha l}}{\alpha}\right). \qquad (8.11)$$

I_{pump} is the pump input intensity. The last term in the expression is the result of integrating the effect through the waveguide. The n_2 that is measured is the perpendicular component of n_2 because the pump and probe are in orthogonal polarizations. The signal measured for given pump delay, τ, is expressed:

$$S(\tau) \propto \int_{-\infty}^{\infty} E_{ref}(t) E_{probe}(t) \cos\left\{ \phi_{nl}(t-\tau) + \phi_b \right\} dt \; . \qquad (8.12)$$

To produce a linear response, the bias is set so $\phi_b = \pi/2$. In this case Equation {8.12} reduces to:

$$S(\tau) \propto - \int_{-\infty}^{\infty} E_{ref}(t) E_{probe}(t)\, \phi_{nl}(t-\tau)\, dt\,. \qquad (8.13)$$

and a negative phase change produces a positive signal. The linear regime holds for phase changes less than $\approx\pi/3$, which is the case for the measurements. The peak of the signal is measured at $\tau=0$, and the value of n_2 is found by using Equation {8.11}. The finite pulse duration is accounted for by dividing the measured pump intensity by a factor of $\sqrt{2}$, which is an approximation based on Gaussian shaped pulses (Cotter et al.).

It is important to consider the effects of amplitude changes on the signal. For the measurement, pump intensities were kept less than 20 MW/cm^2, and a check of the probe transmission with pump-probe measurements indicated pump-induce probe intensity changes were less than 5%. Therefore, the probe electric field changes by less than 2.5%, and so affects the measured value of n_2 by this much. In the high intensity regime where β is a factor, Equation {8.11} will not hold, and the α-dependent term would have an additional βI_p dependence that produces a nonlinear $n_2(I_p)$. To check that nonlinear absorption of the pump is not a factor, the measurement is carried out for two pump intensities, I_p and $I_p/2$, and the value of n_2 must linearly track the two pump intensities.

In the measurements at short wavelengths, in addition to the phase shift at the zero-delay, there is a long-lived phase change that lasts for 100 ps. This phase change is due to carriers generated by linear absorption, as is verified in transmission measurements. This long-lived level was less than 30% of the measured signal. A deconvolution process was used to remove the long part of the signal, which is an integrated effect. There was little effect on the measured phase change at zero delay. Two other factors contribute to the measurement. First, the pulse width of the laser at these intensities broadens slightly due to self-phase modulation, less than 20%, through the waveguide. The pulse broadening effect is somewhat reduced because the intensity is also decreasing through the waveguide from linear absorption. Also, the walk-off between the pump and probe is approximately 100 fs through the 1-mm-long waveguide. This has only a small effect on the measured values for n_2. The other factors that contribute to the calculation are the output coupling from the waveguide into the detector that is used to measure power. This output coupling includes the loss in the output objective due primarily to reflections, and the coupling of the objective. The coupling into the objective is not perfect because the divergence of the thin waveguide core region is very large. There is some inaccuracy in the estimated coupling efficiency. The combined measurement errors and approximations produce an accuracy of about 40% in the measured value of n_2. This is due primarily to uncertainties in the pump intensity, and the pulse spreading.

The measured n_2 as a function of wavelength is shown in Figure {8.20}. Note that the pulse width dependence of n_2 is not known, therefore these results are valid only for ≈ 500 fs pulses. The enhancement in n_2 as the wavelength approaches the band edge is apparent. The sign of n_2 is negative through the entire wavelength range. The mechanism for the phase change is still uncertain. The sign of the process is consistent with band filling. This seems plausible because the n_2 tracks the increase in linear loss, but the fast time response must be accounted for. A fast response could occur if excitons are created, because they subsequently ionize in 300 fs (Chemla and Miller). In fact, recent measurements in InGaAs materials indicate the creation and subsequent decay of excitons (Phillips). The excitons could create a larger phase change than the electrons and holes they generate when they ionize, because they are more efficient at causing band filling phenomena (Chemla). The measured sign of n_2 is also consistent with a blue shift of the exciton peak, which could be induced by light at the pump excitation energies via the optical Stark effect (Schmitt-Rink et al., Schmitt-Rink and Chemla, Schmitt-Rink, Yamanishi and Kurosaki, Mysyrowicz et al., and Von Lehmen et al.). In the future work section, some experiments designed to help determine the nature of the phase change are presented.

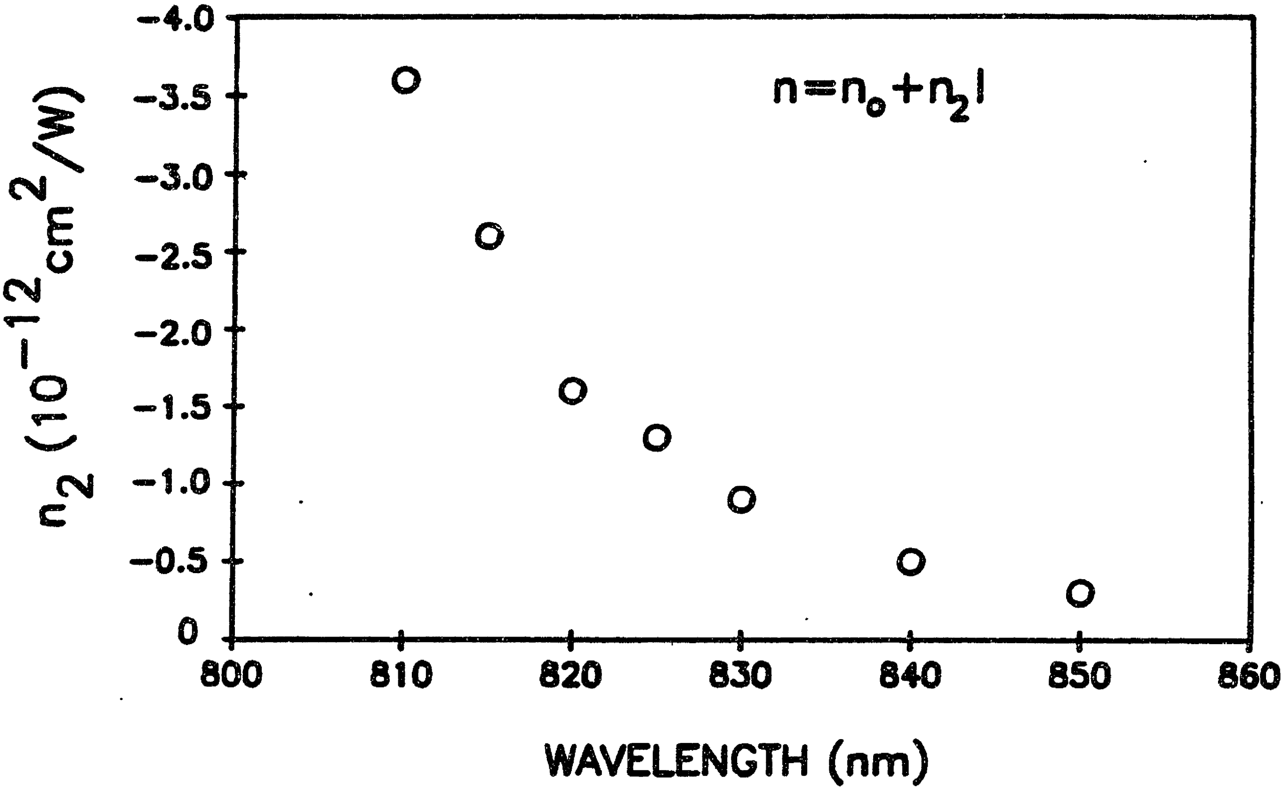

Figure 8.20. Nonlinear index of refraction, n_2, vs wavelength. The perpendicular component is measured because the pump and probe are in orthogonal polarizations.

Section 8.6 Dynamics Experiments

8.6.a Experiments

The measurements described in the previous section concern the magnitude of the various nonlinear processes as a function of wavelength near the band edge of AlGaAs. In addition to this information, the magnitude of the slower free-carrier induced process that was seen in the initial measurements is important. In particular, it is interesting to see whether there is an operating point where the fast phase change is significantly larger than the slow phase change, which indicates the potential for ultra-fast switching. Quantitative information about these changes is complicated by the various mechanisms that influence the phase and amplitude changes near the band edge. However, qualitative conclusions may be made, and they provide important insight into the potential for optical switching in the material as well as the physics of the various processes in the semiconductor. Also the importance of two-photon absorption processes near the band edge can be examined. This information is determined by looking at the dynamics of the phase and amplitude changes at different wavelengths below the band edge for increasing pump power. The relative contributions to the nonlinearities due to fast processes and slower processes are shown for various intensities at the different wavelengths.

The output of the interferometer as a function of time delay of the pump with respect to the probe for wavelengths of 810 nm and 830 nm is given in Figure {8.21}. These wavelengths represent detunings from the AlGaAs band edge of 20 nm and 40 nm respectively. For each wavelength, three traces are shown for input pump intensities inside the front facet of the waveguide of approximately 2 GW/cm^2 , 500 MW/cm^2 , and 40 MW/cm^2 . The actual intensity is dependent on the input coupling, and is not known to better than about 30%. The probe and reference intensities are a factor of five less than the pump intensity for this measurement.

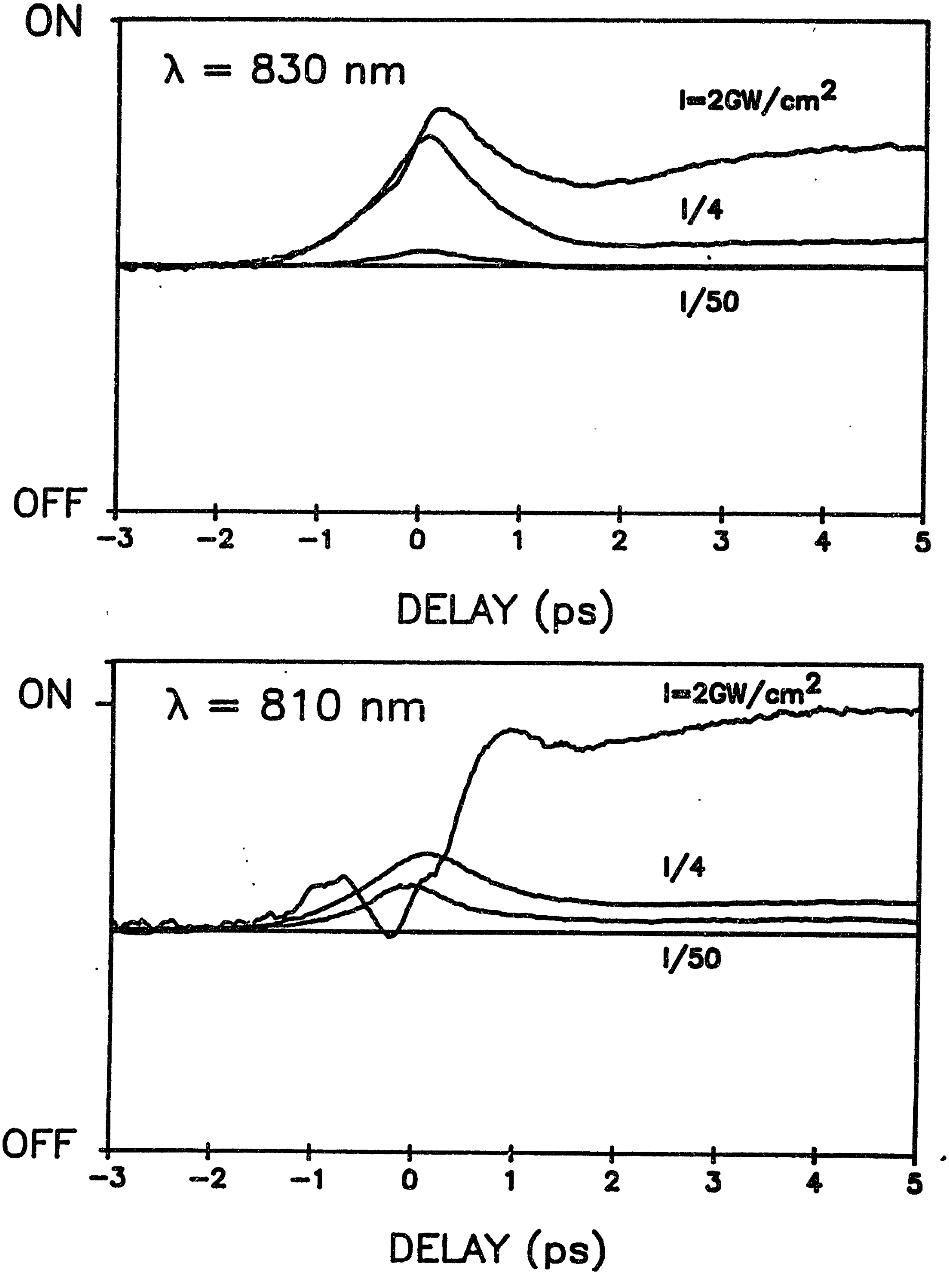

Figure 8.21. Interferometer output vs pump delay for increasing pump intensity. a) for λ=830 nm, and b) for λ=810 nm.

For low pump intensities, the traces are characterized by a phase change at the zero-delay which turns on and off within the pump pulse width. Pulse width is determined by cross-correlation of the pulses at the output of the waveguide. While pulse broadening is less than 20% at the low intensities, there is pulse spreading by a factor of three at the higher intensities. Pulse spreading is more pronounced at shorter wavelengths due to increased dispersion and larger bandwidth due to self-phase-modulation. At 830 nm, there is no measurable phase change at long positive time delays for these low intensities. At 810 nm, there is a phase change evident at the zero delay for the low pump intensities similar to the case at 830 nm . As expected because of the resonant enhancement of n_2 at the shorter wavelengths, the low intensity signal at 810 nm is larger than the comparable intensity trace at 830 nm. This is apparent even though the effective length of the guide is longer at 830 nm due to less absorption. The linear absorption coefficient, quantified in Section {8.5.b}, increases dramatically as the wavelength is tuned closer to the band edge. In addition to being larger, the phase change at 810 nm does not recover completely at the positive time delays. The long lived process evident at 810 nm, but not at 830 nm, is due to carrier generation by linear absorption. Two-photon absorption carrier generation is not a factor at these low intensities. The long lived carrier process is more marked at 810 nm both because of the increased linear absorption coefficient and the increase in the band filling index change at wavelengths close to the band edge. The free-carrier process turns off on a 100 ps time scale as verified by taking a scan to long positive time delays. This turn-off time is consistent with carrier diffusion out of the waveguide core where surface recombination occurs.

As the pump intensity is increased to 2 GW/cm^2, there is a significant phase shift at the long positive time delays for both wavelengths. The magnitude of this long-lived phase change is larger at 810 nm than at 830 nm. At 810 nm, the measured signal at the zero delay is significantly affected by changes in the magnitude of the probe field due to nonlinear absorption at these high intensities, as well as pulse distortion and pulse spreading. The effects are more dramatic at 810 nm than at 830 nm because the magnitude of the processes are larger due to band-edge-resonant enhancement. Figure {8.22} shows the maximum intensity trace at 830 nm out to an 80 ps positive time delay. As evident in this figure, the long-lived phase change rises on a 3 ps time scale, and turns off on a 100 ps time scale. Three picoseconds is consistent with the time for a hot-carrier population to cool down to the lattice temperature (Kessler, 1987) and cause a phase change sensed by the incident probe pulse due to bandfilling. The 100 ps turn-off is consistent with the carrier diffusion time. For the wavelength of 830 nm, the carriers which cause the phase change at positive time delays are primarily caused by the two-photon process, while for the wavelength of 810 nm there are also a significant number of carriers generated by linear absorption.

Transmission measurements were also made to determine the nonlinear transmission properties of the AlGaAs. The dynamics of the nonlinear transmission are obtained by a pump-probe measurement. The results of these pump-probe measurements at wavelengths of 810 nm and 830 nm are shown in Figure {8.23}. Probe transmission is normalized to 100% when the pump follows the probe. Two-photon processes cause induced absorption at zero delay when the pump and probe are overlapped. The magnitude of this induced absorption increases with increasing pump power as expected. At 830 nm the probe intensity completely recovers within the pump pulse duration, as expected from the two-photon absorption process. In contrast, at 810 nm the transmission recovers to a higher level, indicative of absorption saturation. The long time scan for the high pump intensity transmission trace at 810 nm is shown in Figure {8.24}. The absorption saturation has the same three picosecond turn on time apparent in the phase measurements. The turn-off occurs on a 100 ps time scale characteristic of the carrier diffusion as with the phase measurement. The absorption saturation is evidence of state-filling due to carrier populations (Chemla et al.). As the wavelength approaches the band edge, absorption due to band-tail to band-tail transitions becomes important as indicated by the increased linear

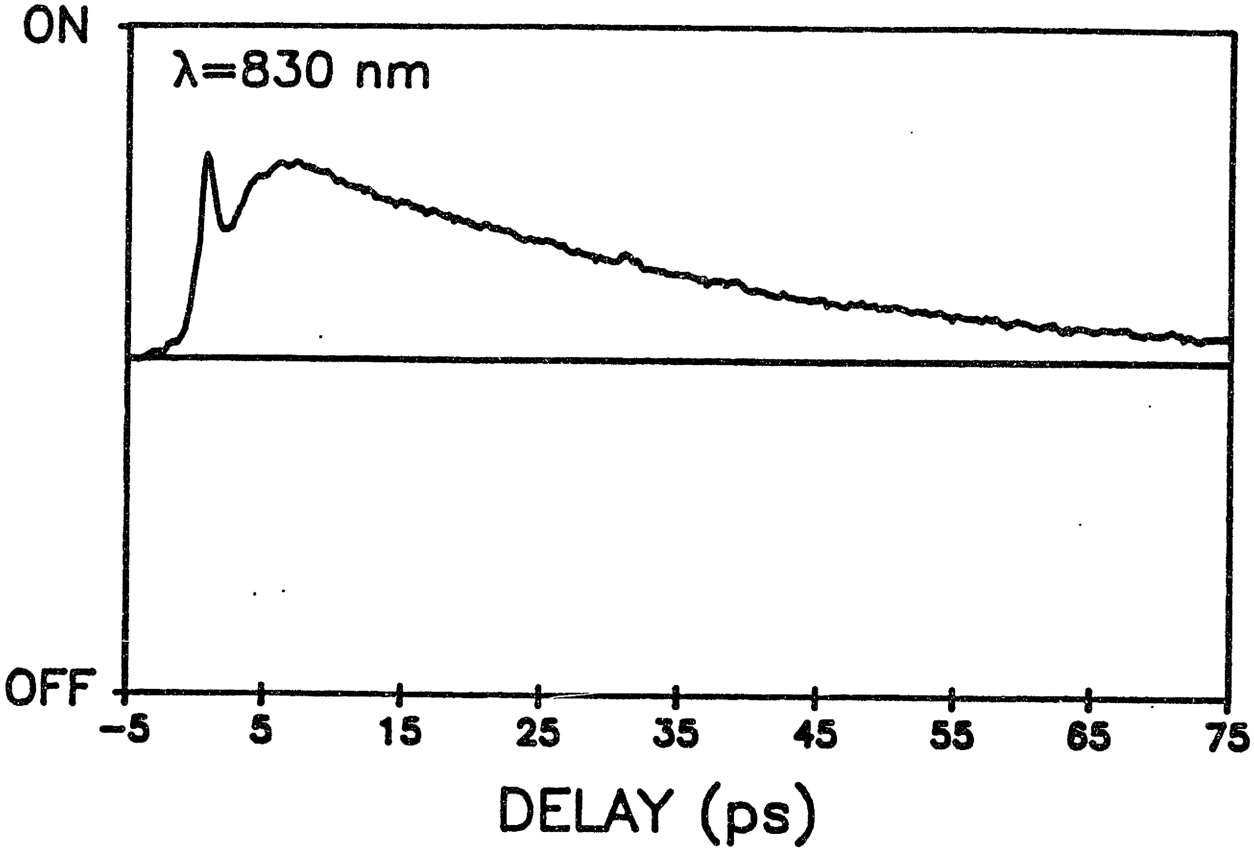

Figure 8.22. Interferometer output vs pump delay for $I \approx 2$ GW/cm^2 at $\lambda = 830$ nm.

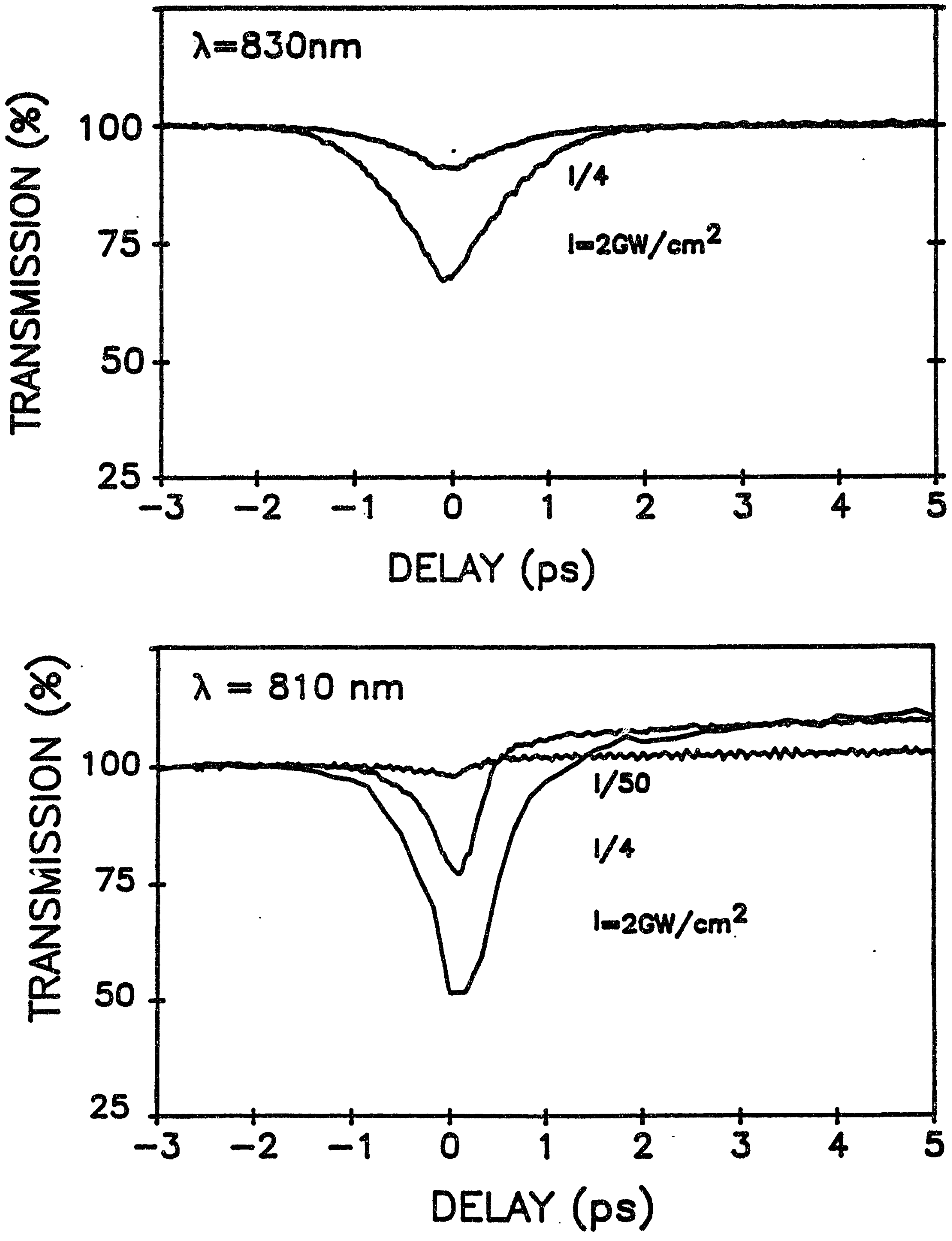

Figure 8.23. Probe transmission vs pump delay for increasing pump intensity. a) for λ=830 m, and b) for λ=810 nm.

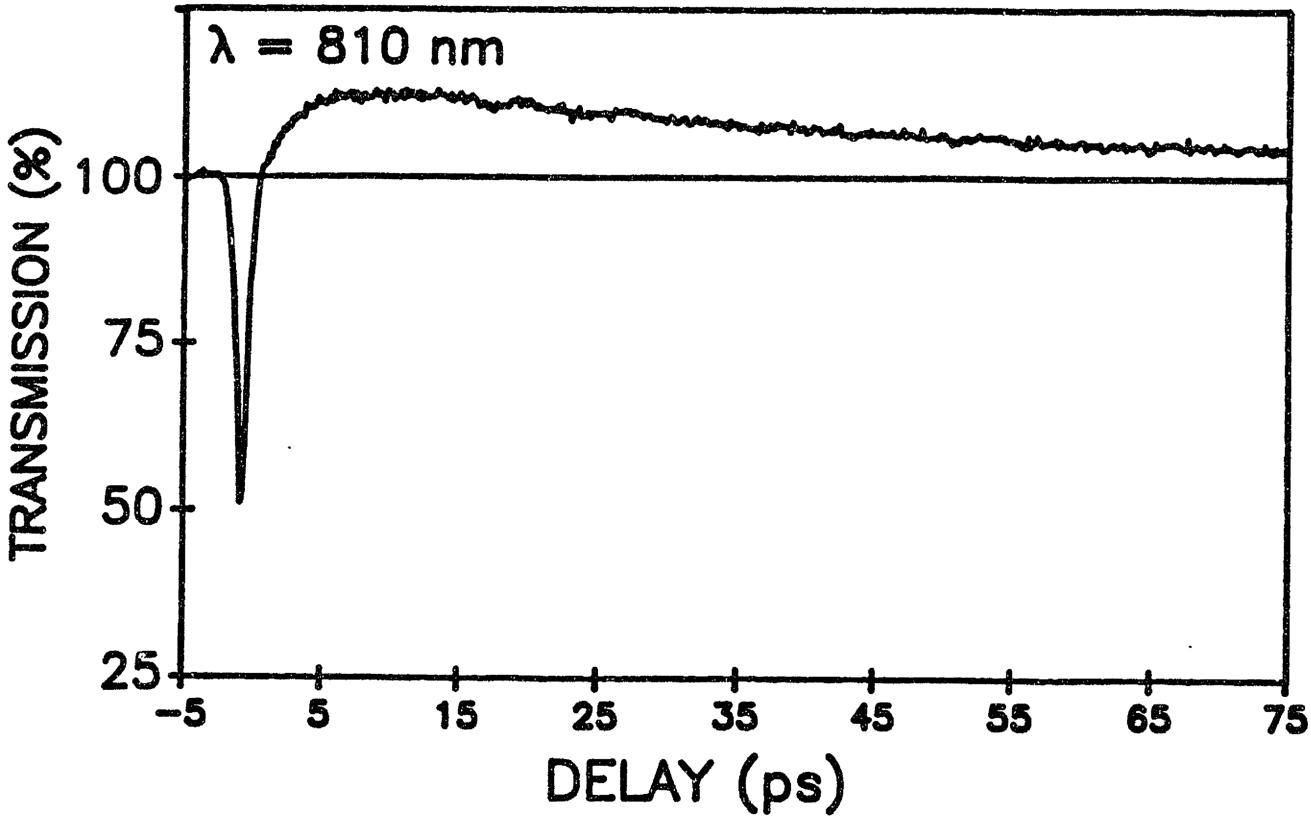

Figure 8.24. Probe transmission vs pump delay for I≈2GW/cm^2 at λ=810 nm.

absorption at these wavelengths. As the two-photon generated carriers cool to the lattice temperature and occupy the states at the bottom of the band, absorption saturation occurs due to state-filling.

8.6.b Discussion

In summary, this section details the wavelength dependence of the dynamics of the intensity dependent optical nonlinear processes near the band edge of AlGaAs. The measurements indicate the importance of the two-photon process which limits the output intensity and causes carrier generation that slows the turn off of the nonlinear phase change. The measurements provide an indication of the relative importance of two-photon absorption and linear absorption at the different wavelengths. Both two-photon absorption and linear absorption generate carriers. While two-photon processes are important both at 810 nm and 830 nm, the linear absorption is more significant at 810 nm. It is well known that although there is a resonant enhancement in n_2 at wavelengths near the band edge, the increasing linear loss degrades the figure of merit for switching devices. Our measurements also indicate that saturation of the signal intensity due to two-photon absorption processes limits the usefulness of the nonlinearity for optical switching. In addition, the carriers created by the absorption process limits the speeds at which the switching phenomena will be useful, and indicates the need to utilize device designs that can remove carriers for practical ultra-fast devices.

Section 8.7 Analysis

Several issues impact the switching properties of AlGaAs. Self-phase modulation coupled with dispersion causes significant pulse broadening at high peak pulse intensities. Linear loss and two-photon absorption affect the turn-off time due to carrier generation, the effective length of interaction and the insertion loss. The wavelength dependence of the various processes must be considered. The long-lived refractive index change due to carriers was not quantified in this thesis, but has been measured by other workers (Park et al.). This effect is also a function of wavelength below the band edge, and together with the measured values of n_2, β, and α found in this thesis, these known quantities allow the switching behavior of AlGaAs to be quantified theoretically. The results of these analyses are contained in this section.

Dispersion was not studied in depth in this thesis. Experimentally, pulse broadening was apparent at the output of the waveguide for all intensities. There was severe pulse broadening and pulse shape distortion at the high intensities. Not only does pulse spreading reduce the repetition rate at which a device can operate, but it reduces the peak intensity of the pulse, and ultimately the accumulated phase shift. At wavelengths around 815 nm, to keep pulse spreading through a 0.1 mm guide less than 30%, the operating intensity must be less than about 100 MW/cm^2. Theoretically, the wavelength dependent group velocity curve shown in Figure {8.15} indicates that the largest change in group velocity with wavelength, $\partial v_g/\partial\lambda$, occurs at shorter wavelengths and begins to decrease slightly at the longer wavelengths. For the wavelength range tested, there is not a significant difference in $\partial v_g/\partial\lambda$. Thus, for a given pulse bandwidth, the dispersion only very slowly drops off for the longer wavelengths. However, the pulse bandwidth does not remain constant. The self-phase modulation brought on by the intensity dependent refractive index causes pulse broadening. The broadening is related to the magnitude of the nonlinearity. Thus, as the wavelength approaches the band edge, and n_2 increases, the bandwidth of the pulses will increase. This would tend to cause more pulse broadening at the shorter wavelengths. As a result, dispersion would tend to favor switching at longer wavelengths with ultrafast pulses, <1 ps in duration. Longer pulses on the order of a few picoseconds would be less sensitive to the effects.

Walk-off due to group velocity mismatch for the two orthogonal modes is also an important consideration. We have measured the walk-off between pulses in the two modes to be about 200 fs in a 1 mm waveguide length. This limits waveguide lengths to be about 0.5 cm for pulses on the order of 1 ps.

One effect evident in the interferometry experiments was the long-lived phase change due to carrier generation. This effect may be approximately quantified theoretically. For a square optical pulse with duration τ, the carrier density, N, generated by two-photon processes is given by the expression:

$$N=\frac{\beta\, I^2\, \tau}{2h\omega} \tag{8.14}$$

when $\tau << 1/r$, for r the carrier recombination rate. In this expression, ω is the frequency of the light. For linear absorption the equation is:

$$N=\frac{\alpha\, I\, \tau}{h\omega} \quad . \tag{8.15}$$

For ultrafast switching the $\tau << 1/r$ condition will hold since $1/r \approx 10^{-9}$ s. The pulse width is taken to be $\tau = 500$ fs. A quantitative analysis of the effects of carriers can be performed using numbers determined from previous measurements of the band filling nonlinearity near resonance (Lee et al., Park et al.). For wavelength detunings from the band edge comparable to those investigated in this thesis, carrier-induced refractive index changes measured by Park et al. are roughly flat with wavelength. They are also approximately linear with carrier density. Using Park et al.'s data with a linear approximation, an expression for Δn, the refractive index change for a carrier density N, is given as:

$$\Delta n= 1.5 \times 10^{-20}\, N \tag{8.16}$$

For linear absorption, carrier generation increases linearly with intensity like the intensity dependent phase shift. The ratio of the ultrafast phase shift caused by n_2 to the phase shift due to carriers is independent of intensity. Using Equations {8.14} and {8.16} it is expressed:

$$\frac{\Delta\Phi_{n2}}{\Delta\Phi_{carrier}} = \frac{n_2}{\Delta n} = \frac{n_2\,(h\omega)}{1.5\text{X}10^{-20}\, \alpha\, \tau} \tag{8.17}$$

This expression is plotted as a function of wavelength in Figure {8.25}. The peak is at 840 nm, and has a value of close to 16. At 810 nm, the ratio has dropped to about 7 indicating that increased linear absorption causes more carrier generation as the wavelength approaches the band edge. For a ratio of ultrafast phase change to long-lived phase change of over 10:1, this calculation indicates the operating wavelength must be longer than 825 nm. The ratio will decrease again at longer wavelengths. A more detailed calculation would include the wavelength dependence of the carrier dependent refractive index change. This would be only a small correction for the wavelength range studied here.

Two-photon absorption generates carriers as the square of the input intensity. Requiring the ultrafast phase change to be larger than the two-photon generated carrier phase change produces a limitation on the operating intensity, I. This analysis ignores the intensity distribution along the waveguide length. For ultrafast phase changes 10 times greater than long-lived phase changes caused by two-photon-absorption-induced carriers, the expression found from Equations {8.15} and {8.16} is:

$$I > \frac{1}{10}\frac{n_2\,(2h\omega)}{1.5X10^{-20}\,\beta\,\tau} \qquad (8.18)$$

This expression for the limitation on I is plotted in Figure {8.26}. The larger n_2 at the short wavelengths reduces the intensity restriction. At 810 nm, intensities as high as 1 GW/cm^2 would cause fast phase changes over ten times greater than the long-lived phase change. This is because the ultrafast phase change at this wavelength is large, not because the long-lived phase change is small. It is important to note that other factors such as dispersion and absorption would ultimately limit the intensities at this wavelength. At 830 nm, the intensity limitation is 280 MW/cm^2, and at 850 nm it is less than 100 MW/cm^2. The low intensity restriction on these longer wavelengths indicates that waveguide devices are essential to accumulate the smaller phase shifts. Waveguide propagation is particularly

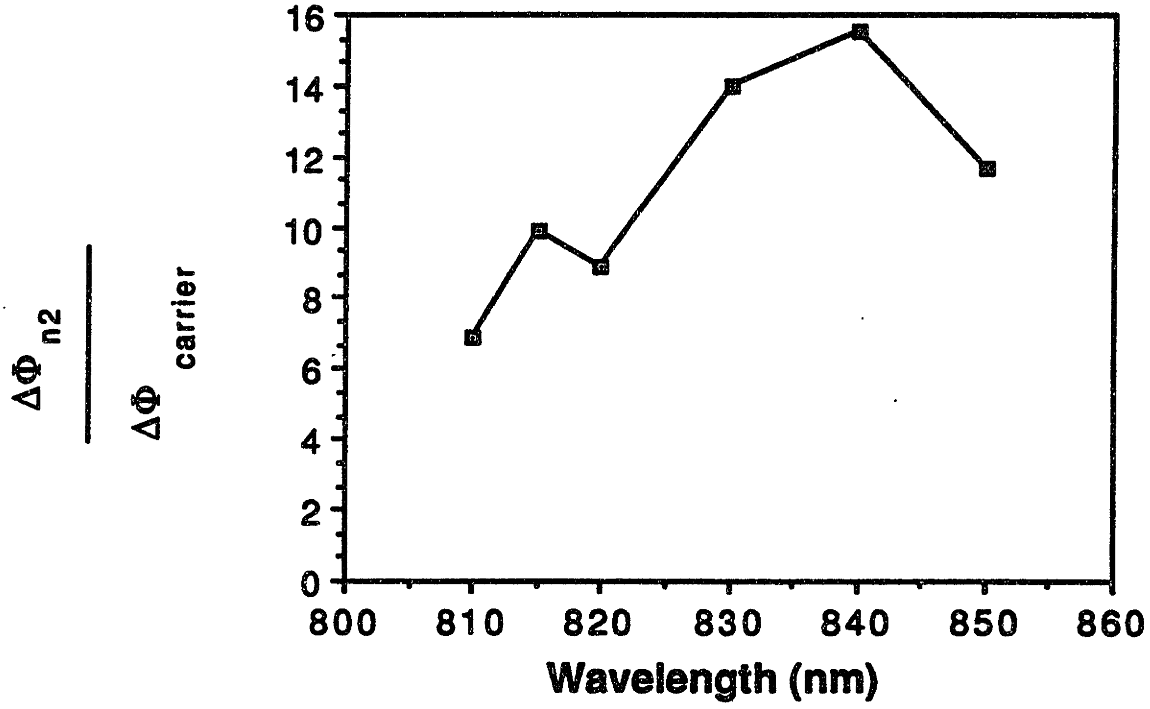

Figure 8.25. Theoretical ratio of the ultrafast nonlinear index of refraction to the long-lived, carrier-based index change vs wavelength. Theory considers only linear absorption processes.

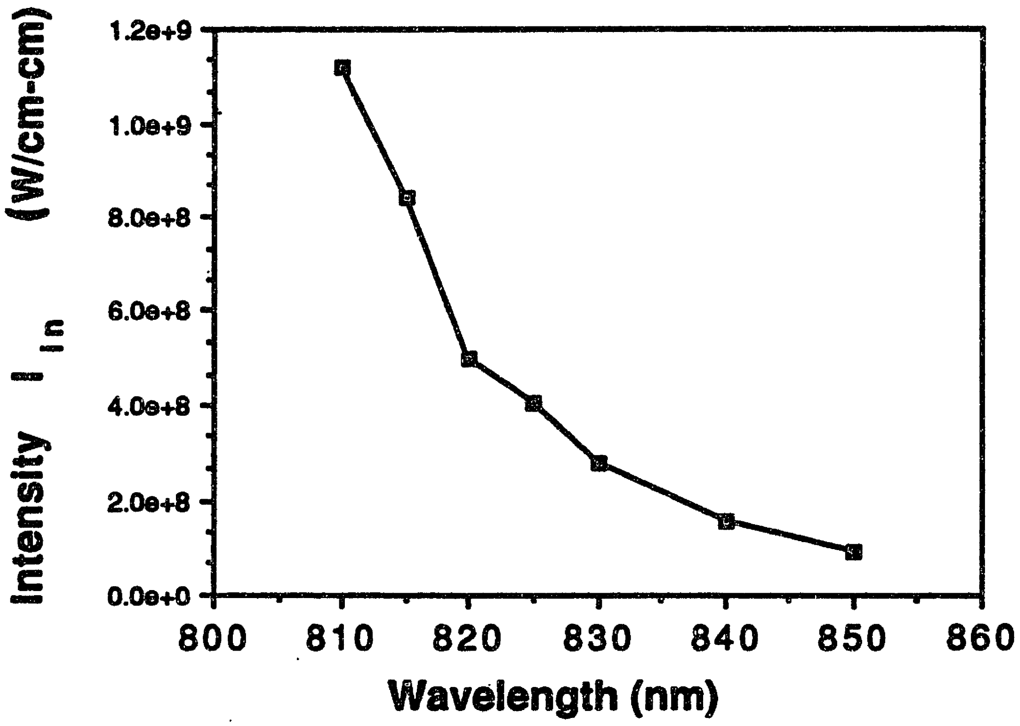

Figure 8.26. Wavelength dependence of the theoretical intensity limitation to produce ultrafast index changes ten times greater than the long-lived, carrier-based index changes created by two-photon absorption processes.

sensitive to amplitude changes due to both linear and nonlinear absorption process. These are discussed in the following paragraphs.

Loss caused by linear absorption has long been used to define a figure of merit in switching devices. The effective length of a waveguide of length l with loss α is:

$$l_{eff} = \frac{1-e^{-\alpha l}}{\alpha} . \qquad (8.19)$$

For large α, l_{eff} goes to zero, for small α, l_{eff} approaches l, and for long l, l_{eff} approaches $1/\alpha$. The accumulated phase shift in the absence of two-photon absorption is proportional to the product of n_2 and l_{eff}. Therefore the figure of merit:

$$FM_{la} = n_2/\alpha \qquad (8.20)$$

indicates the accumulated phase shift possible at the various wavelengths for large l. The figure of merit, using the values of n_2 and α measured in this thesis, is shown in Figure {8.27}. The figure of merit peaks near the 830-840 nm range. At shorter wavelengths linear loss becomes prohibitive, and at longer wavelengths the n_2 drops off.

Loss also results from two-photon absorption effects. In an analysis where spatial decay of the intensity along the guide length is not considered, the additional insertion loss due to the presence of two-photon absorption has the same linear dependence on intensity as the conjugate n_2 process. As a result, the amount of insertion loss for a given phase shift can be quantified by a figure of merit for two-photon effects:

$$FM_{tpa} = \frac{2}{\lambda} \frac{n_2}{\beta} \qquad (8.21)$$

FM_{tpa} indicates the phase shift in π radians that accompanies 1 cm^{-1} of induced absorption loss. A plot of FM_{tpa} as a function of wavelength is shown in Figure {8.28}. It nearly follows the functional form of n_2 because β is constant with wavelength. The large n_2 at shorter wavelengths provides for phase shifts of close to 5π for each 1 cm^{-1} of two-photon induced insertion loss. This value drops to less than 0.5π at 850 nm because of the drop in

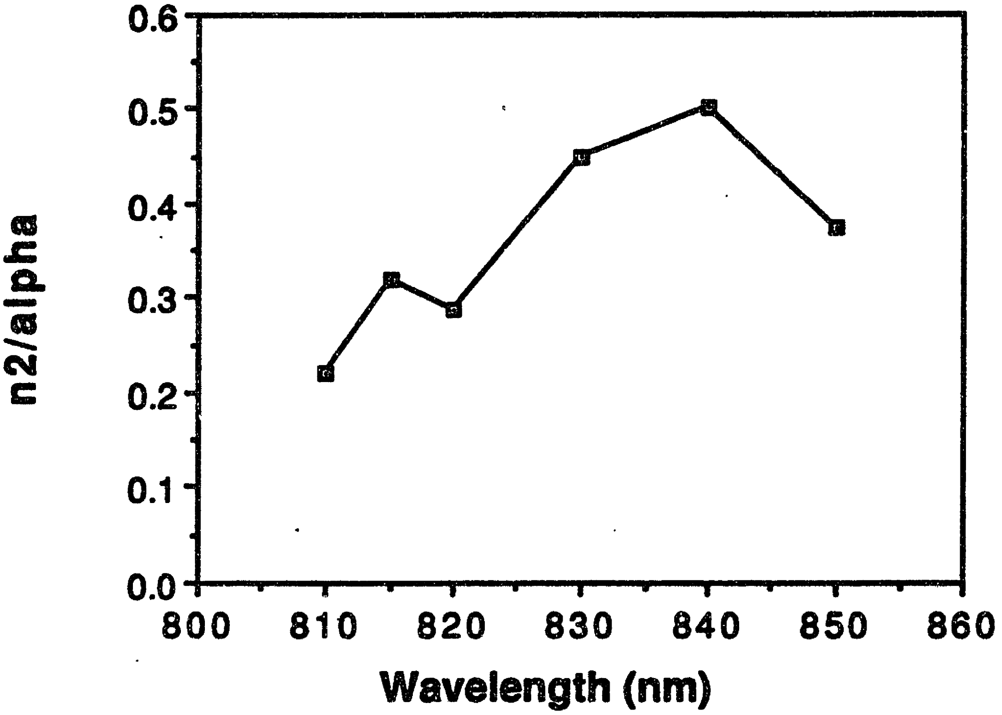

Figure 8.27. Figure of merit considering linear absorption processes, FM_{la}, vs wavelength.

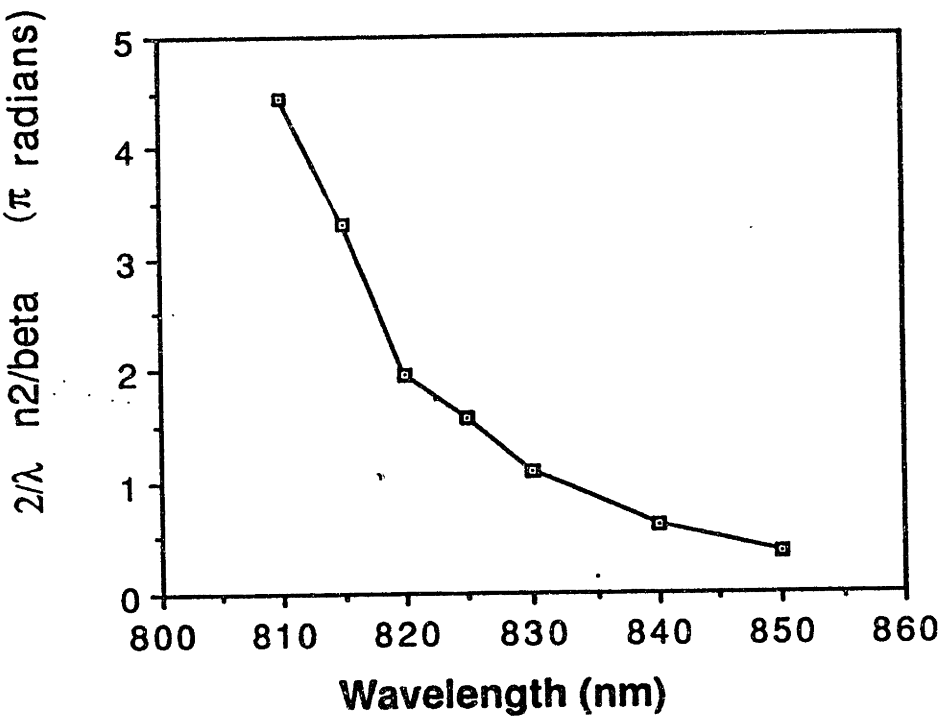

Figure 8.28. Figure of merit considering two-photon absorption processes, FM_{tpa}, vs wavelength.

n_2. At 830 nm, an accumulation of just over π results in 1 cm^{-1} of insertion loss. These results indicate that, for wavelengths close to the band edge, the insertion loss due to two-photon absorption does not prohibit phase shifts of over π, however, the induced absorption limitation becomes more significant at the longer wavelengths. The above analysis of insertion loss may be summarized as follows. Linear insertion loss, which occurs independent of intensity, tends to favor device operation at longer wavelengths, particularly for long devices. The best operating wavelength considering only linear insertion loss is at 830 nm. In contrast, two-photon absorption insertion loss, which is intensity dependent, favors operation at short wavelengths. This is because lower intensities may be used to obtain large phase shifts.

The effects of two-photon absorption in the waveguide geometry can be determined by looking at the expression for the intensity distribution along the length of the waveguide, I(z), Equation {8.10}. The accumulated phase shift in a waveguide is obtained by combining the expression for the phase shift:

$$\Phi = \frac{2\pi}{\lambda} n_2 \int_0^l I(z)\, dz \qquad (8.22)$$

with Equation {8.10} to obtain:

$$\Phi = \frac{2\pi}{\lambda} n_2 \frac{1}{\beta} \ln\left\{1 + \frac{\beta}{\alpha} I_{in} \left[1 - e^{-\alpha l}\right]\right\} \qquad (8.23)$$

where I_{in} is the input intensity after coupling. Equation {8.23} approaches the expression for linear loss alone in the limit of small β or I_{in}. A plot of this expression as a function of I_{in} is shown in Figure {8.29}. The plot includes curves for 810 nm, 830 nm, and 850 nm each for two guide lengths of 0.5 cm and 0.1 cm. Two operating regimes are apparent: a low intensity limit where linear absorption is the dominant effect, and a high intensity limit where two-photon absorption is significant. The low intensity region is shown in more detail in the expanded view of Figure {8.29.b}. The accumulated phase shift in this intensity regime is well predicted by the figure of merit, F given by Equation {8.20}. The

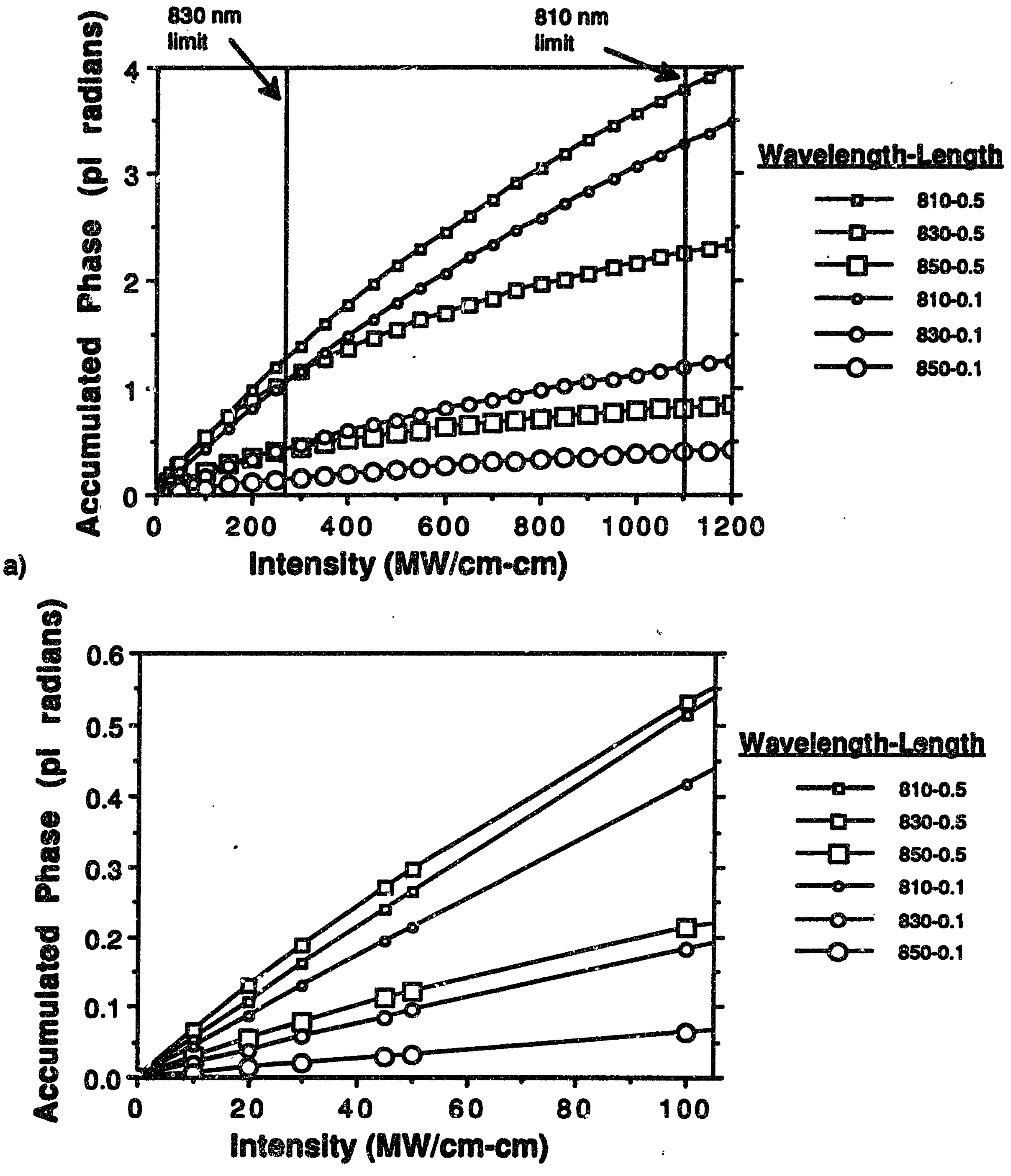

Figure 8.29. Accumulated phase shift vs input intensity through a waveguide considering both linear and two-photon absorption processes. Curves are shown for 810 nm, 830 nm, and 850 nm, for waveguide lengths of 0.1 cm and 0.5 cm as indicated on the figure. a) for an intensity range from 0 to 1.2 GW/cm^2, and b) for an intensity range from 0 to 100 MW/cm^2.

largest phase shifts are accumulated for 830 nm, followed by 810 nm and 850 nm. The maximum accumulated phase shift for the 0.5 cm long guide at 830 nm with I ≈100 MW/cm^2 is 0.55π.

The high intensity limit follows the results expected from the figure of merit FM_{tpa} defined in Equation {8.21}. For the high intensities, the largest phase shifts are accumulated at λ=810 nm and the smallest at 850 nm. This is a result of the fact that two-photon absorption causes a dramatic drop in the intensity during the first section of the guide, which significantly reduces the length of interaction. Since the two-photon absorption coefficient is the same at all wavelengths, the effective length of the guide when two-photon absorption is dominant would be the same at all wavelengths. Since a wavelength of 810 nm has the largest n_2, the accumulated phase will be largest for this wavelength in the high intensity limit.

Two other factors must be considered when interpreting these results. First, the previous analysis of carrier effects provides a theoretical limitation on the intensities that can be used so that residual carriers do not degrade device performance. These intensities for 830 nm and 810 nm are indicated on the graph of Figure {8.29}. For 830 nm, this restriction limits the highest accumulated phase shift to about π. At 810 nm the intensity restriction allows up to about 4π of accumulated phase shift. The other important factor is dispersion. Previous analysis indicates dispersion limits peak intensities to around 100 MW/cm^2 for wavelengths near 810 nm. With this intensity restriction, the phase change accumulated at 810 nm is about π. The results can be summarized as follows: for low intensities <100 MW/cm^2 the optimum operating wavelength is 830 nm, and phase shifts of ≈0.6π can be anticipated from 0.5 cm long devices; for higher intensities the optimal operating wavelength is 810 nm, however high intensity operation will likely be limited by pulse spreading, and accumulated phase shifts of no more than π may be obtained to allow short pulses, 500 fs in duration, to propagate without significant pulse spreading.

One other consideration for switching is the intensity output of the waveguide device. This is particularly important for serial operation of devices. The expression for the output intensity in a waveguide under the influence of two-photon absorption, Equation {8.10}, indicates a limit on the output intensity from the guide, independent of the input intensity. This limitation is given by the expression:

$$I_{lim} = \frac{\alpha}{\beta} \frac{1}{e^{\alpha l} - 1} \qquad (8.24)$$

This is plotted for each wavelength for two guide lengths, 0.5 cm, and 0.1 cm, in Figure {8.30}. The results indicate a drawback to operating a long device at the shorter wavelengths and in the high intensity limits. The output intensity from a 0.5 cm long waveguide at λ=810 nm will be less than 1 MW/cm^2, which eliminates the hope for driving a second device. The restriction is less prohibitive for shorter devices, 0.1 cm long.

Section 8.8 Conclusions

In summary, the experiments and analysis in this chapter provide important insight into the switching behavior of AlGaAs. The results indicate for low intensities linear absorption is dominant and the largest phase shifts in a waveguide geometry would be at 830 nm. In contrast, for high intensities, two-photon absorption dominates, which severely limits the length of interaction in the waveguide, and the optimum operation is at 810 nm. Two-photon induced absorption loss is a significant factor that reduces the potential output intensity for driving another switching element, and eliminates the possibility of operating with long devices at short wavelengths, but does not restrict the operating wavelength for short devices ≈0.1 cm long. To keep the ratio of the ultrafast phase change to the long-lived phase change due to carriers generated by linear absorption better than 10:1, the wavelengths must be longer than 825 nm. Carrier generation due to two-photon absorption limits the operating intensity so the ratio of the ultrafast phase change to the long-lived phase change is large. For a ratio of 10:1 at 850 nm the intensity

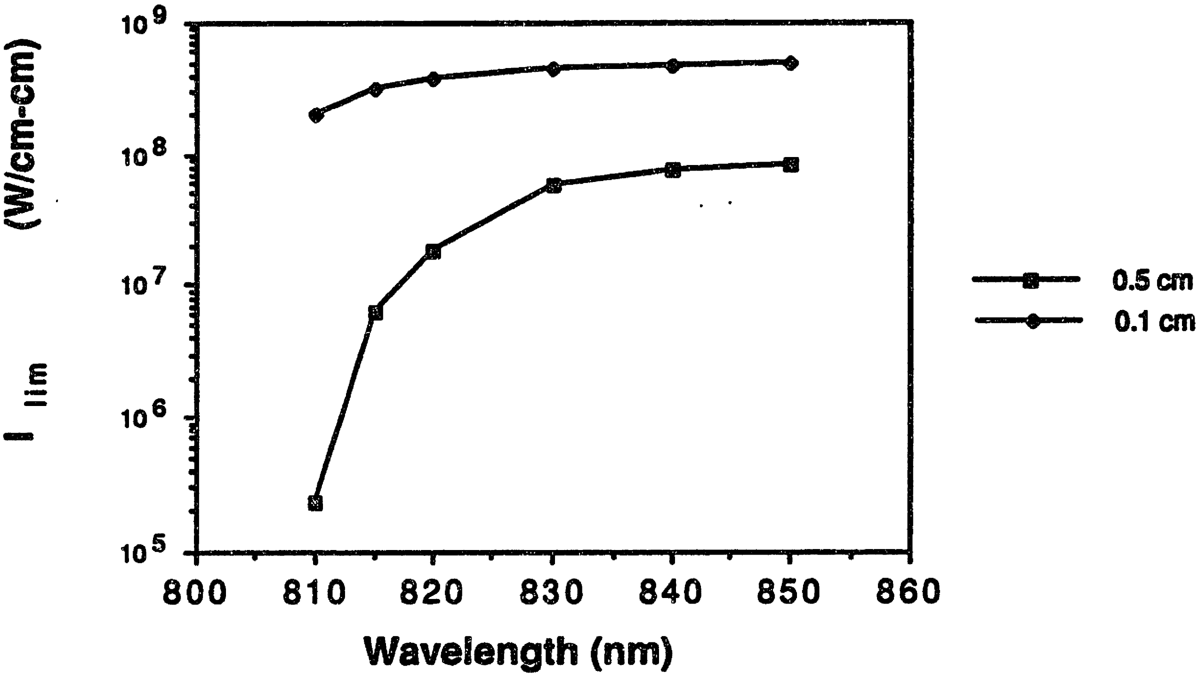

Figure 8.30. Output intensity limit, I_{lim}, vs wavelength for waveguide lengths of 0.5 cm and 0.1 cm.

limit is 100 MW/cm^2, and for 810 nm the limit is 1 GW/cm^2. The other limitation of intensity arises from pulse spreading due to dispersion. Experimentally, this limit was determined to be on the order of 100 MW/cm^2 at 810 nm. With these intensity limitations, the best operating wavelength for a subpicosecond switch is 830 nm. In a 0.5 cm long device, the accumulated phase shift is approximately 0.6π. The results indicate that ultra-fast all-optical directional couplers could not be readily achieved in devices based on bulk AlGaAs semiconductor materials, because phase accumulations of multiple π are needed for these devices (Jensen). However, these results do not preclude the possibility of slower devices being realized, as the magnitude of the band filling nonlinearity can be quite large, and the intensity restrictions due to pulse spreading and carrier generation would not be as severe.

Chapter 9

DISORDERED QUANTUM WELL WAVEGUIDE CHARACTERIZATION

Section 9.1 Background

The study of multiple quantum well materials is motivated by the fact that the well resolved exciton resonances that form the absorption edge can lead to an enhancement of the nonlinearities (Chemla and Miller). While the enhancement on resonance has been verified (Miller et al. 1982), off-resonance comparisons of the nonlinearities in bulk and multiple quantum well materials indicate there is no enhancement (Ovadia et al., and Lee et al., b.). Because the work presented in this thesis provides the first measurement that resolves both fast and slow components of the nonlinearities, the off-resonance behavior the two systems can be readily compared.

Measurements in the multiple quantum well materials are complicated by the anisotropy of the system. Selection rules in the quantum wells prohibit heavy-hole to conduction-band transitions for light polarized perpendicular to the layer plane (Chemla). The anisotropy has been shown in absorption measurements in quantum well waveguides (Weiner et al.). The absorption anisotropy implies anisotropic refractive index in the quantum wells through the Kramers-Kronig relationship. With the lack of heavy hole absorption, the band edge is at a higher frequency which implies a reduction in the refractive index for the perpendicularly polarized light. This in turn implies a different waveguide mode shape. The perpendicular polarization, referred to here as TM, is less well confined than TE. The anisotropic mode size is a small correction. However, anisotropic group velocity is more dramatic, as measurements in this section indicate. The walk-off caused by different group velocities for the two polarizations effectively reduces the interaction length between pump and probe and reduces the accumulated phase shift. Another factor due to anisotropy is the wavelength detuning from the band edge. Any detuning $\Delta\lambda$ from the band edge for the TE polarized wave is a larger detuning for the TM wave. Specifically, the TM wave is at a detuning of $\Delta\lambda + \Delta\lambda_{hh\text{-}lh}$, where $\Delta\lambda_{hh\text{-}lh}$ is the wavelength difference between the heavy hole to conduction band and the light hole to conduction band transitions. This complicates interpretation of "resonant" enhancement. However, the anisotropy is a natural consequence of the layer structure, and as such it will be encountered in any quantum well system. The effect of the anisotropy will vary as the quantum well and barrier thicknesses are changed, so that each measurement will be sensitive to the exact layer structure. In a careful quantitative study of the quantum well system, these effects would have to be carefully considered. The purpose of the measurements presented here is to provide a qualitative look at the quantum well system, and particularly the use of compositionally disordered waveguides as switching elements.

Measurements were made on an ETBD fabricated waveguide. The waveguide used has a small ridge and also has partially intermixed multiple quantum wells in the waveguide core due to a rapid thermal annealing process after fabrication. This is described in Sections {5.2} and {6.4}, These waveguides were fabricated with N^+ bombardment. Unfortunately, though the guides appeared to be fairly low loss, loss measurements could not be performed because only 1-mm-long guides were available. The normal-incidence transmission measurements on the quantum well regions indicate the band edge is at 840 nm. The light is necessarily polarized in the plane of the quantum well layers. Also, exciton peaks are still resolved at room temperature. Therefore, though there is some aluminum present in the quantum well layers, the quantum wells still behave as a 2-dimensional system.

A second set of measurements was attempted on ETBD fabricated waveguides described in Section {7.4}. However, the band edge of these guides was higher because the quantum wells were not partially intermixed. This required changing the dye in the laser to Styrl 13, so that it would tune to longer wavelengths. Because of this change, the peak intensity available dropped by over a factor of 20. Additionally, the coupling into the guides was reduced by a factor of 5. The resulting drop in power did not provide enough signal to measure the behavior of this guide, so the measurements were performed on the waveguide with the partially intermixed quantum well layer.

The measurements on these waveguides indicate the switching behavior of the quantum well system is very similar to the bulk material. The nonlinearity appears larger in the quantum well than in bulk, but not significantly. Measurements of nonlinear phase shift and nonlinear absorption as well as group velocity mismatch are presented in the following section.

Section 9.2 Experiment

The measurement procedures for the various measurements are the same as those described in Section {8.3}. The measurements presented here include group velocity dispersion for the two polarizations, nonlinear phase shift and nonlinear absorption at frequencies close to the band edge.

9.2.a Group Velocity and Walk-off

The group velocity dispersion curve is shown in Figure {9.1}. There is a marked group velocity difference for the two polarizations. The difference gets larger as the wavelength gets closer to the band edge. This is expected because the anisotropic wavelength dependence of the refractive index for the two polarizations is most dramatic near the band edge. Over 1 mm, the time delay between the pump and probe is nearly 0.5 ps at the short wavelengths, and about 0.2 ps at the longer wavelengths. Thus at short wavelengths, the pump and probe are no longer overlapped at the output of the guide. This has the negative effect of limiting the interaction length of the waveguide, but the positive effect of causing the pump and probe to sweep through one another which averages out coherence effects and also sweeps the pump-induced phase shift over the entire probe pulse so that the phase shift occurs across the pulse. If this were not the case, the portion of the

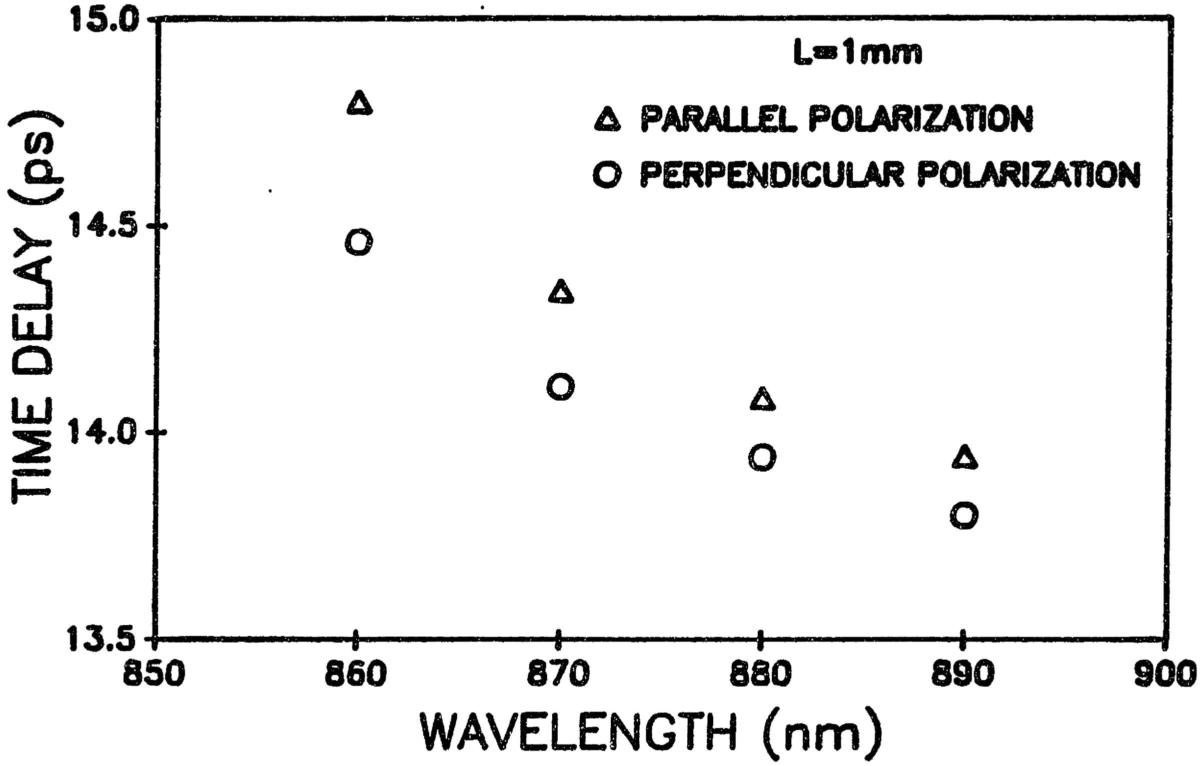

Figure 9.1. Time delay between primary and echo pulse after 1 pass through the 1-mm-long multiple quantum well waveguide. Δ -- polarization parallel to the quantum well layers, O -- polarization perpendicular to the quantum well layers.

probe which senses the tails of the pump pulse has a smaller phase shift than the portion which senses the peak. The measured phase shift is the integral of the phase shift at each point on the probe pulse. If, for example, at the zero-delay, if the peak of the probe pulse experiences a 2π phase shift, the half-power points of the pulse will experience a π phase shift because the pump intensity is down by a factor of 2. The wings of the pulse will begin to subtract from the measured phase shifts, reducing the signal. The effect is minimized with the walk-off due to group velocity mismatch, because at some point in the guide the trailing wings of the probe will see the peak of the pump. The effect is complicated by the reduction in amplitude of the pump and probe due to both linear and two-photon absorption, and therefore is difficult to quantify. Because of this, as well as some other factors discussed below, n_2 in the quantum well was not quantified, but interesting qualitative results were obtained, as described below.

9.2.b Nonlinear Phase

For the nonlinear phase measurements, the probe was polarized perpendicular to the quantum wells, and the pump was polarized parallel to the layers. The pulse duration was about 0.8 ps, almost twice as long as the pulse durations used for the measurements on AlGaAs described in chapter 8. This reduces the peak intensity. Another reduction in the peak intensity results from the waveguide core in the quantum well waveguide being 3 times bigger than the AlGaAs waveguide core. However, some of this loss in peak intensity is made up for by increased coupling efficiency into the larger guide. For the measurements the peak intensity was approximately 500 MW/ cm^2. This value is less certain than in the AlGaAs measurement because the loss coefficient in the quantum well waveguides was not known.

The interferometer output for the quantum well waveguide at a wavelength of 860 nm is shown in Figure {9.2}. This is a 20 nm wavelength detuning from the heavy-hole-to-conduction-band transition and is comparable to AlGaAs measurements at 810 nm. The

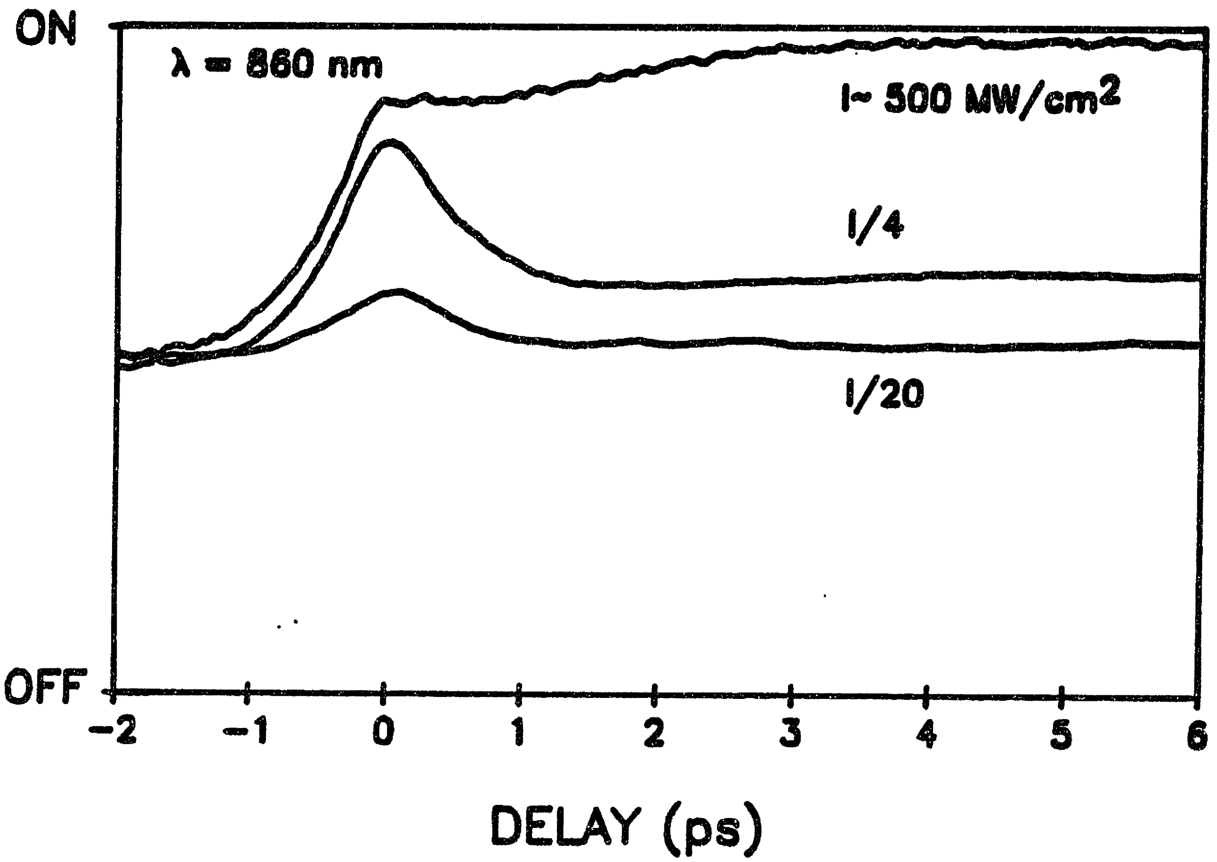

Figure 9.2. Interferometer output for the multiple quantum well waveguide. λ= 860 nm for pump intensities of 500 MW/cm^2, 125 MW/cm^2, and 25 MW/cm^2.

figure illustrates that the behavior is similar to the AlGaAs, particularly at the long positive time delays. The full intensity case, this time with the interferometer biased at the minimum of the cycle, is shown with a long positive time delay in Figure {9.3}. The large signal at the zero-delay does not show the dip in the signal at the zero-delay evident in the AlGaAs measurements at 810 nm. This is true even though the two-photon absorption signal is nearly the same in both systems. This would indicate that the dip in the AlGaAs signal is due to the pulse shape dependence of the phase signal that is reduced for the quantum well system because of walk-off. The long lived response rises in 3 ps and recovers in about 80 ps. Therefore, the rise time is similar in the bulk and quantum well systems. Although the quantum well waveguide is thicker than the corresponding AlGaAs waveguide, there is enhanced carrier recombination in the waveguide cladding due to the residual damage in the intermixed regions that speeds up the recovery of the quantum well. This offers a possible explanation why the recovery times are similar in the bulk and quantum well systems. It is quite possible that the diffusion in the quantum well is dominated by lateral diffusion because the quantum well restricts motion perpendicular to the layer plane. The interferometer signal at 870 nm, slightly further from the band edge is shown in Figure {9.4}. The peak intensity here is also ≈500 MW/cm^2. This measured signal is smaller, as expected because the the detuning is larger.

9.2.c Nonlinear Absorption

The transmission measurements for this system are very interesting, although the interpretation of the results is still unclear. The pump-probe at λ=860 nm is shown in Figure {9.5}, with pump intensities of 500 MW/cm^2 and 125 MW/cm^2. In addition to the two-photon induced absorption at the zero delay, there is a significant induced absorption at the long positive time delays. The long time behavior of the signal for the peak intensity is shown in Figure {9.6}. The induced absorption rises on the 3 ps time scale and turns off in approximately 80 ps. Thus the free-carriers created by two-photon absorption processes

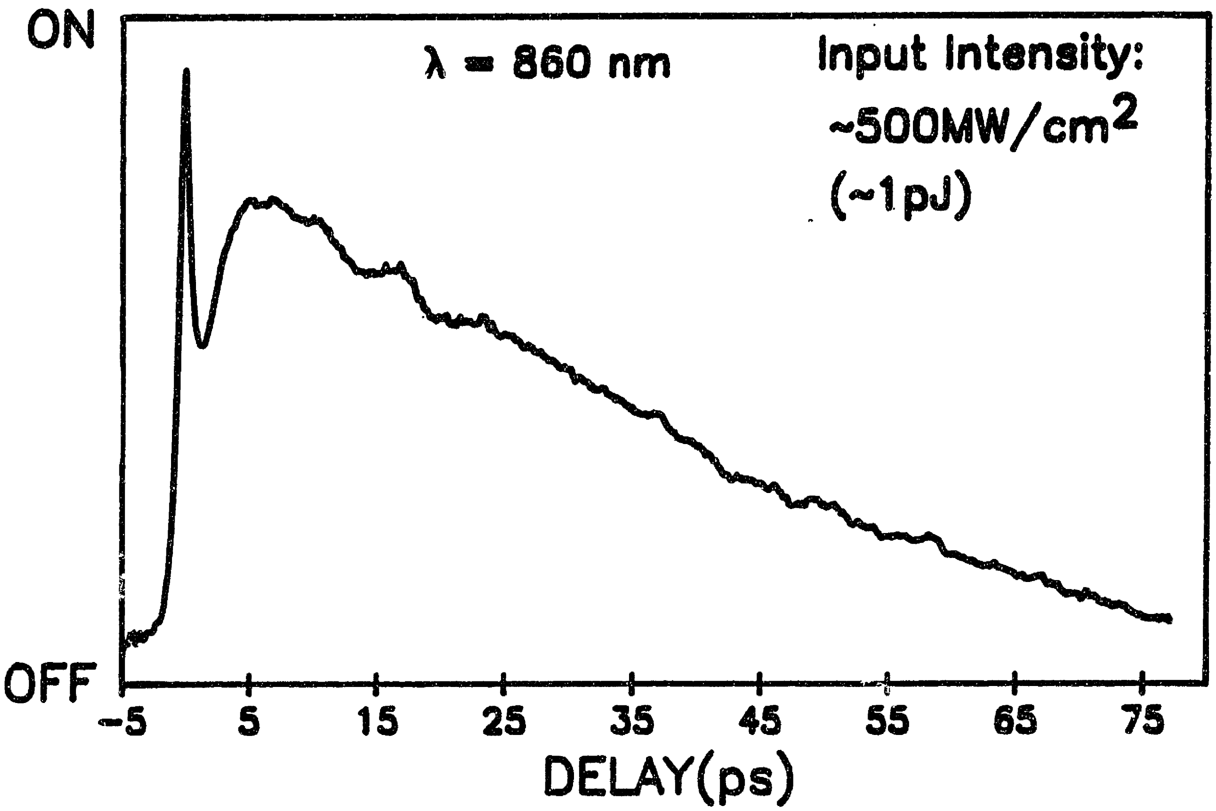

Figure 9.3. Interferometer output for the multiple quantum well waveguide with a pump intensity of 500 MW/cm^2. Bias is from the OFF state.

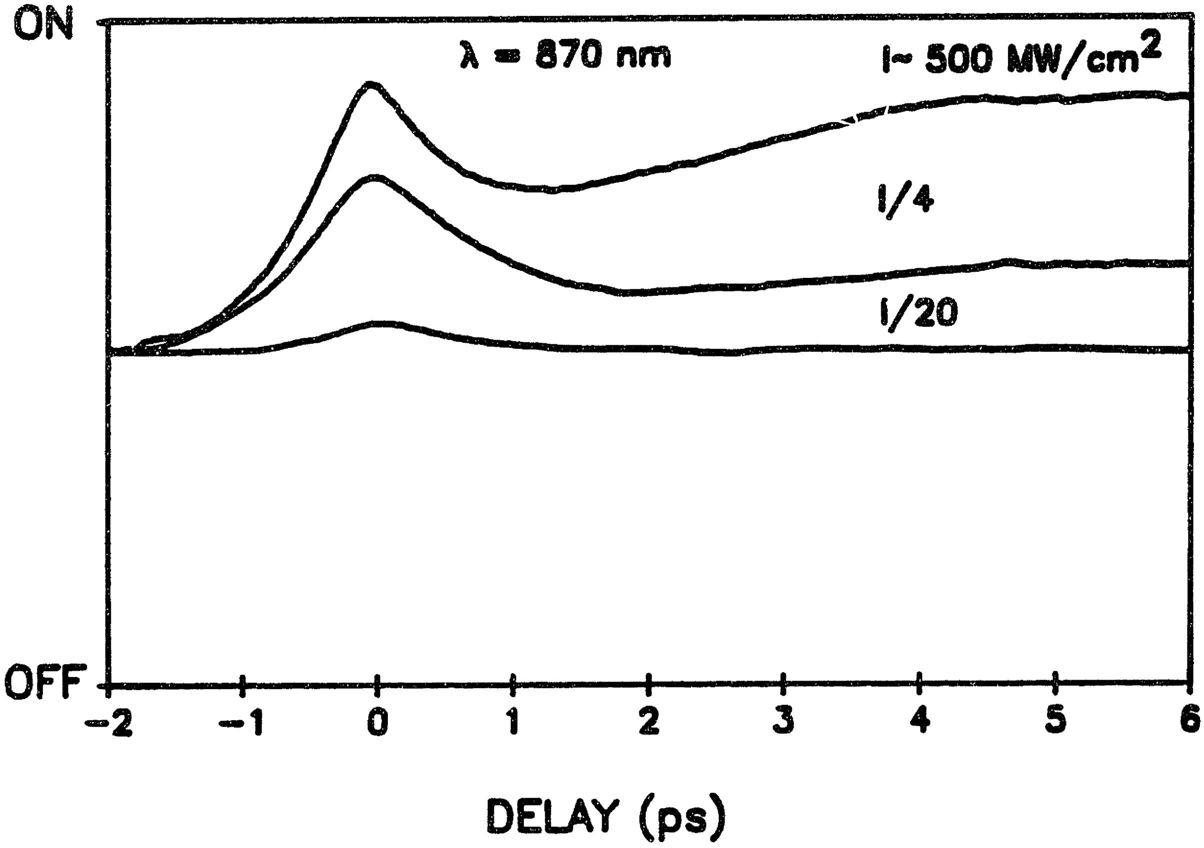

Figure 9.4. Interferometer output for the multiple quantum well waveguide. $\lambda = 870$ nm for pump intensities of 500 MW/cm^2, 125 MW/cm^2, and 25 MW/cm^2.

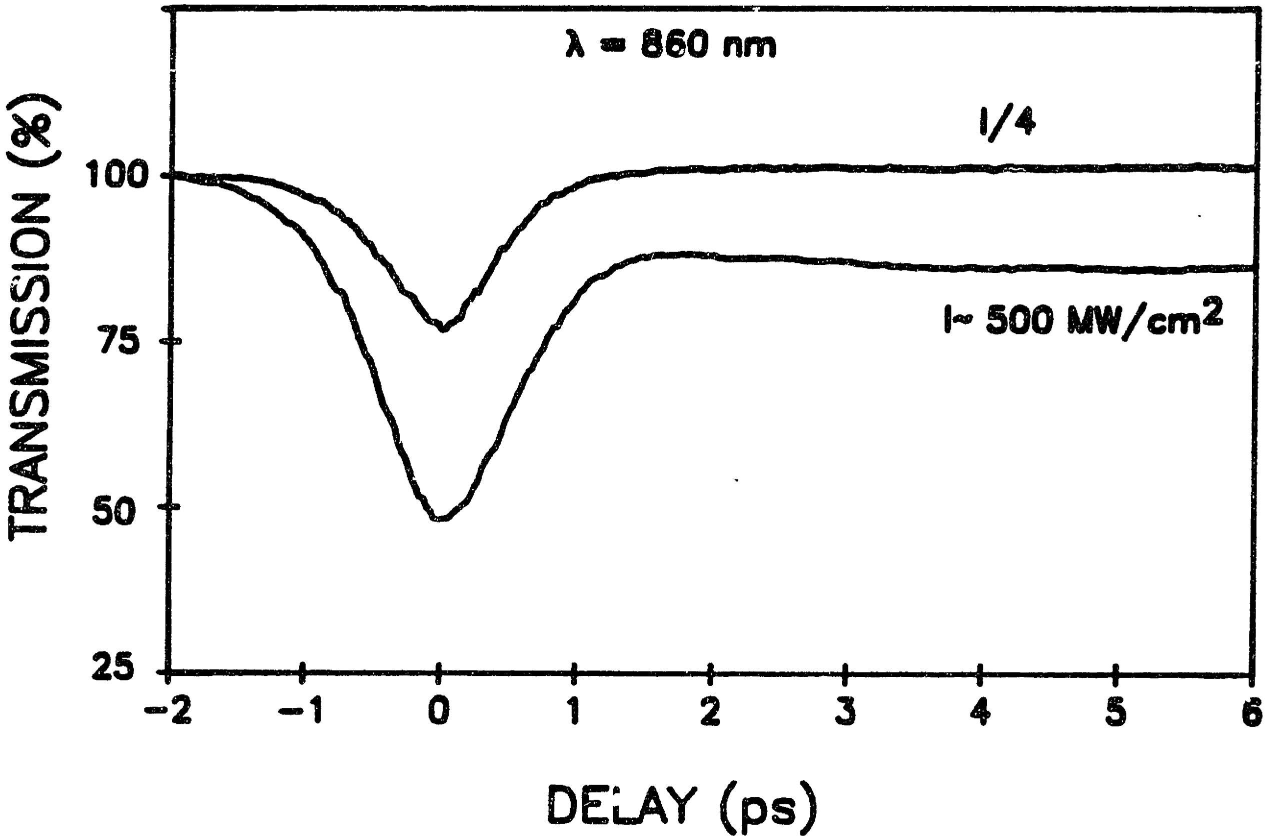

Figure 9.5. Probe transmission vs pump delay for increasing pump intensity in the multiple quantum well waveguide at λ=860 nm.

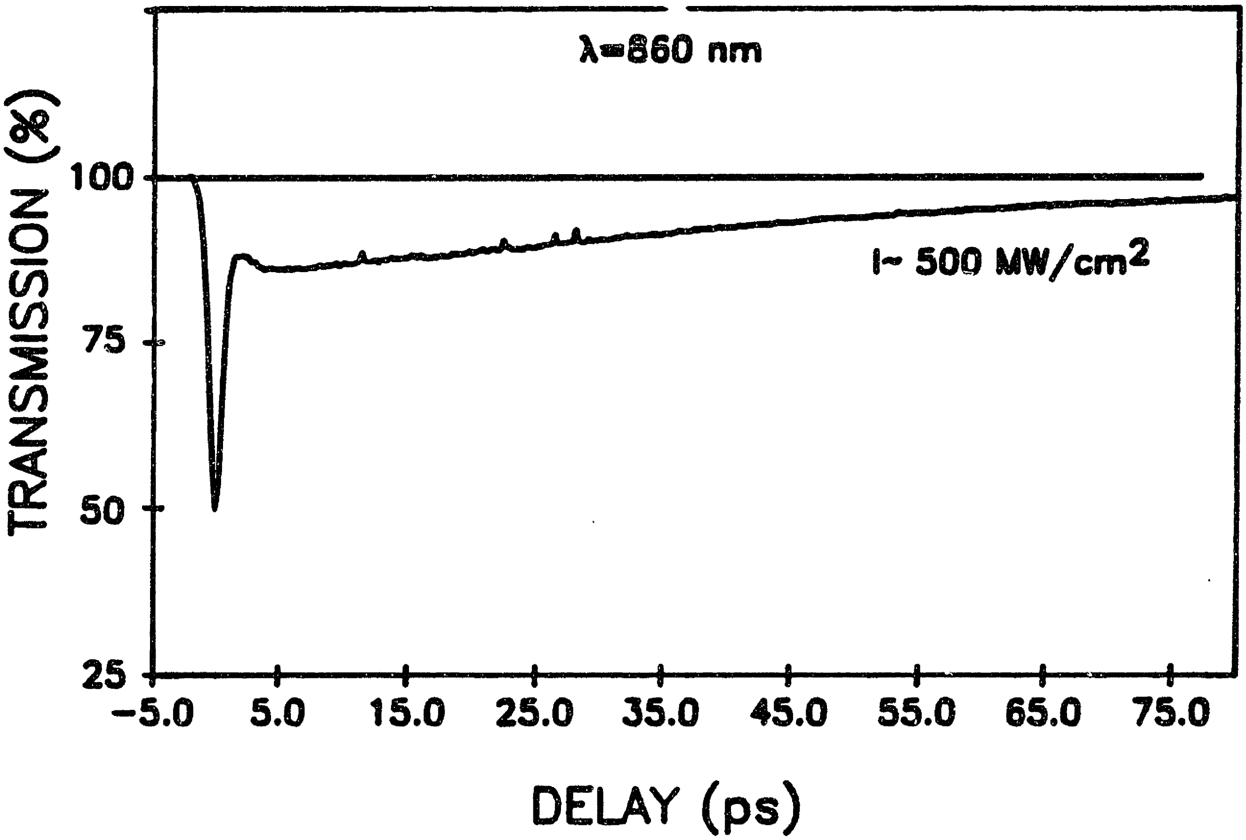

Figure 9.6. Probe transmission vs pump delay for I≈ 500 MW/cm^2 at λ=860 nm.

cause induced absorption. This could be due to band-gap renormalization that shrinks the band gap and increases absorption. The pump-probe at 870 nm, shown in Figure {9.7}, exhibits different behavior. At 870 nm, the two-photon induced absorption is followed by absorption saturation. The long time response of this signal, shown in Figure {9.8}, turns off on the 80 ps time scale of the long time response at 860 nm. The 870 nm measurement is very similar to the bulk measurement, and may be explained by two-photon absorption creating carriers that fill states and cause absorption saturation.

9.2.d Discussion

One interesting question is why the behavior at 860 nm differs from that at 870 nm, and also why the measurements in bulk material at 810 nm do not show similar behavior. The answer may lie in the band gap renormalization process. Band gap renormalization is caused by free carriers, and is therefore a many-body effect. However it may be interpreted as follows (Haug and Schmitt-Rink). Free-carriers gain some energy by avoiding each other, so that as more carriers are created the energy of the lowest lying energy state decreases. Thus the energy band gap for free carriers is reduced as free carriers are created. Excitons, whose allowed energy levels lie below the band edge of the free carriers, are neutral particles and so do not feel the effect of band gap renormalization. It is likely that band gap renormalization effects overcome the absorption saturation closer to the band edge, where the effects would be the largest, and the band filling dominates at the longer wavelengths. The reason why the effect was not seen at 810 nm in bulk could be that the band tails were larger and more gradual in this material so that the induced absorption due to renormalization was not as dramatic. It is also important to point out that the sign of the long lived nonlinearity is not consistent with a red shift of the band edge. More measurements will be needed to better understand the effect.

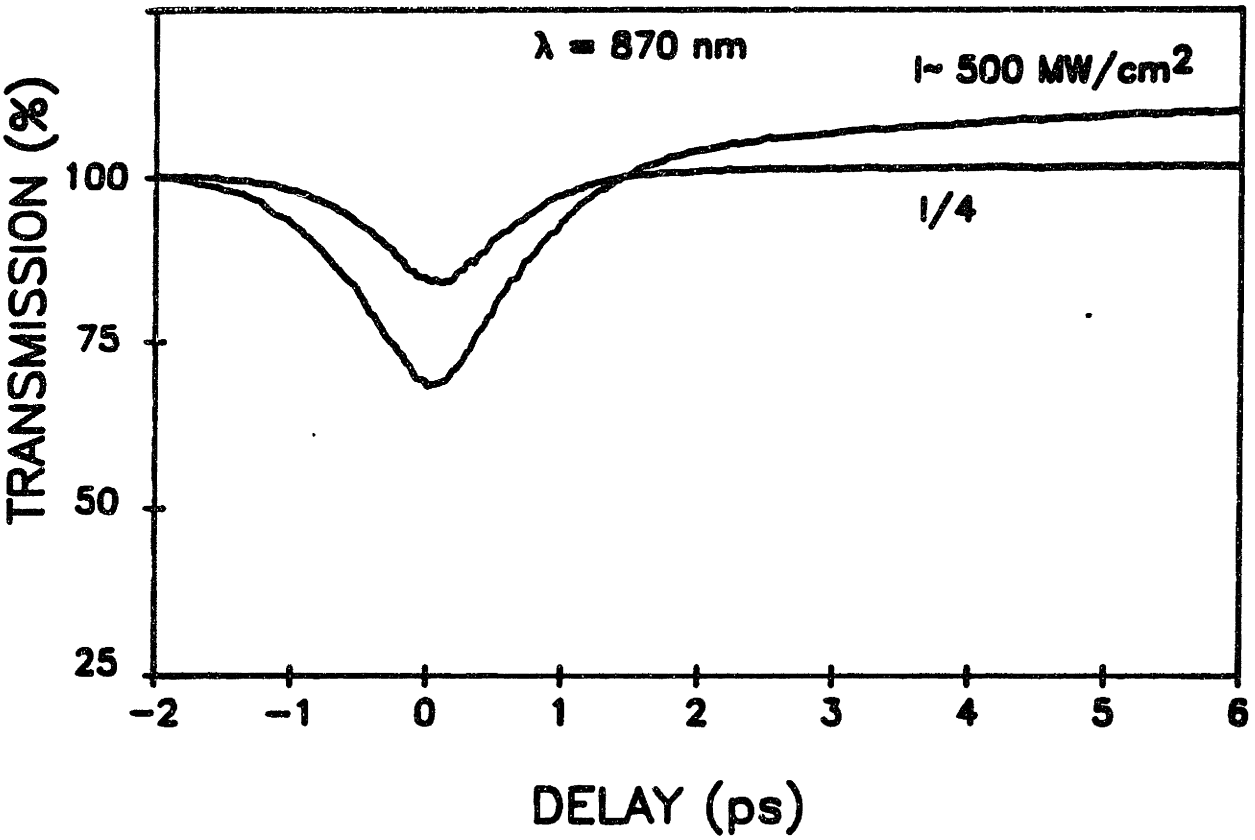

Figure 9.7. Probe transmission vs pump delay for increasing pump intensity in the multiple quantum well waveguide at λ=870 nm.

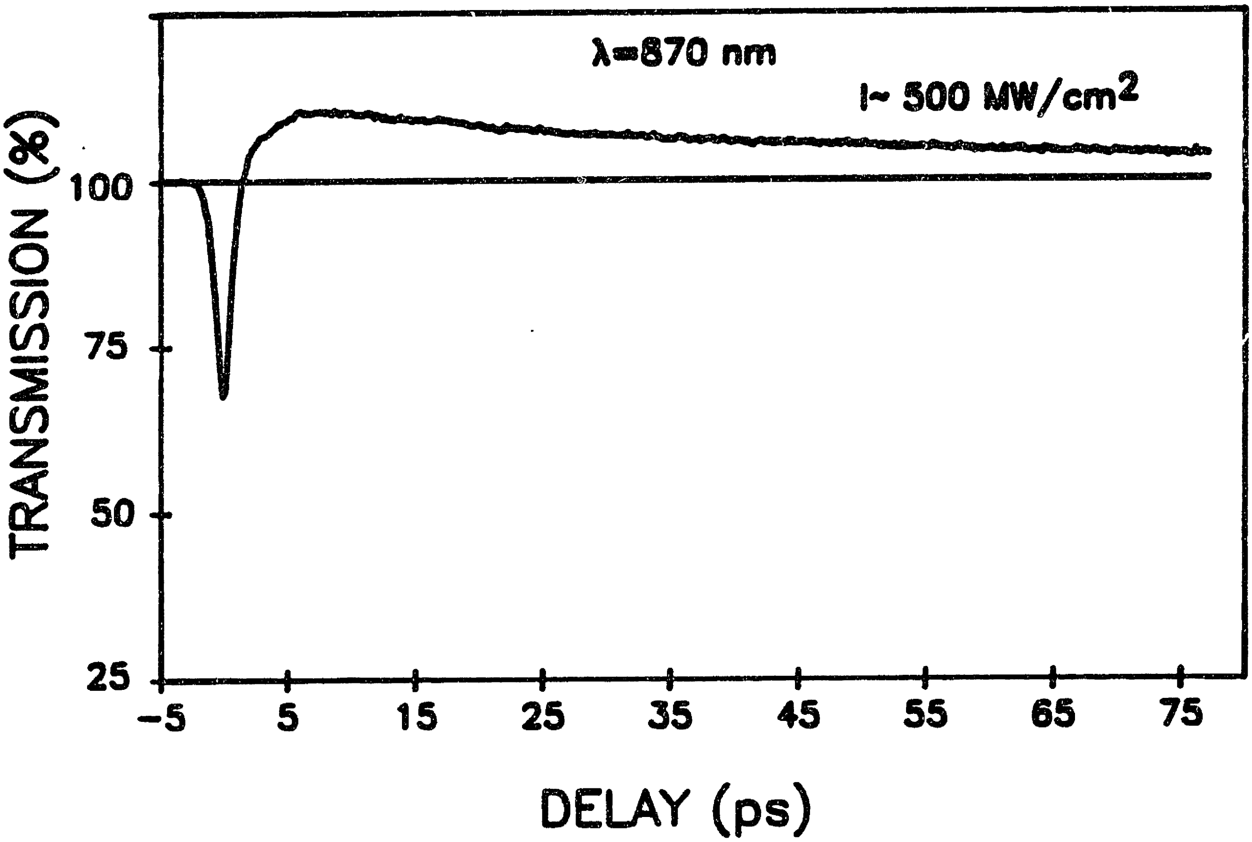

Figure 9.8. Probe transmission vs pump delay fot I= 500 MW/cm^2 at λ=870 nm.

Section 9.3 Conclusions

The quantum well measurements provide some insight into the mechanisms that affect the nonlinearities below the band gap in these materials. The results indicate that the multiple quantum wells behave qualitatively the same as bulk materials. The magnitude of the nonlinearity appears to be within a factor of 5 of the signal for the bulk which indicates there is no significant enhancement for the quantum wells. The relative signal from the ultrafast phase change and the long-lived phase signal show that two-photon absorption will cause the same limitations on optical switching in both materials, however the integrity of the signal at the zero delay indicates that increased walk-off, while reducing the interaction length can improve the signal for pulses with finite width.

The anisotropy of the system leads to other configurations that should be explored. The pump perpendicular to the layers and the probe parallel to the layers would probably show a different response. In this case the probe is closer to the band edge and the pump is further away. Also, parallel pulse polarizations would be interesting to test. In this case the oscillator strengths would be similar for both pump and probe. These various configurations will probably not produce enhancements of more than a factor of 10, because the anisotropy is less than 10 nm.

Chapter 10

CONCLUSIONS

Several important conclusions can be drawn from the work presented in this thesis. One very early conclusion was that strain presents problems in SiO_2/Si_3N_4 encapsulation intermixing techniques. The inability to pattern devices with the technique prompted abandonment of this approach. This led to the development of a new technique, elevated temperature bombardment disordering (ETBD), to intermix multiple quantum well layers. The technique utilizes ion bombardment to create vacancy-interstitial pairs in the layers. This causes enhancement of the atom migration under the influence of the high temperatures, and the heterojunctions degrade. The ion species used for bombardment may be electrically inactive so that dopant-free mixing may be achieved. The advantage of ETBD is that layers may be mixed with lower temperatures and in shorter times than with other techniques. In addition, the elevated temperatures reduce agglomeration of the defects and therefore residual damage is less than with ion implantation at room temperature and subsequent annealing. The experiments indicate that 1-μm-thick multiple quantum well layers may be mixed with temperatures as low as 400°C, and bombardment times as short as 5 min, though higher temperatures are required for the shorter times.

Complete mixing of a multiple quantum well layer results in a uniform alloy material. Because the refractive index of the alloy and the quantum well layer are different close to the band edge, the technique is useful for fabricating optical waveguides. For ETBD to be useful in fabricating waveguides, residual damage had to be minimized, and the process must be patterned. To reduce residual damage, post-ETBD annealing was used. Furnace annealing at 650°C significantly improved material quality. Rapid thermal annealing at 950°C also improved material quality, but caused partial intermixing of the quantum wells from the masked portion of the sample. Two patterning techniques were demonstrated. One used epitaxially grown AlGaAs to stop the incident ions, and the second used a thick SiO_2 layer. Both techniques were successful, however the AlGaAs removal was not complete. With SiO_2 a 1-μm-thick multiple quantum well layer was intermixed in regions less than 2 μm wide. This was limited by the mask width. The negative process of 2 μm wide quantum well layers surrounded by intermixed material was also demonstrated. It appear as though lateral diffusion was minimal during the process.

Multiple quantum well waveguides were fabricated with ETBD. Characterization of the lateral far field of the guides provided evidence for the index guiding expected from the compositional averaging. The measured loss in the waveguides ranges from 3 cm^{-1} to 13 cm^{-1} depending on the specific fabrication procedure. The loss is not nearly as low as high quality ridge waveguides, but is comparable or less than waveguides fabricated with other mixing techniques.

The second part of the thesis concerned ultrafast optical characterization of semiconductor waveguides. A new, single-arm interferometer was demonstrated that allowed nonlinear phase changes to be measured while minimizing thermal contributions. The measurements show an ultrafast phase change with a turn-on and turn-off within the 500 fs measurement resolution. The magnitude of the nonlinear index of refraction, n_2, which leads to this ultrafast signal is $\approx 10^{-12}$ cm^2/W. Careful measurements indicate that n_2 shows a rapid enhancement as wavelengths approach the band edge. Although this is a very large nonresonant n_2, the experiments indicate that as intensities are increased to achieve large phase changes necessary for optical switching, two-photon absorption processes become apparent. The sign of the nonlinearity is negative which is consistent with band filling or a blue shift of the band edge.

Two-photon absorption limits the peak intensity in the guide, and also creates a real carrier population that causes long-lived phase changes due to band filling phenomena. At the peak intensities, this long-lived component that is comparable in magnitude to the ultrafast component of the phase change. The long lived component turns off in about 100 ps, which is consistent with carrier diffusion out of the waveguide core region.

For ultrafast switching therefore, this work indicates it is necessary to limit intensities so two-photon effects are minimal. Low intensities require waveguides to accumulate enough phase shift for device applications. For this low-intensity, ultrafast switching configuration, the optimum operating wavelength would be approximately 40 nm from the band edge. This represents a compromise between excessive loss at shorter wavelengths and a reduced n_2 at longer wavelengths. It was also shown that group velocity walk-off will restrict guide lengths to about 5mm. With this restriction, the accumulated phase shift for optimum operation is $\approx \pi/3$. This small phase shift rules out the possibility of couplers which require over π phase accumulation. This result does not preclude the possibility of larger phase shifts with higher intensities, but for this case, turn-off times would be significantly longer because of two-photon generated carrier effects.

The measurements on the multiple quantum well waveguides indicate that the quantum well operates similarly to the bulk material. The magnitude of n_2 is comparable in the two systems. Two-photon absorption is still a significant factor, and large phase shifts are only possible with significant two-photon generated carrier generation that causes large bandfilling phase changes. These measurements only investigated the case for the pump polarized along the layers, and the probe perpendicular. Other polarization configurations could show different results because of the anisotropy of the system. It is unlikely the difference will be larger than a factor of 5 or 10, because the band edge is not drastically different for the two polarizations.

Chapter 11

FUTURE WORK

Future work in the area of ETBD would include both material process development and applications to fabricating new optical devices. The most pressing issue is the improvement of the material quality. It is apparent that post-ETBD annealing procedures can significantly improve material quality. The work presented in this thesis hints that the amount of residual damage in the layers is likely related to the process parameters. As a simple example, lighter ions leave less residual damage. However, the type of ion, i.e. substitutional elements or column VIII, will probably influence damage effects. Also, lower ion flux and process times will lead to lower doses, and so possibly less damage. The temperature of the target may also influence the amount of damage because it determines the amount of vacancy and interstitial migration. The study of how these issues relate to the damage production could lead to a better process that yields better intermixed material quality.

Higher energy implantations to realize buried structures would also be an important future area of exploration. Recently, reports of MeV Si^+ implantation with post implantation annealing have been presented (Chen et al.). The higher energies could produce multiple implantations that would allow patterning in the transverse as well as the lateral directions. This would have interesting application to two-dimensional optical device fabrication. Another interesting material processing issue would be to try laser assisted localized heating to pattern the disordered regions. This would alleviate the need for masks. The application of using diffusion induced disordering to fabricate quantum wires has been reported (Zarem et al.). The improved pattering capability of ETBD would be very beneficial for this application.

In the area of optical device fabrication, buried waveguide devices would be an important follow up. Improving the loss of the guides would be important. This would require not only improving the material quality, but also improving the fabrication process to achieve better surface quality. The application of ETBD to fabricate buried heterostructure laser devices is currently underway. It is hoped that the impurity-free nature of the process, and improved edge definition will produce low threshold laser devices. Of course the important application of fabricating integrated optical modulators with lasers should also be attempted. Here the technique may improve the quality of the waveguides compared to those fabricated with other disordering techniques because it is impurity-free, but this would have to be examined in more detail.

If the material quality in the disordered region is improved, several interesting applications would be possible. The technique could also be applied to fabrication of nonlinear optical devices that operate on resonance by delineating small regions of multiple quantum wells. If the process could be graded across a wafer, possibly by grading the mask thickness or density, then the refractive index and absorption could be graded across a wafer. This could be used to complement the current work in the area of tapered waveguide fabrication. The other possibilities of changing the laser wavelengths across a wafer would also be achievable.

In the area of optical characterization, of waveguides, one very important issue that should be examined is the mechanism behind the ultrafast phase change. More information leading to the nature of this process could be found by two different experiments. If it is a population effect, the magnitude of n_2 would be pulse width dependent. Therefore, the pulse width dependence of the ultrafast n_2 should be investigated. Care must be taken to eliminate the long lived contribution for wavelengths near the band edge. In addition, a bound electron contribution to n_2 would have a different value for the pump and probe perpendicular than for parallel polarizations. This is a consequence of the symmetry of $\chi^{(3)}$. The population effect in a bulk should be similar in magnitude for both polarizations. Therefore a similar n_2 measurement with parallel pump and probe would be in order.

The application of the interferometer technique to other materials is also important. The technique is completely general, and in fact can be applied to studies of materials as well as devices. The newly emerging area of nonlinear polymers indicates nonlinear characterization of these material would be an interesting and useful study. If indeed the easy-to-make polymer materials do have interesting optical properties, the potential for ultrafast all-optical switching devices would be great.

The results of the experiments indicate that all-optical switching in semiconductors will not be readily achieved. However, the response shows that the numbers are not too far off. In fact, device configurations that produce carrier sweep-out or carrier recombination by stimulated emission could still prove promising methods of achieving all-optical switching in semiconductors.

REFERENCES

Adachi, S., "GaAs, AlAs, and $Al_xGa_{1-x}As$: materials parameters for use in research and device applications," J. Appl. Phys. 58 (1985), p. R1-R29.

Aitchison, J.S., Valera, J.D., and Walker, A.,C., "Whole sample and localized induced-absorption optical bistability in GaAlAs waveguides," Appl. Phys. Lett. 51 (1987), p.561-563.

Anderson, K.K., Donnelly, J.P., Wang, C.A., Woodhouse, J.D., and Haus, H.A., "Compositional disordering of an AlGaAs-GaAs multiple quantum well using ion bombardment at an elevated temperature," Appl. Phys. Lett. 53 (1988), p.1632-1634.

Anderson, K.K., Lagasse, M.J., Haus, H.A., Fujimoto, J.G., and Wang, C.A., "Femtosecond pump-probe interferometry studies of optical switching in AlGaAs waveguides," Conference on Lasers and Electro-Optics, 1989 Technical Digest series, vol. 11 (Optical Society of America), paper THI3, (1989).

Appleton, B.R., "Ion beam and laser mixing: fundamentals and applications," in Ion Implantation and Beam Processing, Williams, J.S., and Poate, J.M., eds., Academic Press, Inc., New York (1984), p. 189-261.

Banyai, W.C., Finlayson, N., Seaton, C.T., Stegeman, G.I., O'Neill, M., Cullen, T.J., and Ironside, C.N., "Saturation of the nonlinear refractive-index change in a semiconductor-doped glass channel waveguide," Appl. Phys. Lett. 54 (1989), p. 481-483.

Banyai, W.C., Finlayson, N., Seaton, C.T., Stegeman, G.I., "Saturation of the optical nonlinearities in semiconductor-doped glass channel waveguide devices," Conference on Lasers and Electro-Optics, 1989 Technical Digest series, vol. 11 (Optical Society of America), paper WA4, (1989).

Bechtel, J.H., and Smith, W.L., "Two-photon absorption in semiconductors with picosecond laser pulses," Phys. Rev.B 13 (1976), p. 3515-3522.

Boggess, T.F., Smirl, A.L., Moss, S. C., Boyd, I.W., and Van Stryland, E.W., "Optical limiting in GaAs," J. of Quantum Electron. QE-21 (1985), p. 488-494.

Burns, W.K., and Bloembergen, N., "Third-harmonic generation in absorbing media of cubic or isotropic symmetry," Phys. Rev. B 4 (1971), p. 3437-3442.

Cada, M., Keyworth, B.P., Glinski, J.M., SpringThorpe, A.J., and Mandeville, P., "Experiment with multiple-quantum-well waveguide switching element," J. Opt. Soc. Am. B 5 (1988), p. 462-465.

Carter, G., and Grant W.G., Ion Implantation of Semiconductors New York: John Wiley and Sons, Inc., 1976, ch. 3.

Casey, Jr., H.C., and Panish, M.B., Heterostructure Lasers Part B: Materials and Operating Characteristics New York: Academic Press, 1978.

Chang, L.L., and Koma, A., "Interdiffusion between GaAs and AlAs," Appl. Phys. Lett. 29 (1976), p.138-141.

Chang, T.Y., "Fast self-induced refractive index changes in optical media: a survey," Opt. Eng. 20 (1981), p. 220-232.

Chemla, D.S., and Miller, D.A.B., "Room-temperature excitonic nonlinear-optical effects in semiconductor quantum-well structures," J. Opt. Soc. Am. B 2 (1985), p.1155-1173.

Chemla, D.S., Miller, D.A.B., and Schmitt-Rink, S.,"Generation of ultrashort electrical pulses through screening by virtual populations in biased quantum wells," Phys. Rev. Lett. 59 (1987), p.1018-1021.

Chemla, D.S., Miller, D.A.B., and Smith, P.W. "Nonlinear optical properties of GaAs/GaAlAs multiple quantum well material: phenomena and applications," Opt. Eng. 24 (1985), p. 556-564.

Chemla, D.S., "Quasi-two-dimensional excitons in GaAs/$Al_xGa_{1-x}As$ semiconductor multiple quantum well structures," Helvetica Physica Acta 56 (1983), p. 607-367.

Chen, S., Tong Lee, S., Braunstein, G., and Rajeswaran, G., "Study of layer disordering in MeV Si implanted III-V superlattices," Mat. Res. Soc. Symp., Nov. 1988, paper W6.7.

Cibert, J., Petroff, P.M., Werder, D.J., Pearton, S.J., Gossard, A.C., and Englidh, J.H., "Kinetics of implantation enhanced interdiffusion of Ga and Al at GaAs-$Ga_xAl_{1-x}As$ interfaces," Appl. Phys. Lett. 49 (1986), p.223-225.

Cotter, D., Ironside, C.N., Ainslie, B.J., and Girdlestone, H.P., "Picosecond pump-probe interferometric measurement of optical nonlinearity in semiconductor doped fibres," Opt. Lett. 14 (1989), p. 317-319.

Dabkowsli, F.P., Gavrilovic, P., Meehan, K., Stutius, W., Williams, J.E., Shahid, M.A., and Mahajan, S., "Disordering of the ordered structure in metalorganic chemical vapor deposition grown GaInP on (001) GaAs substrates by zinc diffusion," Appl. Phys. Lett. 52 (1988), p. 2142-2144.

Deppe, D.G., and Holonyak, Jr., N., "Atomic diffusion and impurity-induced layer disordering in quantum well III-V semiconductor heterostructures," J. Appl. Phys. 64 (1988), p. R93-R113.

Deppe, D.G., Guido, L.J., Holonyak, Jr., N., Hsieh, K.C., Burnham, R.D., Thornton, R.L., and Paoli, T.L., Appl. Phys. Lett. 49 (1986), p.510-512.

Deppe, D.G., Jackson,G.S., Holonyak, Jr., N., Burnham, R.D., and Thornton, R.L., "Coupled-stripe $Al_xGa_{1-x}As$-GaAs quantum well lasers defined by impurity-induced (Si) layer disordering," Appl. Phys. Lett. 50 (1987), p.632-634.

Deri, R.J., Kapon. E., and Schiavone, L.M., "Scattering in low-loss GaAs/AlGaAs rib waveguides," Appl. Phys. Lett. 51 (1987), p.789-791.

Dienes, G.J., and Damask, A.C., "Radiation enhanced diffusion in solids," J. of Appl. Phys 29 (1958), p.1713-1721.

Dobisz, E.A., Tell, B., Craighead, H.G., and Tamargo, M.C., "Disordering of AlAs-GaAs superlattices by Si and S implantation at different implant temperatures," J. Appl. Phys. 60 (1986), p.4150-4153.

Donnelly, J.P., Haus, H.A., and Whitaker, N.A., "Symmetric three guide optical couplers in GaAs," J. Lioghtwave Tech. LT-1 (1983), p. 1147-1151.

Epler, J.E., Burnham, R.D., Thornton, R.L., Paoli, T.L., and Bashaw, M.C., "Laser induced disordering of GaAs-AlGaAs superlattice and incorporation of Si impurity," Appl. Phys. Lett., 49 (1986), p.1447-1449.

Epler, J.E., Ponce, F.A., Endicott, F.J., and Paoli, T.L., "Layer disordering of GaAs-AlGaAs superlattices by diffusion of laser incorporated Si," J. Appl. Phys. 64 (1988), p.3439-3444. a.

Epler, J.E., Thornton, R.L., and Paoli, T.L., "Very low threshold buried heterostructure quantum well lasers by laser assisted disordering," Appl. Phys. Lett. 52 (1988), p. 1371-1373. b.

Friberg, S.R., and Smith, P.W., "Nonlinear optical glasses for ultrafast optical switches," J. of Quantum Electron. QE-23 (1987), p. 2089-2094.

Frohlich D., Reimann, K., and Wille, R., "Optical Stark effect of excitons in semiconductors," J. of Luminescence 38 (1987), p.235-238.

Fukuzawa, T., Semura, S., Saito, H., Ohta, T., Uchida, Y., and Nakashima, H., "GaAlAs buried multiquantum well lasers fabricated by diffusion-induced disordering," Appl. Phys. Lett. 45 (1984), p.1-3.

Gabriel, M.C., Haus, H.A., and Ippen, E.P., "Thermal index changes by optical absorption in group III-V semiconductor waveguides," J. Lightwave Tech. LT-4 (1986), p. 1482-1493.

Gavrilovic, P., Deppe, D.G., Meehan, K., Holonyak, Jr., N., Coleman, J.J., and Burnham, R.D., "Implantation disordering of AlGaAs superlattices," Appl. Phys. Lett. 47 (1985), p.130-132. a.

Gavrilovic, P., Meehan, K., Guido, L.J., Holonyak, Jr., N., Eu, V., Feng, M., Burnham, R.D., "Si-implanted and disordered stripe-geometry $Al_xGa_{1-x}As$-GaAs quantum well lasers," Appl.Phys. Lett. 47 (1985), p. 903-905. b.

Gibbons, J.F., Johnson, W.S., and Myloroie, S.W., Projected Range Statistics: Semiconductors, and Related Materials, 2nd. ed. Strousberg, Pa.: Halsted Press, 1975.

Ghandi, S.K., VLSI Fabrication Principles New York: John Wiley and Sons 1983.

Guha, S., Van Stryland, E.W., and Soileau, M.J., "Self-defocusing in CdSe induced by charge carriers created by two-photon absorption," Opt. Lett. 10 (1985), p. 285-287.

Guido, L.J., Holonyak,Jr., N., Hsieh, K.C., Kaliski, R.W., Plano,W.E., Burnham, R.D., Thornton, R.L., Epler, J.E., and Paoli, T.L., "Effects of dielectric encapsulation and As overpressure on Al-Ga interdiffusion in AlGaAs-GaAs quantum-well heterostructures," J.Appl.Phys. 61 (1987), p.1372-1379. a.

Guido, L.J., Jackson, G.S., Plano, W.E., Hsieh, K.C., Holonyak, Jr., N., Burnham, R.D., Epler, J.E., Thornton, R.L., and Paoli, T.L., "Index-guided $Al_xGa_{1-x}As$-GaAs quantum-well heterostructure lasers fabricated by vacancy-enhanced impurity-induced layer disordering from an internal $(Si_2)_y(GaAs)_{1-y}$ source," Appl. Phys. Lett. 50 (1987), p.609-611.b.

Guseva, M.I., and Mansurova, A.N., "Radiation-enhanced diffusion of boron in germanium during ion implantation," Radiation Effects, 20 (1973), p.207-210.

Haug, H., and Schmitt-Rink, S., "Basic mechanisms of the optical nonlinearities of semiconductors near the band edge," J. Opt. Soc. Am. B2 (1985), p. 1135-1142.

Haus, H.A., and Whitaker, N.A., "All-optical logic devices using group III-V semiconductor waveguides," SPIE: International Conference on Integrated Optical Circuit Engineering, 578 (1985), p.122-129.

Haus, H.A., Waves and Fields in Optoelectronics Englewood Cliffs, New Jersey: Prentice-Hall, Inc. 1984.

Hirayama,Y., Suzuki,Y., Tarucha,S., and Okamoto, H., "Compositional disordering of GaAs-AlGaAs superlattice by focused ion beam implantation and its application to submicron structure fabrication, " Japan. J. of Appl. Phys. 24 (1985), p.L516-L518.

Holonyak, Jr., N., Laidig, W.D., Camras, M.D., Coleman,J.J., and Dapkus, P.D., "IR-red GaAs-AlAs superlattice laser monolithically integrated in a yellow-gap cavity," Appl. Phys. Lett. 39 (1981), p.102 -105.

Hulin, D., Mysyrowicz, A., Antonetti, A., Migus, A., Masselink, W.T., Morkoc, H., Gibbs, H.M., Peyghambarian, N., "Ultrafast all-optical gate with subpicosecond ON and OFF response time," Appl. Phys. Lett. 49 (1986), p.749-751.

Ishda, K., Matsui, K., Fukunaga, T., Kobayashi, J., Morita, T., Miyauchi, E., and Nakashima, H., "Scan speed effects on enhanced disordering of GaAs-AlGaAs superlattices by focused Si ion beam implantation," Appl. Phys. Lett. 51 (1987), p. 109-111.

Jain, R.K., and Klein, M.B., "Degenerate four-wave mixing near the band gap of semiconductors," Appl. Phys. Lett., 35 (1979), p.454-456.

Jensen, B., and Torabi, A., "Dispersion of the refractive index of GaAs and $Al_xGa_{1-x}As$," J. of Quantum Electron. 19 (1983), p.877-882.

Jensen, S.M., "The nonlinear coherent coupler," J. Quantum Electron. QE-18 (1982), p.1580-1583.

Jha, S.S., and Bloembergen, N., "Nonlinear optical susceptibilities in group-IV and III-V semiconductors," Phys. Rev. 171 (1968), p. 891-898.

Jin, R., Chuang, C.L., Gibbs, H.M., Koch, S.W., Polky, J.N., and Pubnaz, G.A., "Picosecond all-optical switching in single-mode GaAs/AlGaAs strip-loaded nonlinear directional couplers," Appl.Phys. Lett. 53 (1988), p. 1791-1793.

Julien, F., Swanson, P.D., Emanuel, M.A., Deppe, D.G., DeTemple, T.A., Coleman, J.J., and Holonyak,Jr., N., "Impurity induced disorder-delineated optical waveguides in GaAs-AlGaAs superlattices," Appl. Phys. Lett. 50 (1987), p.866-869.

Kafke, J.D., and Baer, T., Proc. Soc. Photo.-Opt.Instrum. Eng. 533 (1985), p.38.

Kahen, K.B., and Leburton, J.P., "Exciton effects on the index of refraction of multiple quantum wells and superlattices," Appl. Phys. Lett. 49 (1986), p.734-736. a.

Kahen, K.B., and Leburton, J.P., "Optical constants of GaAs-$Al_xGa_{1-x}As$ superlattices and multiple quantum wells," Phys. Rev. B 33 (1986), p.5465-5472. b.

Kahen, K.B., Rajeswaran, G., and Lee, S.T., "Mechanism for ion-induced mixing of GaAs-AlGaAs interfaces by rapid-thermal annealing," Appl. Phys. Lett. 53 (1988), p. 1635-1637.

Kaliski, R.W., Gavrilovic, P., Meehan, K., Gavrilovic, J., Hsieh, K.C., Jackson, G.S., Holonyak, Jr., N., Coleman, J.J., Burnham, R.D., Thronton, R.L., and Paoli, T.L., "Photoluminescence and stimulated emission in Si- and Ge-disordered $Al_xGa_{1-x}As$-GaAs superlattices," J. Appl. Phys. 58 (1985), p. 101.

Kaliski, R.W., Nam, D.W., Deppe, D.G., Holonyak, Jr., N., Hsieh, K.C., and Burnhan, R.D., J. Appl. Phys. 62 (1987), p. 998.

Kam Wa, P.L., and Robson, P.N., "Optical nonlinearities in a passive GaAs/ GaAlAs multiple quantum well strain-induced waveguide," J. of Quantum Electron. 23 (1987), p. 1962-1967.

Kamata, N., Kobyashi, K., Endo, K., Suzuki, T., and Misu, A., Jpn. J. Appl. Phys. 26 (1987), p. 1092.

Kessler, M.P., Ph.D. Thesis, Massachusetts Institute of Technology Department of Electrical Engineering and Computer Science. 1987.

Knox, W.H., Conference for Lasers and Electro-Optics, Baltimore, Maryland (1989).

Knox, W.H., "Fork, R.F., Downer, M.C., Miller, D.A.B., Chemla, D.S., and Shank, C.V.," Phys. Rev. Lett. 54 (1985), p.1306-1309.

Kobayashi, J., Fukunaga, T., Ishida, K., Nakashima, H., Flood, J.D., Bahir, G., and Merz, J.L., "Effect of rapid thermal annealing for the compositional disordering of Si-implanted AlGaAs/GaAs superlattices," Appl. Phys. Lett. 50 (1987), p. 519-520.

Koch, S.W., Peyghambarian, N., and Gibbs, H.M., "Band-edge nonlinearities in direct-gap semiconductors and their application to optical bistability and optical computing," J. Appl. Phys. 63 (1988), p. R1-R11.

Kressel, H., and Butler, J.K., Semiconductor Lasers and Heterojunction LED's New York: Academic Press, 1977, p.413.

LaGasse, M.J., Anderson, K.K., Haus, H.A., and Fujimoto, J.G., "Direct femtosecond measurements of the nonlinear index in AlGaAs" Appl. Phys. Lett., to be published.

LaGasse, M.J., Anderson, K.K., Haus, H.A., and Fujimoto, J.G., "Femtosecond all-optical switching in AlGaAs waveguides using a time-division interferometer," Appl. Phys. Lett. 54 (1989), p.2068-2070. a.

LaGasse, M.J., Wong, D.L., Haus, H.A., and Fujimoto, J.G., "Ultrafast switching with a single-fiber interferometer," Optics Lett. 14 (1989) p.311-313 . b.

Laidig, W.D., Holonyak, Jr., N., Camras, M.D., Hess, K., Coleman, J.J., Dapkus, P.D., and Bardeen, J., "Disorder of an AlAs-GaAs superlattice by impurity diffusion," Appl. Phys. Lett. 38 (1981), p.776-778.

Lattes, A., Haus, H.A., Leonberger, F.J., and Ippen, E.P., "An ultrafast all-optical gate," J. of Quantum Electron. QE-19 (1983), p.1818-1723.

Lee, Y.H., Chavez-Pirson, A., Koch, S.W., Gibbs, H.M., Park, S.H., Morhange, J., Jeffery, A., Banyai, L., Gossard, A.C., and Wiegmann, W., "Room-temperature optical nonlinearities in GaAs," Phys. Rev. Lett. 57 (1986), p.2446-2449. b.

Lee, Y.H., Warren, M., Olbright, G.R., Gibbs, H.M., Peyghambarian, N., Venkaatesan, T., Smith, J.S., and Yariv, A., "Streak-camera observation of 200-ps recovery of an optical gate in a windowless GaAs etalon array," Appl. Phys. Lett., 48 (1986), p. 754-756. a.

Lindhard,J., Scharff, M., and Schiott, Mat. Fys. Medd. Dan. Vid. Selsk. 33 (1963).

Longini, R.L., "Rapid zinc diffusion in gallium arsenide," Solid State Electronics 5 (1962), p. 127-130.

Manning, J.R., Diffusion Kinetics for Atoms in Crystals Princeton, New Jersey: D. Van Nostrand Company, Inc. 1968.

Matsui, K., Takamori, T., Fukunaga, T., Marusawa, T., Nakashima, H., "Ion-implantation induced damage in $Al_xGa_{1-x}As$ and superlattices studied by Rutherford backscattering," Japan. J. of Appl. Phys. 26 (1987), p. 482-486.

Meehan, K., Holonyak, Jr., N., Brown, J.M., Nixon, M.A., Gavrilovoc, P., and Burnham, R.D., "Disorder of an AlGaAs-GaAs superlattice by donor diffusion," Appl. Phys. Lett. 45 (1984), p.549-551.

Mei, P., Venkatesan, T., Schwarz, S.A., Stoffel, N.G., Hart, D.L., Florez, L.A., "Comparative studies of ion-induced mixing of GaAs-AlAs superlattices," Appl. Phys. Lett., 52 (1988), p.1487-1489.

Miller, D.A.B., Chemla, D.S., Eilenberger, D.J., Smith, P.W., Gossard, and A.C., Tsang, W.T., "Large room-temperature optical nonlinearity in $GaAs/Ga_{1-x}Al_xAs$ multiple quantum well structures," Appl. Phys. Lett. 41 (1982), p. 679-681.

Miller, D.A.B., Seaton, C.T., Prise, M.E., and Smith, S.D., "Band-gap-resonant nonlinear refraction in III-V semiconductors," Phys. Rev. Lett. 47 (1981) p.197-199.

Myers, D.R., Arnold, G.W., Dawson, L.R., Biefeld, R.M., Hills, C.R., and Doyle, B.L., "Temperature dependent damage production in ion-implanted strained layer superlattices," Appl. Phys. Lett. 51 (1987), p.517-519.

Myers, D.R., Arnold, G.W., Zipperian, T.E., Dawson, L.R., Biefeld, R.M., Fritz, I.J., and Barnes, C.E.., "Zinc-implantation-disordered (InGa)As/GaAs strained-layer superlattice diodes," J. Appl. Phys. 60 (1986), p.1131-1134.

Mysyrowicz, A., Hulin, D., Antonetti, A., Migus, A., Masselink, W.T., and Morkoc, H., "Dressed excitons in a multiple-quantum-well structure: evidence for an optical Stark effect with femtosecond response time," Phys. Rev. Lett. 56 (1986), p.2748-2751.

Namba, S., Masuda, K., Gamo, K., and Doi, A., "Enhanced diffusion in ion implanted silicon," Radiation Effects 6 (1973), p.115-120.

Olbright, G.R., and Peyghambarian, N., "Interferometric measurement of the nonlinear index of refraction , n_2, of CdS_xSe_{1-x}-doped glasses," Appl. Phys. Lett. 48 (1986), p. 1184-1186.

Ovadia, S., Gibbs, H.M., Jewell, J.L., Sarid, D., and Peyghambarian, N., "Evidence that room temperature optical bistability is excitonic in both bulk and multiple-quantum-well gallium arsenide," Opt. Eng. 24 (1985), p.585-568.

Pape, I.J., Kam Wa, P.L., David, J.P.R., Claxton, P.A., and Robson, P.N., "Disordering of GaInAs/InP multiple quantum well layers by sulpher diffusion, " Electron. Lett. 24 (1988), p. 1217-1218.

Park, S.H., Morhange, J.F., Jeffery, A.D., Morgan, R.A., Chavez-Pirson, A., Gibbs, H.M., Koch, S.W., Peyghambarian, N., Derstine, M., Gossard, A.C., English, J.H., and Weigmann, W., "Measurements of room-temperature band-gap-resonant optical nonlinearities of GaAs/AlGaAs multiple quantum wells and bulk GaAs," Appl. Phys. Lett. 52 p.1201-1203, (1988).

Peyghambarian, N., and Gibbs, H.M., "Optical nonlinearity, bistability, and signal processing in semiconductors," J. Opt. Soc. Am. B 2 (1985), p.1215-1227.

Phillips, M.W., private communication.

Pidgeon, C.R., Wherrett, B.S., Johnston, A.M., Dempsey, J., and Miller, A., "Two-photon absorption in zinc-blende semiconductors," Phys. Rev. Lett. 42 (1979), p. 1785-1788.

Pikar, K.A., "Ion implantation in silicon--physics, processing, and microelectronic devices," Appl. Sold State Sci. Adv. in Mater. and Device Res., 5 (1975), p.151-249.

Ralston, J., Wicks, G.W., Eastman, L.F., DeCoopman, B.C., and Carter, C.B., "Defect structure and intermixing of ion-implanted AlGaAs/GaAs superlattices," J.Appl. Phys. 59 (1986), p.120-123.

Ralston, J.D., Schaff, W.J., Bour, D.P., and Eastman, L.F., "Room-temperature exciton electroabsorption in partially intermixed GaAs/AlGaAs quantum well waveguides," Appl. Phys. Lett. 54 (1989), p. 534-536.

Rao, E.K.V., Ossart, P. Alexandre, F., and Thibierge, H., Appl. Phys. Lett. 50 (1987), p.588-590.

Rao, E.K.V., Thibierge, H., Brillouet, F., Alexandre, F., and Azoulay, R., Appl. Phys. Lett. 46 (1985), p. 867-869.

Rief, R., Semiconductor Processing Technology , Massachusetts Institute of Technology Department of Electrical Engineering and Computer Science, course notes.

Schlesinger, T.E., Lee, J., and Kuech, T.F., "Interdiffusion of Al and Ga in (Al,Ga)As/ GaAs quantum wells," Proc. Materials Research Society (1987), p.241-246.

Schmitt-Rink, S., and Chemla, D.S., "Collective excitations and the dynamical optical Stark effect in a coherently driven system," Phys. Rev. Lett. 57 (1986), p. 2752-2755.

Schmitt-Rink, S., Chemla, D.S., and Miller, D.A.B., "Theory of transient excitonic optical nonlinearities in semiconductor quantum well structures," Phys. Rev. B 32 (1985), p.6601-6609.

Schmitt-Rink, S., "Coherent nonlinear optical processes in semiconductors. Physics and applications," Phys. Stat. Sol. 150 (1988), p.349-356.

Schwarz, S.A., Venkatesan, T., Hwang, D.M., Yoon, H.W., and Bhat, R., "Process dependence of AlAs/GaAs superlattice mixing induced by silicon implantation," Appl. Phys. Lett. 50 (1987), p.281-283.

Shirasaki, M., Haus, H.A., and Wong, D.L., "A nonlinear fiber interferometer and logic gate," Conference for Lasers and Electro-Optics, Baltimore, MD, April 1987.

Silberberg, Y., Smith, P.W., Miller, D.A.B., Tell, B., Gossard, A.C., and Wiegmann, W., "Fast nonlinear optical response from proton-bombarded multiple quantum well structures," Appl. Phys. Lett. 46 (1985), p. 701-703.

Smirl, A.L., Valley, G.C., Bohnert, K.M., and Boggess, T.F., "Picosecond photorefractive and free-carrier energy transfer in GaAs at 1 μm," J. of Quantum Electron. QE-24 (1988), p. 289-303.

Spector, H.N., "Two-photon absorption in semiconducting quantum-well structures," Phys. Rev.B 35 (1987), p.5876-5879.

Stegeman, G.I., "Guided wave approaches of optical bistability," J. of Quantum Electron. QE-18 (1982), p. 1610-1619.

Stegeman, G.I., Wright, E.M., Finlayson, N., Zanoni, R., and Seaton, C.T., "Third order nonlinear integrated optics," J. of Lightwave Tech. 6 (1988), p. 953-970.

Sumida, H., Asahi, H., Jae Yu, S., Asami, K.. Gonda, S., and Tanoue, H., "Intermixing of InGaAs/InP multiple quantum well structures by Ga implantation," Appl. Phys. Lett. 54 (1989), p. 520-522.

Tai, K., Mysyrowicz, A., Fischerm R.J., Slusher, R.E., and Cho, A.Y., "Two-photon absorption spectroscopy in GaAs quantum wells," Phys. Rev. Lett. 62 (1989), p.1784-1787.

Tan, T.Y., and Gosele, U., "Diffusion mechanisms and superlattice disordering in GaAs," Mat. Sci. and Eng. B1 (1988), p. 47-65.

Thornton, R.L., Burnham, R.D., Paoli, T.L., Holonyak, Jr., N., and Deppe, D.G., "Highly efficient multiple emitter index guided array lasers fabricated by silicon impurity induced disordering," Appl. Phys. Lett. 48 (1986), p.7-9.

Thornton, R.L., Epler, J.E., and Paoli, T.L., "Monolithic integration of a transparent dielectric waveguide into an active laser cavity by impurity induced disordering," Appl. Phys.Lett. 51 (1987), p.1983-1985.

Tong-Lee, S., Braunstein, G., Fellinger, P., Kahen, K.B., and Rajeswaren, G., "Disordering of Si-implanted GaAs-AlGaAs superlattices by rapid thermal annealing," Appl. Phys. Lett. 53 (1988), p. 2531-2533.

Tsuchimoto, T., and Tokuyama, T., "Enhanced diffusion of boron and phosphorous in silicon during hot substrate ion implantation," Radiation Effects 6 (1970), p.121-129.

Van Stryland, E.W., Vanherzeele, H., Woodall, M.A., Soileau, M.J., Smirl, A.L., Guha, S., and Boggess, T.F., "Two photon absorption, nonlinear refraction, and optical limiting in semiconductors," Opt. Eng. 24 (1985), p. 613-623.

van der Ziel, J.P., Ilegems, M., and Mikulyak, R.M., "Optical birefringence of thin GaAs-AlAl multilayer films," Appl. Phys. Lett. 28 (1976), p.735-737.

VanVechten, J.A.,"Intermixing of an AlAs-GaAs superlattice by zinc diffusion," J.Appl. Phys. 53 (1982), p.7082.

Venkatesan, T., Schwarz, S.A., Hwang, D.M., Bhat, R., Koza, M., Yoon, H.W., Mei, P., Arakawa, Y., and Yariv, A., "Dose dependent mixing of AlAs-GaAs superlattices by Si ion implantation," Appl.Phys.Lett. 49 (1986), p.701-703.

Von Lehmen, A., Chemla, D.S., Zucker, J.E., and Heritage, J.P., "Optical Stark effect on excitons in GaAs quantum wells," Opt. Lett. 11 (1986), p.609-611.

Vossen, J.L., and Kern, W., Thin Film Processes Academic Press, Inc. 1978.

Wang, C.A., Patnaik, S., Caunt, J.W., and Brown, R.A., J. Cryst. Growth, to be published.

Warren, M., Gibbons, W., Komatsu, K., Sarid, D., Hendricks, D., Gibbs, H.M., and Sugimoto, M., "Electronic optical bistability in GaAs/AlGaAs strip-loaded waveguide," Appl. Phys. Lett. 51 (1987), p. 1209-1211.

Weiler, M.H., "Nonparabolicity and exciton effects in two-photon absorption in zincblende semiconductors," Solid State Comm. 39 (1981), p.937-940.

Weiner, J.S., Chemla, D.S., Miller, D.A.B., Haus, H.A., Gossard, A.C., Wiegmann, W., and Burrus, C.A., "Highly anisotropic optical properties of single quantum well waveguides," Appl. Phys. Lett. 47 (1985), p.664-666.

Werner, J., Kapon, E., Von Lehmwn, A.C., Bhat, R., Colas, E., Stoffel, N.G., and Schwarz, S.A., "Reduced optical waveguide losses of a partially disordered GaAs/AlGaAs single quantum well laser structure for photonic integrated circuits," Appl. Phys. Lett. 53 (1988), p. 1693-1695.

Wherrett, B.S., "Scaling rules for multiphoton interband absorption in semiconductors," J. Opt. Soc. Am.B 1 (1984), p. 67-72.

Wood, T.H., Burrus, C.A., Miller, D.A.B., Chemla, D.S., Damen, T.C., Gossard, A.C., and Wiegmann, W., "131 ps optical modulation in semiconductor multiple quantum wells (MQW's), J. of Quantum Electron. 21 (1985), p.117-118.

Wu, X.S., Coldren, L.A., and Merz, J.L., "Selective etching characteristics of HF for $Al_xGa_{1-x}As/GaAs$," Electron. Lett. 21 (1985).

Yamanishi, M., and Kurosaki, M., "Ultrafast optical nonlinearity by virtual charge polarization in DC-biased quantum well structures," J. of Quantum Electron. 24 (1988), p.325-331.

Yuen, S.Y., "Fast relaxing absorptive nonlinear refraction in superlattices," Appl. Phys. Lett. 43 (1983), p. 813-815.

Zarem, H.A., Sercel, P.C., Hoenk, M.E., Lebens, J.A., and Vahala, K.J., "Nanometer scale wire structures fabricated by diffusion-induced selective disordering of a GaAs(AlGaAs) quantum well," Appl. Phys. Lett. 54 (1989), p. 2692-2694.